SYNTHESIS, CHARACTERIZATION AND PHASE EQUILIBRIUM OF PEROVSKITE OXIDES AND DEVELOPMENT OF INTERMEDIATE TEMPERATURE SOLID OXIDE FUEL CELLS

THESIS

Submitted to the

UNIVERSITY OF MADRAS

in partial fulfillment of the requirements

for the award of the degree of

DOCTOR OF PHILOSOPHY

in

CHEMISTRY

By

M. KUMAR

NATIONAL METALLURGICAL LABORATORY (MADRAS CENTRE)
CSIR MADRAS COMPLEX,
TARAMANI, CHENNAI-600 113, INDIA

June 2010

ACKNOWLEDGMENTS

I would like to express my sincere gratitude to my supervisor, ***Dr. S. Srikanth,*** *Director, National Metallurgical Laboratory, Jamshedpur, for his constant encouragement, motivation, contributions, guidance and invaluable discussions.*

I am also thankful to ***Dr. G. Bhaskaraju*** *(Scientist-in-Charge, NML Madras Centre) and* ***Dr. S. Prabhakar (Scientist)*** *for their valuable suggestions.*

I would like to pay my sincere thanks to ***Prof. S.P. Mehrotra*** *(former Director, NML, Jamshedpur) and* ***Dr. Sukmal Ghosh*** *(acting Director, NML Jamshedpur) for providing permission and the necessary facilities to carry out my research work.*

I am grateful to ***Dr. B. R. V. Narashimman*** *and* ***Dr. D.S. Rao*** *for their invaluable suggestion and support in the experimental works.*

I am thankful to ***Mr. B. Ravikumar*** *for his assistance in carrying out XRD,* ***Dr. T.C. Alex*** *for assistance in the thermal analysis and* ***Mr. Swapan Das*** *for help in SEM analysis.*

I express my special thanks to ***Dr. I. Arulraj*** *and* ***Dr. S. D. Dheenadyalan*** *for their constant motivation and encouragement.*

I am indebted to my friends ***Mrs. K. Janaki, Mrs. M. Ravia, Mr. T. Balaji, Mrs. J.P. Deebasree, Mr. S. Sakthivel, Mr. K. Balaji, Mrs. R. Veena, Mr. K. Chennakesavalu, Mr. P. Lakshmipathiraj, Mr. M.T. Karuppiah*** *for their help and support.*

I also convey my thanks to all my friends and colleagues at the NML Madras Centre for their companionship and help.

I am grateful to CSIR for financial support through the award of Research Associateship during the period of my research.

My heartfelt thanks to my parents, my brothers and all my family members for their wishes, encouragement and their prayers for my success.

A large part of this work was carried out under a NMITLI project on Hydrogen Energy and Fuel Cells. I am indebted to CSIR for providing me this opportunity to work in this area.

Finally, my thanks to the power of nature for better understanding.

(Kumar. M)

DECLARATION

I hereby declare that the Ph.D thesis entitled **"SYNTHESIS, CHARACTERIZATION AND PHASE EQUILIBRIUM OF PEROVSKITE OXIDES AND DEVELOPMENT OF INTERMEDIATE TEMPERATURE SOLID OXIDE FUEL CELLS"** submitted for the award of the degree of Doctor of Philosophy is the bonafide record of independent research work done by me at National Metallurgical Laboratory Madras Centre, during the period from April 2006 to June 2010 under the supervision of **Dr. S. SRIKANTH** the then Scientist-in-charge, National Metallurgical Laboratory Madras Centre, CSIR Complex, Taramani, Chennai-600113 and has not formed the basis for the award of any Degree, Diploma, Associateship, Fellowship or other similar titles in this or any other university.

(KUMAR. M)

National Metallurgical Laboratory
Madras Centre, CSIR Complex
Taramani, Chennai-600113

TABLE OF CONTENTS

CHAPTER I
INTRODUCTION

CHAPTER II
REVIEW OF LITERATURE

CHAPTER III
EXPERIMENTAL METHODS

CHAPTER IV
RESULTS AND DISCUSSION

CHAPTER V

CONCLUSIONS AND SCOPE FOR FUTURE WORK

BIBILOGRAPHY

CHAPTER I

INTRODUCTION

1.1. FUEL CELLS: OVERVIEW

1.1.1. Fuel cell

A fuel cell is a device which directly converts chemical energy into electrical energy without any intermediate steps. As long as the fuel and oxidant are continuously supplied, it can continue to generate heat and electricity. A fuel cell consists of an exclusive ion-conducting electrolyte between an anode (negatively charged electrode where electrochemical oxidation occurs) and a cathode (a positively charged electrode where electrochemical reduction occurs). At the anode, the electrochemical oxidation reaction occurs generating electrons and ions and since the electrolyte permits only ionic transport and blocks electronic transport, the electrons flow through the outer circuit towards the cathode, where it is consumed through an electrochemical reduction reaction. A schematic of a hydrogen fuel cell is shown in Fig.1.1

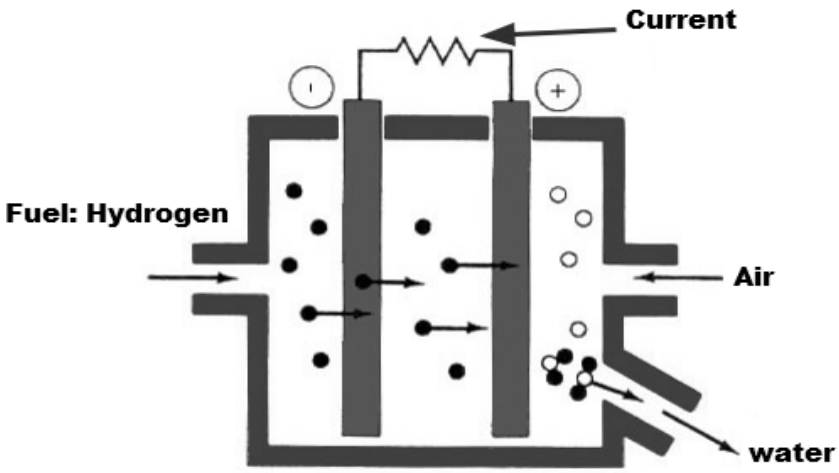

Fig.1.1 A Schematic of a Fuel Cell

1.1.2. Types of fuel cells

Fuel cells are categorized based on the type of electrolyte i.e., the nature of the ionic conductor. The various types of fuel cells are compared in Table 1.1. Several differences exist between the various fuel cells in application, design, size, costs and operating range. The nature of electrolyte determines the nature of fuel and operating temperature, which has consequences for the design, the efficiency of the fuel cell and, indirectly, for the choice of other materials needed for the assembly of the fuel cell.

Table 1.1 Comparison of different types of fuel cells [Vielstich et al, 2003]

	PEFC	AFC	PAFC	MCFC	ITSOFC	TSOFC
Electrolyte	Nafion Polymer membrane	NaOH+KOH bath	Phosphoric acid	Li_2CO_3+ K_2CO_3 bath	Gadolinia doped ceria, doped lanthanum gallate	$(Y_2O_3)ZrO_2$
Operating Temperature	80 ^oC	65-220 ^oC	205 ^oC	650 ^oC	600-800^oC	600-1000^oC
Charge carrier	H^+	OH^-	H^+	CO_3^{2-}	O^{2-}	O^{2-}
External reformer for CH_4 (below)	Yes	Yes	Yes	No	No	No
Primary Cell Components	Carbon based	Carbon based	Graphite - based	Stainless-based	Ceramic	Ceramic
Catalyst	Platinum	Platinum	Platinum	Nickel	Perovskites	Perovskites
Product Water Management	Evaporative	Evaporative	Evaporative	Gaseous Product	Gaseous Product	Gaseous Product
Product heat Management	Process Gas+ Independent Cooling Medium	Process Gas+ Electrolyte Calculation	Process Gas+ Independent Cooling Medium	Internal Reforming + Process gas	Internal Reforming + Process gas	Internal Reforming+ Process gas

The temperature also imposes an additional restriction on the nature of fuel that may be used. For high temperature fuel cells such as the molten carbonate fuel cell (MCFC) and the Solid Oxide Fuel Cell (SOFC), it is in principle possible to use a wide range of hydrocarbons such as natural gas, bio-gas or coal-gas which can be reformed internally to hydrogen and carbon-monoxide. Up to an operating temperature of 600^{o}C (such as in MCFC), a catalyst is required especially for the oxygen reduction reaction. However, at operating temperatures of 900 to 1000 ^{o}C (such as in SOFC), catalysts are not required either to promote the anode and cathode reactions or for the reforming of the hydrocarbons. The high operating temperatures of MCFC and SOFC make various applications possible, including co-generation of electricity and Fiscer-Tropsch synthesis of chemicals [Vayenas et al, 1991], electrolysis to produce hydrogen or production of high purity oxygen (reversed fuel cell mode). Low temperature fuel cells [proton membrane fuel cells (PEFC), alkaline fuel cells (AFC) and phosphoric acid fuel cells (PAFC) operate at temperatures insufficient to enable either reforming or direct oxidation of hydrocarbon fuels. For these fuel cells, the usual choice of fuel is hydrogen or methanol. Because of their low temperature of operation, these fuel cells are the best

candidates for small scale applications such as for transportation. A detailed description of the different types of fuel cells can be found elsewhere [Steele, 1990; Kordesch, 1990; Bossel, 1993, Vielstich et al, 2003].

1.1.3. History of SOFC

The history of the fuel cell dates back to 1839 when Sir William Grove first described its principle and demonstrated a fuel cell at room temperature using a liquid electrolyte. In 1899, Nernst discovered the oxide solid electrolyte when using stabilized zirconia in making filaments for electric glowers [Nernst, 1899]. Exclusive oxygen ion conductivity in stabilized cubic zirconia was established by Wagner and Schottky. In 1935, Schottky suggested the use of oxygen ion conducting ceramics as electrolyte in solid oxide fuel cells [Schottky, 1935]. Two years later, the first working SOFC was demonstrated by Baur and Preis using stabilized zirconia as electrolyte [Baur and Preis, 1937]. A current density somewhat less than 1 mA/cm^2 was obtained at a cell voltage of 650 mV. Even today, stabilized zirconia is the most favoured electrolyte for SOFC applications.

The theory describing oxygen ion transport in ceramic oxides was developed by Wagner [Wagner, 1943]. He pointed out that ionic conduction in stabilized zirconia proceeds through the oxygen ion vacancies. These vacancies are introduced by adding dopants such as calcium or yttrium having a lower valence than the cation of the host lattice. It took another twenty five years before large R&D programs in the early sixties, inspired by the energy needs of military, space and transport applications accelerated SOFC developments.

1.1.4. Solid Oxide Fuel Cell (SOFC)

1.1.4.1. The principle and operation

The principle of an SOFC is illustrated in Fig.1.2. Electrodes are placed at either sides of the electrolyte (stabilized zirconia) plate or tube wall. The electrodes are porous to enable gas phase transport and made from mixed conducting (high electronic and ionic conductivity) ceramics to promote a large triple phase junction area where the electrochemical reaction occurs. At the cathode, oxygen molecules from the gas phase are reduced to oxygen ions according to the reaction:

$$O_2 + 4e^- \rightarrow 2O^{2-} \qquad [1.1]$$

The oxygen ions are incorporated into the electrolyte where they diffuse across the electrolyte under an oxygen chemical potential gradient to the anode. At the anode, the electrochemical oxidation of the fuel occurs generating electrons:

$$2H_2 \rightarrow 4H^+ + 4e^- \qquad [1.2]$$

The electrons generated flow through the outer circuit whereas the hydrogen ions generated at the anode either diffuses through the electrolyte (in case of protonic conductors) and combines with the oxygen at the anode or combines with the oxygen ions transported through the electrolyte (in case of oxygen ion conductors):

$$2O^{2-} + 4H^+ \rightarrow 2H_2O \qquad [1.3]$$

If there is no passage of electronic current through the electrolyte, the oxygen partial pressure or chemical potential on either sides of the electrolyte is fixed by the respective equilibrium chemical potentials, μ^a_{O2} and μ^c_{O2}. The SOFC under equilibrium conditions can thus be regarded as an oxygen concentration cell. The electromotive force (emf) or reversible (thermodynamic) cell voltage, E_r, is given by

$$E_r = -\frac{1}{4F}\int_{\mu^c_{O2}}^{\mu^a_{O2}} t_{ion}\, d\mu_{O_2} \qquad [1.4]$$

The ionic transference number t_{ion} *(ratio of ionic to total conductivity)* of stabilized zirconia in a wide range of temperature and oxygen partial pressure is unity. Using the relationship, $\mu_{O2} = \mu^o + RT\ ln\ pO_2$, Eq.[1.4] can be transformed into the well known Nernst equation,

$$E_r = -\frac{RT}{nF}\ln\left(\frac{pO_{2(c)}}{pO_{2(a)}}\right) \qquad [1.5]$$

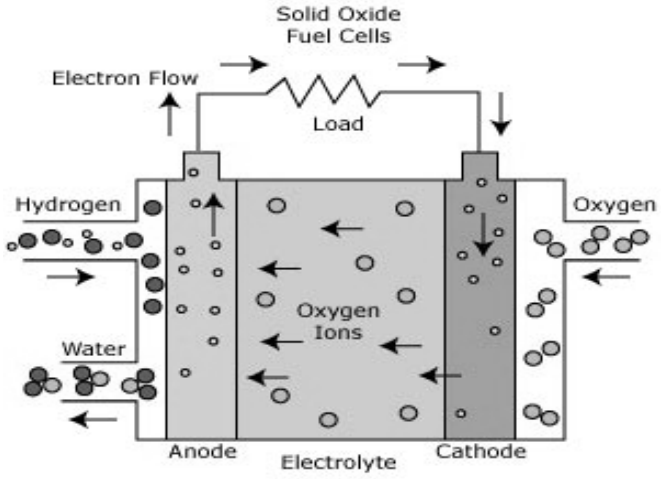

Fig.1.2 The Principle of SOFC

At equilibrium, the potential measured in open circuit condition (no flow of current) should agree with the Nernstian emf. Deviations from the Nernstian emf may be due to electrochemical semi-permeability, non-attainment of equilibrium at the electrode-electrolyte interface, physical permeation of gas between the electrodes or side reactions at the electrodes or electrode-electrolyte interfaces.

The fuel cell produces electrical energy when connected to an external load. In such a case when there is a finite flow of current, the cell voltage is lower than the thermodynamic Nernstian emf because of polarization losses. The polarization losses are a function of current density. These can be ohmic losses, which show a linear dependence on the current density (follows ohm's law), or non-ohmic, which show a non-linear dependence. The cell voltage, E_c, under load is given by

$$E_c = E_r - iR_i - \eta \qquad [1.6]$$

where, i is the current, R_i the total internal cell resistance and η is the polarization loss at the electrodes. Ohmic losses are determined by the electronic resistance of the electrodes, ionic resistance of the electrolyte and contact resistances. Polarization losses occurring at the electrodes are in general non-ohmic. They can be charge transfer or activation polarization η_A, diffusion or concentration polarization η_D, and reaction polarization η_R

$$\eta = \eta_A + \eta_D + \eta_R \qquad [1.7]$$

The losses η_D and η_R are also often called mass transport losses. Equation [1.7] applies for losses at both the cathode and the anode. A schematic of a polarization plot (or i-V curve) is shown in Fig. 1.3.

Charge transfer or activation polarization is due to the energy barrier that must be surpassed before an electrochemical reaction can take place and dominates at low current density. Because the reaction rate increases with increasing temperature, the activation polarization decreases with increasing temperature. At the high operating temperature of SOFC's, the charge transfer or activation loss is usually small. Diffusion or concentration polarization occurs, for instance, when reaction products are removed slower than the formation of these products, or when the reactant feed is lower than that consumed by the reaction. Concentration polarization is predominant at higher current densities. A detailed treatment of polarization in fuel cells can be found elsewhere [Minh and Takahashi, 1995; Bard and Faulkner, 1980, Bockris and Reddy, 1977].

Solid oxide fuel cells can have different types of configuration. These include tubular configuration, planar configuration, monolithic and segmented-cell-in series.

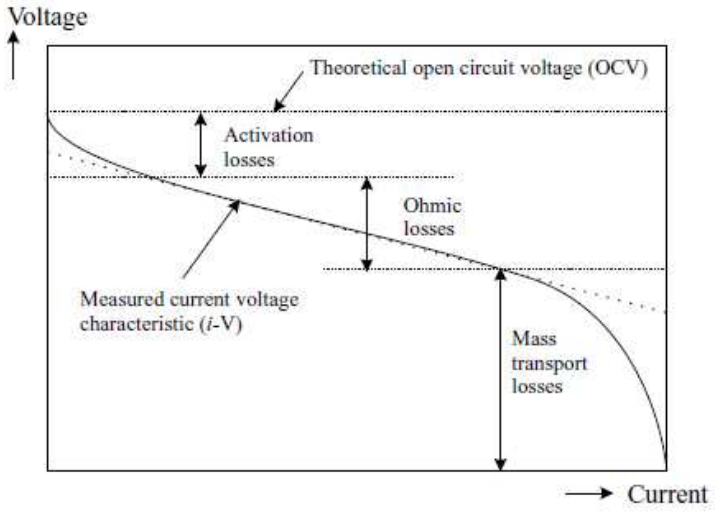

Fig. 1.3 A schematic representation of an I-V curve

These are described in detail in the review paper of Minh [1993] and Vielstich and co-workers [2003]. The more common types are the planar and tubular configuration as given in Fig. 1.4. In the planar configuration, the current paths are short and therefore result in lower polarization losses and yield high power densities. However, the main drawback of the planar architecture is the use of sealants at high temperatures to isolate the cathode and anode compartments. The tubular configuration does not require sealing. The tubular configuration leads to long current paths and results in a lower power density. Recent designs of the stack aim at improving the power density of the cell [Ding and Liu, 2009].

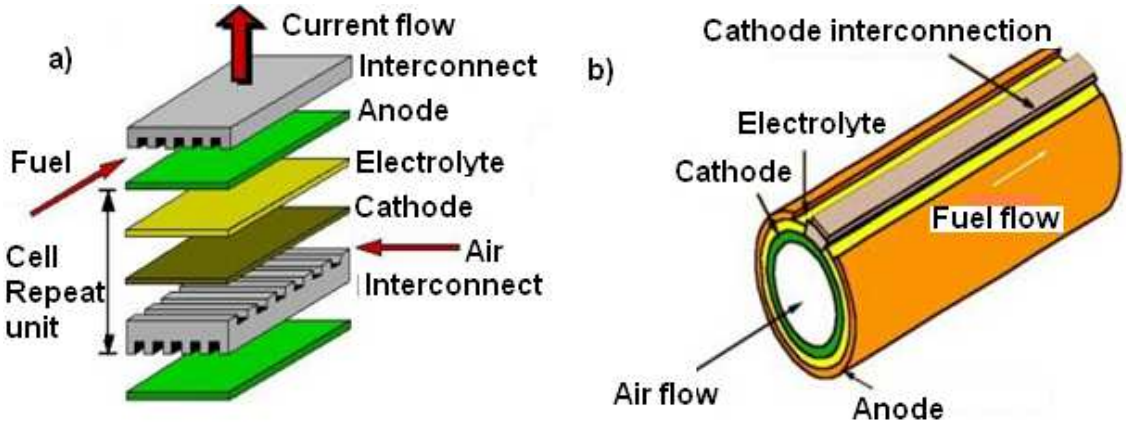

Fig.1.4 Configuration for a) Planar and b) tubular design SOFC

1.1.4.2. Cell Components

The main cell components of a solid oxide fuel cell are electrolyte, cathode, anode and interconnect. Their essential requirements are discussed below:

1.1.4.2.1. Cathode

Cathode (also called as air electrode) material in solid oxide fuel cell should satisfy the requirements of high electronic (hole) conductivity to transport electrons, good ionic conductivity to increase the electrochemical reaction surface area, chemically compatibility with the other cell components (electrolyte and interconnect), similar thermal expansion coefficient as the electrolyte and high catalytic activity with respect to the oxygen reduction reaction (Eq. 1.1). The cathode should have a porous structure to enable gas phase transport of reactants and products as well as to provide large reaction interfacial area. The electrochemical reaction takes place at the triple phase boundary (TPB) of the cathode-electrolyte-oxygen. For catalyzed reactions, the availability of the active catalyst at the triple phase boundary is also a requirement for the electrochemical reaction to occur. The possible reaction paths at the TPB are discussed in the literature [Fleig et al, 2001; 2002]. As mentioned, the cathode should be a good hole conductor as well as a good oxygen ion conductor. Conductivity is directly related to the charge carrier concentrations such as oxygen ion vacancies (for ionic conductivity) and/or holes, their charge and mobility. Charge carrier concentrations can be enhanced by doping of aliovalent cations to the oxide cathode material. Transition metal elements are useful for the creation of electronic defects because of the stability of multiple valence states.

The performance of a cathode depends on the ionic and hole conductivities, the rates of interfacial reactions such as oxygen dissociation, atomic oxygen diffusion to the TPB, charge-transfer and gas diffusion. Cathode polarization is one of the most important factors determining the cell performance in SOFCs [Kenjo and Kanehira, 2002]. The oxygen charge-transfer reaction is reported to have the slowest kinetics among all the steps. One of the most important properties for a SOFC cathode is the steady-state polarization, which depends mainly on the current density [Fleig et al, 2002]. Because of the large cathode polarization at low temperatures, there is a need for considerable improvement in cathode materials and microstructures for improvement in the power density of fuel cells. Proper control of the microstructure of the cathode material is also important to obtain good electrode performance [Inagaki et al, 2000].

Perovskite oxides based on $LaSrMnO_3$ (Lanthanum strontium manganite i.e., LSM) [Charojrochkul et al, 1999; Boehm et al, 2003; Van Herle et al, 2001; De Souza et al, 1997; Tsai and Barnett, 1997], $(LaSr)CoO_3$ (lanthanum strontium cobalitite i.e., LSC) [Charojrochkul et al, 1999; Wang and Barnett, 1995; Uchida et al, 2000] and $(LaSr)FeO_3$ (lanthanum strontium ferrite i.e., LSF) [Simner et al, 2003] have been extensively used as cathode materials for SOFC operating with YSZ electrolyte. Additionally, Ag – YSZ [Wang and Barnett, 1992] and Pt – YSZ [Wang and Barnett, 1995] cermet cathodes, mixed ionic-electronic conducting oxides (MIEC) such as $SrFeCoO_3$, $SrCoFeO_3$, and $La(Sr)Fe(Co)O_3$ based oxides [Shizhong et al, 1999] have been investigated for YSZ – electrolyte SOFCs.

$La(Sr)Co(Fe)O_3$ [Livermore et al, 2000; Sahibzada et al 1997,1998,1999; Bae and Steele, 1998; Maguire et al, 2000] based cathode material is the most studied air electrode for SOFCs operating with ceria-based electrolytes. $(LaSr)CoO_3$ [Uchida et al, 2000], strontium-doped gadolinium manganite [Yoon et al, 2001], and some composites [Figueiredo et al, 2000; Hart et al, 2002] are other cathode materials investigated for the ceria-based electrolytes.

$La(Sr)CoO_3$ [Inagaki et al, 2000; Huang et al, 1998; Horita et al, 2001; Kostogloudis et al, 2000] has been reported to be the most suitable cathode material operating with the strontium and magnesium-doped lanthanum gallate electrolytes. There are also studies on other mixed conducting perovskite-oxides as the cathode material [Ullmann et al, 2000].

1.1.4.2.2. Electrolyte

The solid electrolyte is the most critical component of SOFC. The requirements of the SOFC electrolyte in the operating temperature and oxygen partial pressure range are:

(i) High ionic conductivity, (ii) chemical stability, (iii) negligible electronic or hole conductivity, (iv) mechanical stability, (v) thermal stability and thermal expansion compatibility with electrodes and interconnect, (vi) thickness, (vii) gas – tightness, (viii) compatibility with other SOFC components including the sealants and (ix) processing cost.

Oxygen ion conductivity in oxygen solid electrolytes occurs through diffusion along the oxygen ion vacancies [Kilner, 2000]. In addition to the crystal structure, the

oxygen vacancy concentration and its mobility are important parameters for the electrolyte. Almost all the oxygen ion conductors reported in the literature have a close packed cubic structure. The oxygen vacancy concentration depends on the extent of aliovalent doping without a change in crystal structure and the mobility of the oxygen ions depend on temperature. Diffusion rate increases exponentially with increasing temperature (Arrhenius behavior). Further, there are several other advantages of high temperature operation such as low interfacial resistance, faster kinetics, internal reforming of the hydrocarbons and the possibility of co-generation. However, the higher temperature of operation of solid oxide fuel cells results in several material problems, requirement of high temperature sealing and therefore a high cost. From the materials and cost point of view, it is advantageous to operate the fuel cells at intermediate temperatures of 600-800 ^{o}C, which retains the advantages of internal reforming and co-generation but imposes less stringent requirements on the materials. At lower temperatures, one can use less expensive and well-established ferritic stainless steel, which has a reasonable thermal expansion compatibility with the cell materials for interconnect and cell construction. Further, at lower temperatures, because of lower thermal stresses and slower kinetics, the thermal and chemical compatibility requirements are much less stringent. Therefore electrolyte material with high oxygen ion conductivity at low temperatures (< 800 ^{o}C) is essential.

The thickness of the electrolyte is another important parameter in terms of ionic conductivity and SOFC operation temperature. In addition to lower cell resistance, in thinner electrolytes, oxygen ion travels more easily and at lower temperatures, same (or higher) ionic conductivities can be obtained, compared to thicker electrolytes [Huijsmans, 2001]. However, the minimum thickness of the electrolyte to be employed depends on whether the electrolyte supports the cell, the limitations of the processing technique, density achievable to limit physical permeability of gases and electrochemical semi-permeability of the electrolyte.

Electronic and hole conductivity of the electrolyte material should be as low as possible in order to minimize short circuiting and maximize the cell voltage. In addition to the intrinsic (band gap) and extrinsic properties of the material, electronic and hole conductivity depends on the oxygen partial pressure and temperature range of operation of the cell. Lower band gaps readily lead to electrons and holes at higher temperatures. Further extrinsic aliovalent doping of transition metal oxides leads to charge compensation through the generation of electrons or holes. At high oxygen partial

pressures, hole conductivity predominates whereas at low oxygen partial pressures, electronic conductivity predominates.

In fuel cells, anode and cathode are exposed to fuel and oxidant respectively. In case of hydrocarbon fuel usage, CO_2 is also present at the anode. The electrolyte material must be stable in both the oxidizing and reducing atmospheres.

The effect of grain boundaries on ionic conductivity of solid electrolytes have also been investigated [Fleig et al, 2001]. There are two schools of thought on the effect of grain boundaries. One school of thought is that the grain boundaries provide an easy path for oxygen ion diffusion and therefore the ionic conductivity will increase as grain boundary area increases. Another school of thought is that the disordered regions of the grain boundaries will enhance the resistance [Fleig et al, 2001]. Additionally, the insulating impurity phases tend to segregate at the grain boundaries. Highly resistive grain boundaries lead to an additional semicircle in the complex impedance plane and impedance spectroscopy can be used to separate grain boundary and bulk resistances. Different models are discussed to explain grain boundary resistances, such as i) complete wetting, highly resistive grain boundary phase, ii) space charge depletion layers, or iii) current restriction due to partially wetting, ionically blocking grain boundary phase. Generally, experimental evidence mainly with stabilized zirconia electrolytes indicates a decrease in bulk ionic conductivity as grain size decreases. However, stabilized zirconia invariably has silica as an impurity which segregates to the grain boundaries and impedes oxygen ion transport. It would be interesting to see the effect of grain size in pure ionic conductors free of any impurity phase.

In general, three types of electrolyte materials; stabilized zirconia, doped ceria (GDC or CGO), and strontium and magnesium-doped lanthanum gallate (LSGM) are being considered for Solid Oxide Fuel Cells.

1.1.4.2.3. Anode

The function of an anode (also called as fuel electrode) in a solid oxide fuel cell is to promote the oxidation reaction and provide electrons to the external circuit. Similar to the cathode, the anode should have large triple phase boundary areas (anode-electrolyte-fuel gas boundary) where the electrochemical oxidation occurs. The TPB area is defined as the product of the TPB length and the active anode thickness. Development of mixed conducting oxides as electrodes is an attractive approach. In these oxides, both electrons and oxide ions exhibit high mobility, so that the

electrochemical reaction can occur at the electrode/gas interface as opposed to only at the TPBs [Irvine et al, 1997]. A porous anode material is desired for the gas phase transport and to provide high surface area for the anodic reactions to take place. High catalytic activity to CO and H_2 oxidation, and good stability under reducing atmospheres are the other necessary parameters of a SOFC anode material.

The most effective anode material in terms of catalytic properties with respect to H_2 oxidation is nickel [Irvine et al, 1997]. Sintering and coarsening of Ni particles at high temperatures leads to a reduction of the porosity and TPB length. Adding YSZ particles and forming Ni/YSZ cermet can eliminate not only the sintering problem but also enhance the ionic conductivity of the anode [De Boer et al, 2000]. However, the amount of Ni and stabilized zirconia in the anode is also determined by the thermal expansion coefficient, which should be close to that of the electrolyte. A porous cermet of nickel and yttria-stabilized zirconia (Ni/YSZ) is generally used as the anode material in solid oxide fuel cells with YSZ electrolyte [De Boer et al, 2000; Li et al, 2001]. Mixture of NiO and YSZ powders are used such that NiO is reduced to metallic nickel when the SOFC is exposed to the fuel. By this way, a porous anode structure can be obtained. The performance of Ni/YSZ anode depends strongly on its nickel content and its microstructure [Li, 2001]. Studies have been conducted to determine the optimal morphology, porosity and thickness of such cermet anodes [Fleig et al, 2001]. The major disadvantage of Ni/YSZ cermet anode is the promotion of competitive catalytic cracking of hydrocarbon reactions [Irvine et al, 1997] and soot deposition at the anode surfaces. With the use of natural gas as fuel at Ni cermet anodes, presence of sulfur in fuel results in the deposition of deleterious nickel sulphide at the anode [Irvine et al, 1997].

Several alternate anode materials have been reported in the literature for YSZ-electrolyte based SOFCs. Copper-stabilized zirconia [Dongare et al, 2002], Cu-Ni-YSZ cermet [Zhe et al, 2002], lanthanum-doped strontium titanate [Marina et al, 2002], doped lanthanum chromites [Sauvet et al, 2001; 2002] and mixed ionic-electronic conducting oxides [Shizhong et al, 1999] are some of the anode materials for YSZ-electrolyte SOFCs.

Different anode materials have to be used depending on the electrolyte used for the SOFC. The anodes should have chemical and thermal compatibility with the electrolyte. Ni/CGO cermet [Livermore et al, 2000; Steele, 2000], Ni/YSZ cermet

[Sahibzada et al, 1997, 1999, 2000], and Sr and Fe-doped $LaCoO_3$ [Hartley et al, 2000] anodes are the main candidates for gadolinium-doped ceria electrolytes. Ni-$Ce_{1-x}Sm_xO_{2-\delta}$ cermet [Huang and Goodenough, 2000; Kuroda et al, 2000; Inagaki et al, 2000] is reported to be the most suitable anode material for strontium and magnesium-doped lanthanum gallate electrolyte.

1.1.4.2.4. Interconnect

Interconnects are necessary to combine single cells to form a stack by connecting the cathode of the one cell to the anode of the adjacent one. The requirements of interconnect are as follows:

- High electronic conductivity (>1 S/cm) in the oxygen partial pressure range (from air to fuel gas) of operation of the cell.
- Chemical and phase stability in both air and fuel atmospheres during fabrication and operation of the cell.
- Thermal expansion coefficient close to that of the electrolyte and the other cell components.
- Resistance to thermal shock.
- Physical and electrochemical gas tightness.

At present, Sr-doped $LaCrO_3$ which has a perovskite structure is the common interconnect material [Tietz et al, 2002]. The two major problems with this material are: 1) thermal expansion mismatch with stabilized zirconia and 2) poor sinterability in oxidizing conditions. The volatilization of chromium oxides at higher temperatures is also a serious problem.

Metallic interconnects can be used, but their chemical and thermal compatibility has to be established and further, these tend to be expensive. Inconel and stainless steels have been proposed particularly for stacks that can operate at 800^oC [Tietz et al, 2002]. Conventional steels also have a mismatch in thermal expansion coefficient with the YSZ electrolyte. In the case of intermediate temperature solid oxide fuel cells, austenitic steels free of chromium can be used as interconnect. Metal interconnects also tend to form oxide coatings, which can limit their electrical conductivity and acts as a barrier to mass transport.

1.1.4.2.5. Sealants

A key issue with SOFCs, particularly with planar SOFCs, is the method of sealing the anode and cathode compartments to obtain gas tightness. The usual approach is to use glasses that have transition temperatures close to the operating temperature of the cell. These materials soften as the cells are heated up and form a seal all around the cell. A particular problem is the migration of silica from such glasses, especially onto the anodes causing degradation in cell performance. Recently, some metallic seals (Au and Ag) have also been tried for both high temperature and intermediate temperature SOFCs respectively.

1.1.4.2.6. Advantages and disadvantages of SOFCs

Advantages

- The use of expensive catalysts such as platinum or ruthenium is not necessary because of the high temperature of operation.
- The high quality of exhaust heat (800-900^{o}C) is useful for cogeneration application in industry.
- High efficiency for electricity production can be achieved in combined cycles.
- Internal reforming of natural gas may considerably reduce costs.
- Electrolyte losses as well as electrode corrosion are eliminated.
- The cell life is increased due to higher tolerance to impurities such as sulfur in fuel.
- Chemical cogeneration is possible in producing electricity and chemical compounds when appropriate electro-catalytic anodes are used.
- SOFCs can be used as high temperature water electrolyzers without major modification.
- Finally, SOFCs offer flexibility in the planning and sitting of power generation capacity as a result of their modular nature.

Disadvantages

- Electrolyte resistivity and electrode polarization are still too high.
- The formation of low conducting phases by solid state reactions at the electrode/electrolyte interfaces result in the degradation of the cell.

- The brittleness of the ceramic components makes it difficult to use cell sizes larger than 0.2 m^2. This limitation is a major problem for scaling up SOFC power plants to megawatt size.
- SOFC's for large scale power generation presently involves a high capital cost to performance ratio.

1.1.5. Intermediate Temperature Solid Oxide Fuel Cell (ITSOFC)

By lowering the temperature of operation, a wide range of materials can be used that allow cheaper fabrication, particularly in relation to interconnect and balance-of-plant (BoP) components. Lower temperature operation also affords more rapid start-up and shut-down, reduced corrosion rate of metallic components, improved durability (sintering and component inter-diffusion is accelerated at higher temperatures), more robust construction through the use of compressive seals and metallic interconnects. There are two main routes by which SOFCs can be operated at lower temperatures, while still attaining performance comparable to the higher temperature cells. The thickness of the electrolyte can be reduced, thus reducing the area specific resistance of the fuel cell, and/or materials development can bring about the same result by improving the ionic conductivity of the electrolyte at lower temperatures and bring about improvements in the performance of electrodes. Since metallic interconnects and non-ceramic seals can be used at lower temperatures, IT-SOFCs are more conducive to the planar stack architecture than HT-SOFCs.

1.1.6. Synthesis of SOFC Components

Synthesis of the cell materials is one of the most important steps in the realization of SOFC performance and service. Further, any decrease in the cost of the oxide synthesis will result in a decrease of the overall SOFC production cost. The compositions of the anode, cathode, electrolyte and interconnect is designed to exhibit the best performance under SOFC operating conditions. Even a small deviation in the material composition results in a poorer performance of SOFC. For example, the best ionic conductivity values for the electrolyte can be achieved with $La_{0.9}Sr_{0.1}Ga_{0.83}Mg_{0.17}O_{3-\delta}$ composition. Small deviations from that composition mostly result in decrease in the ionic conductivity. Therefore, to be able to operate the SOFC at a desired efficiency, pure single-phase synthesis of SOFC components in desired

compositions is extremely important. Several techniques for multi-cation oxide material synthesis are described in the following sections.

1.1.6.1. Solid-State Reaction Technique

Solid-state reaction technique is the most common method for synthesizing SOFC materials. In this synthesis method, constituent oxides and/or carbonates are mixed in the desired stoichiometry. After a long wet grinding operation, which results in a homogeneously mixed powder it is calcined. Since the desired phase formation in this technique is based on solid-state diffusion of atoms, high calcination temperatures and long holding times at that temperature are required to obtain single-phase oxide material. Thus, laborious and time consuming powder preparation, high calcination temperatures and long holding times at high temperatures increase the cost of the powder synthesis. Moreover, in case of improper powder preparation, undesired phases may appear in the final powder.

1.1.6.2. Co-precipitation Technique

Co-precipitation method is another technique that is used to synthesize SOFC components. This method involves “co-precipitation” of a precursor salt, and then thermal decomposition (or called calcination) to the desired oxide composition. The advantage of co-precipitation technique in the synthesis of oxide powders is mixing at a molecular level, unlike the solid-state reaction technique which involves long diffusion distances.

A solution of metal salts, i.e. nitrates, sulfates etc. are mixed with a precipitation agent such as oxalic, citric, or other organic acid or ammonium hydroxide. The reason for using these precipitation agents is the low solubility of metal oxalates, citrates, or hydroxides. During precipitation, there are generally two possibilities; i) precipitation of a mixed metal precursor crystal with a specific stoichiometric ratio of the metals, or ii) segregative precipitation of individual particles, such as precipitation of different metal oxalates that are colloidally unstable and hetero-coagulation into a mixed aggregate particle.

In order to achieve precipitation, decrease in the solubility limit of the desired phase has to be achieved. Generally, temperature, pressure, pH of the solution, and chemical precipitant (redox potential) are the factors affecting the solubility of the phase to be precipitated.

During precipitation, the pH of the solution may vary markedly and the powder composition and homogeneity may be affected. Further, the powders must be separated from their supernatants, dried, and calcined to the desired composition. The drying and calcination steps often lead to aggregates. Special precautions such as calcination in dry atmospheres must be used to prevent formation of aggregates. Moreover, extremely rapid precipitation may result in trapping of foreign ions in the particles.

There are several more recent powder synthesis techniques for the synthesis of homogeneous, pure, and single-phase mixed oxides in the desired composition.

1.1.6.3. Organic Precursor Technique

Organic precursor technique has been more recently employed widely in mixed oxide powder synthesis. In this method, the synthesis stages are i) dissolution of stoichiometric amounts of cation salts in a proper solvent, ii) dissolution of desired amount of organic carrier material(s), where molecular ratio of cation to organic carrier material is important, iii) proper mixing of the constituents in the solution and solvent evaporation, and iv) calcination of the formed precursor powder to obtain the oxide powder in desired composition.

The predicted mechanism in organic precursor method for achieving a stable precursor is chelating/complexing the metal cations by the functional groups of the organic carrier materials in the solution. This chelating/complexing action is believed to be due to columbic attraction forces between the carboxylic and/or hydroxyl groups of the carrier materials and metal cations. The molecular geometry of the functional groups is also believed to play an important role in the chelating/complexing action. As a result of this action, metal cations are believed to have a perfect-homogeneous distribution in the solution and in the precursor after solvent removal. This cation distribution results in an amorphous powder at room temperature. In the calcination stage, crystallization of the desired composition takes place. Due to the homogeneity at molecular level, lower diffusion distances than for the solid-state reaction process is required to obtain the desired crystal phase. This in turn may result in much lower calcination temperatures compared to the solid-state reaction technique. Moreover, combustion of the organic materials result in a local temperature increase, which helps the diffusion process and final crystallization.

Different types of the organic carrier materials can be used in oxide synthesis, but one of the most successful techniques for single phase mixed oxide powders is the

Pechini process. The Pechini process operates through polyesterfication between hydrocarboxylic acids such as citric acid and polyhydroxy alcohols such as ethylene glycol. According to the ester reaction shown below, carboxyl end of citric acid and hydroxyl end of ethylene glycol binds and a water molecule is released. The acid acts as a chelating agent which chemically binds the cations that are dissolved in the solution.

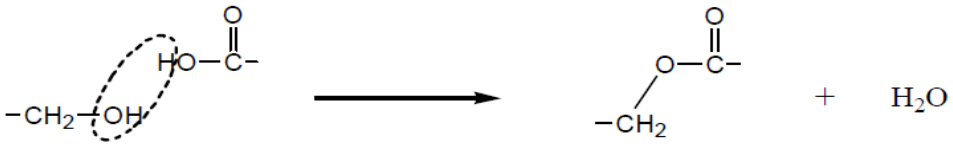

The polymerization is based on the polyesterfication between the metal-chelate complexes and polyhdroxyl alcohols. By polyesterification process, randomly coiled macromolecular chains are obtained. These chains may chelate cations uniformly and form very stable complexes. Moreover, due to chelating action and high viscosity polymeric network, cation segregation is hindered. The resultant ceramic powders possess better chemical homogeneity and smaller particle size. There are other organic precursor methods with different organic carrier materials, such as citrate synthesis, polymeric precursor synthesis, and urea method.

It is believed that organic precursor synthesis methods can eliminate the problems associated with other synthesis techniques, such as high calcination temperatures, undesired phase formation in the final powders and laborious powder preparation stages.

1.2. CHARACTERIZATION TECHNIQUES

Characterization (structural, physical, chemical and electrical) of the materials synthesized are necessary prior to their processing and use in SOFC. The common characterization methods adopted is briefly discussed below:

1.2.1. X-ray diffraction (XRD)

1.2.1.1. Phase identification

Crystalline materials produce distinct x-ray diffraction patterns that can be used for the identification of the phases present in a material. Phase identification using x-ray diffraction relies mainly on the positions of the peaks in a diffraction profile and quantitative estimations of these phases depend on the relative intensities of these peaks. The International Centre for Diffraction Data (ICDD) maintains a diffraction file

(PDF), a database of single phase powder diffraction patterns currently numbering over 60,000. Today, it is supplied in a CD-ROM and is equipped with a first generation search or match software which uses a list of d-spacing and intensities from the measured pattern as input. Current approaches do not require individual peak picking, has powerful peak deconvolution techniques and uses the entire background subtracted spectrum.

1.2.1.2. Lattice Parameter calculations

The lattice parameter of the different phases can be calculated from the interplanar spacings derived from the X-ray diffractogram. For a cubic phase, this relationship is given by:

$$d_{hkl} = \frac{a}{\sqrt{h^2 + k^2 + l^2}} \qquad [1.8]$$

Similar relations between interplanar spacings, Bravais indices and lattice parameters are available for the more complex crystal structures [Cullity and stock, 2001].

1.2.1.3. Calculation of the crystallite size

The crystallite size of the calcined powders can be calculated from the line broadening observed in the XRD pattern. The most common method adopted for this purpose is the Scherrer's formula:

$$B_t^2 = \left[\frac{0.9\lambda}{D\cos\theta} \right]^2 + \left[4\varepsilon \tan\theta\right]^2 + B_0^2 \qquad [1.9]$$

where, B_t is the full width at half maximum (FWHM) intensity of the peak, λ the wavelength of the radiation used, D is the average crystallite size, ε the lattice strain, θ the diffraction angle and B_0 is the instrumental line broadening. Another method commonly used for the estimation of crystallite size and lattice strain from the X-ray line broadening profile is the Hall-Williamson method [Williamson and Hall, 1953]. Here a plot of $B\cos\theta$ vs $\sin\theta/\lambda$ is constructed and the crystallite size and strain deduced from the intercept and slope respectively.

The X-ray diffraction line broadening (B) i.e., the peak width (usually the Full Width at Half Maximum and sometimes the integrated peak width defined as the integral area/peak height) to be considered for the estimation of crystallite size and strain is purely sample dependent and free from all instrumental broadening effects.

Standard α-alumina of crystallite size >2000 A is used as a standard sample to determine the instrumental broadening:

$$\beta_{1/2}{}^2 = \beta_{obs}{}^2 + \beta_m{}^2 \qquad [1.10]$$

where B_{obs} is the measured peak width in radians at half peak height and B_m is the corresponding width of the standard material.

Warren and Averbach's method takes not only the peak width into account but also the shape of the peak. This method is based on a Fourier deconvolution of the measured peaks and the instrument broadening to obtain the true diffraction profile. This method is capable of yielding both the crystallite size distribution and lattice microstrain.

The Scherrer and the Warren-Averbach methods do not give the same value for the crystallite size. That is because they each yield different characteristic averages from the crystallite size distribution. The Scherrer and Warren-Averbach methods yield different characteristic averages of the column length *L*. The Scherrer method yields $\langle L \rangle_{vol}$ while Warren-Averbach yields $\langle L \rangle_{area}$. In order to obtain a measure of the crystallite size one may assume a shape for the particles. Assuming spherical crystallites, the diameter of the sphere can be estimated. However, by combining the results of the Scherrer and the Warren-Averbach methods and making reasonable assumptions regarding crystallite shape and size distribution it is possible to arrive at a single size distribution.

1.2.2. Scanning Electron Microscopy (SEM)

Scanning electron microscopy is most commonly employed for the study of powder morphology. Two modes of imaging are available in a scanning electron microscope: secondary electron imaging and back-scattered electron imaging.

1.2.2.1. Secondary Electron Imaging (SE) - This mode provides high-resolution imaging of fine surface morphology. Inelastic electron scattering is caused by the interaction between the sample's electrons and the incident electrons, which results in the emission of low-energy electrons from near the sample's surface. The topography of surface features influences the number of electrons that reach the secondary electron detector from any point on the scanned surface. This local variation in electron intensity creates the image contrast that reveals the surface morphology. The secondary electron image resolution for an ideal sample is about 3.5 nm for a tungsten-filament electron source SEM or 1.5 nm for field emission SEM.

1.2.2.2. Backscatter Electron Imaging (BSE) - This mode provides image contrast as a function of elemental composition, as well as, surface topography. Backscattered electrons are produced by the elastic interactions between the sample and the incident electron beam. These high-energy electrons can escape from much deeper portions of the sample than secondary electrons, so surface topography in this mode is not as accurately resolved as in secondary electron imaging. The production efficiency for backscattered electrons is proportional to the sample material's mean atomic number, which results in image contrast as a function of composition, i.e., higher atomic number elements appears brighter than low atomic number elements in a backscattered electron image. The optimum resolution for backscattered electron imaging is about 5.5 nm.

Scanning electron microscopy can only be used for surface images and both resolution and crystallographic information provided are limited. Other constraints are that the samples must be conductive, so non-conductive materials are either carbon or gold-coated and secondly and elements with atomic number smaller than the carbon are not detected with SEM. Modern scanning electron microscopes can detect quantitatively elements with atomic number up to boron.

1.2.2.3. Energy Dispersive X-Ray Spectroscopy (EDAX)

Energy Dispersive X-Ray Spectroscopy (EDS or EDAX) is a chemical microanalysis technique used in conjunction with scanning electron microscopy (SEM). The EDS technique detects X-rays emitted from the sample during bombardment by an electron beam to characterize the elemental composition of the analyzed volume. Features or phases as small as 1 μm or less can be analyzed. When the sample is bombarded by the electron beam, electrons are ejected from the atoms of the sample's surface. The resulting electron vacancies are filled by electrons from a higher state, and an X-ray is emitted to balance the energy difference between the two electronic states. The X-ray energy is characteristic of the element from which it was emitted. The EDAX X-ray detector measures the relative abundance of emitted X-rays versus their energy. Quantitative results can be obtained from the relative X-ray counts at the characteristic energy levels for the sample constituents. Semi-quantitative results are readily available without standards by using mathematical corrections based on the analysis parameters and the sample composition. The accuracy of standard-less analysis depends on the sample composition. Greater accuracy is obtained using known standards with similar structure and composition to that of the unknown sample.

1.2.3. Fourier Transform-Infrared Spectroscopy (FTIR)

Fourier Transform-Infrared Spectroscopy (FTIR) is an analytical technique used to identify organic (and in some cases inorganic) materials. This technique measures the absorption of infrared radiation by the sample material as a function of wavelength. The infrared absorption bands identify molecular components and structures. When a material is irradiated with infrared radiation, absorbed IR radiation usually excites molecules into a higher vibrational state. The wavelength of light absorbed by a particular molecule is a function of the energy difference between the at-rest and excited vibrational states. The wavelengths that are absorbed by the sample are characteristic of its molecular structure. The FTIR spectrometer uses an interferometer to modulate the wavelength from a broadband infrared source. A detector measures the intensity of transmitted or reflected light as a function of its wavelength. The signal obtained from the detector is an interferogram, which is analyzed with a computer using Fourier transforms to obtain a single-beam infrared spectrum. The FTIR spectra are usually presented as plots of intensity versus wave number (in cm^{-1}). The intensity can be plotted as the percentage of light transmittance or absorbance at each wave number.

11.2.3.1. Qualitative Material Identification: To identify the material being analyzed, the unknown IR absorption spectrum is compared with standard spectra in computer databases or with a spectrum obtained from a known material. Spectrum matches identify the polymer or other constituent(s) in the sample. Absorption bands in the range of 4000 - 1500 cm^{-1} are typically due to functional groups (e.g., -OH, C=O, N-H, CH_3, etc.). The region from 1500 - 400 cm^{-1} is referred to as the fingerprint region. Absorption bands in this region are generally due to intramolecular phenomena and are highly specific to each material. The specificity of these bands allows computerized data searches within reference libraries to identify a material.

***1.2.3.2. Quantitative studies using FTIR*:** Quantitative concentration of a compound can be determined from the area under the curve in characteristic regions of the IR spectrum. Concentration calibration is obtained by establishing a standard curve from spectra for known concentrations.

1.2.4. Particle Size Measurement by Laser Light Scattering

The Low Angle Laser Light Scattering (LALLS) technique relies on the fact that the diffraction angle is inversely proportional to particle size. When the laser irradiates

the particles, if the particle size exceeds the wavelength of the laser, most of the particles will scatter the light in the same direction as the laser light (forward scattering). On the other hand, when the particle size is almost the same or smaller than the wavelength of the light, the scattered light increases in the perpendicular direction (lateral), and in the direction towards the light source (backward). The particle size can be calculated from the scattering pattern by using Mie scattering theory. Mie developed a general solution for the scattering of light by spherical particles of any size and any refractive index. The result of Mie treatment is the appearance of many maxima in the intensity of the scattered light as a function of scattering angle. The number and position of these maxima depend on the refractive index difference and size of the particle. When a sample contains particles of various sizes, the scattering pattern will represent the sum of each particle sizes. This measured composite scattering pattern can be used to determine particle-size distribution by comparing it with pre-calculated scattering patterns of particles in this size range.

1.2.5. BET Surface Area Measurements

BET (Stephen Brunauer, Paul Hugh Emmett, and Edward Teller, 1938) theory is a rule for the physical adsorption of gas molecules on a solid surface and serves as the basis for the measurement of the specific surface area of a material The concept is an extension of the Langmuir theory, which describes monolayer molecular adsorption to multilayer adsorption. The premises of the theory hold under the following hypotheses:

(a) Solid surface possess uniform, localized sites and that adsoption at one site does not affect adsorption at neighboring sites

(b) Molecules can be adsorbed in second, third…. and nth layer, the surface area available for the nth layer being equal to the coverage of the (n-1)th layer.

(c) The energy of adsorption in the first layer, E_1, is assumed to be constant and the energy of adsoption in succeeding layers is assumed to be same as E_L, the energy of liquefaction of the gas.

Based on the above assumptions, Brunauer, Emmett, and Teller derived the following equation, called BET equation,

$$\frac{p}{v_{total}(p-p_o)} = \frac{1}{v_{mono}c} + \frac{c-1}{v_{mono}c}\left(\frac{p}{p_o}\right) \qquad [1.11]$$

where V_{total} is the volume of the gas adsorbed at the pressure P, V_{mono} is the volume adsorbed when the surface of the solid is covered completely with a monolayer of the adsorbed molecules of the gas and c is a constant depending upon the nature of the gas which is equal to c= exp $(E_1-E_L)/RT$, where E_1 is the heat of adsorption in the first layer and E_L is the heat of liquefaction of the gas. Since c is a constant for a given gas and V_{mono} is a constant for a given gas-solid system, the plot of $P/V_{total}(P_o-P)$ against P/P_o should give a straight line. The slope of the linear plot gives the values of $(c-1)/(V_{mono}c)$ while the intercept yields the value of $1/(V_{mono}c)$. Thus, from the slope and intercept, both V_{mono} and c can be evaluated. The surface area of the adsorbent is calculated using the following equation:

$$S_{total} = \frac{V_m \times N}{22414} A_{xs} \qquad [1.12]$$

where, N - Avogadro's number and A_{xs} - cross-sectional area of adsorbate molecule. A large number of adsorption isotherms of gases on a variety of adsorbents at different temperatures are determined.

1.2.6. Thermal Analysis Methods

Thermal analysis comprises a group of techniques in which a physical property of a substance is measured as a function of temperature, while the substance is subjected to a controlled temperature program. In differential thermal analysis (DTA), the temperature difference is measured between a sample and an inert reference material when both are subjected to an identical temperature program. Differential scanning calorimetry (DSC) relies on the differences in heat input required to maintain the sample and reference at an identical temperature. Length or volume changes as a function of temperature can be measured by dilatometry. Both thermogravimetry and evolved gas analysis are techniques which rely on samples which decompose at elevated temperatures. The former monitors changes in the mass of the specimen on heating, whereas in the latter the gases evolved on heating the sample is simultaneously analyzed along with thermogravimetry.

1.2.6.1. Differential Thermal Analysis (DTA)

Differential thermal analysis is one in which heat effects associated with chemical and physical changes of a substance are recorded when it is heated at a linear rate. The difference in temperature between sample and reference is plotted against time, or against temperature. Changes in the sample which lead to the absorption or evolution of heat can be detected relative to an inert reference. The baseline of the DTA curve should then exhibit discontinuities at the transition temperatures and the slope of the curve at any point will depend on the microstructural constitution at that temperature. The area under a DTA peak can be used to estimate the enthalpy change.

A simple DTA curve may consist of linear portions displaced from the abscissa because the heat capacities and thermal conductivities of the sample and reference materials are not identical. There are difficulties with the measurement of transition temperatures using DTA curves. The onset of the DTA peak in principle gives the start temperature, but there may be temperature lags depending on the location of the thermocouple with respect to the reference and samples or the DTA block. It is necessary to calibrate the apparatus with materials of precisely known melting points. The area under the peak (A) is directly proportional to the heat of the reaction of the sample. The peak area is given by

$$A = \frac{mq}{gK} \qquad [1.13]$$

where, m is the sample mass, q is the enthalpy change per unit mass, g is a measured shape factor and K is the thermal conductivity of sample. The DTA apparatus is calibrated for enthalpy by measuring peak areas on standard samples over specified temperature ranges. The calibration should be based upon at least two different samples and employing both heating and cooling experiments.

1.2.6.2. Thermogravimetric Analysis (TGA)

Thermogravimetric analysis is concerned with the analysis of the sample weight change as a function of temperature, as the temperature is increased at a predetermined and preferably linear rate. The sample is placed in a small inert pan connected to a microbalance and heated in a controlled manner and/or held isothermally for a specified time. The atmosphere around the sample may consist of an inert gas, such as nitrogen, or a reactive gas, such as air or oxygen. The heating program may start in an inert atmosphere and then be switched to air at a certain point to complete the analysis.

Weight changes observed at specific temperatures correlate to volatilization of sample components, decomposition, oxidation/reduction reactions, or other reactions involving mass changes. Phase transformations that do not involve mass change cannot be detected by thermogravimetry.

1.2.7. Conductivity Measurements

Two methods are commonly used for the measurement of conductivity.

1.2.7.1. DC method

Conductivity of the sample can be measured directly using dc methods. This method usually involves applying a small amplitude dc signal (either voltage or current to the sample) and measuring the resulting current or voltage respectively. The change in voltage divided by the change in current gives the bulk resistance. In the 2- probe dc method, one of the probes is used to apply the signal and the other used to measure the response. On the other hand, in the 4-probe measurement, two of the probes are used to source current and the other two probes are used to measure voltage. Using four probes eliminates measurement errors because of the probe resistance, the spreading resistance under each probe, and the contact resistance between each metal probe and the material. This technique involves bringing four equally spaced probes into contact with the material of unknown resistance.

1.2.7.2. AC method

This method is alternatively called as electrochemical impedance or ac impedance method. Usually a small ac voltage signal is applied and the resulting current measured. The actual measurements are similar to the common dc electrochemical methods in that a current response to an applied voltage is determined. The interpretation of data requires different approaches.

The terms resistance and impedance both denote an opposition to the flow of electrons or current. In direct current (dc) circuits, only resistors produce this effect. However, in alternate current (ac) circuits, two other circuit elements, capacitors and inductors impede the flow of electrons. Impedance can be expressed as a complex number, where the resistance is the real component and the combined capacitance and inductance is the imaginary component. The total impedance in a circuit is the combined opposition of all its resistors, capacitors, and inductors to the flow of

electrons. Capacitors and inductors affect not only the magnitude of an alternating current but also its time-dependent characteristics or phase.

1.2.7.2.1 Measurement of Impedance spectra

Impedance measurements use an ac generator/analyzer [usually frequency response analyzer] to provide a voltage signal and analyze current and voltage outputs from a potentiostat. The setup of the circuit is similar to dc potentio-dynamic measurements.

1.2.7.2.2. Two, three and four electrodes measurements

Generally, potentiostat or frequency response analyzer consists of four terminals: working electrode, low and high reference electrode and counter or auxiliary electrodes. The two, three, and four electrode setup is shown in Fig.1.5. The major difference between these types of cell arrangement is that a reference electrode is not required for the two electrode measurements. The auxiliary electrode, often also called the counter electrode, is an electrode used in a three electrode electrochemical cell for reactions in which an electrical current is expected to flow. The auxiliary electrode is distinct from the reference electrode, which establishes the electrical potential against which other potentials may be measured, and the working electrode, at which the cell reaction takes place.

1.2.7.2.3. Impedance plots

Once an experiment is complete, the raw data at each measured frequency consists of these components:

- The real component of voltage (E’)
- The imaginary component of voltage (E”)
- The real component of current (I’)
- The imaginary component of current (I”)

From this data, one can compute the phase shift (θ) and total impedance (Z) for each applied frequency, as well as capacitance, dielectrics etc.

1.2.7.2.4. The Nyquist Plot

Nyquist plot is one of the popular methods for evaluating electrochemical impedance data. A typical Nyquist plot is shown in Fig. 1.6. This format is also known

as a Cole-Cole plot or a complex impedance plane plot. The Nyquist plot has several advantages.

- It is easy to investigate the effects of the ohmic resistance.
- It emphasizes circuit components that are in series, such as R_{Ω}.

The Nyquist plot format also has some disadvantages.

- Frequency does not appear explicitly.
- Ohmic resistance and polarization resistance can be easily read directly from the Nyquist plot, but the electrode capacitance can be calculated only after the frequency information is known.

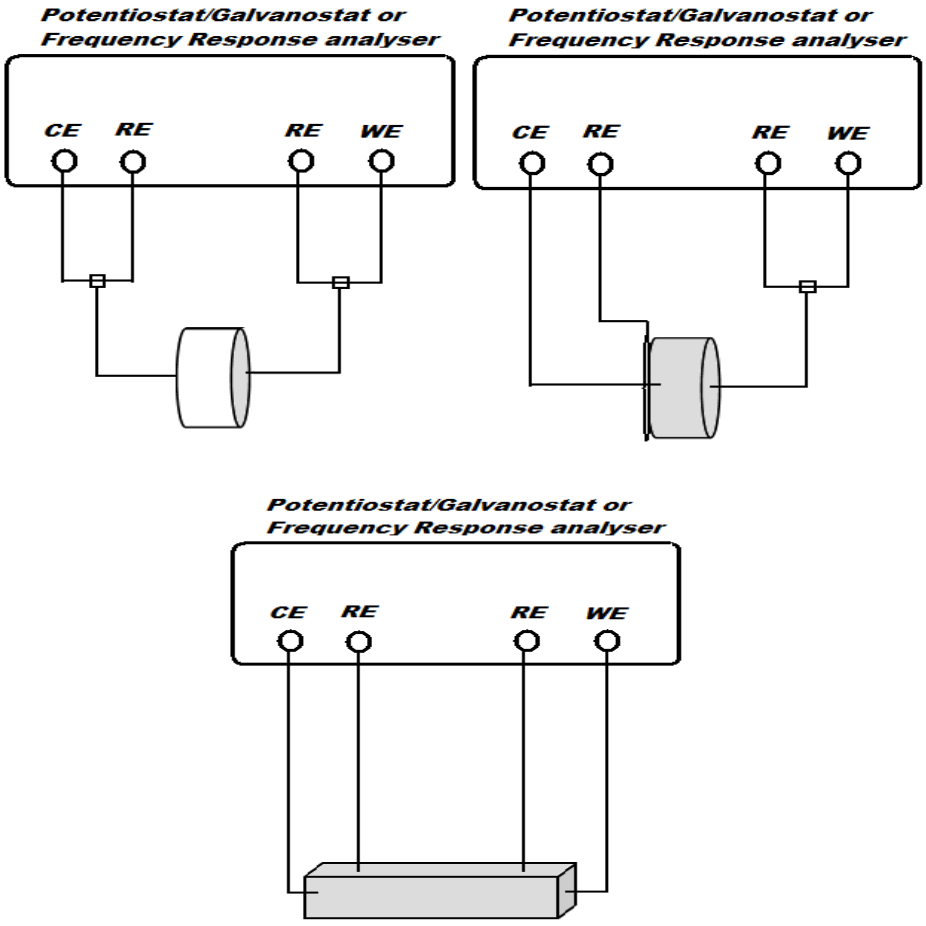

Fig.1.5 Two, three and four electrode setup for both frequency response analyzer and potentiostat /galvanostat measurements

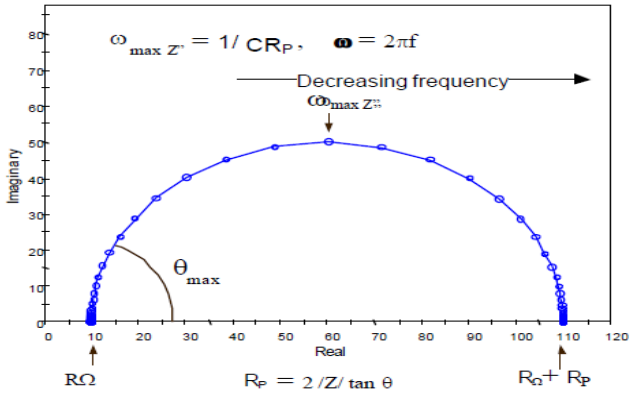

Fig.1.6 Nyquist Plot for a Simple Electrochemical System

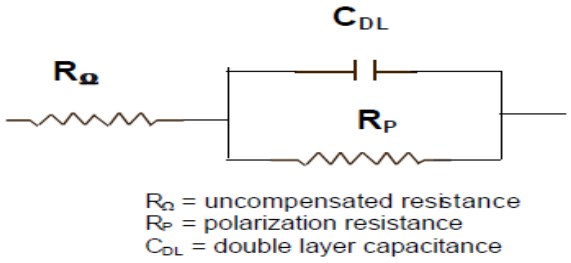

Fig.1.7 Equivalent Circuit for a Single Electrochemical Cell

As shown in Fig 1.6, the frequency corresponding to the top of the semicircle, ω(θ = MAX), can be used to calculate the capacitance if Rp is known. The corresponding equivalent circuit of this plot is shown in Fig.1.7**.** Other plots such as the Bode and Randles plot exist for the analysis of electrochemical impedance spectroscopy results. However, these are not discussed here and one is referred to the literature [Cottis, 1999].

1.2.7.2.5. Area Specific Resistance (ASR) Measurements

Area Specific Resistance is also a cell's electrochemical property and its behavior as a function of temperature and gas flow rate provides vital information on the polarization losses, especially at the interfaces. It is dependent on the cell dimensions. ASR is expressed in units of Ωcm^2. The measured area specific resistance for a complete cell is dominated by the electrolyte or membrane in electrolyte supported fuel cells. Area specific resistance is calculated by multiplying the area with the resistance:

$$ASR = R \times A \qquad [1.14]$$

On the other hand, it can also be calculated by multiplying the current density (A/cm^2) and overpotential (mV).

1.2.8. Measurement of Ionic or Electronic Conductivity in Mixed Conductors

1.2.8.1. Hebb-Wagner Method

Measurement of oxygen ion or electronic conductivity of mixed conductors i.e., the transport number (t_{ion}) is usually carried out using an electron blocking/ion blocking electrode technique called Hebb-Wagner polarization method. Fig.1.8 depicts the schematic diagram of ion blocking electrode cell to measure the electronic conductivity of MIEC (Mixed Ionic Electronic Conductor). Consider a MIEC consisting of metal oxide MO, which is an electron (e^-) and cation (M^+) conductor. Electrode R on the left hand side is a reversible electrode (M^+ and e^- both can flow through the electrode) while electrode C on right hand side is an ion blocking electrode (only electrons can flow through this electrode). When current is passed through the circuit, the following reaction takes place:

$$M_{(R)} \rightarrow M^+ + e^- \qquad [1.15]$$

M^+ ions flow through MIEC but are blocked at blocking electrode C. Electrons can complete the circuit by passing through electrode C. Thus, whatever voltage drop is observed across the MIEC is due to the passage of electrons and the value of electronic conductivity can be calculated. Similarly, ionic conductivity of the MIEC can be measured by blocking the passage of electrons (this can be done by using an electron blocking electrode such as an exclusive ionic conductor instead of an ion blocking electrode).

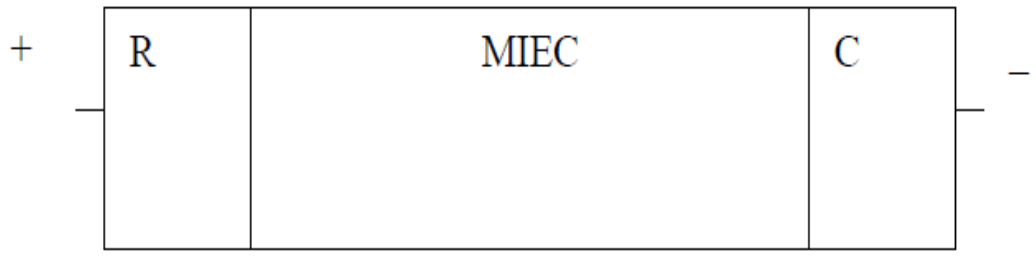

Fig.1.8 Hebb-Wagner polarization measuring cell.

1.2.8.2. Ionic transport number measurement by EMF method

Another method used for the measurement of the ionic transport number is the EMF technique. In EMF measurements, the open circuit voltage across the electrochemical cell is measured at different and known chemical potentials of the mobile species at the two electrodes i.e., under a chemical potential gradient. The gradient can be established by supplying different gas compositions to the two sides of the sample or with the use of standard reference electrodes. The voltage is measured using a high impedance voltmeter, and is a measure of ionic transport numbers of the electrolyte. The ionic transport number is the ratio between the measured voltage and the thermodynamic Nernstian voltage:

$$t_{ion} = \frac{E_{measured}}{E_{Nernstian}} \qquad [1.16]$$

1.3. FABRICATION PROCESSES

Several fabrication techniques have been used for the processing of thick and thin films of electrode and electrolyte materials and assembly of a SOFC. These include tape casting [McPheeters and Claar, 1986; Bagger, 1992, Naiqing et al, 2006, Jang et al, 2002], slurry casting [Hoshina et al, 1990; Murakami et al,1991; Arai, 1989], screen printing [Ji et al, 2003; Matsuzaki and Yasuda, 2002; Gong et al, 2006, 2004; Lu et al, 2004; Fukui et al, 2002], slip casting [Arai, 1989; Setoguchi et al,1990], chemical vapor deposition [Lin et al, 1989; De Haart et al,1991], sol-gel coating [Jang et al, 2002], electrophoretic deposition [Negishi et al, 2004; Yamashita et al, 1997; Kruger et al, 2004; Zhitomirsky and Petric, 2004], isostatic pressing [Maffei and Kuriakose, 1998; Ishikawa et al, 2007] and uniaxial pressing [Ji et al, 2003; Huang and Goodenough, 2000; Zheng and Chen, 2008; Gong et al, 2006, 2004; Lu et al, 2004; Fukui et al, 2002; Zhao and Virkar, 2004]. The processed green components are required to be fired at high temperature to attain the necessary properties such as density, phase purity, microstructure etc. Sintering or densification occurs during this heat treatment and is associated with joining together of particles, volume reduction, decrease in porosity and increase in grain size. The main aim of the sintering process is to produce microstructures suitable for particular applications. Some of these techniques are briefly described below:

1.3.1. Uniaxial pressing

In uniaxial pressing, a hard steel die is filled with either dry powder or a powder with binder and a metal punch is driven into the die to form a coherent compact. Van der waals forces cause aggregation of fine powders. Binders such as polyvinyl alcohol and lubricants are incorporated into them in order to improve their flow properties and homogeneity of the product. It is important that the unfired or green body has adequate strength for handling before the firing operation, during which organic additives are decomposed. Uniaxial pressing is particularly suited for forming components with a simple shape such as flat discs and rings that can be produced to close dimensional tolerances, thus avoiding post firing diamond machining operations.

1.3.2. Hot uniaxial pressing

Hot pressing involves simultaneous application of heat and uniaxial pressure during sintering. A refractory die, usually graphite, is filled with the powder, which after compaction, is heated in an inert atmosphere. Hot-pressing produces higher density and smaller grain sizes at lower temperatures compared to uniaxial pressing and is particularly suited for fabrication of flat plates and blocks. Stresses set up by the applied pressure on contacts between particles increase the driving force for sintering and remove the need for very fine particle sizes.

1.3.3. Isostatic pressing

Hot pressing is limited by the strength of graphite dies and fabrication of articles with simple shapes. In isostatic pressing, a mold is filled with powder and then subjected to high isostatic pressure transmitted through a liquid in a pressure vessel. The mold deforms to compress the powder and regains its original shape when the pressure is released. Both cold and hot isostatic pressing are used for fabrication, the latter referred to as HIP. Compared to uniaxial pressing techniques, isostatic pressing yields green compacts with higher and more uniform density in a wider variety of geometries although accurate shaping is difficult.

1.3.4. Screen printing

Screen printing is a mechanical printing process. Here, a paste is squeezed through the screen opening and adheres to the underlying object. The high-viscosity paste contains particles, binder and solvent. After drying, i.e. evaporation of the solvent, a layer adheres to the object. Screen printing is used in polygraphy to manufacture

posters and pictures, in the ceramics industry to shape ceramic articles, and in the electronics industry to manufacture printed circuit boards and conductive layers. The advantages of the process are reproducibility, continuity and low material consumption. The limitations are the requirement of an even substrate, size of the screen and resolution, given by the mesh opening. Another limitation is the layer thickness. Only certain values of thickness are producible as the thickness of the resulting layer is given by the screen. Nevertheless, the resolution is sufficient for the use in SOFC layer production.

1.3.5. Vacuum slip casting process

The slip casting process is usually used to manufacture three-dimensional ceramic components. In the vacuum slip casting process, the process flow is accelerated using a vacuum. In principle, slip casting processes are based upon filling a porous casting mould with a solid-containing suspension (slip). The solvents of the slip will be drawn into the pores of the casting mould, taking along the solid. The solid is deposited at the outline of the casting mould and adds up in a layer that can be separated from the casting mould after drying. For the production of thin anode functional layers and electrolyte layers when producing planar Solid Oxide Fuel Cells a modified slip casting process is used. Here, a suspension is applied on a planar, porous anode substrate in a special apparatus and the solvent is drawn through the pores. The solids of the suspension are deposited if the substrate is aligned planar and evenly on the surface. This process shows some advantages for thin film processing:

- easy and straightforward handling
- serial production, if automated
- excellent quality of the produced layers
- reproducibility of the layer thickness, uniform thickness and structure throughout the layer
- 2 to 50 μm layers
- little waste (the solvent can be re-used)
- long-term stable suspensions can be produced without effort

The disadvantage of this process is the handling of large quantities of solvents and the limitation in the thickness of the layer. There is also a big influence of the structure of the substrate (surface topography, pore size, pore distribution, density distribution, and absorbency) on the quality of the layer in terms of voids and impermeability.

1.3.6. Electrophoretic deposition (EPD)

Electrophoretic deposition (EPD) is recognized as the most versatile technique for particulate processing in terms of the wide range of dimensions it can be applied to, the thickness of deposits it can produce as compared to other powder processing routes, and its applicability to nanoparticles and nanopowder assembly. A schematic of the EPD process is shown in Fig. 1.9. Electrophoretic Deposition (EPD) is a forming process where charged particles in a solution are consolidated on a substrate in a DC electric field. This field causes the particles to move, and deposit on, the oppositely charged electrode. EPD is a combination of two processes, i.e. electrophoresis and deposition. Electrophoresis controls the motion of the charged particles in the electric field while the deposition mechanisms control the buildup of the dense particle layer on the electrode. EPD should not be confused with electro-deposition, where ions are deposited and discharged at the electrode. EPD requires colloidally stable suspensions where the particles carry a substantial charge.

The most common dispersion medium used in EPD is ethanol, because aqueous-based suspensions have the disadvantage of electrolysis. Although electrostatic stabilization is considered most effective in aqueous medium, a substantial surface charge density with the associated counter ion layer in solution can also be created in ethanol media. In aqueous media, high surface charge densities can be obtained by working far away from the point of zero charge (p^H_{pzc}) of the powder. A similar approach can also be used in non-aqueous media, provided that an operational pH scale (p^H*) and thus an isoelectric point, $pH*_{iep}$, for the specific solvent can be defined. The operational pH can be controlled by adding strong acids and bases to the suspension, e.g. HCl and LiOH.

The rate of formation of the consolidated layer during EPD is directly proportional to the amount of charge that has passed through the cell. When EPD proceeds under constant-current conditions, the deposited weight increases linearly with time. However, in order to maintain constant-current conditions, the voltage has to be continuously increased as the deposit induces an increased electrical resistance to the

system. Under constant-voltage conditions, the potential between the electrodes is maintained constant, which results in a decreased deposition rate as the deposit builds up.

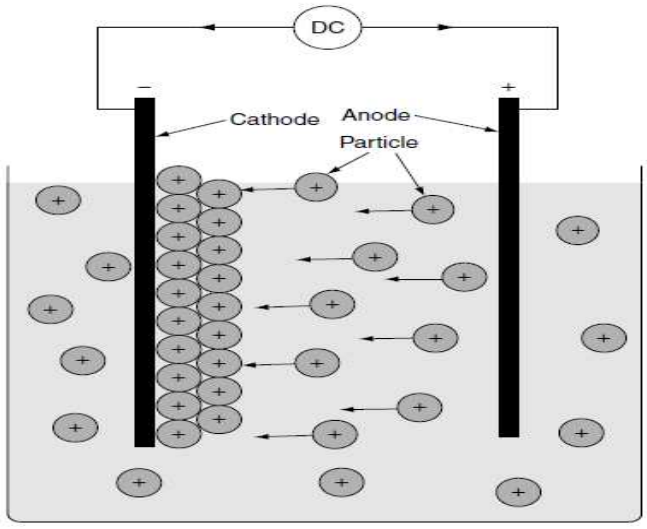

Fig.1.9 Schematic representation of the electrophoretic deposition process.

1.3.7. Tape casting techniques

Tape casting is a well-known low cost process for ceramic material shaping and is particularly well-suited for the fabrication of thin (20 μm up to 500 μm) components. It can be used to produce a wide variety of controlled morphologies, from highly porous to fully dense microstructures. Tape casting also offers a very useful possibility of stacking green tapes to obtain a multilayered final product. For a given powder, the sintering behaviour of green tapes, and hence their final microstructure, depends on the arrangement, dispersion and homogeneity of the starting ceramic powder particles in the slurry. As a consequence, the slurry formulation is the most crucial step in the shaping process.

Generally, the slurry is composed of a mixture of several organic and inorganic compounds. The organic components are usually the binder, the dispersant, the plasticizer, the solvent in the case of organic tape casting, and possibly some other additives like wetting agents, defoamers or pore formers if porosity is desired in the final microstructure. The inorganic compounds include the ceramic powders to be shaped, sintering additives, and water as the solvent for aqueous tape casting. All the organic components remain in the green tape after drying. Since they are removed when heated at elevated temperature, they give rise to pores, which cannot always be eliminated during the sintering treatment. Consequently, the ratio of the amount of

powder and organic compounds, and hence the final formulation of the slurry, must be fine-tuned in order to tailor the final microstructure. Amongst the slurry characteristics, the stability is of utmost importance. Polarization interactions take place at the solid–liquid interface, interactions whose intensity governs the slurry stability. Consequently, the value of the dielectric constant of the liquid determines the slurry stability, and hence the choice of solvent, which in turn determines the choice of all the other additives. The other forces acting on the particles in the slurry are gravity, which depends on the particle mass (and indirectly size), and the attractive Van der Waals interactions, which promote flocculation and act against the stability of the slurry. On the other hand, thermal agitation, electrostatic and steric repulsive forces promote the dispersion of the particles and therefore increase the stability of the slurry. The role of the dispersant agent is precisely to enhance the intensity of these dispersive forces. The second important slurry characteristic is the viscosity, which determines the viability of the process to cast green tapes. The slurry viscosity varies as a function of the amount of solvent per unit volume; it needs to be precisely adjusted to allow for a good dispersion of the powder as well as for efficient dissolution of the binder.

1.3.8. Solid state sintering

The driving force for sintering is the reduction in surface free energy associated with a decrease of surface area in powder compacts. The vapor pressure difference across a curved interface can enhance evaporation from particle surfaces and condensation at the neck between two particles. Although, this evaporation-condensation process produces changes in pore shape and joins particles together, the centre-to-centre distance between particles remains constant so that shrinkage and densification do not occur. For ceramic powders with low vapor pressure, the driving force is the difference in free energy between the neck region and surface of particles. As for the evaporation-condensation pathway, transport from surface to neck by surface and lattice diffusion does not cause densification. This is produced only by diffusion from the grain boundary between particles and from the bulk lattice. Covalent ceramics such as Si_3N_4 are more difficult to sinter to high density than ionic solids for example Al_2O_3 because of lower atomic mobilities, although difficulties can be overcome by using very fine powders (<0.1 μm), high temperature and pressure.

1.4. SCOPE OF THE THESIS

1.4.1. Relevance

Fuel cells are envisaged to be among the potential future power generators because they offer a clean, pollution free technology for the generation of electricity with high efficiency. Solid oxide fuel cells are expected to be useful both for captive and distributed power generation. Conventional solid oxide fuel cells using stabilized zirconia as the solid electrolyte operate at around 1000^{o}C because the ionic conductivity of the electrolyte is not sufficient at lower temperatures. At these high temperatures several problems associated with materials of construction, thermal mismatch between cell components, development of sealants to withstand high temperatures and formation of insulating phases at the electrode-electrolyte interface are present. Solid oxide fuel cells operating at lower temperatures (600-800^{o}C) will offer tremendous advantages. The main aim of this thesis is to develop materials for electrolyte and electrodes (cathode and anode) for intermediate temperature solid oxide fuel cells that have high conductivity and have thermal compatibility between them.

1.4.2. Objectives

- Synthesis of various perovskite oxides used in Intermediate Temperature solid Oxide Fuel cells by various wet chemical routes and characterization of their structural, physical and electrical properties.
- Synthesis of pure phases of doped lanthanum gallate, LSGM [$La_{1-x}Sr_xGa_{1-y}Mg_yO_{3-\delta}$, (x=0.0-0.3, y=0.0-0.3)] and investigation of the composition range of stability of $La_{1-x}Sr_xGa_{1-y}Mg_yO_{3-\delta}$ at 700 and 1500 ^{o}C with respect to doping at the A- and B-sites by phase equilibration.
- Measurement of the electrical conductivity of LSGM ($La_{1-x}Sr_xGa_{1-y}Mg_yO_{3-\delta}$ x=0.0-0.2, y=0.0-0.3) as a function of temperature and composition.
- Single cell assembly, area specific resistance measurement and testing of electrolyte supported single cells in gas atmospheres.

The overall objective is the development and testing of intermediate temperature solid oxide fuel cells.

CHAPTER II

REVIEW OF LITERATURE

2.1. INTRODUCTION

The state of the art solid oxide fuel cells are based on $(Y_2O_3)ZrO_2$ solid electrolyte, lanthanum manganite as cathode, Ni-ZrO_2 cermet as anode and lanthanum chromite as interconnect [Minh, 1993; Basu et al, 2005; Van Herle et al, 2001]. They have a planar configuration and operate in the temperature range of 800-1000^oC [Basu et al 2005; Hwang et al 2005; Duquette and Petric 2004; Ishihara et al 2004]. High temperature of operation of the SOFC is dictated by the ionic conductivity requirement of the solid electrolyte (>0.1 S/cm). Further, there are several other advantages of high temperature operation such as high ionic conductivity, low interfacial resistance, faster kinetics, the elimination of a reformer for the hydrocarbons and the possibility of co-generation. However, the higher temperature of operation of solid oxide fuel cells results in several material problems, requirement of high temperature sealing and therefore a high cost. Therefore, from the materials and cost point of view, it is advantageous to operate the fuel cells at intermediate temperatures of 600-800^oC, which retains the advantages of not having a separate reformer and co-generation but imposes less stringent requirements on the materials. At these temperatures, one can use less expensive and well-established ferritic stainless steel for interconnect and cell construction. Further, at lower temperatures, because of lower thermal stresses and slower kinetics, the thermal and chemical compatibility requirements are much less stringent. However, the main limitation of operating the solid oxide fuel cell at lower temperature is to find alternate oxygen ion conducting electrolyte materials, which have comparable ionic conductivities at these lower temperatures. Further, lower temperatures also result in higher interfacial resistances, slower electrode reactions and low reforming efficiency. In addition to the conductivity requirements of the solid electrolyte, thermal and chemical compatibility with the anode and cathode as well as stability under both oxidizing and reducing conditions are the other essential requirements.

2.2. MATERIALS FOR INTERMEDIATE TEMPERATURE SOLID OXIDE FUEL CELLS

Since the discovery of high and exclusive oxygen ion conductivity in doped cubic zirconia by Kiukkola and Wagner [1957]; several other materials with high oxygen ion conductivity have been reported in the literature. Oxygen ion conductivity has not only been restricted to the cubic fluorite structure, but has been found in perovskite and pyrochlore structures [Routbort et al, 2000; Doshi and coworkers, 1999; Burggraaf et al, 1981; Van Dijk et al, 1983 and 1985; Moriga et al, 1989; Shukla and Gopalakrishnan, 1995; Moon and Tuller, 1989; Kramer et al, 1994; Kharton et al, 2004; and Skinner, 2001]. The latest developments in oxygen ion conducting solid electrolytes have been reviewed recently [Kharton et al, 2004; Goodenough, 1997; Skinner and Kilner, 2003; Boivin, 2001; Goodenough, 2003]. The oxygen ion conductivity as a function of temperature for several solid electrolytes is shown in Fig.2.1 [Krumpelt et al, 2002]. It is seen that there are several materials that have much superior ionic conductivity at lower temperatures than $(Y_2O_3)ZrO_2$. These include δ-Bi_2O_3, $Ce_{0.9}Gd_{0.1}O_{2-\delta}$ and $La_{0.8}Sr_{0.2}Ga_{0.8}Mg_{0.2}O_{3-\delta}$. Among these, δ-Bi_2O_3 is not stable and dissociates at lower p_{O2} and higher temperature and $Ce_{0.9}Gd_{0.1}O_{2-\delta}$ exhibits significant electronic conductivity at lower oxygen partial pressures because of reduction from Ce^{+4} to Ce^{+3}. The most promising electrolyte candidate for low or intermediate temperature SOFC is $La(Sr)Ga(Mg)O_3$ known as LSGM which has a perovskite structure and ionic conductivity about three orders of magnitude higher than $(Y_2O_3)ZrO_2$ in the temperature range of 600-800^oC. Although $La(Sr)Ga(Mg)O_3$ has a thermal conductivity similar to $(Y_2O_3)ZrO_2$ and therefore the same cathode and anode materials can in principle be used, the chemical compatibility between these materials are not well established. It has been reported that ZrO_2 reacts with lanthanum oxide and forms several stable interoxide compounds [Minh, 1993; Basu et al, 2005; Van Herle et al, 2001] and therefore zirconia-based material is not suitable for use as anode when LSGM is used as an electrolyte.

Further, lanthanum-manganite, which is used as a cathode in the conventional SOFC offers very high interfacial resistance at the cathode-electrolyte interface. This is shown in Fig. 2.2 in comparison to several other perovskite oxides, which have high mixed (electronic and ionic) conductivity and are alternative cathode materials for use in LSGM based SOFC [Gong et al, 2004]. Among these, lanthanum cobaltite has a

lower electronic conductivity but higher thermal expansion compatibility with LSGM, whereas lanthanum ferrite (LSF) has lower thermal expansion compatibility but higher electronic conductivity [Kawada and Yokokawa, 1997]. It has been reported that mixed La(Sr)Fe(Co)O_3 (LSCF) has the optimum combination of electronic conductivity and thermal expansion compatibility with LSGM. Nickel- or cobalt-based LSGM cermets can be used as anode.

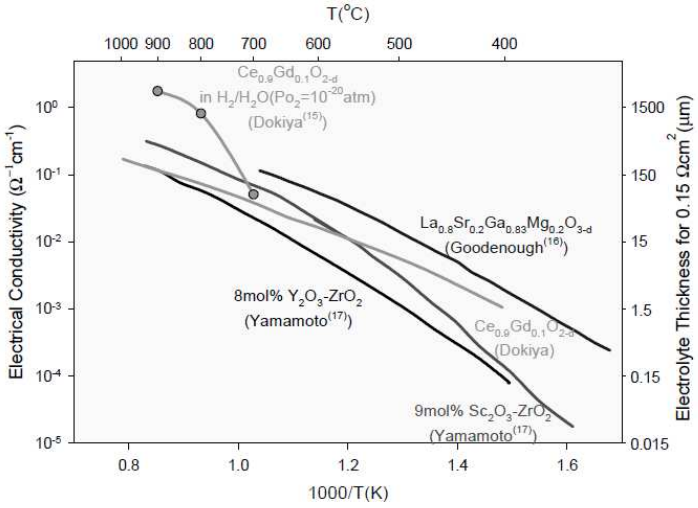

Fig.2.1 The conductivities of potential solid oxygen ion electrolytes [Krumpelt et al, 2002]

In recent times, La(Sr)Cr(Mn)O_3 is also reported to be having the requisite electronic and ionic conductivity and stability under reducing atmosphere for use as an anode [Atkinson et al, 2004].

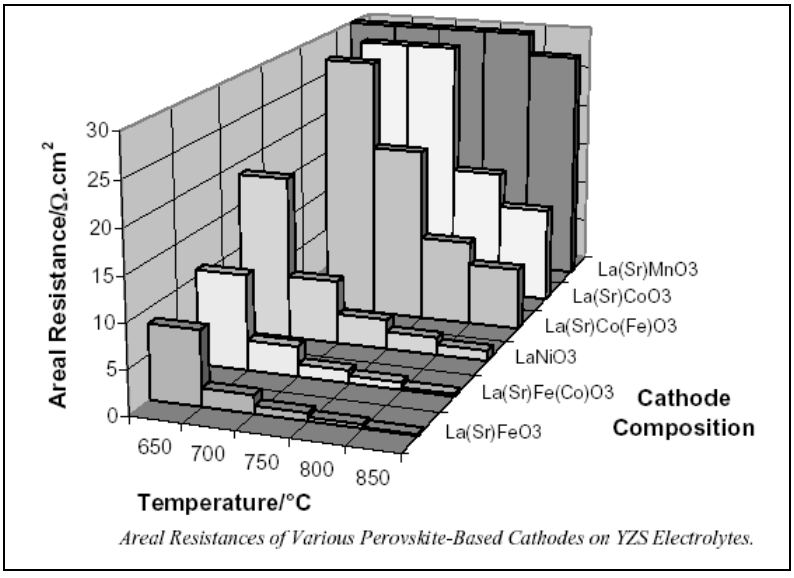

Fig.2.2.Interfacial resistance of various perovskite-based cathodes on YSZ electrolytes [Krumpelt et al, 2002]

2.3. SYNTHESIS METHODS

The conventional solid-state reaction method is in general employed to prepare mixed oxide compounds because of its lower manufacturing cost and simplicity. Several investigators [Westphal et al, 2000; Sammes et al, 1998; Matsuda et al, 2004; Cheng and Navrotsky, 2004; Gorelov et al, 2001; Kim and Yoo, 2001] have employed a solid-state reaction method to synthesize perovskite ceramic oxides pertinent to IT-SOFC. However, this method, in general requires calcination temperatures higher than 1500^{o}C and time period in excess of 24 hours to obtain a pure single phase resulting in coarse particle sizes. In order to overcome these disadvantages, a number of synthetic routes like citrate - gel [Spinicci et al, 2001; Baythoun and Sale, 1982; Tas and coworkers, 2000; Sinquin et al, 2001; Stolen et al, 1998; Polini and coworkers, 2004; Basu et al, 2004; Amow et al, 2004], co-precipitation [Johnson et al, 1976; Prokudina et al, 1974; Jiang, 2003; Jiang and Love, 2003; Tadokoro et al, 2004; Zhang et al, 2003], combustion [Coffey et al, 2003; Aruna et al, 1997; Zhu et al, 2005; Rossignol and coworkers, 2004; Anderson et al, 2004; Gao et al, 2003] and super-homogenous co-precipitation [Chiang et al, 1997; Huang and coworkers, 1996; Gonzalez et al, 1997] methods have been reported in the literature for the preparation of these oxides.

2.4. SYNTHESIS-PROCESSING-STRUCTURE – PROPERTY CORRELATION

Zheng and Pederson [1999, [a]1999] have studied the crystal structure and thermodynamic properties of lanthanum strontium manganites. They found that the Sr-content and A:B cation ratio influences the perovskite structure. An orthorhombic distortion occurs when 0.2 mol of Sr is doped in the perovskite structure. For $0.2 \leq Sr \leq 0.3$ mol, this changed to a monoclinic or hexagonal structure. For higher Sr contents, it transforms again to an orthorhombic structure. Kharton et al [1999] have observed that the incorporation of Ni in lanthanum ferrite results in increasing oxygen non-stoichiometry, electrical conductivity and thermal expansion coefficient. As the Ni content increases, the oxygen permeation increases due to increased vacancy concentration and bulk conductivity.

The properties of A-site deficient $La_{0.6}Sr_{0.4}Co_{0.2}Fe_{0.8}O_{3-\delta}$ have been studied by Kostogloudis and Ftikos [1999]. They observed that A-site deficiency leads to a rhombohedral deviation from the perovskite structure. The lattice parameters increased with A-site deficiency. The electrical conductivity of the materials also increased up to 600^{o}C and thereafter decreased due to loss of lattice oxygen. Tu et al [1999] observed

that the electrical conductivity of $Ln_{0.4}Sr_{0.6}Co_{0.8}Fe_{0.2}O_{3-\delta}$ (Ln = La, Pr, Nd, Sm or Gd) shows a semi-conducting behavior at low temperature and metallic behaviour at high temperatures. Among these, Nd at the A-site showed the best catalytic activity for oxygen reduction. Kharton and coworkers [2001] found that sub-micron $LaCoO_3$ powders obtained through a cellulose precursor technique or a combustion synthesis process showed a much better sinterability in comparison to the powder prepared by the standard solid state synthesis technique. Further, they also found that the influence of the processing route on lattice parameter, electronic conductivity and thermal expansion of $LaCoO_3$ was negligible.

The effect of synthetic route on sintering behavior, phase purity and conductivity of $La_{1-x}Sr_xGa_{1-y}Mg_yO_3$ powders containing different amounts of Sr^{+2} and Mg^{+2} was studied by Polini et al [2004]. They could not obtain pure powder even after 10 hours of calcination at 1500 ^oC. The amount of Sr- and Ga- containing secondary phase was found to depend on the concentration of dopants. Gao et al [2003] investigated the electrochemical behaviour of $Ln_{0.6}Sr_{0.4}Co_{0.2}Fe_{0.8}O_{3-\delta}$ (Ln = Ce, Gd, Sm, Dy) for use as cathode in ITSOFC. They observed that all the compounds investigated by them have a good chemical compatibility with Sm-doped CeO_2 electrolyte. $Dy_{0.6}Sr_{0.4}Co_{0.2}Fe_{0.8}O_{3-\delta}$ showed higher catalytic activity for oxygen dissociation. Matsuda and coworkers [2004] have studied the influence of Ga-doping at the Co-site on lattice parameter, microstructure, thermal expansion coefficient and electrical conductivity of $La_{0.6}Sr_{0.4}CoO_3$ (LSC). They observed that the lattice parameters of this compound increased with Ga-doping up to X_{Ga}=0.2 and un-indexed secondary phases formed when $X_{Ga} \geq 0.3$. It was also found that the inter-diffusion of Ga into LSC causes unfavorable changes in the cathode performance. Spinicci et al [2001] have investigated the catalytic activity of $LaMO_3$ (M = Mn, Co and Fe) for hexane total oxidation. The activity for the hexane oxidation was found to increase in the order: $LaFeO_3 > LaCoO_3 > LaMnO_3 > PdO/Al_2O_3$. The thermodynamic properties of $LaFeO_3$ and $LaCoO_3$ from T = 13 to 1000 K have been investigated by Stolen and coworkers [1998]. They found that both compounds undergo electronic transitions; $LaFeO_3$ a magnetic order-disorder transition at 735 K and $LaCoO_3$, a continuous low to intermediate to high spin transition which gives rise to heat capacity maxima at 60 K and 530 K.

Nakayama et al [2003] have studied the synthesis of $LaCoO_3$ by different routes (namely solid state synthesis from La_2O_3 and CoO, co-precipitation from $La_2(C_2O_4)_3$

n.H_2O and CoC_2O_4.m H_2O and hetero complex La $[Co(C_2O_4)_3]$. 8.5 H_2O and evaluated them for homogeneity, sinterability and conductivity. They found that the homogeneity was more in the hetero-complex but the conductivity was lower by an order of magnitude than that of $LaCoO_3$ from the other two methods. Sinquin et al [2001] studied the formation of $LaMO_3$ (M = Co, Mn) by propionate precursors. They attributed the better stability of $LaMnO_3$ in the presence of Cl_2 to a better thermodynamic stability of the oxygen-rich $LaMnO_{3+\delta}$ phase obtained after calcination. Berger et al [2003] carried out a structural and morphological investigation on pure and doped-$La_{1-x}M_xCoO_3$ (M=Sr,Ca; x=0,0.1) synthesized using alanine-based precursors. They found that the alanine nitrate method resulted in nano sized powders of the perovskite phase (with rhombohedral distortion) with very large surface area. Aruna and coworkers [1997] studied the synthesis and calcination behavior of pure and Sr-doped lanthanum manganites. They observed that the Mn^{+4} content in $LaMnO_3$ decreases on calcination resulting in a phase transformation from cubic to rhombohedral structure at high temperature. They also observed an increase in thermal expansion coefficient with increasing Sr content.

Lanthanum gallate powders doped with alkaline rare earth oxides were densified using an activated microwave sintering process [Kesapragada et al 2003]. They found that a dense electrolyte layer could be developed by this method for application in intermediate temperature solid oxide fuel cells. Huang and coworkers [1998] have synthesized Sr- and Mg- doped lanthanum gallate using sol-gel, Pechini and hydrothermal preparation techniques. They could obtain single phase LSGM by sol-gel and Pechini methods, but not by hydrothermal treatment. The powders showed a mean particle size of 50 nm (TEM) with a BET surface area of 5 m^2/g but hydrothermal treatment of the gel did not produce well-crystallized powders. The primary as well as secondary phases formed in Sr- and Mg- doped lanthanum gallate as the dopant concentration is changed was studied by Du and Sammes [2001]. They found that when the ratio of A- to B-site exceeded unity, trace amount of secondary phases appeared along with the primary perovskite-phase. When changing the doping content and varying the A/B ratio (less than unity), one can create sufficient oxygen deficiency and high concentration of oxygen vacancies required to facilitate high oxygen ionic conductivity. Du and Sammes [2001] studied the fabrication procedure, parameter optimization and selection of additives towards the extrusion of tubular form of Sr- and Mg- doped lanthanum gallate. Kurumada et al [2005] measured the electrical

conductivity of Sr-doped gallate as a function of temperature by ac and dc impedance techniques. They observed that the migration energy of oxide ions within the grains becomes considerably large when Sr dopant concentration in the A-site increases from 0 to 0.1. They attributed this to lattice distortion caused by a large difference in ionic radii of Mg^{+2} and Ga^{+3}.

2.5. STABILITY RANGE AND PHASE EQUILIBRIUM IN Sr, Mg- DOPED LANTHANUM GALLATE

The perovskite phase $La_{1-x}Sr_xGa_{1-y}Mg_yO_{3-(x+y)/2}$ (LSGM) has superior oxygen ion conductivity compared to yttria or scandia doped cubic zirconia in the temperature range 600-1000^oC [Ishihara et al, 1994; Inaba and Tagawa, 1996]. The oxygen ion conductivity depends on the oxygen vacancy concentration introduced by the doping of aliovalent cations (Sr and Mg) at the A- and B-sites of the perovskite structure. However, synthesis of the pure perovskite phase in Sr and Mg doped lanthanum gallate has been found to be difficult. The synthesized LSGM in many cases is reported to contain small amount of undesired phases such as $LaSrGa_3O_7$ and $LaSrGaO_4$ [Djurado and Labeau, 1998; Khanlou et al, 2000]. A variety of other phases (La_2O_3, MgO, $Sr_3Ga_2O_6$, $La_4Ga_2O_9$, $La_3Ga_5O_{12}$, $MgGa_2O_4$, La_2SrO_x, $MgGaLa_3O_7$) has also been reported to co-exist with the perovskite phase $LaGaO_3$ [Djurado and labeau, 1998; Matraszek et al, 2004]. Presence of non-conducting secondary phases seriously impedes the oxygen ion mobility and thereby conductivity. Knowledge of the solubility of Sr and Mg at the A- and B- sites and phase relations in the quaternary system La_2O_3-SrO-Ga_2O_3-MgO at the operational temperature range of the fuel cells is essential to optimize the processing conditions for achieving the highest dopant concentration without the precipitation of the secondary phases.

The phase diagram of the La_2O_3-Ga_2O_3 system [Mizuno et al, 1985; Zinkevich et al, 2006] indicates that the compound $LaGaO_3$ is stoichiometric (negligible solubility of La_2O_3 and Ga_2O_3) melting congruently at 1715 ^oC (Fig.2.3). At La/Ga<1, it is in equilibrium with Ga_2O_3 at 1345 ^oC, after which, it is in equilibrium with a eutectic liquid. At La/Ga>1, it is in equilibrium with another stoichiometric compound $La_4Ga_2O_9$. No information is available in the literature on the solubility of SrO in La_2O_3 although the presence of two binary compounds La_4SrO_7 and $La_2Sr_2O_5$ in this system has been reported [Zheng and Pederson, 2004; Majewski et al, 2001]. Similarly, although the complete phase diagram of the MgO-Ga_2O_3 system is not available, a

partial phase diagram of the sub-solidus range was given by Schmalzried [1961]. The solubility of MgO in Ga_2O_3 is stipulated to be less than 40 mol % beyond which it is in equilibrium with a spinel phase $MgGa_2O_4$ [Majewski et al, 2001]. At larger Mg concentrations, the perovskite phase is shown to be in equilibrium with MgO [Majewski et al, 2001].

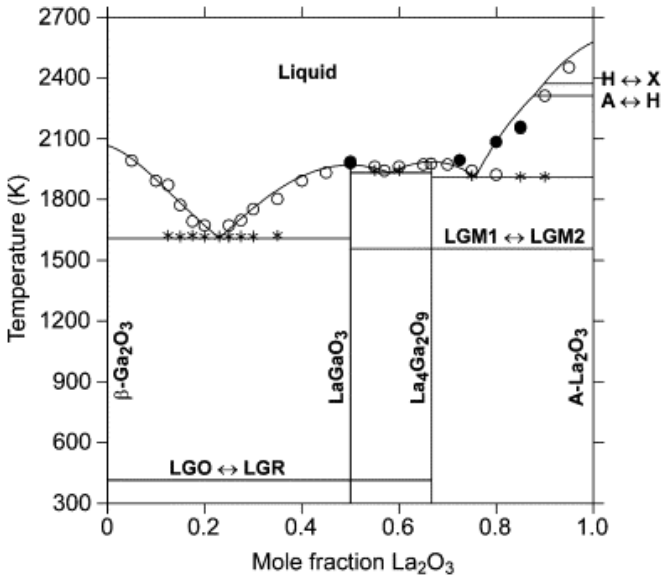

Fig.2.3 Phase diagram of the La_2O_3-Ga_2O_3 system [Mizuno et al, 1985]

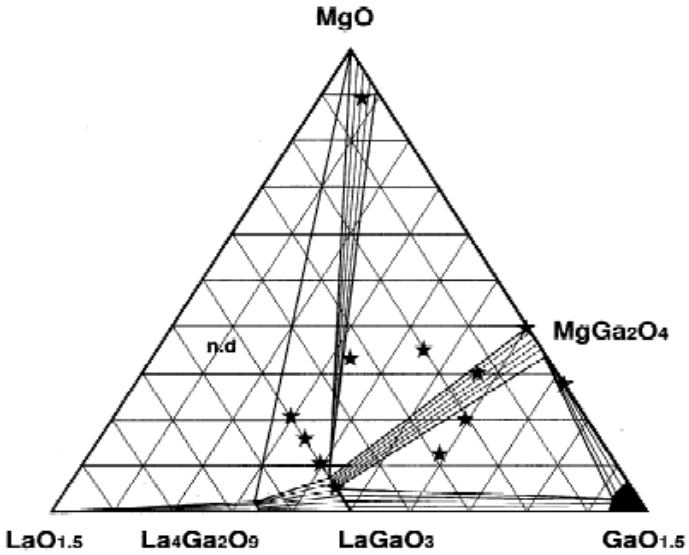

Fig.2.4 Phase diagram of the $LaO_{1.5}$-$GaO_{1.5}$-MgO system at 1400^{o}C [Majewski et al, 2001]

The spinel phase exists over a stoichiometric range (Mg:Ga ratio from 35:65 to 40:60) and melts congruently above 1600 ^{o}C. One stoichiometric compound $MgLa_2O_4$ has been reported in the binary La_2O_3-MgO system. Phase equilibria in the ternary sub-systems La_2O_3-Ga_2O_3-SrO and La_2O_3-Ga_2O_3-MgO have been studied by Majewski and

co-workers [2001] at 1400 ^{o}C in air and Matraszek et al [2004] at 900 and 1400 ^{o}C. Majewski and co-workers [2001] reported a maximum solubility of Sr in $LaGaO_3$ of 4-6 mol% and they found $LaGaO_3$ to be in equilibrium with Ga_2O_3, $La_4Ga_2O_9$ and $LaSrGa_3O_7$. Interestingly, it is seen from their phase diagram that $LaGaO_3$ cannot be in thermodynamic equilibrium with $LaSrGaO_4$. At equilibrium, as Sr is doped to pure $LaGaO_3$, first $LaSrGa_3O_7$ forms after saturation solubility is reached and further increase of Sr doping results in the three phase equilibrium $LaGaO_3$-$LaSrGa_3O_7$-$La_4Ga_2O_9$. $LaSrGaO_4$ can only form at the expense of $LaGaO_3$ when the Ga concentration goes below 40-50 mol % or SrO concentration exceeds 15 mol %. The phase $LaSrGa_3O_7$ was found to exhibit an extended homogeneity region ranging from $La_{1.5}Sr_{0.5}Ga_3O_7$ to $La_{0.8}Sr_{1.2}Ga_3O_{6.9}$. Matraszek et al [2004] reported a maximum solubility of 2 mol % Sr in $LaGaO_3$. They also confirmed the non-stoichiometry range for $LaSrGa_3O_7$ and could not identify the phase $LaSrGaO_4$ in equilibrium with $LaGaO_3$. Majewski and co-workers [2001] found that in the ternary system La_2O_3-Ga_2O_3-MgO at 1400 ^{o}C, the maximum solubility of Mg in $LaGaO_3$ was only 4-5 mol % and that $LaGaO_3$ was found to be in thermodynamic equilibrium with Ga_2O_3, $La_4Ga_2O_9$, $MgGa_2O_4$ and MgO. At equilibrium, as Mg was doped to pure $LaGaO_3$, after saturation solubility, initially Ga_2O_3 was in equilibrium with $LaGaO_3$, further Mg addition resulted in a shift to perovskite+$MgGa_2O_4$ equilibrium and beyond 20 mol% Mg resulted in the formation of MgO in equilibrium with the perovskite phase. Depletion of gallium below the stoichiometric value will result in the formation of $La_4Ga_2O_9$ and also promote the formation of MgO in preference to $MgGa_2O_4$. Although Matraszek and coworkers [2004] also observed that $LaGaO_3$ was in thermodynamic equilibrium only with Ga_2O_3, $La_4Ga_2O_9$, $MgGa_2O_4$ and MgO, they found two additional compounds $MgGaLa_3O_7$ and $MgGa_{11}LaO_{19}$ in this system. Further, they observed in their study that the solubility of MgO in $LaGaO_3$ was far higher (up to 20 mol %). In contrast, Sammes et al [1998] found by XRD and Raman spectroscopy that up to 20 mol % Sr and only 5 mol % Mg could be doped in pure $LaGaO_3$ at 1500 ^{o}C without the formation of the second phase. With increasing Sr, $LaSrGa_3O_7$ and with increasing Mg, $La_4Ga_2O_9$ was found to form as the second phase in their study. The formation of $La_4Ga_2O_9$ at only 5 mol % Mg in $LaGaO_3$ might have been influenced by the vaporization of Ga at 1500 ^{o}C and the consequent change in bulk composition. Chen and Fung [2004] reported a maximum solubility of less than 10 mol % SrO in pure $LaGaO_3$ and MgO solubility in excess of 20% in pure $LaGaO_3$.

The quaternary system $LaO_{1.5}$-$GaO_{1.5}$-SrO-MgO has also been investigated by Huang and coworkers [1998, 2000] between 800-1500 ^oC, Majewski et al [2001] at 1400 ^oC, Rozumek and coworkers [2003] between 1100-1500 ^oC, Matraszek et al [2004], Zheng and co-workers [2004] at 1500 ^oC and Liu et al [2006] at 1500 ^oC. Huang and coworkers [1998, 2000] showed a stoichiometry range of more than 10 mol % for pure $LaGaO_3$ which is inconsistent with the binary phase diagram of this system and previous reports They observed that the solubility of SrO and MgO in the perovskite phase were 20 mol % each when doped together. In the phase diagram depicted by them for the temperature range 800-1500 ^oC, the perovskite phase was shown to be in equilibrium with $LaSrGa_3O_7$ and $LaSrGaO_4$. From the ternary diagram for the $LaO_{1.5}$-$GaO_{1.5}$-SrO system, it is clear that $LaGaO_3$ cannot be in equilibrium with $LaSrGaO_4$ and therefore the phase diagram shown by them is metastable. If partial vaporization of Ga occurs, then the bulk composition shifts towards SrO rich regions wherein the formation of $LaSrGaO_4$ is feasible. Majewski and co-workers [2001] also observed that when both Sr and Mg were doped at the La and Ga sites, the solubility was enhanced from 4-5 mol% individually in $LaGaO_3$ to 20 mol % each at 1673 K. They observed that the solubility of both Sr and Mg when simultaneously doped decreased drastically with temperature and at 1100 ^oC, the combined solubility of Sr and Mg was less than 2-3 mol %. However, the phase equilibration studies carried out by Rozumek and co-workers [2003] at 650 ^oC (for up to 1500 h) indicated a reasonably large compositional range of stability and failed to detect any secondary phases which they attributed to non-attainment of equilibrium. Majewski et al [2001] postulated four 3-phase regions; $LaGaO_3$+$LaSrGaO_4$+$LaSrGa_3O_7$, $LaGaO_3$+$LaSrGa_3O_7$+MgO, $LaGaO_3$+$LaSrGaO_4$+MgO and $LaGaO_3$+$La_4Ga_2O_9$+MgO and one 4-phase region $LaGaO_3$+$LaSrGaO_4$+$LaSrGa_3O_7$+MgO to co-exist with the perovskite phase at 1400 ^oC. The phase diagram depicted by Majewski and coworkers [2001] at 1673 K is in-consistent in several respects and appears to correspond to metastable equilibria. The relevant 2-phase regions separating the 3-phase regions have not been shown in their diagram. Further, for a 4-component system at constant temperature and pressure, 4-phase equilibrium is invariant. They have shown the 4-phase equilibrium to exist over a wide composition range. The equilibrium co-existence of $LaGaO_3$ with $LaSrGaO_4$ is also inconsistent with the corresponding ternary diagram for the $LaO_{1.5}$-$GaO_{1.5}$-SrO system. Rozumek and co-workers [2003] constructed isothermal phase diagrams at 1100, 1200, 1400 and 1500 ^oC of the $LaGaO_3$-$SrGaO_{2.5}$-$LaMgO_{2.5}$ system and have

shown the perovskite LSGM phase to be surrounded by three- and four- phase regions; $LaGaO_3$+$LaSrGaO_4$+MgO, $LaGaO_3$+$LaSrGaO_4$+$LaSrGa_3O_7$+MgO and $LaGaO_3$+$LaSrGaO_4$+$La_4Ga_2O_9$+MgO at all these temperatures. They mentioned that the phase diagram depictions did not fully comply with the theoretical rules for the topological design of quaternary phase diagrams in terms of the absence of two-phase regions separating the 3- and 4-phase regions. However, the presence of two 4-phase equilibria at constant T and P over a composition range was not explained by them. Matraszek et al [2004] studied the solid phase equilibria in the system La_2O_3-Ga_2O_3-MgO-SrO near the solubility lobe of the LSGM phase in air at 900 ^oC (equilibration for 720 h) and 1400 ^oC (240 h equilibration). The samples for equilibration were prepared by the Pechini method ensuring atomic scale mixing. They found that complete equilibration was not achieved at 900 ^oC (because of the co-existence of the phases $LaGaO_3$, $La_4Ga_2O_9$, $SrLaGaO_5$ and $SrLaGa_3O_7$ at 900 ^oC which according to them is thermodynamically impossible) and therefore reported the phase diagram only at 1400 ^oC. It is difficult to perceive non-attainment of equilibrium in 720 h at 900 ^oC especially since Pechini method of synthesis would have resulted in atomic level mixing and much smaller diffusion distances. The simultaneous solubility of Sr and Mg in the LSGM phase was found to be in excess of 20 mol % each at 1400 ^oC. They also observed that the perovskite LSGM phase was bound by three- and four- phase regions; LSGM+$MgGaLa_3O_7$+MgO, LSGM+$MgGaLa_3O_7$+MgO+$SrLaGaO_4$, LSGM+$SrLaGaO_4$+MgO, LSGM+$SrLaGaO_4$+$SrLaGa_3O_7$+MgO and LSGM+$SrLaGaO_4$+$SrLaGa_3O_7$. They stipulated the possibility of two other 3-phase equilibria $LaGaO_3$+$MgGa_2O_4$+MgO and $LaGaO_3$+$MgGaLa_3O_7$+$La_4Ga_2O_9$ at 1400 ^oC. The phase equilibria stipulated by Matraszek and coworkers [2004] was different from that postulated by Majewski et al [2001] and Rozumek and co-workers [2003]. Matraszek et al [2004] reported an additional phase $MgGaLa_3O_7$ to co-exist in equilibrium with the perovskite phase. Surprisingly, in their study, according to the ternary phase diagram for the Ga_2O_3-La_2O_3-MgO system constructed by them, the perovskite phase $LaGaO_3$ cannot co-exist with $MgGaLa_3O_7$ i.e., their ternary and quaternary diagrams are mutually inconsistent. Their phase diagram also did not comply with the topological rules for the quaternary phase diagram with respect to the existence of 2-phase regions and the existence of 4-phase equilibria over a range of composition at constant T and P. Zheng and co-workers [2004] investigated phase constitution in Sr and Mg doped $LaGaO_3$ system at 1500 ^oC (equilibration for 9 h) in

terms of doping at the A- and B-sites (0-20 mol% at each site) as well as a function of A/B ratio (between 0.95 to 1.05). They observed that for the stoichiometric LSGM phase (i.e., A/B=1), up to 10 mol % Sr and 20 mol % Mg could be simultaneously doped without the formation of secondary phases. Ga_2O_3 and $SrLaGa_3O_7$ co-existed in equilibrium with the perovskite LSGM phase at A/B ratios<1 and $La_4Ga_2O_9$, La_4SrO_7 and $SrLaGaO_4$ coexisted with LSGM at A/B ratios>1. Liu et al [2006] also constructed the phase diagram at the $LaGaO_3$ rich end of the $LaGaO_3$-$SrGaO_{2.5}$-$LaMgO_{2.5}$ system at 1500 ^oC (equilibration time up to 36 h). They observed that although the solubility of Sr in $LaGaO_3$ was only 4 mol % and that of Mg was 28 mol % in pure $LaGaO_3$, when doubly doped the solubility limit of Sr was raised to more than 25 mol % and that of Mg to more than 28 mol %. However, they have depicted the single phase perovskite region to be interrupted by two 2-phase regions LSGM+$LaSrGaO_4$ and LSGM+$LaSrGa_3O_7$ as the Sr content is increased. This defies the rules of phase diagram construction and does not have any meaning. The perovskite LSGM phase was bound at the outside by a three phase region LSGM+$LaSrGaO_4$+$LaSrGa_3O_7$ as Sr content was increased. However, the secondary phase precipitating from the perovskite phase when Mg solubility in the perovskite phase was exceeded was not depicted. Huang and coworkers [1996] found that by doubly doping Sr and Mg at the A- and B-sites, the solubility of Sr and Mg could be enhanced to 25 and 20 mol % respectively at 1470 ^oC, beyond which $LaSrGaO_4$ precipitated upon increasing Mg content and $LaSrGa_3O_7$ precipitated when the solubility of Sr was exceeded. They also found regions of three phase equilibrium corresponding to LSGM+$LaSrGaO_4$+$LaSrGa_3O_7$. Gorelov and co-workers [2001] observed that when Sr and Mg was simultaneously doped in the perovskite phase $LaGaO_3$, the limiting solubility was enhanced to x=y=0.16 at 1743 K. If excess Sr and/or Mg is added, $LaSrGa_3O_7$ and/or $La_4Ga_2O_9$ phases formed respectively in addition to the $LaGaO_3$ perovskite phase. The phase $La_4Ga_2O_9$ possibly formed because of the evaporation of gallium and the consequent shift in bulk composition of $LaGaO_3$. Datta and co-workers [2007] made a semi-quantitative estimation of the impurity phases $LaSrGa_3O_7$, $LaSrGaO_4$ and $La_4Ga_2O_9$ formed as a function of concentration of Sr and Mg at the A and B sites in LSGM synthesized by solid state reaction method and sintered at 1500 ^oC for 12 h in static air atmosphere. They noticed that at a given Sr content, the relative amount of secondary phases decreased with increase in Mg concentration and at a given Mg content, it increased with Sr content. It is therefore clear that the solubility limits of Sr and Mg in

the LSGM phase as well as phase equilibrium in the quaternary system La_2O_3-Ga_2O_3-SrO-MgO has not been well established. The phase diagrams projected in the literature are in several respects inconsistent with phase rules. Further, systematic studies on the phase equilibrium in LSGM as a function of Sr and Mg concentrations at the operational range of temperature of Intermediate temperature solid oxide fuel Cell (600-800 ^oC) which is of foremost importance to ascertain the time dependent degradation of the cell is lacking.

It has been reported that the phase purity and the nature and amounts of the secondary phases that form not only depend on the concentration of dopants in the A- and B- sites and the A/B ratio, but is also a function of the synthesis method, sintering temperature and time, oxidizing or reducing atmosphere and whether the equilibration was done on powders or pellets [Djurado and Labeau 1998; Polini et al 2004]. Djurado and Labeau [1998] found that solid state synthesis from oxides at 1500 ^oC for 6 h resulted in the pure perovskite phase, whereas solid state reaction from carbonates and ultrasonic spray pyrolysis yielded secondary phases at the inside of the pellet. The main impurity phase was reported to be $LaSrGa_3O_7$ for the solid state synthesis from oxides and $Sr_3Ga_2O_6$ and $La_4Ga_2O_9$ for synthesis through ultrasonic spray pyrolysis. Datta and co-workers [2007] indicated that the compound identified as $Sr_3Ga_2O_6$ by Djurado and Labeau [1998] was in fact $LaSrGaO_4$. Djurado and Labeau [1998] also observed that a minimum sintering temperature of 1500 ^oC was required for complete reaction for all the methods. However, many other investigators suggested that for chemical methods of synthesis, sintering between 1400-1500 ^oC was sufficient for complete phase formation [Majewski et al 2001; Huang and Goodenough, 1998; Huang and Goodenough, 2000; Polini et al 2004; Tas et al 2000, Cheng and Navrotsky, 2004; Shi et al, 2006; Chae et al, 2008; and Ishikawa and coworkers, 2007]. In the studies of Djurado and Labeau [1998], the impurity phases were different at the surface and centre of the pellets. For $La_{0.9}Sr_{0.1}Ga_{0.8}Mg_{0.2}O_{2.85}$ (LSGM9182), sintering at 1673 K for less than 6 hour yielded $Sr_3Ga_2O_6$ ($LaSrGaO_4$?) as the impurity phase, whereas $La_4Ga_2O_9$ formed for sintering beyond 6 hours. As the sintering temperature increased, the concentration of $La_4Ga_2O_9$ decreased and that of $Sr_3Ga_2O_6$ ($LaSrGaO_4$?) increased to become the main impurity after 1500 ^oC. This is consistent with the phase diagram wherein depletion of Ga due to vaporization is expected to promote the formation of initially $La_4Ga_2O_9$ and thereafter $LaSrGaO_4$. The amount of second phases in LSGM9182 detected by Djurado and Labeau [1998] was much larger when sintering

was carried out at 1400 ^{o}C in inert and reducing atmospheres. They recommended a sintering temperature of 1500 ^{o}C for 6 h in air. Although the synthesis method, nature of sample (powder or pellet) and time of sintering would affect the kinetics of secondary phase formation, the equilibrium phase constitution is not likely to change unless partial Ga evaporation occurs. This was evident from the fact that in several of the literature reports [Djurado and Labeau, 1998; Majewski et al, 2001; Huang and Goodenough, 1998; Liu et al, 2006; Gorelov and coworkers, 2001; Datta, 2007, Polini et al, 2004; Tas et al, 2000; Cheng & Navrotsky, 2004; Shi et al, 2006; Chae et al, 2008; Ishikawa and coworkers, 2007; Majewski et al, 2002; Yi and Choi, 2005; Yamaji et al, 2000; Yamaji et al, 2002 and Azad and Er, 2000], irrespective of the method of synthesis (solid state reaction, Pechini, citrate-gel, solution combustion, sol-gel, carbonate decomposition, co-precipitation and thermal spray pyrolysis), the main impurity phases to form when sintered between 1400-1500 ^{o}C for 6-8 hours in air were $LaSrGa_3O_7$, $LaSrGaO_4$ and to a smaller extent $La_4Ga_2O_9$ and MgO.

At higher temperatures and for higher sintering times or for sintering in inert and reducing atmospheres, evaporation of Ga was facilitated resulting in a shift in the bulk composition and the formation of several other impurity phases [Yi and Choi, 2005; Yamaji et al, 2000; Yamaji et al, 2002 and Stevenson et al, 1997]. Stevenson et al [1997] observed decomposition of LSGM even in air especially when sintered at a temperature greater than 1600 ^{o}C due to the tendency of gallium (III) oxide reduction to gallium (I) oxide. Yamaji et al [1999] observed significant changes in the surface morphology of the electrolyte and formation of $La(OH)_3$ and $LaSrGaO_4$ when annealed at 1000 ^{o}C. Yi and Choi [2005] also reported the dissociation of LSGM to form La_2O_3, $La(OH)_3$ and $LaSrGaO_4$ in reducing atmospheres They also found that the addition of Sr to the La sites accelerated the Ga depletion, whereas the addition of Mg to Ga sites did not. Below 750 ^{o}C, no gallium depletion was detected even in reducing atmospheres [Yamaji et al, 2000 and 2002].

Gorelov and coworkers [2001] studied the effect of Sr- and Mg- doping and processing conditions on the electrical transport properties of $La_{1-x}Sr_xGa_{1-y}Mg_yO_3$. The Sr- and Mg-solubility limit was found to be at $x = y = 0.16$. If excess Sr and/or Mg were added to the $LaGaO_3$ phase, they detected the formation of $LaSrGa_3O_7$ and /or $La_4Ga_2O_9$ phases in addition to the $LaGaO_3$ phase.

2.6. ELECTRICAL CONDUCTIVITY OF Sr-AND Mg-DOPED LANTHANUM GALLATE

Systematic studies on the electrical conductivity of LSGM as a function of Sr and Mg concentrations at the A- and B- sites and temperature are few [Huang and Goodenough, 2000; Liu et al, 2006; Huang et al, 1996; and Gorelov and coworkers, 2001] and the results are conflicting. Huang et al [1996] measured the conductivity of LSGM with Sr and Mg varying from 5 to 30 mol % in the temperature range 320-800 ^{o}C by AC impedance analysis. They drew iso-conductivity contours as a function of dopant concentrations at different temperatures. They also calculated the activation energies as a function of Sr and Mg concentration in LSGM. The activation energies showed two straight lines with different slopes, one in the low temperature regime corresponding to the trapping of oxygen vacancies by the cations and clustering of vacancies (E_1) and another at the high temperature range corresponding to migration of vacancies (E_2). They obtained a maximum iso-conductivity contour of 0.14 S/cm at 800 ^{o}C for simultaneous doping of Sr and Mg with concentrations in the range of 12.5-25 mol%. The conductivities decreased at dopant concentrations less than 15 mol % because of lower oxygen vacancy concentration and for more than 25 mol%, possibly because of the increased volume of low conducting secondary phases. However, the variation of activation energy with dopant concentrations at the A- and B- sites showed a different behavior. The activation energy corresponding to vacancy trapping (E1) showed a minimum at of ~0.6 eV for Sr concentrations ranging from 20-25 mol % and Mg concentration of 5 mol %. The activation energy for oxygen vacancy migration (E2) showed a minimum of ~0.6-0.7 eV at Sr concentrations ranging from 15-20% and Mg concentration of 5 mol %. They rationalized this observation by pointing out that the superior oxygen ion conductivity in LSGM was associated with the Ga^{3+} and not the La^{3+} ion, and that the oxygen vacancy was more strongly trapped by a Ga-O-Mg bond pair than by a La-Sr-O pair. In another study on single cells based on LSGM, Huang and Goodenough [2000] reported maximum oxide ion conductivities of 0.17, 0.08 and 0.03 S/cm for the composition $La_{0.8}Sr_{0.2}Ga_{0.83}Mg_{0.17}O_{2.815}$ at 800, 700 and 500 ^{o}C respectively. At this composition, the microstructures and XRD corresponded to a pure perovskite phase. Chen and Fung [2004] also measured the conductivity as a function of Sr and Mg concentrations in LSGM and analyzed the behavior of activation energy with dopant concentrations at the A and B sites of the perovskite structure. Similar to

the observation of Huang et al [1998], they observed that the activation energy for oxygen migration decreased with increasing Sr at the A-site and increased with increasing Mg at the B-site. They explained this in terms of the larger ionic radius of Mg compared to Ga and the resultant free space available in the lattice for oxygen ion migration. However, size mismatch between Ga and Mg would be expected to restrict the solubility of Mg in Ga, which was not observed in their study. Gorelov and co-workers [2001] measured the electrical conductivity of LSGM as a function of Sr and Mg concentrations in the temperature range 613-1023 ^{o}C by a square pulse method using an assembled bridge circuit. However, they doped equal amounts of Sr and Mg, namely 5, 10, 15 and 20 mol % respectively of each dopant. The electrical conductivity was found to increase with dopant concentrations up to the point of maximum solubility at x=y=0.15 beyond which it decreased because of the formation of the secondary phases $LaSrGa_3O_7$ and $La_4Ga_2O_9$. In their studies too, the Arrhenius plots showed two distinct behavior at the low and high temperature regions. Liu et al [2006] also measured the electrical conductivity of LSGM as a function of Sr and Mg concentrations in the temperature range 500-800 ^{o}C using 4-probe DC measurements. They observed that the conductivities of LSGM increased with increase in Sr and/or Mg addition, attained a maximum and then decreased. The maximum in conductivities (0.15 S/cm) were achieved for Sr in the concentration range of 14-20 mol % and Mg in the range of 15-25 mol%. In their study, the maximum in conductivity was attained at Sr and Mg dopant levels lower than the saturation solubility. Vasylechko et al [2003] reported activation energies as low as 0.54 eV for oxygen vacancy migration and 0.84 eV for vacancy trapping. They measured the conductivity of single crystals of $La_{0.95}Sr_{0.05}Ga_{0.9}Mg_{0.1}O_{3-\delta}$ and $La_{0.9}Sr_{0.1}Ga_{0.8}Mg_{0.2}O_{3-\delta}$ as a function of frequency (100-100000 Hz) in the temperature range 27-1027^{o}C K by AC impedance analysis. They found that beyond 227 ^{o}C, the measured conductivity values were the same at all frequencies. The conductivity of the oxygen deficient perovskite phase was shown to be purely ionic (range where conductivity is independent of oxygen partial pressure) over a wide range of oxygen partial pressure $10^{-22} \leq pO_2 \leq 1$ atm for all compositions investigated [Huang and Goodenough, 2000, Jang and Choi, 2002]. Jang and Choi [2002] measured and reported partial electronic conductivities of LSGM9191, LSGM9182 and LSGM8282 using Hebb-Wagner ion-blocking electrodes between 973-1173 K and p_{O2} range from 1 to 10^{-22} atm. They found that as the Sr and Mg content

increased, both the hole and electronic conductivity decreased together with increasing activation energy for conduction. The electronic transference numbers reported by them for these three compositions were in the range of 10^{-2} to 10^{-3}. The oxygen ion transference numbers of LSGM9182 prepared by sintering at 1400 ^{o}C for 0.5-120 h were determined by Kharton et al, [2003] by a modified Faradaic efficiency technique. They found that the transference numbers varied in the range of 0.984-0.998 decreasing when temperature or oxygen partial pressure increased. The electron-hole transport was found to decrease when the sintering time increased from 0.5 to 40 h.

Cong and coworkers [2003] reported that the conductivity of $La_{0.8}Sr_{0.2}Ga_{0.85}Mg_{0.15}O_{3-\delta}$ measured as a function of sintering temperature between 1400 K-1550 ^{o}C (for 4 h) showed a maximum at 1500 ^{o}C. The loss of conductivity at higher sintering temperatures can be either due to the formation of insulating secondary phases or vaporization of Ga. They could also separate, the bulk, grain boundary and electrode processes conductivity below 500 ^{o}C from the impedance plots and deduced that the grain boundary conductivity was lower for samples synthesized by glycine-nitrate method compared to solid state reaction. Zha and coworkers [2001] reported that the total conductivity depended on the sintering time; the peak in conductivity was achieved (0.096 S/cm at 800 ^{o}C) when the pellet was sintered at 1450 ^{o}C K for 24 h. They also observed a transition temperature (at about 675 ^{o}C) in the plot of $\ln(\sigma_T)$ vs 1/T, below which it exhibited a somewhat higher activation energy due to the trapping of vacancies by the dopant cations for all sintering conditions. The increase in conductivity with sintering time up to 24 h was attributed to the densification of grains and the decrease thereafter to the precipitation of secondary phases.

2.7. TRANSPORT PROPERTIES OF ELECTRODE MATERIALS

Bucher and coworkers [2001] studied the transport properties of $La_{0.4}Sr_{0.6}CoO_3$. They found that the non-stoichiometry increased with increasing temperature and decreasing partial pressure of oxygen. At low temperatures, the oxygen exchange process may be incomplete due to slow exchange kinetics. Yi and Choi [2005] studied the cathodic properties of $La_{0.9}Sr_{0.1}MnO_3$ electrode on $LaGaO_3$ solid electrolyte. When LSM was mixed with LSGM, the resulting cathode showed lower over potential than that for LSM. The cathodic over-potential of LSM however, was much higher on LSGM electrolyte than on YSZ electrolyte possibly due to insulating secondary phases produced by the reaction between LSM and LSGM. Mai et al [2004] examined the

oxygen uptake and release of Sr-doped iron and cobalt containing perovskite-oxide powders. They observed that $La_{0.6}Sr_{0.4}Co_{0.2}Fe_{0.8}O_{3-\delta}$ was a superior cathode material compared to $La_{0.8}Sr_{0.2}Co_{0.2}Fe_{0.8}O_{3-\delta}$ or $La_{0.8}Sr_{0.2}FeO_3$.

Elshof et al [1995, 1996] studied the oxygen transport properties of Sr-doped lanthanum ferrite in air/He and air/CO, CO_2 atmosphere. It was shown that the oxygen permeability of Sr-ferrite membranes increased significantly by exposure of the membrane to the lower partial pressure side containing CO.

2.8. ELECTRICAL PROPERTIES OF SECONDARY PHASES $La_4Ga_2O_9$, $LaSrGaO_4$, $LaSrGa_3O_7$ AND $MgGa_2O_4$

In general, the main impurity phases reported to form in the perovskite phase when sintered in air between 1400-1500^oC were $LaSrGa_3O_7$, $LaSrGaO_4$ and to a smaller extent $La_4Ga_2O_9$, $MgGa_2O_4$ and MgO [Khanlou et al, 2000; Polini et al, 2004; Matraszek et al, 2004]. As mentioned earlier, the phase diagrams of the ternary systems La_2O_3-Ga_2O_3-SrO and La_2O_3-Ga_2O_3-MgO [Majewski et al, 2001] showed the equilibrium existence of all these compounds. The spinel phase $MgGa_2O_4$ existed over a stoichiometric range (Mg:Ga ratio from 35:65 to 40:60) and melted congruently above 1600^oC. The phase $LaSrGaO_4$ is stoichiometric and melts congruently at ~1600^oC. However, $LaSrGa_3O_7$ was found to exhibit an extended homogeneity region ranging from $La_{1.5}Sr_{0.5}Ga_3O_7$ to $La_{0.8}Sr_{1.2}Ga_3O_7$ [Majewski et al, 2001]. $LaSrGa_3O_7$ has applications in solid state lasers [Malinowski et al, 1996; Romanowski et al, 1997], $LaSrGaO_4$ has applications in high temperature super conductors [Berkowski, 1997, Pajaczkowska and Gloubokov, 1998] and $MgGa_2O_4$ has applications in optoelectronics [Moriga et al, 1999].

Although it is known that the presence of these phases seriously impedes the oxygen ion migration resulting in significantly lower ionic conductivity [Khanlou et al, 2000; Chen and Fung, 2004], no information was available in the literature (except for MgO) either on the synthesis of these pure phases or on their electrical properties as a function of temperature. However, JCPDS files for all these compounds are available [$LaSrGaO_4$ (JCPDS file No. 83-1004), $LaSrGa_3O_7$ (JCPDS file No. 86-1839), $La_4Ga_2O_9$ (JCPDS file No. 53-1108) and $MgGa_2O_4$ (JCPDS file No. 10-0113)].

2.9. ELECTROCHEMICAL PERFORMANCE OF LANTHANUM GALLATE BASED FUEL CELLS

Huang and co-workers [2000] studied the properties of Sr- and Mg- doped $LaGaO_3$ (LSGM) and its performance in a single cell employing Ni-LSGM as anode and LSCF as cathode. He found that LSGM reacted with Ni at the anode interface and suggested the use of a thin interlayer ($Ce_{0.8}Sm_{0.2}O_{1.9}$) at the anode/electrolyte interface to prevent formation of lanthanum nickelate. They achieved a peak power density of 100 mW/cm^2, which was higher than that of the standard cell without the interlayer. They attributed the improvement in peak power density with the use of the interlayer to a significant reduction of the anode over potential. However, they observed that the over potential of the cathode remained unchanged. Inagaki and coworkers [2000] investigated the performance of a electrolyte supported single cell consisting of 0.5 mm thick $La_{0.9}Sr_{0.1}Ga_{0.8}Mg_{0.2}O_{3-\delta}$ electrolyte, $La_{0.6}Sr_{0.4}CoO_3$ cathode and Ni-Sm doped ceria anode. They observed cathodic polarization of about 25mV at 300 mA/cm^2 for a cathode prepared by sintering at 1000^{o}C and showed that the polarization of the LSC cathode increased with operating time for cell lifetime tests.

Single cell testing using LSGM as an electrolyte was also carried out with different cathodes such as Ba(Sr)Co(Fe)O_3 and $GaBaCo_2O_{5+\delta}$ [Martinez et al, 2008], $LaSrMgO_3$ [Ma et al, 2005], LSCF [Fu et al, 2003], Pt, La(Sr)Ga(Co)O_3 and La(Sr)CoO_3 [Chen and Liu, 1998], La(Sr)MnO3, La(Sr)Co(Fe)O_3, La(Sr)MnO_3+La(Sr)Ga(Mg)O_3, LSCF+La(Sr)Ga(Mg)O_3 [Gong et al, 2004], La(Sr)Ga(Ni)O_3 [Lecarpentier et al, 2000], Sm(Sr)CoO_3 [Nishiwaki and coworkers, 2006], $(Pr_{0.7}Ca_{0.3})_{0.9}MnO_3$ [Huang et al, 2007], and anodes such as La(Sr)Cr(Mn)$O_{3-\delta}$ [Huang et al, 2007], [Ni-Ce(Sm)$O_{2-\delta}$ [Nishiwaki et al, 2006], Ni+Ce(Gd)O_2 [Gong et al, 2004], Pt, La(Sr)Ga(Mn)O_3 [Chen and Liu, 1998; Fu et al, 2003], Ni-YSZ [Ma et al, 2005] and Ni-CeO_2 [Chen and Liu, 1998, Martinez et al, 2008] at below 800^{o}C.

A single cell of Sr-and Mg doped lanthanum gallate as electrolyte and platinum as electrodes was tested by [Chen and Liu, 1998] and yielded a maximum power density of 20mW/cm^2 at 800^{o}C. Instead of Pt, $La_{0.9}Sr_{0.1}Ga_{0.8}Co_{0.2}O_3$ and $La_{0.6}Sr_{0.4}CoO_3$; $La_{0.9}Sr_{0.1}Ga_{0.8}Mn_{0.2}O_3$, and Ni-$CeO_2$ have been used as cathodes and anodes respectively for LSGM electrolyte supported single cell, which showed a power density of 88 and 61 mW/cm^2 for $La_{0.9}Sr_{0.1}Ga_{0.8}Co_{0.2}O_3$/La(Sr)Ga(Mg)$O_3$/ $La_{0.9}Sr_{0.1}Ga_{0.8}Mn_{0.2}O_3$ and $La_{0.6}Sr_{0.4}CoO_3$/La(Sr)Ga(Mg)O_3/Ni-CeO_2 respectively

[Chen and Liu, 1998]. Area Specific Resistance (ASR) measurement of $Ba(Sr)Co(Fe)O_3$(BSCF) and $GaBaCo_2O_{5+\delta}$(GBCO) cathodes for $La_{0.9}Sr_{0.1}Ga_{0.8}Mg_{0.2}O_3$ was carried out by [Martinez et al, 2008] and they report a smaller value of ASR for BSCF cathode compared to GBCO. Power densities of 240 and 180 mW/cm^2 at 800^{o}C were achieved for the single cell $Ba(Sr)Co(Fe)O_3$(BSCF)/ $La_{0.9}Sr_{0.1}Ga_{0.8}Mg_{0.2}O_3$(LSGM)/Ni-$CeO_2$(Ni-CSO) and $GaBaCo_2O_{5+\delta}$(GBCO) /$La_{0.9}Sr_{0.1}Ga_{0.8}Mg_{0.2}O_3$/Ni-$CeO_2$ respectively [Martinez et al 2008]. Ma et.al [2005] reported power density in the range 80-150 mW/cm^2 for a $LaSrMgO_3$/La(Sr)Ga(Mg)O_3/Ni-YSZ single cell at 500-800^{o}C. Electrochemical performance of LSCF/LSGM/LSGM single cell was evaluated by Fu et al [2003] and they report a peak power density of 180 mW/cm^2 at 800^{o}C. Gong et.al [2004] carried out polarization studies using various cathodes and Ni-GDC anode for LSGM electrolyte. They reported that the LSCF cathode had a significantly lower polarization resistance compared to the other cathodes i.e., La(Sr)MnO_3, La(Sr)MnO_3-La(Sr)Ga(Mg)O_3, La(Sr)$Co(Fe)O_3$-La(Sr)Ga(Mg)O_3 and also found that Ni-LSGM, anode lowered the cell performance because of interfacial reaction between Ni and LSGM. Single cell of La(Sr)$Cr(Mn)O_3$/La(Sr)Ga(Mg)O_3/$(Pr_{0.7}Ca_{0.3})_{0.9}MnO_3$ was tested in two different fuel atmospheres; humidified hydrogen and ethanol. The power density achieved with both humidified hydrogen and ethanol was almost identical (58-165 mW/cm^2) at 750-850^{o}C. They also observed no significant degradation of cell components under ethanol atmosphere in 60 hours [Huang et al, 2007]. Naiqing et al [2006] also measured the open circuit potential and polarization behavior of tape cast LSGM based single cell. They reported an open circuit voltage of 1.067 V at 800^{o}C and the current density and power density achieved were 0.56 A/cm^2 and 0.147 W/cm^2 respectively at 800^{o}C. Cathodic-interfacial polarization of LSM, LSM-LSGM and LSCF for LSGM electrolytes was studied and reported by Gong et al [2004]. They observed that LSCF electrode had a lower polarization resistance than LSM and LSM-LSGM electrodes. Fukui et al [2002] developed a LSGM based single cell using Ni-SDC and La(Sr)CoO_3 as anode and cathode respectively, which exhibited a power density of 0.7 W/cm^2 at 800^{o}C and 0.4 W/cm^2 at 700 ^{o}C. A Ni/LSGM9182/$Sm_{0.5}Sr_{0.5}CoO_3$ single cell exhibited a power density of 245 mW/cm^2 at 800 ^{o}C [Ishikawa et al, 2007]. Maffei et al [1998] tested several LSGM based single cells and reported current densities less than 50 mA/cm^2 for Pt/LSGM/Pt, NiO-CeO_2/LSGM/LCFC and NiO-CeO_2/LSGM/LSC cells. Lu and coworkers [2004] studied

the electrochemical performance of intermediate temperature SOFC single cells with different electrolytes; LSGM, scandia stabilized zirconia (ScSZ) and samarium doped ceria (SDC) under both hydrogen and n-butane atmosphere. The open circuit voltage of LSGM and ScSZ based cells using hydrogen was 1.2 V and maximum power densities of 0.30, 0.22 and 0.29 W/cm^2 at 700^{o}C respectively were achieved. With butane as fuel, the power densities attained were 0.09, 0.15 and 0.18 W/cm^2 for LSGM, ScSZ and SDC electrolytes respectively. Gong et al [2006] studied the electrical performance of LSGM electrolyte supported SOFC with a lanthanum doped ceria (LDC) layer on the anode side. They obtained power densities of 190 mW/cm^2 at 800 ^{o}C and 30 mW/cm^2 at 600^{o}C for the LSCF+LSGM/LSGM/LDC/Ni+LDC cell configuration. The single cell NiO+CSO-20/LSGM/Sm(Sr)CoO_3 showed a poor performance due to the detrimental interfacial reactions [Zheng and Chen, 2008]. Huang et al [2000] investigated the performance of LSGM based cells with NiO+SDC (samaria doped ceria) and NiO+LSGM anodes. NiO-LSGM anode was found to be unsuitable for LSGM based cell because of interfacial reactions. With a SDC buffer layer at the anode-electrolyte interface, the over potential of the anode was lower. The maximum power densities achieved were 550, 440 and 270 mW/cm^2 for SDC/SDC+Ni, SDC+Ni and LSGM+Ni anodes respectively at 800^{o}C.

CHAPTER-III

EXPERIMENTAL METHODS

3.1. MATERIALS

High purity lanthanum oxide, (AR, CDH), strontium nitrate, (GR, Merck), metallic gallium 99.99% (ACROS Organics), ferric nitrate nanohydrate, (AR, CDH), cobalt nitrate hexahydrate, (AR, CDH), magnesium nitrate hexahydrate (AR, CDH), glycine (AR, CDH), oxalic acid (AR, S.D. Fine-chem.), polyvinyl alcohol (AR, CDH), citric acid monohydrate (extra pure, Merck) and ethylene glycol (AR, CDH) were used as starting materials. Gadolinia doped ceria (American Elements), nickel oxide, (Alfa Ascer, Johnson Mathew), silver foil (Alfa Ascer, Johnson Mathew) and ceramic adhesives (Aremco) were used for cell assembly and testing.

3.2. EXPERIMENTAL METHODS

3.2.1. Synthesis Methods

3.2.1.1. Glycine-nitrate combustion method

In this technique, the various perovskite oxides were prepared by the combustion of the corresponding metal nitrate – glycine mixtures. Stoichiometric compositions of mixtures were used for the synthesis. This method involved rapid heating of an aqueous concentrated solution containing the respective starting materials to about 500^{o}C. The solution initially boiled, underwent rapid degradation and foaming followed by decomposition and vigorous generation of gases such as CO_2, N_2, H_2O. In order to avoid the spillage of the powder during combustion, some amount of excess fuel was added. The combustion products were subjected to simultaneous thermogravimetric (TG) and differential thermal analysis (DTA) in ambient air as well as FTIR-spectroscopy to determine their calcination behavior. The as-synthesized powders were subjected to calcination in air at a temperature of 900^{o}C for 3 hours to get the single phase for pure and Sr-doped lanthanum ferrite and cobaltite and 1500^{o}C for 3 hours for lanthanum gallate and LSGM.

3.2.1.2. Co-precipitation method

In the co-precipitation method, fine particles of lanthanum cobaltite (LCO), lanthanum ferrite (LFO), lanthanum-strontium cobaltite (LSC), lanthanum-strontium ferrite (LSF), lanthanum gallate (LGO) and lanthanum-strontium-magnesium gallate

(LSGM) were prepared by mixing stoichiometric amounts of the corresponding metal nitrate and polyvinyl alcohol with oxalic acid as the precipitating agent. The amount of oxalic acid, polyvinyl alcohol and drying conditions were optimized in the initial experiments. First, one molar solution of the respective nitrates and 2 molar solution of oxalic acid along with 3 wt % of polyvinyl alcohol were prepared. The homogenous solution was prepared by mixing the respective elemental nitrate solution with continuous stirring (the pH of the solution was maintained at 1), and to this, the prepared oxalic acid solution was added. This yielded a precipitate of the respective oxalate which was washed and dried at 80 ^{O}C. Simultaneous thermogravimetric and differential thermal analysis experiments in static air as well as FTIR spectroscopy were carried out on the precipitate. The dried precipitate was subjected to heating at a temperature of 900^{o}C for three hours in an attempt to produce the crystalline pure phases. However, since calcination at 900^{o}C did not yield pure phases for either of the oxides, a systematic calcination study in the temperature range 900-1500^{o}C was taken up. Experiments were also undertaken with liquid ammonia as the precipitating agent in the pH range of 8.5 to 9.5. These were then subject to the same calcination treatment as described above.

3.2.1.3. Pechini method

In this technique, the pure phases were prepared by the mixing of the corresponding metal nitrates and citric acid in ethylene glycol. In the case of gallium, nitrate was first prepared from the pure metal by dissolution in nitric acid and precipitation. A small amount of HCl (5% by volume) addition was found to accelerate the dissolution of gallium. First, a one-molar solution of respective nitrates was prepared using citric acid and ethylene glycol as sol and gel forming agents respectively. The homogenous solution was prepared by mixing of all the respective elemental nitrate solution in ethylene glycol and water (1:1 ratio) as solvent with stirring and heating at 60^{o}C. To this, the prepared 1 M citric acid dissolved in ethylene glycol was added with continuous stirring and heating at 80^{o}C, to initially form a sol and finally get a resin during heating. The resin was dried in air at 500^{o}C for 3 hours to yield a dry gel. The resin as well as the dried gel was subject to simultaneous TG/DTA in static air to study the progress of the reaction. Based on the TG/DTA results, calcination was carried out at a temperature of 900 ^{o}C for 3 hrs to get a single phase for

pure and Sr-doped lanthanum ferrite and cobaltite and 1500^{o}C for 3 hours for lanthanum gallate and LSGM.

3.2.1.4. Synthesis of mixed oxides by Pechini method

The $La_{1-x}Sr_xGa_{1-y}Mg_yO_{3-\delta}$ (LSGM) (where x = 0-0.3 and y = 0-0.3 mol), $La_4Ga_2O_9$, $LaSrGO_4$, $LaSrGa_3O_7$ and $MgGa_2O_4$ phases were prepared by the citrate gel (Pechini) method. Eighty different compositions of LSGM (Sr = 0.01, 0.02, 0.03, 0.04, 0.05, 0.10, 0.15, 0.20, 0.25, 0.30 and Mg = 0, 0.02, 0.05, 0.10, 0.15, 0.20, 0.25, 0.30) were prepared for the phase equilibrium and conductivity measurements. The prepared powders were subjected to calcination at a temperature of 900 ^{o}C for 3 hrs.

3.3. SAMPLE PREPARATION FOR THE EQUILIBRATION STUDIES

The calcined powders of all compositions were compacted by uni-axial pressing at 256 MPa into circular pellets of 10 mm diameter and about 2.5 mm thickness for the isothermal equilibration measurements. Sr- and Mg- doped lanthanum gallate pellets were subjected to isothermal equilibration at 1500 ^{o}C for 8 and 20 hrs and 700 ^{o}C for 720 hours in two separate furnaces (LINN GmbH Model No HT-1800M with a chamber size of 250x250x200 mm for high temperatures and LENTON Model No.AWF 13/12 with a chamber size of 200x200x300 mm for 700 ^{o}C). Both the furnaces were backed up by an uninterrupted power supply system, which also includes a voltage and frequency stabilizer. The temperature of the furnace was controlled to within ±1^{o}C for the LENTON furnace and to within ±2^{o}C for the LINN high temperature furnace. The samples after equilibration were allowed to cool in the furnace for the 1500 ^{o}C equilibrated doped lanthanum gallate samples and quenched in air for the 700 ^{o}C equilibrated doped lanthanum gallate samples. Samples of all compositions were equilibrated simultaneously in the furnace. The mass and dimensions of the samples were recorded prior to and after each isothermal equilibration.

3.4. ELECTRICAL CONDUCTIVITY MEASUREMENTS

The electrical conductivity of the LSGM pellets of all the synthesized compositions was carried out both by electrochemical impedance analysis as well as 2-probe DC measurements. The DC conductivity measurements were used mainly for verification. It was observed that the conductivity measured by direct DC method agreed within 3-5% with that measured by AC impedance analysis. AC impedance

measurements were carried out using a frequency response analyzer (Materials Mates 7260) in the frequency range of 10 Hz to 10 MHz and temperature range of 500 to 1000^{o}C ($\pm$1^{o}C) at an interval of 100^{o}C. The pellets were placed in the constant temperature zone of a tubular furnace LENTON Model No.LTF 12/75/610 with Eurotherm temperature controller, Model No. 3216P1) for the measurements. The furnace was calibrated to identify the constant temperature zone prior to the conductivity measurements. A constant AC voltage of 100 mV was used for the impedance measurements for all the temperatures and frequencies. Prior to the experiment, the sintered pellets were coated with platinum ink on both surfaces and subjected to heating at 900^{o}C for 0.5 h. Pt leads were used to connect the sample to the frequency response analyzer. The DC conductivity measurements were carried out on the pellets using a potentiostat/galvanostat (AMEL 7060) in the potentiostatic mode. A potential range of +2 to -2 volts was used for the DC measurements. Pt ink coated surfaces and Pt leads were used for the DC measurements and the lead resistance was subtracted from the measured values. For the conductivity measurements, the pellets were equilibrated at the set temperature for 30 minutes prior to the measurement.

3.5. AREA SPECIFIC RESISTANCE MEASUREMENTS

The ASR symmetric as well as the complete electrochemical cells under reducing and oxidizing atmospheres was carried out by electrochemical impedance spectroscopy (Materials Mates 7260). The fabricated button cell was mounted onto alumina tube using sealants (silver foil and ceramic) in the Probastat (NORECs) instrument, which was then connected to the frequency response analyzer. The conditions of measurement were the same as that used for the conductivity measurements on individual pellets mentioned earlier.

3.6. SINGLE CELL ASSEMBLY AND TESTING

3.6.1. Preparation of cell components

The electrolyte and cathode materials such as $La_{0.9}Sr_{0.1}Ga_{0.8}Mg_{0.2}O_{3-\delta}$ and $La_{0.6}Sr_{0.4}Co_{0.2}Fe_{0.8}O_{3-\delta}$ were synthesized by Pechini method as described earlier. NiO+$La_{0.9}Sr_{0.1}Ga_{0.8}Mg_{0.2}O_{3-\delta}$ (LSGM) and NiO+$Ce_{0.9}Gd_{0.1}O_{2-\delta}$ (GDC) cermets were prepared by thorough mixing and grinding of NiO with LSGM and GDC powders (50:50 by weight) respectively and heat treated at 900^{o}C for 3h. Circular thin disks of LSGM (20 mm of diameter and ~ 1.2mm of thickness) were made by pressing the

electrolyte powder using an uni-axial pressure of 656 MPa. The prepared green pellet was then subjected to sintering at 1500^{o}C at a heating rate of 2^{o}C/min for 10 h. The slurries of cathode and anode were prepared by mixing of LSCF and NiO-LSGM with an organic solvent, glycerol.

3.6.2. Cell fabrication

Typical symmetrical cell configurations were as follows:

Pt, O_2/LSCF/LSGM/NiO+LSGM, H_2, Pt and

Pt, O_2, LSCF/LSGM/NiO+LSGM, H_2, Pt

A thin layer of anode was coated on one surface of the sintered electrolyte disc. After drying, the anode coated component was sintered at 1200^{o}C for 2 h at a heating rate of 5^{o}C/min. After completion of the sintering, a thin layer of LSCF was painted on the other surface of the disc and sintered at 1100^{o}C for 2 h at a heating rate of 5^{o}C/min. The active area of the electrode was 1.13 cm^2 which was used for the current density and area specific resistance calculations. For area specific resistance measurements, symmetric cells using various cathode materials (LSC, LSF, LSCF) and LSGM9182 as electrolyte under oxygen atmosphere and different anode materials (GDC+NiO, LSGM+NiO) under hydrogen atmosphere were also used.

3.6.3. Cell testing

The fabricated electrolyte supported single cell was mounted on a test fixture (Probastat, NorECs) in a vertical split furnace, as shown in Fig.3.1. Platinum wires were connected to platinum meshes pressed against the cathode and anode respectively. Two set of Pt leads, one on each side were used for current collection and voltage measurement. Silver and ceramic adhesives were tested as sealant to separate the anode and cathode compartments (to avoid the gas mixing). In the case of silver sealant, the cell was initially heated up to 950^{o}C at a heating rate of 2^{o}C/min (for the purposes of sealing) with a continuous flow of hydrogen gas (50-60 ml/min) at the anode and pure oxygen gas at the cathode and subsequently, the temperature was reduced to 800^{o}C. In the case of the ceramic adhesive, the cell was cured at room temperature for 4 h, followed by heating the assembly to 92^{o}C at the rate of 2^{o}C/min, hold for 2 h and then heat to 260^{o}C for 2 h at a heating rate of 2^{o}C/min. The temperature was then raised to the respective temperatures for cell testing at the heating rate of 2^{o}C. The cell was held at the experimental temperature for 1 h prior to the electrochemical measurements. The

overall impedance and polarization characteristics (voltage and power density vs current density) were measured using a frequency response analyzer (Materials Mates, Model No 7260) and galvanostat/potentiostat (AMEL, model No. 7060) respectively. The open circuit potential was measured as a function of time (for up to 6 h) at different temperatures using the potentiostat.

Fig.3.1 A schematic view of the Single cell test bench with split furnace (Probastat, NorECs)

Voltage – Current polarization studies were carried out by electronic load bank (K-Pas Instrument) with maximum voltage and current of 2V and 5A respectively.

3.7. CHARACTERIZATION METHODS

3.7.1. X-ray diffraction

Phase identification and unit cell parameters of the synthesized samples of various compositions were studied by X-ray powder diffraction technique. The X-ray diffraction measurement was carried out using a Siemens D-500 diffractometer and Bruker D8 diffractometer. The samples were analyzed with Co-K_α radiation (λ=1.79026 A) at a scan rate of 1^o/min. The indexing of the X-ray diffraction patterns was carried out using the JCPDS (Joint Committee on Powder Diffraction Standards - International Centre for Diffraction Data, JCPDS-ICPDD) files. The lattice parameters were determined manually as well as using the software X-ray Diffraction Analysis (1992-93).

3.7.2. Particle size measurement

The particle size distribution of the various perovskite oxides prepared by different wet chemical methods was determined using a laser diffraction analyzer (CILAS 1180, France). The instrument has a particle size measurement range of 0.04 to 2500 μm. All the particle size measurements were carried out in an aqueous medium. The particles were dispersed in water and stirred ultrasonically to avoid agglomeration of powder particles.

3.7.3. BET surface area measurement

The surface area of the prepared oxides was measured using a multipoint BET technique (Micrometrics ASAP 2020). The technique is based on the physical adsorption of helium gas molecules on a solid surface at 77 K (Brunauer et al., 1938). The instrument has a surface area measurement range from 0.001 to 3000 m^2/g. A high vacuum option provided in the instrument was used to measure small surface areas. The specific surface area was derived from the measured data using the software available (ASAP 2020) with the equipment.

3.7.4. Fourier Transform Infrared spectroscopy

The structural and functional group of precursors prepared by different methods such as combustion, co-precipitation and Pechini methods were studied by Fourier Transform Infrared method (FTIR) spectroscopy (Perkin Elmer, Model: spectrum one FT-IR spectrometer). The spectrum was taken using KBr pellets in the wave number range of 400-4000 cm^{-1}. About 50mg of sample was used for each experiment.

3.7.5. Thermogravimetric and Differential Thermal Analysis

The precursors from different wet chemical methods were subjected to thermal analysis using a simultaneous TG/DTA analyzer (Seiko, Japan, Model No. 320). The experiments were carried out in static air atmosphere. The stability of the synthesized powders in controlled oxidizing (99.9% pure O_2) and reducing (80%N_2+20%H_2) atmospheres were studied by thermogravimetry (Thermoelectron Corporation, Versa Therm, TGA). About 50 mg of the sample was used for each experiment. α-alumina was used as a reference material. A dynamic measurement in the temperature range of 35 to 800^oC for stability studies and up to 1200 ^oC for precursors at a heating rate of 10^oC/min was adopted.

3.7.6. Microscopy

3.7.6.1. Stereo microscopy

The bulk powder morphology of as-synthesized powders was examined by stereo microscopy (Leica, MZ6).

3.7.6.2. Scanning electron microscopy with EDAX

The samples were carbon coated (fine carbon tape) to study the morphology. The phase constitution after equilibration was characterized by scanning electron microscopy both in the back scattered and secondary electron imaging mode (HITACHI, Model No. S-3400N). The bulk composition of the equilibrated samples as well as the chemical composition of all the phases observed under the scanning electron microscope was determined using an EDAX analyzer (Thermo Electron Noran System (NSS-300) EDS) attached to the SEM. The EDAX analyzer could also detect oxygen concentration.

CHAPTER IV

RESULTS AND DISCUSSION

The focus of this thesis is on the synthesis of the various materials, their characterization for the applicability in SOFC, the development of intermediate temperature solid oxide fuel cell and testing its functioning. The experimental results obtained on these are reported in this chapter and discussed.

4.1. MATERIALS FOR INTERMEDIATE TEMPERATURE SOLID OXIDE FUEL CELLS

Various materials relevant for their use in intermediate temperature solid oxide fuel cell i.e., lanthanum cobaltite (LCO), lanthanum ferrite (LFO), Sr-doped lanthanum cobaltite (LSC) and lanthanum ferrite (LSF), lanthanum gallate (LGO) and Sr- and Mg-doped lanthanum gallate (LSGM) were synthesized through various wet chemical routes including combustion synthesis, co-precipitation, citrate-gel (Pechini) method and homogenous co-precipitation and their processing conditions optimized.

4.1.1. Structural characterization of precursors prepared from different wet chemical methods

The precursors prepared by combustion, co-precipitation and Pechini methods prior to calcination were characterized by Fourier Transform Infrared Spectroscopy for identification of functional groups and Thermogravimetric and Differential Thermal Analysis (TGA/DTA) for studying the calcination behavior.

4.1.1.1. Fourier Transform Infrared spectroscopy

The FT-IR spectra of all the powders prepared by solution combustion method prior to calcination are shown in Figs. 4.1.1-4.1.6. They showed two broad absorption bands in the frequency range of 500-750 cm^{-1}, which was attributed to BO_6 octahedron of bending vibrations of metal cations [Miao et al, 2000]. The FTIR spectra of pre-calcined LCO and LSC showed two main absorption bands at the frequency of 670 and 583 cm^{-1} (as shown in Figs 4.1.1 & 4.1.2). The peaks at 583 and 670 cm^{-1} was attributed to the stretching vibrations of metal cations situated at the octahedral site (i.e., Co-O) and Co^{+4} ion formation respectively [Berger et al, 2003, De Souza et al, 2005]. The IR spectra of precursors for LFO (Fig. 4.1.3) and LSF (Fig. 4.1.4) showed a single broad absorption band in the frequency range of 550-575 cm^{-1} which was also attributed to the

Fe-O stretching vibrations [Augustin et al, 2005]. In the case of lanthanum gallate and Sr-and Mg-doped lanthanum gallate precursors, the FTIR spectra as shown in Figs 4.1.5 and 4.1.6 showed only one broad band at the frequency range of 630-650 cm^{-1}, that was ascribed to the M-O vibrations [Nakayama et al, 2003; De Souza et al, 2005]. The IR bands observed in the frequency range of 3400-3450 cm^{-1}, 1600-1650 cm^{-1}, 1450-1500 cm^{-1} and 1040-1060 cm^{-1} are attributed to O-H stretching, CH_3-COO^-, COO^-, and trace of nitrate ions [Tas et al, 2000, Nakayama et al, 2003; Huang and Goodenough, 1994]. The identified functional groups matched well with the starting compounds taken for the combustion reaction namely metal nitrates, glycine and water. When the complex precursors were subjected to thermal analysis, the corresponding functional groups were removed as H_2O, CO, CO_2 and NO_x or N_2 by dehydration and decomposition reactions.

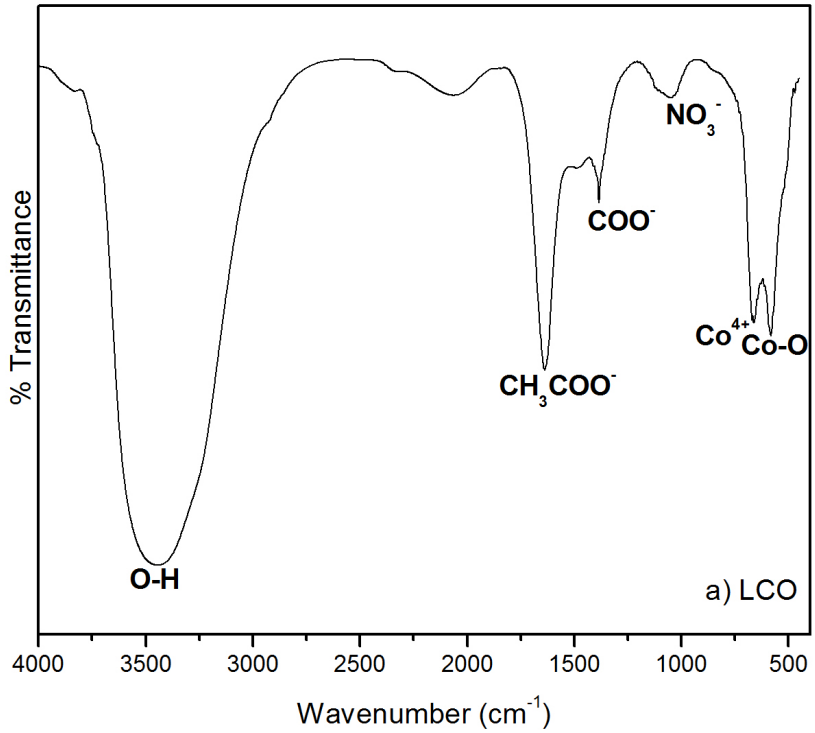

Fig. 4.1.1 FTIR spectrum of lanthanum cobaltite precursors prepared by combustion method

The FTIR spectra of the pre-calcined powders of LCO, LSC, LFO, LSF, LGO and LSGM obtained by co-precipitation method are shown in Figs. 4.1.7-4.1.12. The peaks at 492 cm^{-1} was attributed to the stretching vibrations of metal cations (La^{+3}) situated in the dodecahedral coordination (i.e., La-O) [Ganguly and Vasanthacharrya, 1986], which was not observed in the combustion method. Similarly, the B-site metal-oxygen frequency band was not observed in the given frequency range. It might have shifted to the lower frequency range.

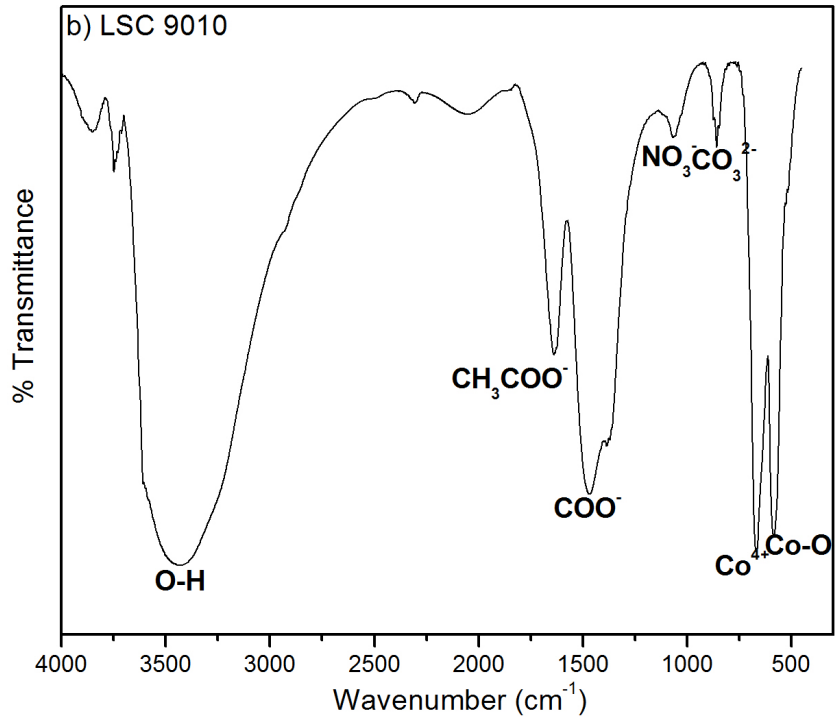

Fig. 4.1.2 FTIR spectrum of lanthanum strontium cobaltite precursors prepared by combustion method

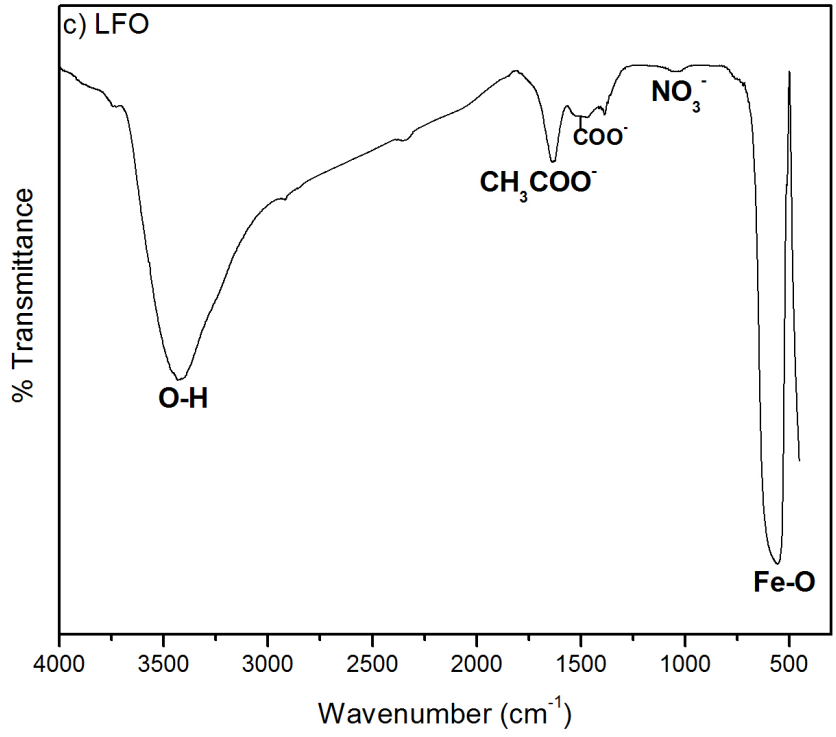

Fig. 4.1.3 FTIR spectrum of lanthanum ferrite precursors prepared by combustion method

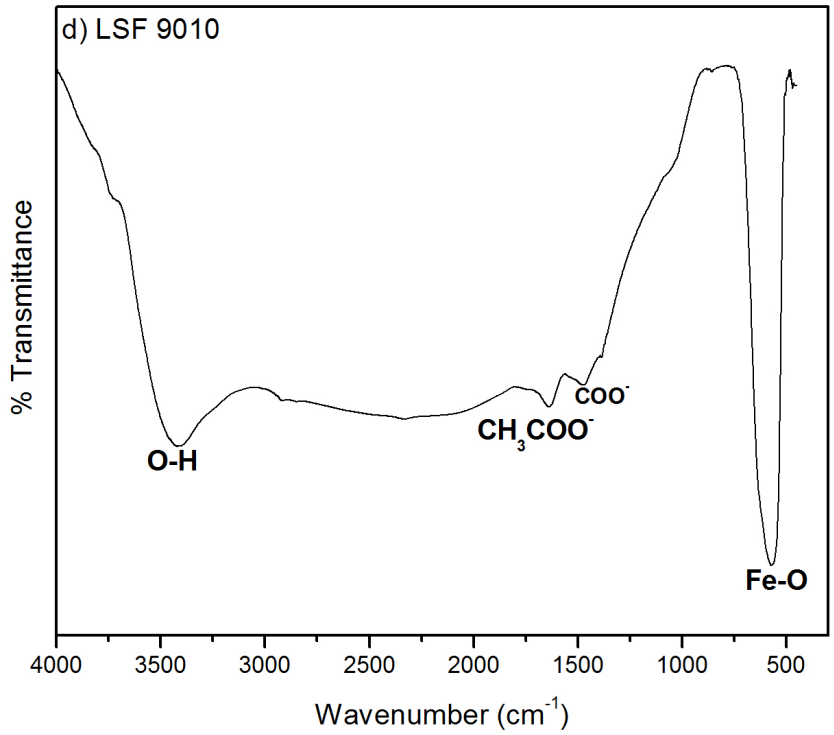

Fig. 4.1.4 FTIR spectrum of lanthanum strontium ferrite precursors prepared by combustion method

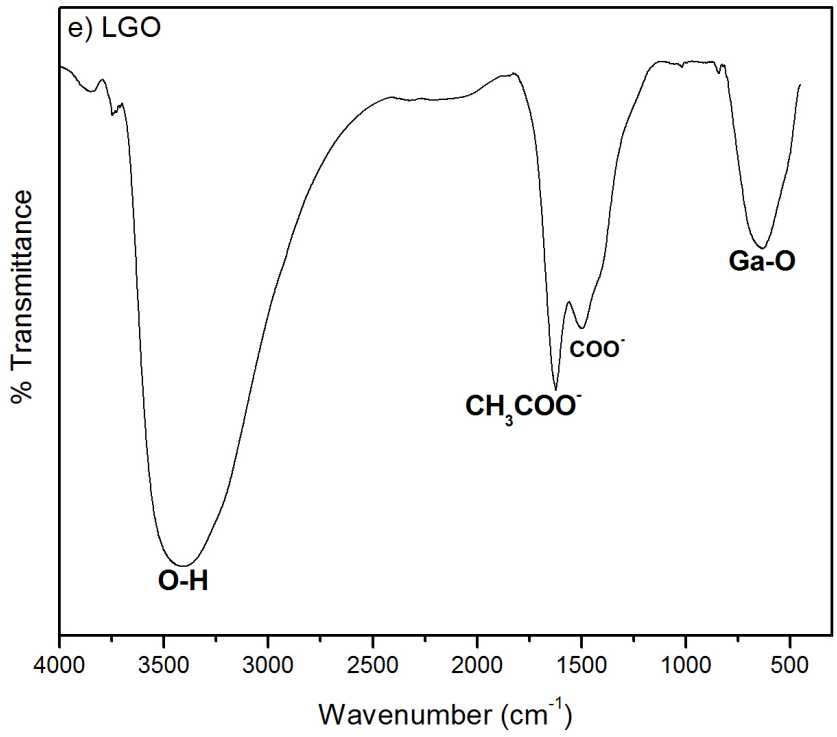

Fig. 4.1.5 FTIR spectrum of lanthanum gallate precursors prepared by combustion method

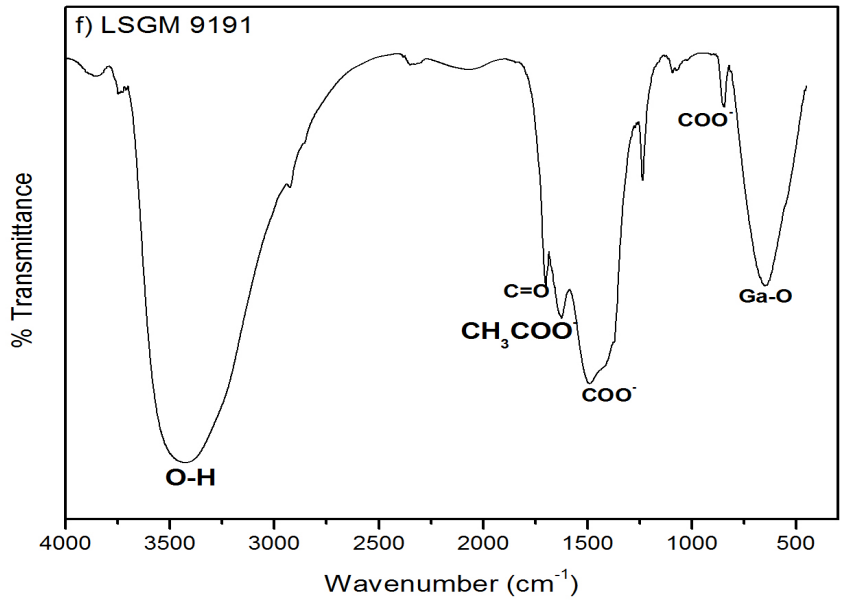

Fig. 4.1.6 FTIR spectrum of lanthanum strontium magnesium gallate precursors prepared by combustion method

Figures 4.1.7-4.1.12 shows the bands in the frequency of 3350-3425 cm^{-1}, 1615-1623 cm^{-1}, 1310-1360 cm^{-1} and 775-900 cm^{-1} which corresponded to the O-H stretching vibrations, COO^-, trace of nitrate ions and carbonate ions (CO_3^{-2}) respectively. The functional groups of O-H stretching from water, COO^- and CO_3^{2-} from oxalic acid and nitrate ion from metal nitrates were identified by FTIR. These functional groups were reflected in the thermogravimetry and differential thermal analysis plots through a three-stage mass loss and thermal effect corresponding to dehydration, decomposition and decarboxylation.

The IR spectra of precursors from Pechini method are shown in Figs. 4.1.13 - 4.1.18. Peaks were observed in the frequency range of 500-750 cm^{-1} which was attributed to BO_6 octahedron of bending vibrations of metal ions [Miao et al, 2000]. The bands observed at the frequency of 3425-3350 cm^{-1}, 2954 cm^{-1}, 1730 cm^{-1}, 1620-1650 cm^{-1}, 1400-1300 cm^{-1} and 1070-1030 cm^{-1}, 1070-1090 cm^{-1} and around 800 and 900 cm^{-1} were ascribed to the functional groups of O-H stretching, citrate ions, COO^-, CH_3-COO^-, trace of nitrate ions, carbonyl group (C=O) and carbonate ions (CO_3^{-2}) [Tas et al, 2000, Nakayama et al, 2003]. The precursors from both combustion and Pechini methods yielded a similar spectrum except that in the case of Pechini method, the spectrum showed a peak for citrate ions. In Pechini method, the functional groups corresponding to the nitrate ions, citrate ions, hydroxyl ions, carboxyl ions and acetyl ions arose from the metal nitrates, citric acid and ethylene glycol which were used as

the raw material in the synthesis. The decomposition, dehydration and oxidation reactions corresponding to these functional groups were also reflected in the TGA-DTA results.

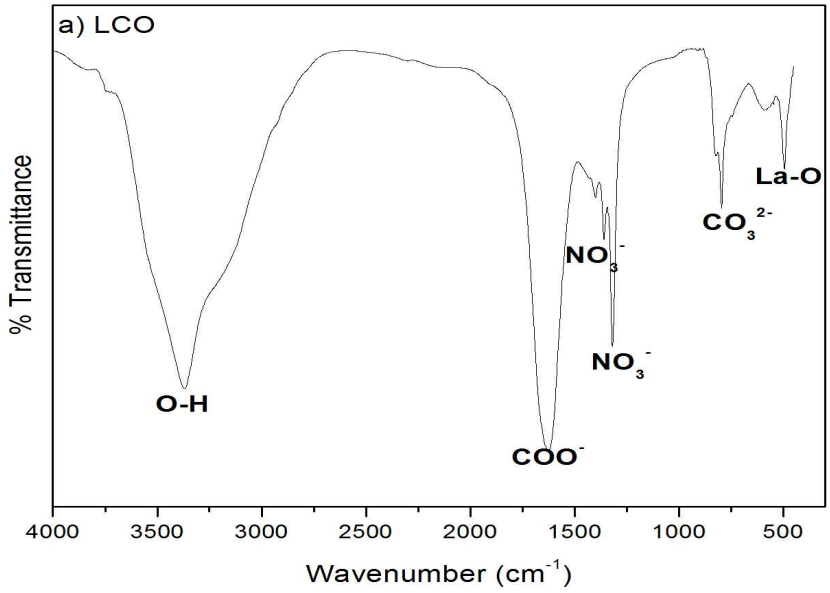

Fig. 4.1.7 FTIR spectrum of lanthanum cobaltite precursors prepared by co-precipitation method

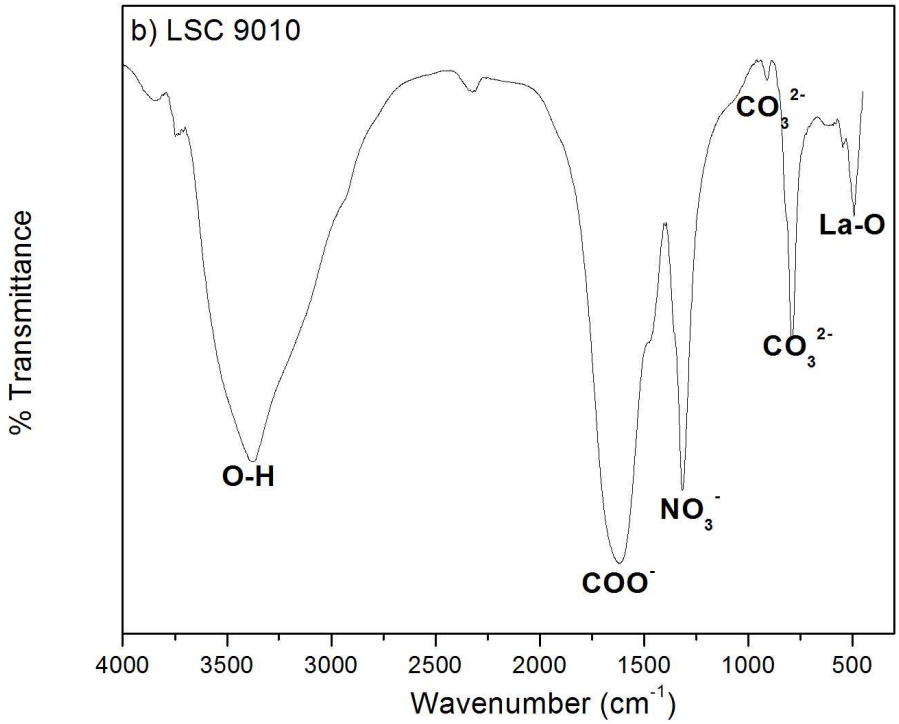

Fig. 4.1.8 FTIR spectrum of lanthanum strontium cobaltite precursors prepared by co-precipitation method

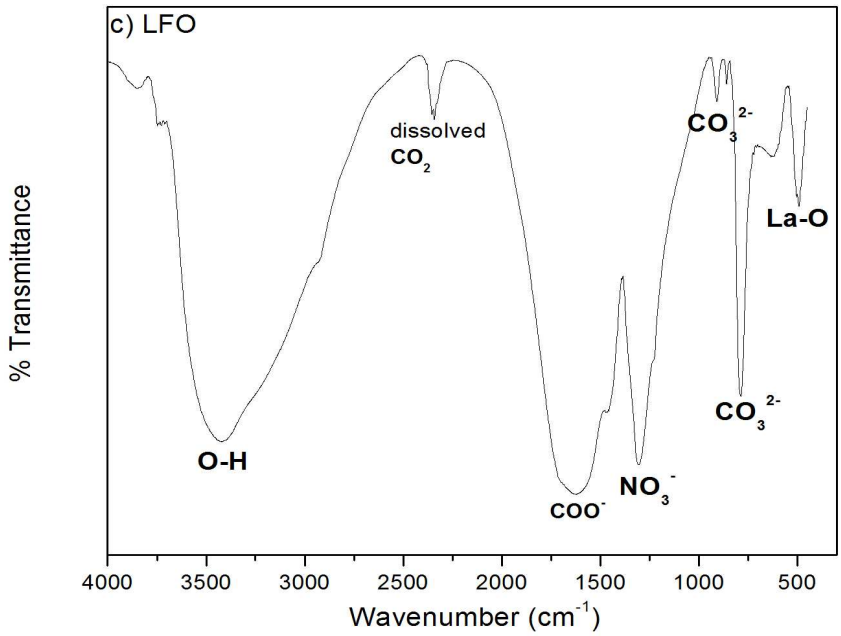

Fig. 4.1.9 FTIR spectrum of lanthanum ferrite precursors prepared by co-precipitation method

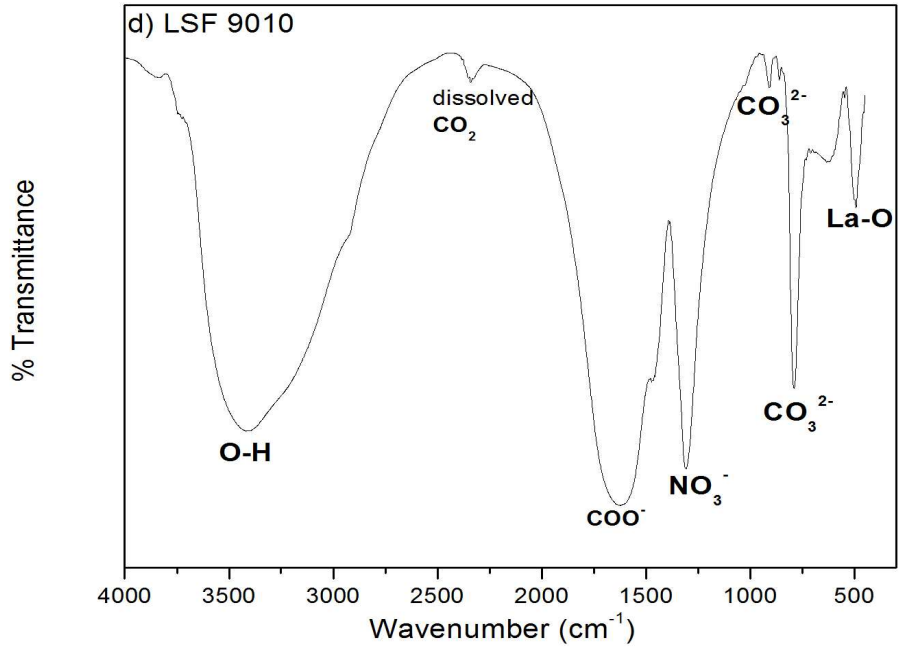

Fig. 4.1.10 FTIR spectrum of lanthanum strontium ferrite precursors prepared by co-precipitation method

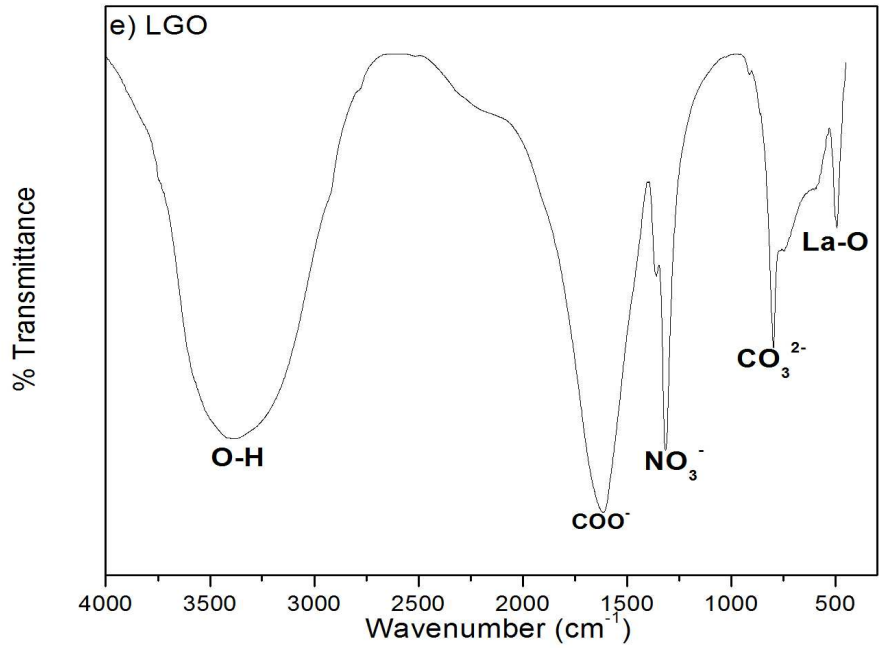

Fig. 4.1.11 FTIR spectrum of lanthanum gallate precursors prepared by co-precipitation method

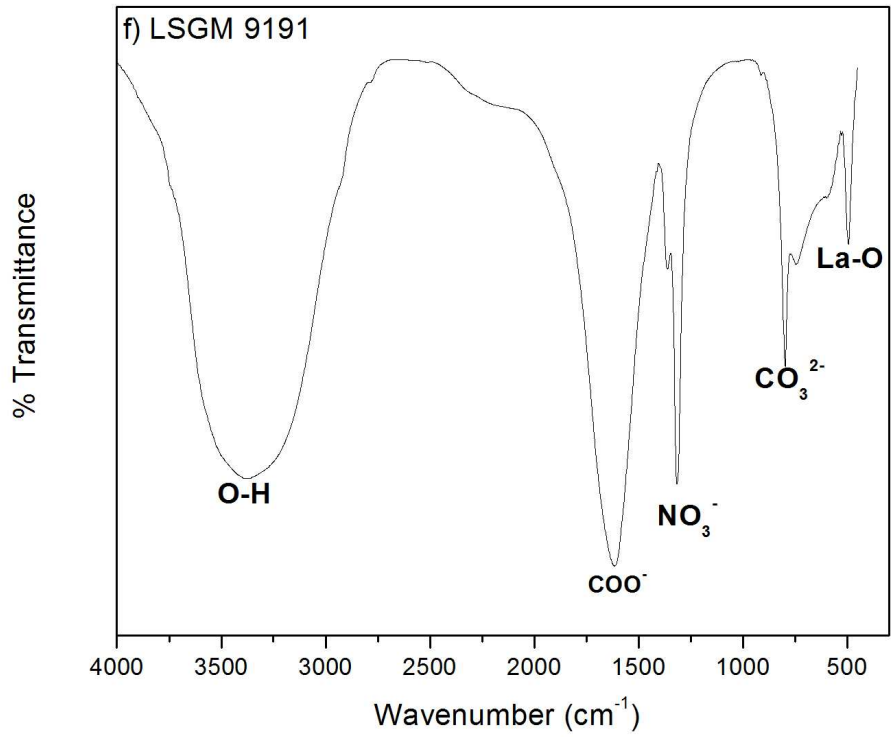

Fig. 4.1.12 FTIR spectrum of lanthanum strontium magnesium gallate precursors prepared by co-precipitation method

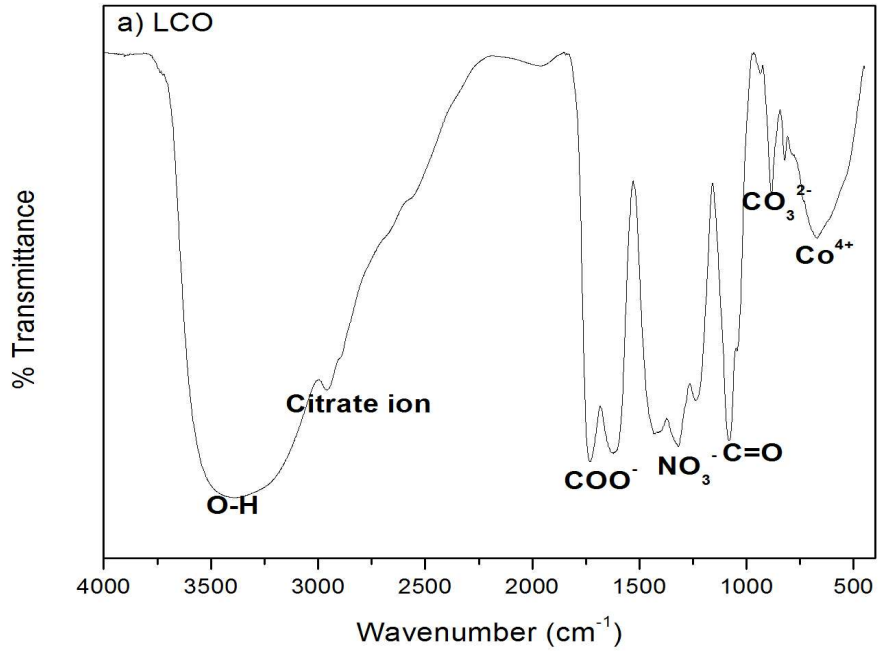

Fig. 4.1.13 FTIR spectrum of lanthanum cobaltite precursors prepared by Pechini method

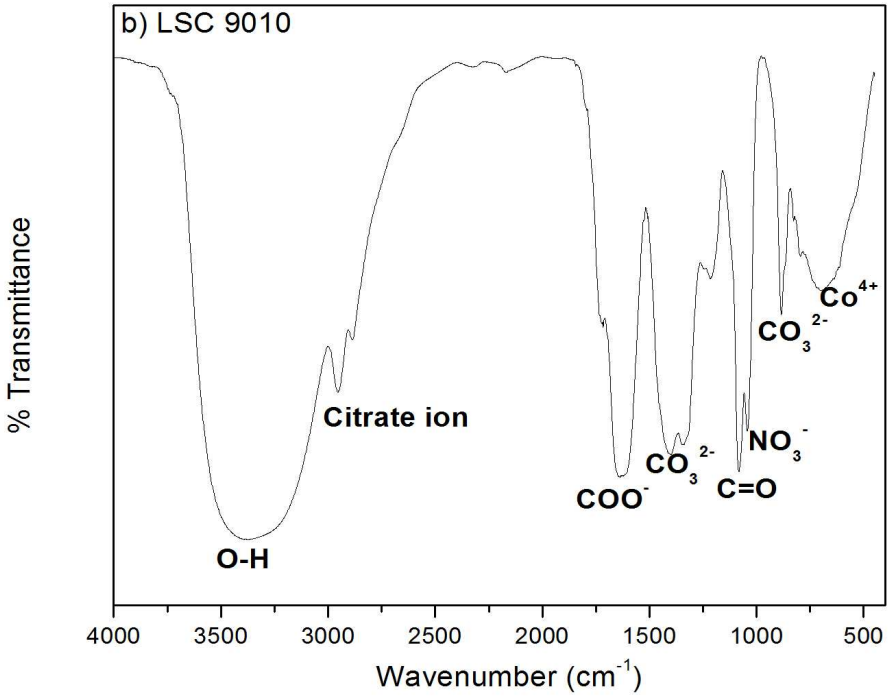

Fig. 4.1.14 FTIR spectrum of lanthanum strontium cobaltite precursors prepared by Pechini method

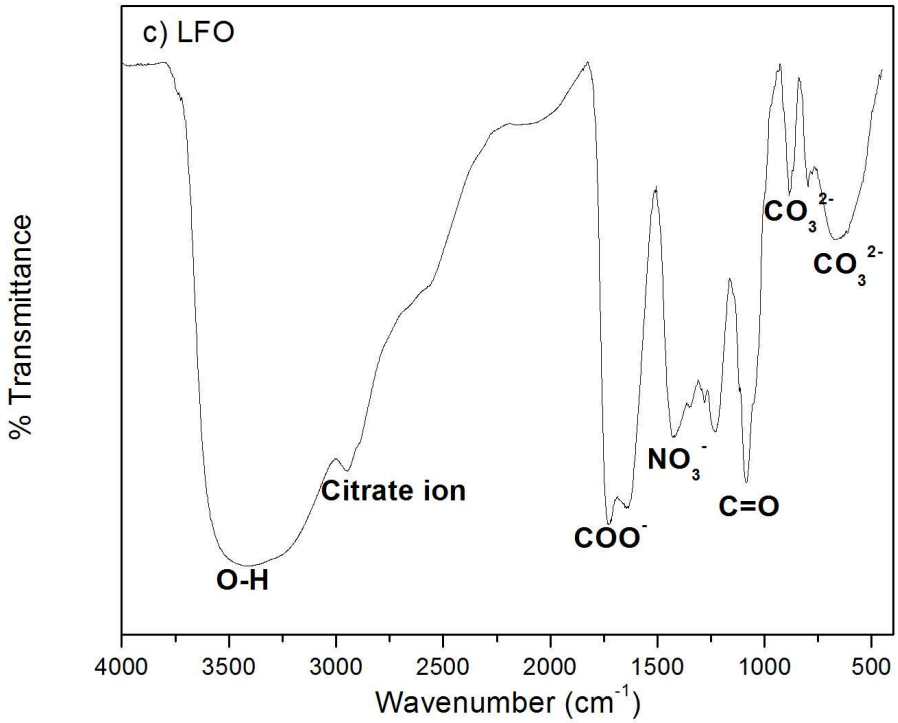

Fig. 4.1.15 FTIR spectrum of lanthanum ferrite precursors prepared by Pechini method

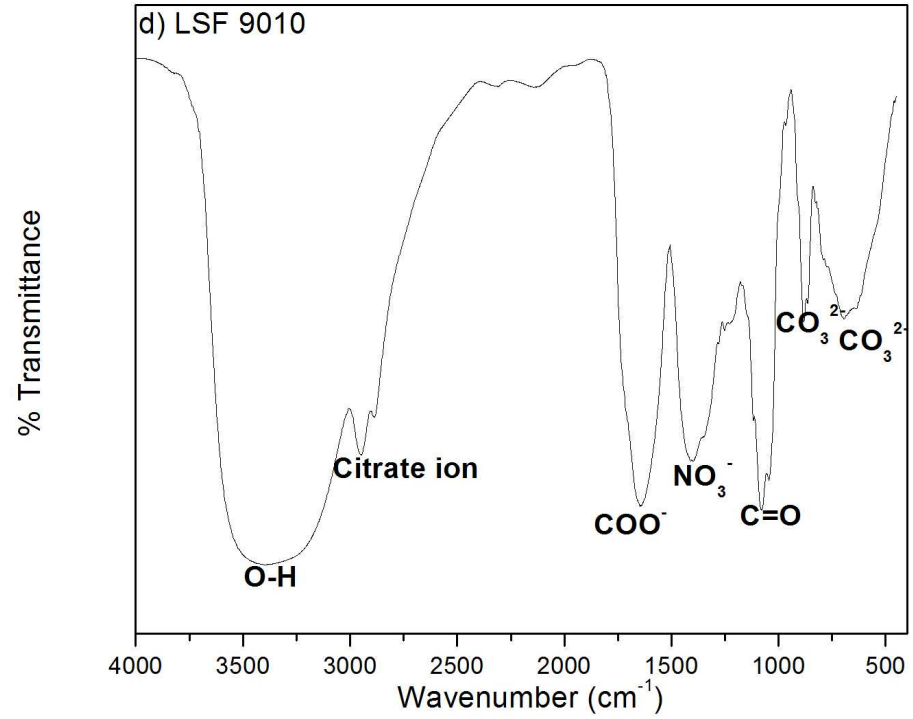

Fig. 4.1.16 FTIR spectrum of lanthanum strontium ferrite precursors prepared by Pechini method

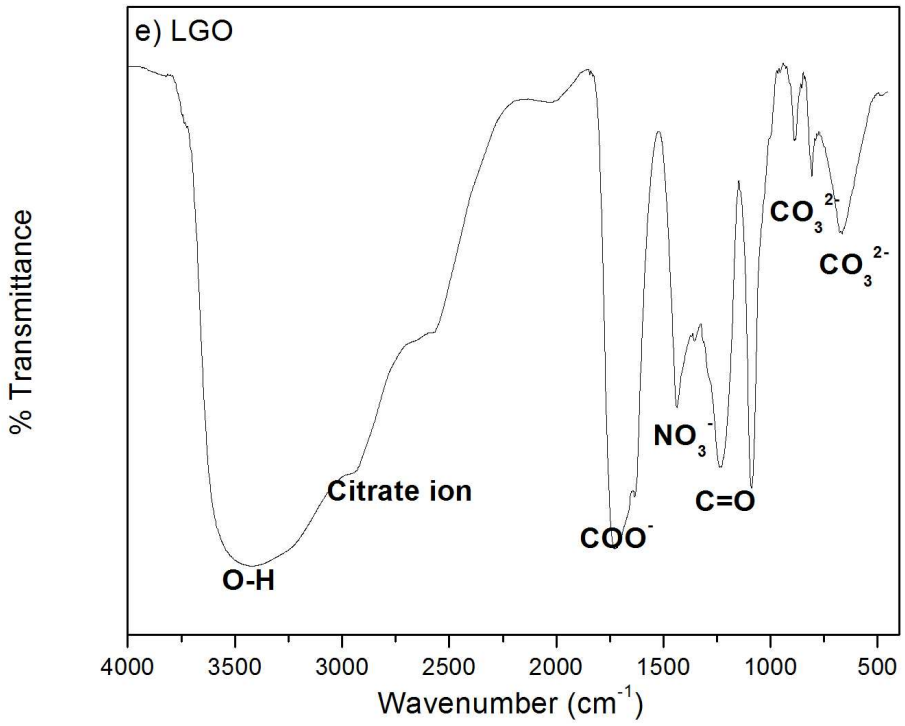

Fig. 4.1.17 FTIR spectrum of lanthanum gallate precursors prepared by Pechini method

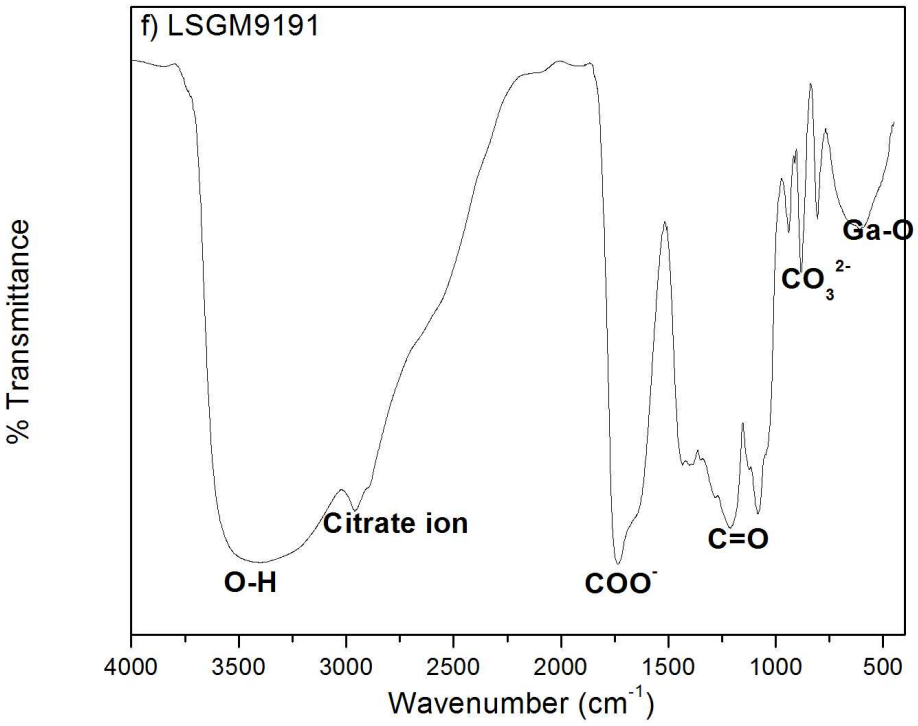

Fig. 4.1.18 FTIR spectrum of lanthanum strontium magnesium gallate precursors prepared by Pechini method

4.1.1.2. Thermogravimetric and Differential Thermal Analysis

The thermogravimetric and differential thermal analysis plots for all precursor samples prepared by combustion, co-precipitation and citrate-gel methods prior to calcination are displayed in Figs 4.1.19 to 4.1.24. The various stages of removal of organics, combustion and decarboxylation reactions, crystallization, phase transformations and the stabilization of the pure phase at higher temperatures could be inferred from these thermal analysis plots. The thermogravimetric plots of the combustion products shown in Fig. 4.1.19 indicated no further weight loss for the pure and Sr-doped lanthanum ferrite and cobaltite phases. A minor weight loss was noticed for LSC indicating the completion of the combustion reaction at 500^{o}C.

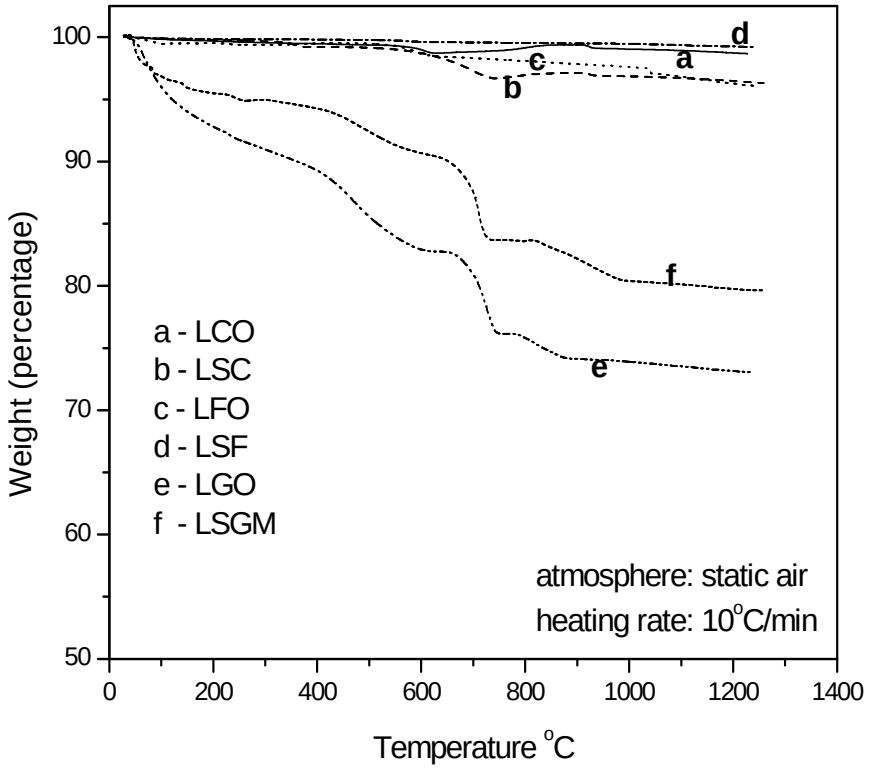

Fig. 4.1.19 TG profiles of materials prepared by combustion method

Although the ignition temperature was 500^{o}C, the actual temperature of the product would have been much higher because of the combustion process. Berger and co-workers [2003] also reported the completion of the combustion reaction when the initiation temperature was 500^{o}C through simultaneous TG/DTA of the $LaCoO_3$ alanine-based precursor. The corresponding DTA plots for pure and Sr-doped lanthanum ferrites showed no thermal effects. However for Sr-doped lanthanum cobaltite, a minor endothermic effect at 300^{o}C and an exothermic reaction was noticed at 740^{o}C and a small endothermic peak at 920^{o}C was observed for both pure LCO and

LSC. The exothermic reaction at 740^{o}C associated with a minor mass loss could be attributed to the residual combustion reaction whereas the endothermic effects at around 300 and 920^{o}C without any mass loss were possibly due to structural transformations, although the nature of structural transformations were not clear. Berger et al [2003] observed a minor endothermic effect in the DTA of pure and Sr-doped lanthanum cobaltite at 320^{o}C (peak position at 345^{o}C), which they incorrectly attributed to a crystallization process (crystallization process is exothermic). Stolen et al [1998] attributed the maximum in heat capacity observed in their measurements on $LaCoO_3$ at 257^{o}C to a continuous low to high spin state electronic transition. Berger and coworkers [2003] also did not notice any structural transformation in lanthanum cobaltite at 920^{o}C in their TG/DTA result. However, Popa and Kakihana [2002] observed a minor endothermic reaction with no associated mass loss in their DTA of $LaCoO_3$ at ~875^{O}C. Tikhonovich and coworkers [2003] carried out TG/DTA on $Sr(Co,Fe)O_{3-\delta}$ in air in the temperature range 200 to 1000^{o}C. They also observed an explicit endothermic effect at 890±10^{o}C associated with a drastic decrease in the oxygen content (decrease in δ up to 0.02) supporting the structural transformation at this temperature. Specific heat measurements on this phase up to 900^{o}C would have provided conclusive evidence on the phase transformation. Unfortunately, Stolen et al [1998] carried out heat capacity measurements on $LaCoO_3$ only up to 727^{o}C. A rhombohedral to orthorhombic phase transformation was also reported in $La_{0.58}Sr_{0.4}Co_{0.2}Fe_{0.8}O_{3-\delta}$ between 1250 to 1400^{o}C [Zinkevich et al, 2004]. The thermogravimetric behavior of LGO and LSGM suggested that the combustion reaction was not complete at 500^{o}C and two separate stages of mass loss corresponding to combustion reactions were observed between 800 and 1000^{o}C. This was also substantiated by the broad exothermic peak in the corresponding temperature range in the DTA (e and f of Fig. 4.1.20).

A higher calcination temperature would therefore be required for the synthesis of pure and Sr, Mg-doped lanthanum gallate compared to lanthanum ferrite and cobaltite. The thermogravimetric plot of the co-precipitated products shown in Fig. 4.1.21 showed three stages of mass loss for all the precursors; the first up to 150^{o}C due to dehydration, the 2nd steep mass loss between 250^{o}C to 500^{o}C and the third at 700^{o}C. The corresponding DTA (Fig. 4.1.22) indicated an endothermic peak at 150^{o}C and a large exothermic peak for the 2nd stage of mass loss (two large peaks in the case of LSC). The transformation depicted in the TG at 700^{o}C was not associated with any heat

effects in the DTA. The general trend of TG/DTA was similar for all the co-precipitated precursors (except for LSC) used in this study.

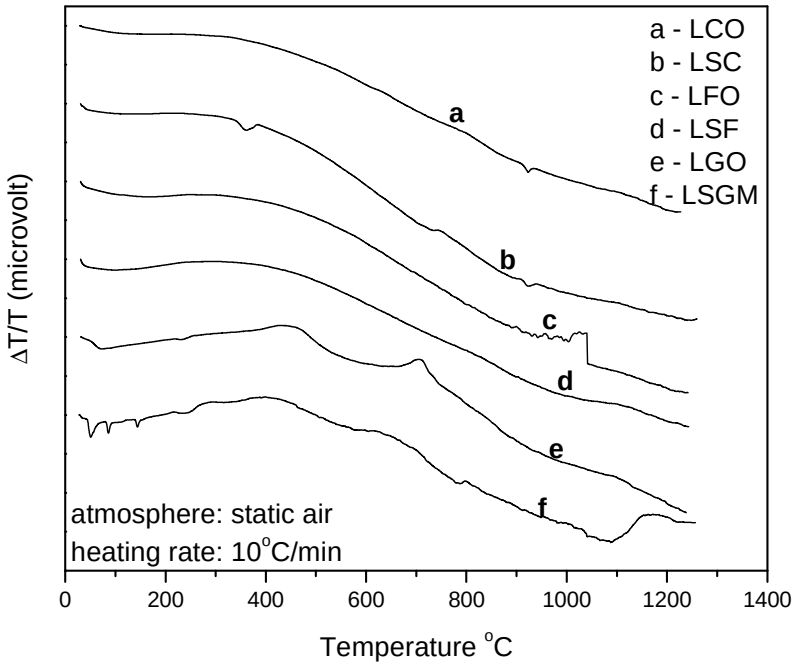

Fig.4.1.20 DTA plots of materials prepared by combustion method

Nakayama and coworkers [2003] carried out a detailed investigation on the calcination behavior of coprecipitates of $La_2(C_2O_4)_3.nH_2O$ and $CoC_2O_4.mH_2O$ using thermogravimetry and IR spectra of samples calcined at several temperatures. They also observed the decomposition to occur in three steps: dehydration up to 150°C, an abrupt 2nd stage of weight loss at 270°C attributed to decomposition of the oxalate and finally the decomposition of the carbonates above 700°C. The results obtained in the present study were consistent with the observations of Nakayama et al [2003], except for the third stage of carbonate decomposition. The decomposition of carbonates is associated with an endothermic effect which was not detected in the present study. Nakayama and co-workers [2003] observed that high calcination temperatures (>1200°C) was required to synthesize $LaCoO_3$ from their oxalate precursors by co-precipitation. This was consistent with the present study where a calcination temperature of 1300°C was required to synthesize pure and Sr-doped $LaCoO_3$. Although the TG plots obtained for the various oxalate precursors showed constancy in mass beyond 1000°C, XRD of the calcined products at 1300°C **(**Fig. 4.1.33) showed that except for LCO and LSC, pure phases were not formed by co-precipitation (with the use of both oxalic acid and liquid ammonia as precipitating agents). However, interestingly, Huang and coworkers [1996] could synthesize pure crystalline $La_{0.9}Sr_{0.1}Ga_{0.8}Mg_{0.2}O_{2.85}$ (minor amounts of secondary

phases were observed even here) through the sol-gel route by sintering the amorphous gel calcined at 600^{o}C to 1370^{o}C for 72 hours in air and vacuum. Further, they observed no mass loss or DTA signal above 500^{o}C in their TG-DTA measurements on the gel (formed from acetate precursor solution peptized with ammonium hydroxide and dried) although they had to sinter the gel calcined at 600^{o}C to ~1370^{o}C for 72 hours to get the crystalline phase.

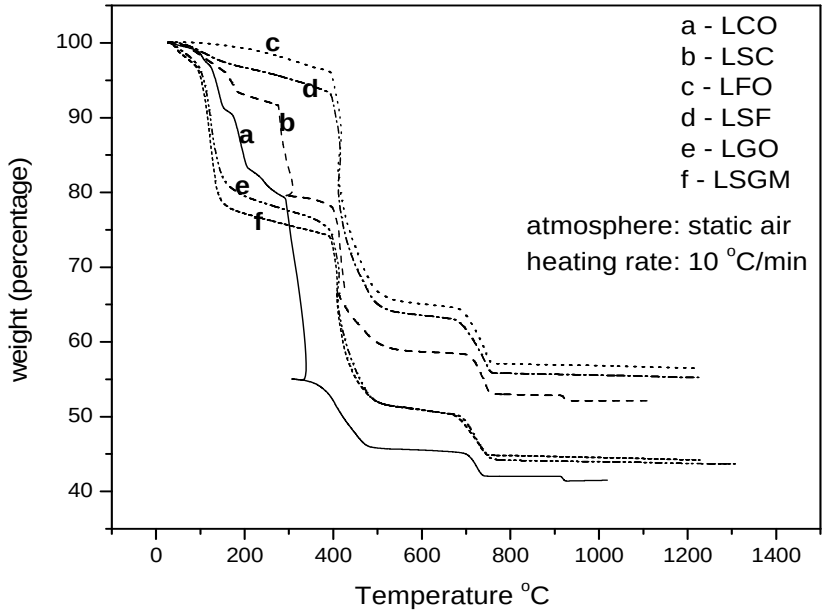

Fig. 4.1.21 TG plots for materials prepared by co-precipitation method

The thermogravimetric and differential thermal analysis results on the amorphous gel synthesized by the citrate-gel method (prior to calcination at 500^{o}C) in this study are shown in Figs. 4.1.23 and 4.1.24 respectively.

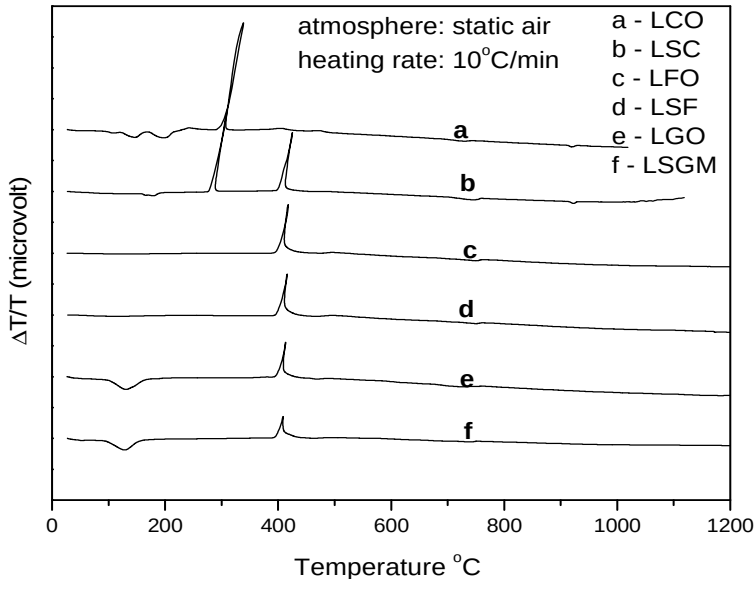

Fig. 4.1.22 DTA plots for materials prepared by co-precipitation method

The thermal analysis behavior of the precursors derived by the Pechini method was very similar to that observed for the co-precipitated precursors, except that the reactions occurred over a narrower temperature range. The thermogravimetric plot showed three stages of mass loss for all the precursors; the first up to 150^{o}C due to dehydration, the 2nd steep mass loss between 200^{o}C to 400^{o}C and the third between 500 to 700^{o}C depending upon the nature of the precursor. The corresponding DTA **(**Fig. 4.1.24**)** indicated an endothermic peak at 150^{o}C and two overlapping exothermic peaks for the 2nd stage of mass loss between 200 to 400^{o}C (the two peaks were separated in the case of LGO). The 3rd stage of mass loss was not accompanied by any heat effects, except for LGO which showed a minor exothermic effect at ~700^{o}C. The 1st stage of mass loss and the associated endothermic effect was due to moisture loss whereas the 2nd stage of mass loss associated with large exothermicity was due to the oxidation reactions.

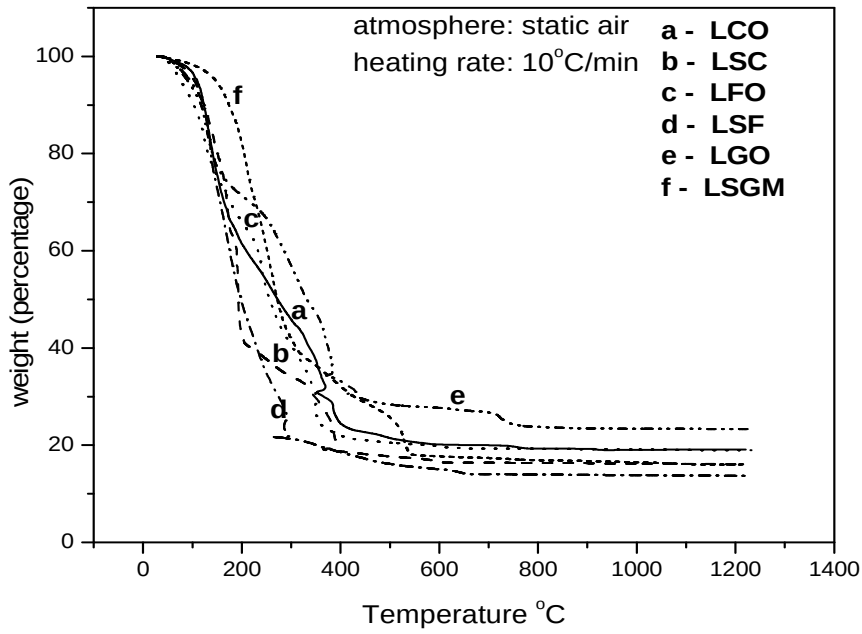

Fig. 4.1.23 Thermogravimetric plot of the precursor resins (prior to calcination) prepared by Pechini method

Polini and coworkers [2004] as well as Tas et al [2000] carried out simultaneous TG-DTA on the LSGM resins synthesized by the Pechini method (using citric acid and ethylene glycol) prior to calcination. Polini et al [2004] observed a similar thermal analysis behavior on the LSGM foam obtained by sol-gel citrate synthesis and dried at 200^{o}C overnight (three stages of mass loss, endotherm at 200^{o}C corresponding to moisture loss and three exothermic peaks between 300 to 600^{o}C corresponding to the oxidation reactions). However, Polini and coworkers observed an additional exothermic

peak without any associated mass gain/loss at 1250^{o}C which they attributed to a solid state reaction between the dissociated reactants.

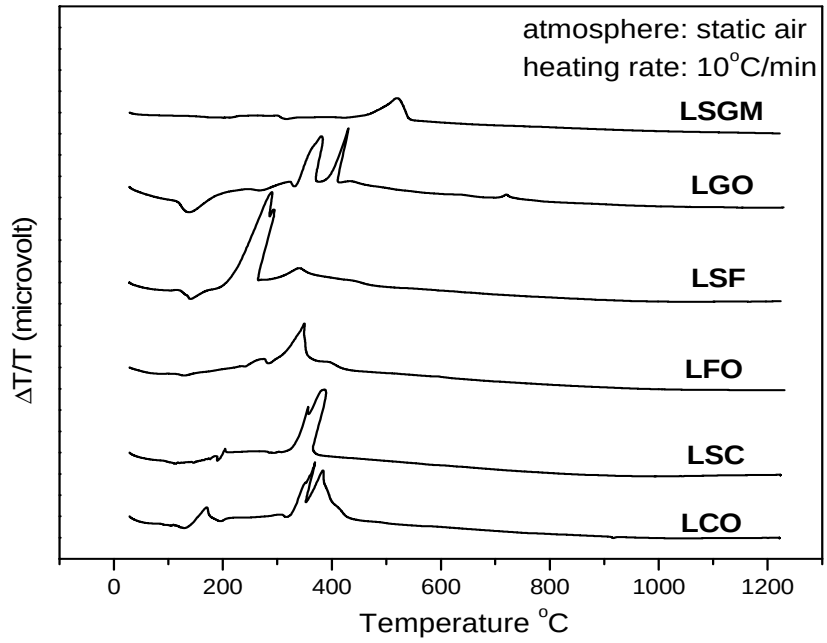

Fig. 4.1.24 Differential thermal analysis of the precursor resins (prior to calcination) prepared by Pechini method

Tas and co-workers [2000] also observed a similar behavior in the TG/DTA of LSGM precursors prepared by the Pechini method. They observed a total mass loss of 55% in 3 stages up to 700^{o}C after which there was no mass loss. They observed exothermic peaks at 350, 400, 480 and 600^{o}C corresponding to the various stages of oxidation. A calcination treatment between 500 to 600^{o}C of the gel is expected to take the oxidation reaction to completion and result in an amorphous product. The DTA plots of the gel calcined at 500^{o}C in this study is depicted in Fig. 4.1.25**.** Interestingly, the DTA of the pure and Sr-doped lanthanum cobaltite and pure lanthanum ferrite calcine do not show any thermal effects at lower temperatures. As observed earlier, the DTA of the Sr-doped lanthanum cobaltite showed a minor endothermic peak at ~1150^{o}C which is probably associated with the rhombohedral→orthorhombic phase transformation in this compound as reported earlier by Buchler et al [2007]. For Sr-doped lanthanum ferrite, a large exothermic peak at ~350^{o}C and a minor exothermic deviation at ~500^{o}C were noticed although these were not associated with any mass loss. The exothermic reaction at 350^{o}C was possibly due to the oxidation of the residual reactants whereas the reason for the minor exotherm at 500^{o}C was not clear. Incidentally, a second order magnetic order-disorder transition was reported by Stolen

et al [1998] at 462^{o}C based on heat capacity measurements. The DTA for the LGO and LSGM samples showed the start of a minor endothermic effect at 320^{o}C (peak at 375^{o}C) without any associated mass effects. Again, the reason for this was not clear. Although an orthorhombic to rhombohedral phase transformation was reported to occur at around 147^{o}C [Zinkevich et al, 2004] in pure $LaGaO_3$, the endothermic effect observed was unlikely to be due to this structural transformation since the crystallinity of the calcined product was in doubt.

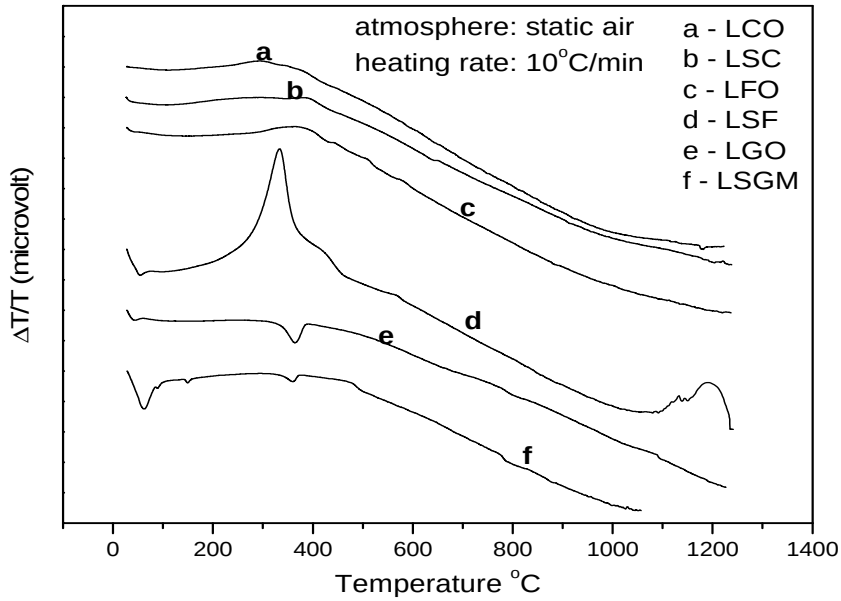

Fig. 4.1.25 Differential thermal analysis of the calcined powders prepared by Pechini method

4.1.1.3. Bulk powder morphology by stereomicroscopy

The bulk powder morphology of the as-synthesized pure $LaCoO_3$ phase is shown in Fig 4.1.26 for combustion, co-precipitation and Pechini methods respectively. The morphology of the other pure crystalline phases was similar. The stereo images revealed that the structure obtained for products derived from combustion synthesis (Fig. 4.1.26a) and citrate-gel method (Fig. 4.1.26c) was similar and appeared porous and networked in nature, although in terms of particle size and hardness, the combustion derived powders were hard (simple observation by feeling the powder) and coarse compared to that synthesized by Pechini method.

Despite the coarser mean particle size for combustion synthesis, these powders still showed some tendency for agglomeration of particles, which might be attributed to the high in-situ combustion temperature. In the case of co-precipitation, the morphology of precipitated powders (oxalate of respective element) appeared porous

and agglomerated, as could be seen in Fig. 4.1.26 b**.** The agglomeration of particles depends on the processing condition and calcination temperature. The presence of agglomerated particles is detrimental to the final state of sintering and introduces heterogeneities in the microstructure of the sintered ceramics that cannot be eliminated readily. These agglomerated particles act as defect centers [Ramanathan el al, 2003] and therefore the agglomerates need to be eliminated by grinding. The wet grinding process is effective in reducing agglomeration.

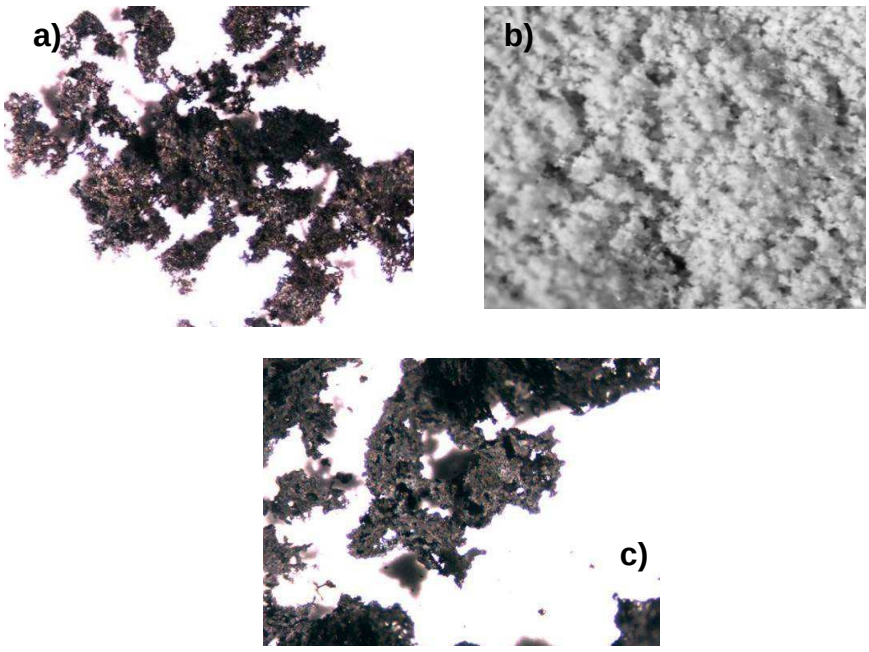

Fig. 4.1.26 As-synthesized powder morphology of 2.4X by stereo microscopy for a) Combustion, b) Co-precipitation and c) Pechini synthesized $LaCoO_3$

4.1.2. Calcination of prepared powders

The prepared powders from combustion, co-precipitation and Pechini methods were subjected to calcination to obtain a pure single phase. Further, the calcined powders were characterized for studying the thermal stability under oxidizing and reducing atmospheres, phase purity and particulate properties towards their application in Intermediate Temperature Solid Oxide Fuel Cells.

4.1.2.1. Thermal stability of calcined powders under reducing and oxidizing atmospheres

Thermogravimetric studies on pure crystalline solid lanthanum cobaltite and ferrite and Sr-doped lanthanum cobaltite and ferrite; and Sr- and Mg- doped lanthanum

gallate powders prepared from Pechini method were also carried out in both oxidizing (pure O_2) and reducing atmosphere (80% N_2 + 20% H_2) to study their stability in these atmospheres. These results are shown in Figs. 4.1.27 and 4.1.28. All the compounds were found to be stable in oxidizing atmosphere over the temperature range of measurement (30 to 900^{o}C), whereas pure and Sr-doped lanthanum cobaltite was found to dissociate in the reducing atmosphere.

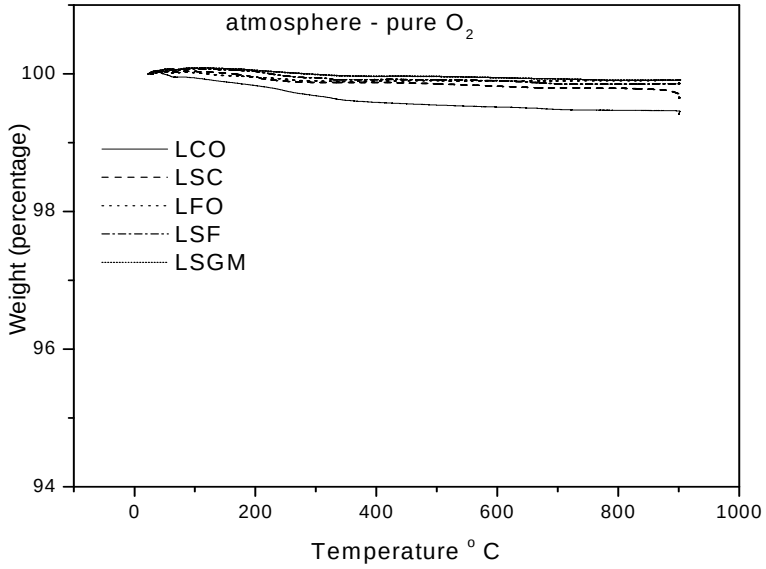

Fig. 4.1.27 Stability of materials prepared from Pechini method in oxidizing atmosphere.

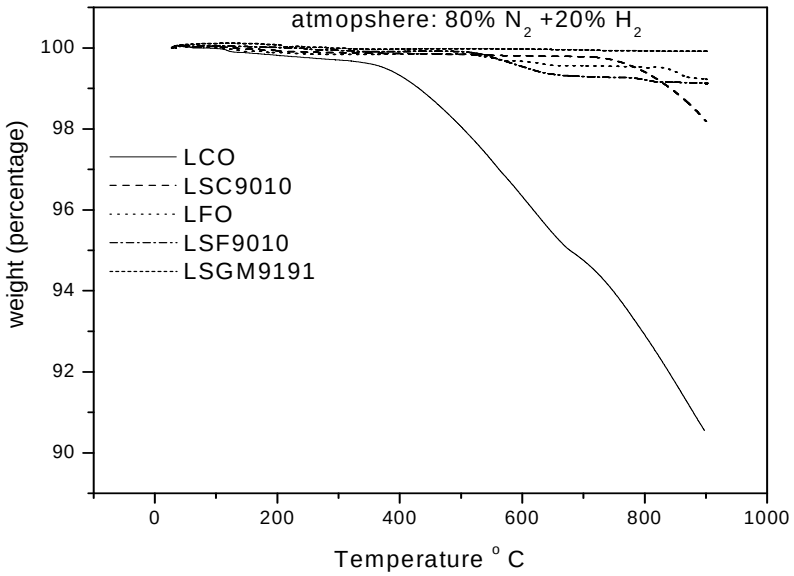

Fig. 4.1.28 Stability of materials prepared from Pechini method in reducing atmosphere

The X-ray diffractograms of the respective oxides after the TG run in the reducing atmosphere is depicted in Fig. 4.1.29. It was observed that both lanthanum cobaltite ($LaCoO_3$) as well as Sr-doped $LaCoO_3$ were partially reduced to Co^{+2} form in hydrogen atmosphere. The X ray diffraction pattern of both these samples subjected to

thermogravimetry under reducing conditions showed the formation of La_2CoO_4 (72-0937). The stability of these compounds in reducing atmosphere was not reported in the literature earlier.

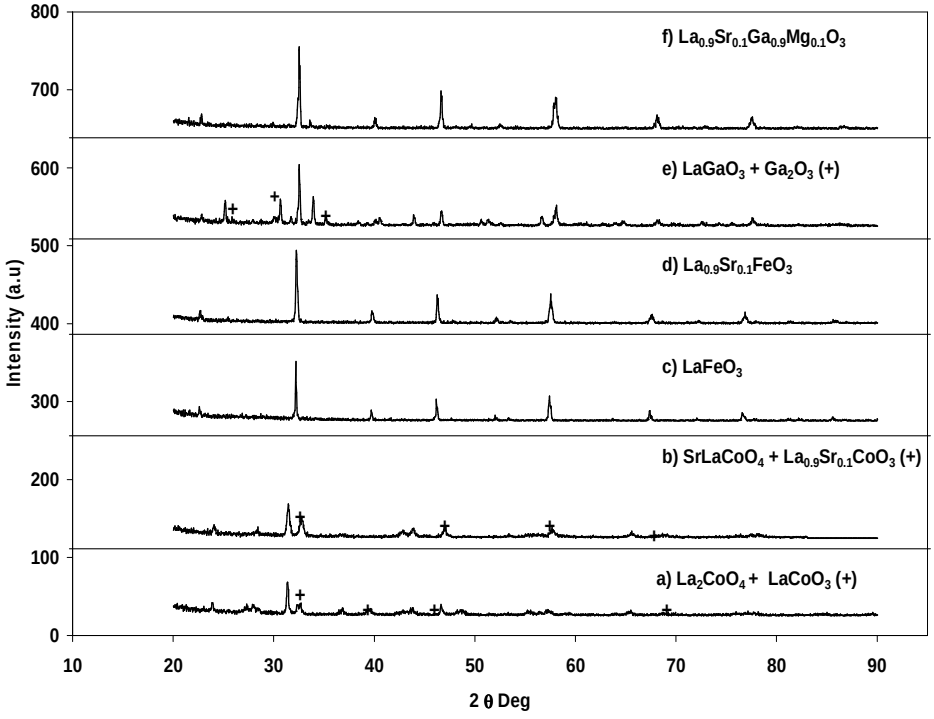

Fig. 4.1.29 X-ray diffractogram of the oxides after thermogravimetric analysis under reducing atmosphere

4.1.2.2. Phase purity by X-ray diffraction

The X- ray diffraction pattern of $LaCoO_3$ (LCO), $La_{0.9}Sr_{0.1}CoO_{3-\delta}$ (LSC), $LaFeO_3$ (LFO), $La_{0.9}Sr_{0.1}FeO_{3-\delta}$ (LSF), $LaGaO_3$ (LGO) and $La_{0.9}Sr_{0.1}Ga_{0.9}Mg_{0.1}O_{3-\delta}$ (LSGM) from combustion and Pechini methods is shown in Figs. 4.1.30 to 4.1.32 respectively. It was seen that the XRD pattern of all the materials namely $LaCoO_3$, $La_{0.90}Sr_{0.10}CoO_{3-\delta}$, $LaFeO_3$, $La_{0.90}Sr_{0.10}FeO_{3-\delta}$, and $LaGaO_3$, showed the formation of a single phase and perfectly matched with the JCPDS files (25-1060 for LCO, 36-1392 for LSC, 37-1493 for LFO and LSF and 24-1102 for LGO). However, at lower calcination temperatures (900-1300^oC), the LGO and LSGM phases did not form completely, whereas at higher temperature (1500^oC), the LSGM powder prepared from both combustion and citrate-gel methods were found to contain about 5 % of $LaSrGa_3O_7$ (JCPDS: 45-0637) as an impurity phase. Synthesis of pure LSGM was reported to be extremely difficult and traces of $LaSrGa_3O_7$ or $La_4Ga_2O_9$ or $LaSrGaO_4$ phases were frequently detected especially when the solid state synthesis was adopted [Huang et al, 1998; Ishihara et al, 1996; Djurado and Labeau , 1998; Gorelov et al,

2001; Cheng and Navrotsky, 2004; Westphal et al, 2000; and Sammes et al, 1998]. However, it was observed that increasing the doping of Mg in the B- site of LGO stabilized the formation of the pure perovskite phase. A representative XRD of pure single phase $La_{0.90}Sr_{0.10}Ga_{0.80}Mg_{0.20}O_{3-\delta}$ (the impurity phase of $LaSrGa_3O_7$ was absent here) obtained from the Pechini method and calcined at 1500^{o}C is also included in Fig. 4.1.32. Majewski and co-workers [2002] have also reported the formation of pure $La_{0.90}Sr_{0.10}Ga_{0.80}Mg_{0.20}O_{3-\delta}$ by the citrate-gel method when calcined at 1500^{o}C.

Huang and coworkers [1996] have discussed in detail the formation of the secondary phases during the synthesis of cubic perovskite LSGM phase by various routes. For the co-precipitation method (using both oxalic acid and liquid ammonia as the precipitating agents), all the samples (pure and Sr-doped lanthanum ferrite, cobaltite and gallate) calcined at 900^{o}C showed the presence of additional hydroxide phases. Therefore, for the co-precipitation method, the synthesized powders were subjected to calcination in the temperature range 900-1300 ^{o}C for pure and Sr-doped lanthanum ferrite and cobaltite and 900-1500^{o}C for LGO and Mg, Sr-doped $LaGaO_3$ at an interval of 100^{o}C and the calcined powder subjected to XRD.

The phases identified at different temperatures of calcination during the synthesis of the various oxides by co-precipitation are summarized in Table 4.1.1. It was observed that single phases of several of the oxides (notably LFO, LSF, LGO and LSGM) could not be synthesized by co-precipitation at calcination temperatures up to 1300^{o}C for pure and Sr-doped lanthanum ferrite and up to 1500^{o}C for doped lanthanum gallate. However, the co-precipitation method yielded pure single phases of $LaCoO_3$ and $La(Sr)CoO_3$ when calcined at 1300^{o}C. X-ray diffractograms of the oxide phases synthesized by co-precipitation method and calcined at 1300^{o}C are given in Fig. 4.1.33. Similarly, none of the pure phases could be synthesized when liquid ammonia was used as the precipitating agent despite carrying out calcination up to 1500^{o}C.

Although the synthesis of yttria and gadolinia doped ceria by co-precipitation has been reported in the literature [Zhang et al, 2003; Tadokoro et al, 2004], the oxalate route of co-precipitation has not been reported for the synthesis of pure and Sr-doped lanthanum gallate, ferrite and cobaltite.

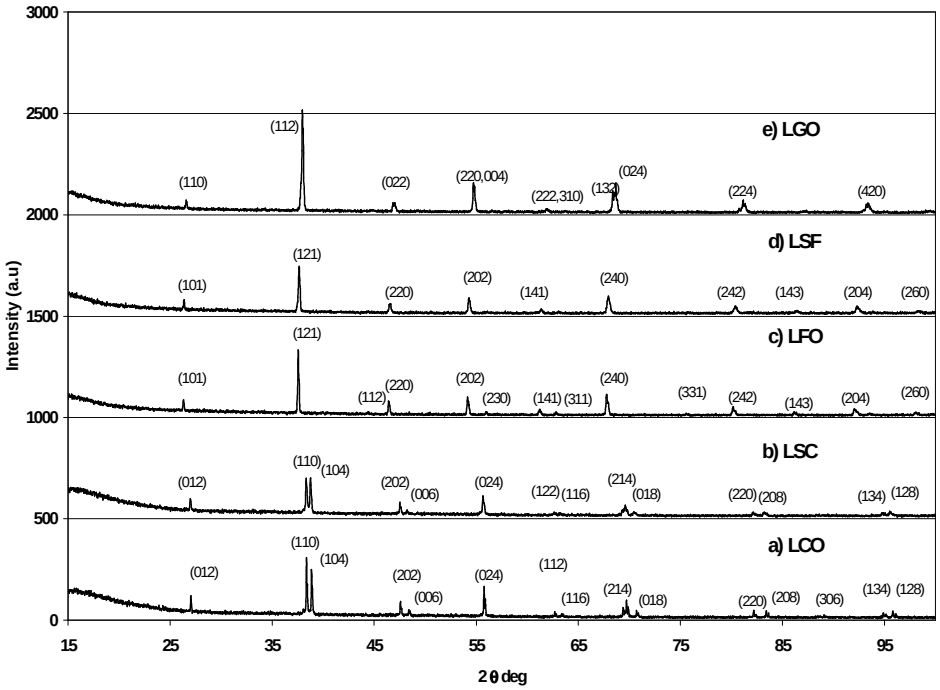

Fig. 4.1.30 XRD pattern of a) LCO, b) LSC 9010, c) LFO, d) LSF 9010 and e) LGO prepared by combustion method.

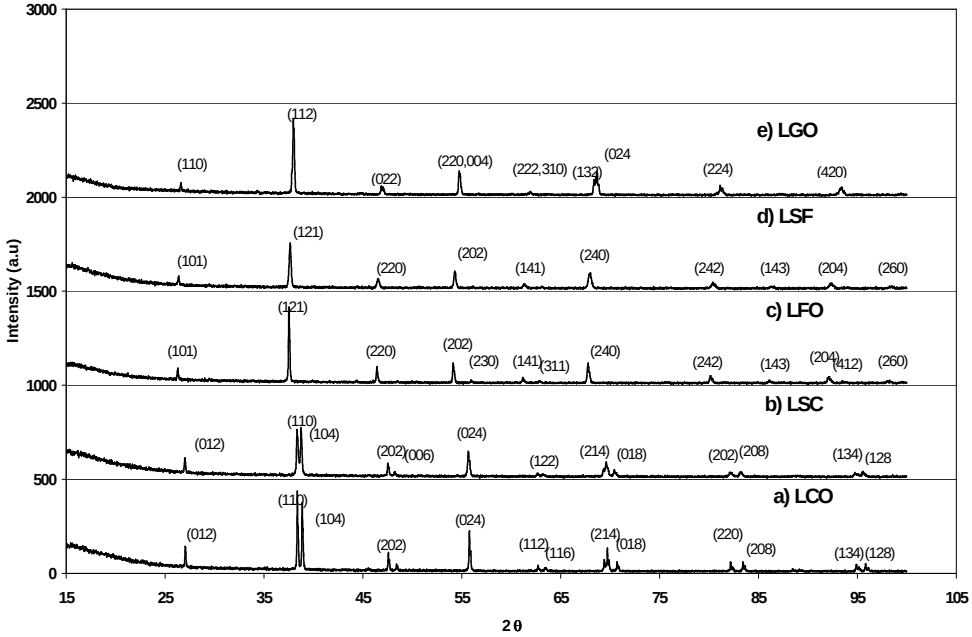

Fig.4.1.31 XRD pattern of a) LCO, b) LSC 9010, c) LFO, d) LSF 9010 and e) LGO prepared by Pechini method.

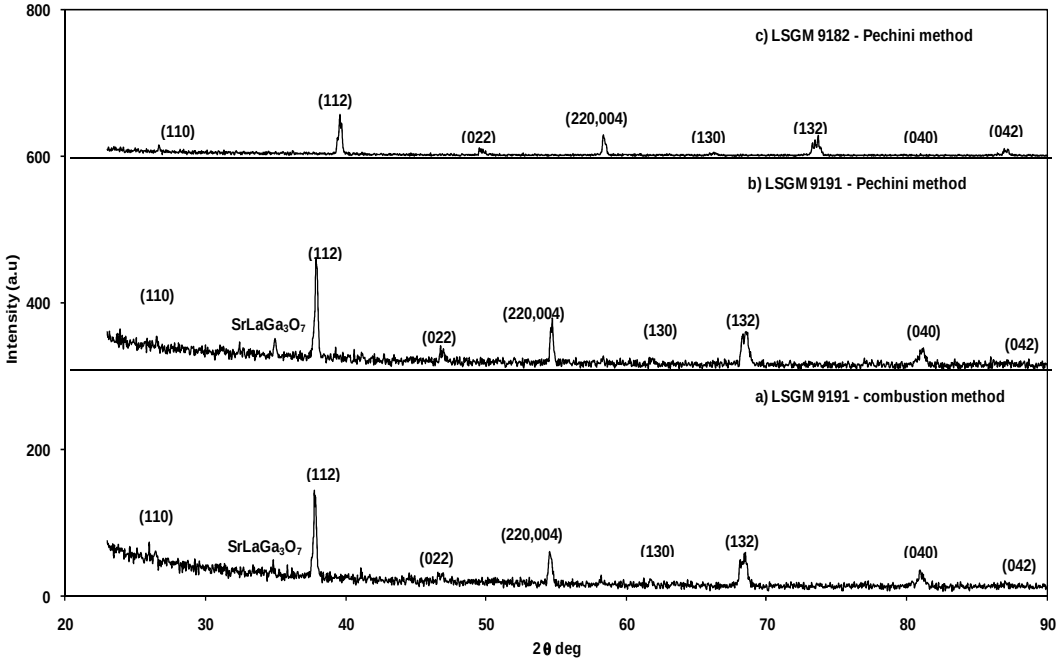

Fig. 4.1.32 X-ray diffractogram of Sr and Mg doped lanthanum gallate prepared through a) combustion method and b) Pechini method.

The density of the synthesized pure phases was calculated from XRD data using the following equation [Cullity and Stock, 2001]:

$$\rho = \frac{z\,M}{N\,V} \qquad [4.1]$$

where ρ is the density in g/cc; z is the number of atoms in the unit cell; M is the molecular weight of the material; N is the Avogadro number and V is the unit cell volume in m^3.

$LaCoO_3$ (LCO) and $La_{0.9}Sr_{0.1}CoO_{3-\delta}$ (LSC) crystallized in the rhombohedral structure whereas $LaFeO_3$ (LFO) and $La_{0.9}Sr_{0.1}FeO_{3-\delta}$ (LSF); $LaGaO_3$ (LGO) and $La_{0.9}Sr_{0.1}Ga_{0.9}Mg_{0.1}O_{3-\delta}$ (LSGM) crystallized in the orthorhombic structure. Hence, the lattice parameter of the synthesized perovskite oxides from combustion, co-precipitation and Pechini methods were calculated from the corresponding d-spacing of the X-ray diffraction pattern using the following equations:

For rhombohedral-hexagonal system,

$$\frac{1}{d^2} = \frac{4}{3}\left(\frac{h^2 + hk + k^2}{a^2}\right) + \frac{l^2}{c^2} \qquad [4.2]$$

Table 4.1.1 Phase purity of the various oxides prepared from co-precipitation method as a function of calcination temperatures.

Materials	**Phases identified at different temperatures**			
	900^o C	**1100^o C**	**1300^o C**	**1500^o C**
LCO	La_2O_3	Pure	-	-
LSC 9010	La_2O_3	Pure	-	-
LFO	$La(OH)_3$	$La(OH)_3$	$La(OH)_3$	-
LSF 9010	$La(OH)_3$+ La_2SrO_x	$La(OH)_3$+ La_2SrO_x	$La(OH)_3$	-
LGO	$La(OH)_3$	$La(OH)_3$	$La(OH)_3$	-
LSGM 9191	$La(OH)_3$+ La_2SrO_x+ La_2MgO_x	$La(OH)_3$+ La_2SrO_x+ La_2MgO_x	$La(OH)_3$+ $LaSrGa_3O_7$	$La(OH)_3$+ $LaSrGa_3O_7$

For orthorhombic system,

$$\frac{1}{d^2} = \frac{h^2}{a^2} + \frac{k^2}{b^2} + \frac{l^2}{c^2} \qquad [4.3]$$

The calculated lattice parameters and density of the synthesized pure phases from XRD data are given in Table 4.1.2. It was found that the calculated lattice parameters for LCO, LSC, LFO, LSF, LGO and LSGM prepared from combustion, Pechini and co-precipitation methods were in close agreement with those reported in the respective JCPDS files.

Table 4.1.2 Crystallographic properties of materials prepared from different synthetic routes

Properties	Crystal Structure	Calculated unit cell parameters (A^o)			Unit cell volume $(A^o)^3$	Calculated X-ray density (g/cc)	d_{50} particle diameter (micron) (mea)
		a	b	c			
LCO – GN	Rhombohedral	5.440	-	13.144	336.94	7.23	6.87
LSC9010 – GN	Rhombohedral	5.446	-	13.155	338.02	7.09	10.71
LFO-GN	Orthorhombic	5.551	7.856	5.559	242.48	6.64	18.99
LSF 9010-GN	Orthorhombic	5.542	7.834	5.543	240.71	6.68	15.96
LGO-GN	Orthorhombic	5.497	5.480	7.785	234.49	7.26	3.64
LSGM 9191-GN	Orthorhombic	5.594	5.514	7.763	239.50	6.85	3.08
LCO – P	Rhombohedral	5.442	-	13.090	335.80	7.29	1.17
LSC9010 – P	Rhombohedral	5.445	-	13.141	337.43	7.11	0.24
LFO-P	Orthorhombic	5.555	7.868	5.521	241.37	6.56	2.62
LSF 9010-P	Orthorhombic	5.551	7.832	5.538	240.82	6.55	1.64
LGO-P	Orthorhombic	5.529	5.476	7.784	235.70	7.23	1.93
LSGM 9191-P	Orthorhombic	5.495	5.530	7.785	236.63	6.93	3.21
LCO – CP	Rhombohedral	5.448	-	13.110	337.08	7.27	2.40
LSC9010 – CP	Rhombohedral	5.443	-	13.096	336.04	7.14	2.99

GN- Glycine nitrate combustion method, P- Pechini method and CP-Co-precipitation method

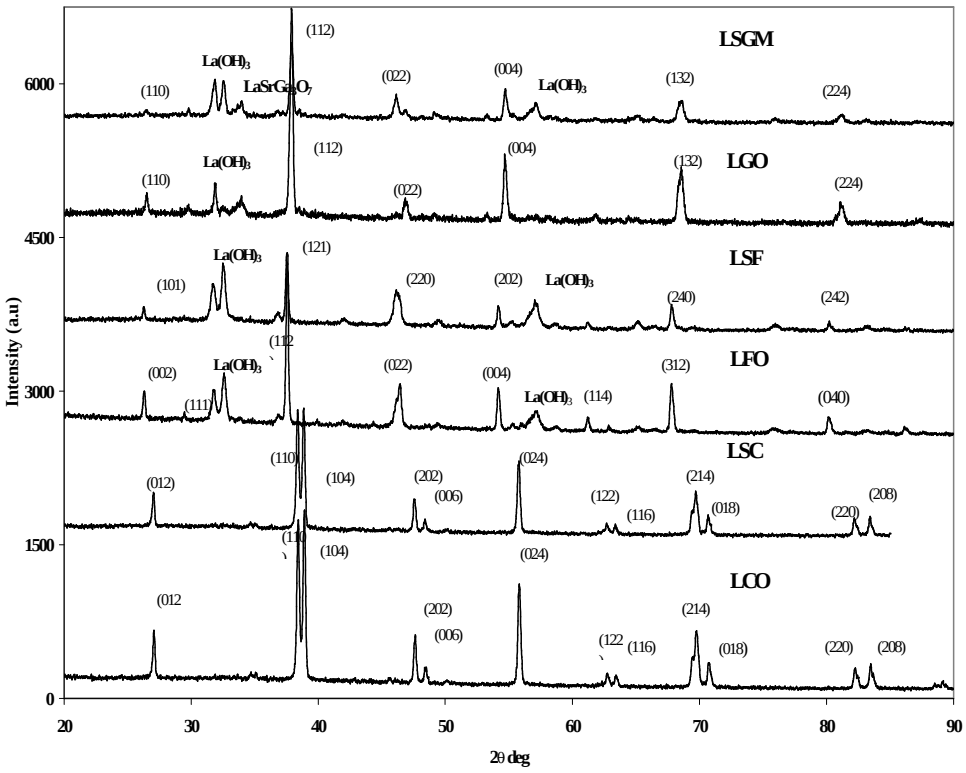

Fig.4.1.33 XRD of a) LCO, b) LSC 9010, c) LFO, d) LSF 9010 e) LGO and f) LSGM 9191 prepared by co-precipitation method

4.1.2.3. Particle size distribution and surface area

The particle size distribution of crystalline LCO, LSC, LFO, LSF, LGO and LSGM powders synthesized by combustion, Pechini and co-precipitation methods is shown in Figs. 4.1.34, 4.1.35 and 4.1.36 respectively. It was found that the dry ground powders prepared by combustion synthesis possessed particle size with d_{50} (size below which 50 vol.% of the powders exist) ranging from 7 to 19 micron for LCO, LSC, LFO and LSF and around 3 μm for LGO and LSGM. For the powders synthesized by the citrate-gel method, the mean particle size was in the range of 0.5-3.0 microns. The mean particle size of powders from the co-precipitation method was also less than 3 microns. The mean particle size of the powders prepared from the different routes is summarized in Table 4.1.2. The larger particle size for the combustion synthesized powders might be attributed to the high combustion temperature attained during the process of synthesis. To study the effect of calcination temperature on particle growth, the single phase powders synthesized by the co-precipitation method (LCO and LSC) were subject to calcination in the temperature range of 900-1300^{o}C for 3 h and particle

sizes measured. The mean particle sizes of these two oxides synthesized by co-precipitation and calcined at different temperatures are given in Table 4.1.3. It was seen that there was an increase in mean particle size as a function of calcination temperature because of the growth of particles.

Table 4.1.3 Variation of particle size with calcinations temperature for materials prepared by co-precipitation method

	Mean Particle Size (microns)				
Temperatures ^{o}C	**900**	**1000**	**1100**	**1200**	**1300**
$LaCoO_3$	2.40	2.50	2.74	2.81	3.65
$La_{0.90}Sr_{0.10}CoO_3$	2.99	4.66	5.17	5.40	5.94

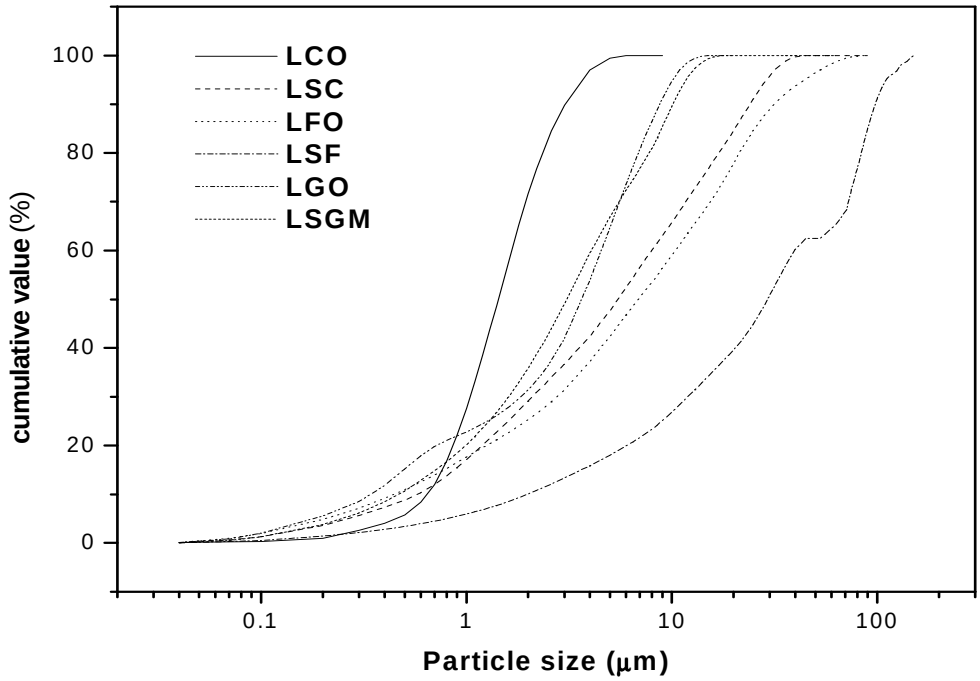

Fig. 4.1.34 Particle size distribution of the various oxides prepared by combustion method.

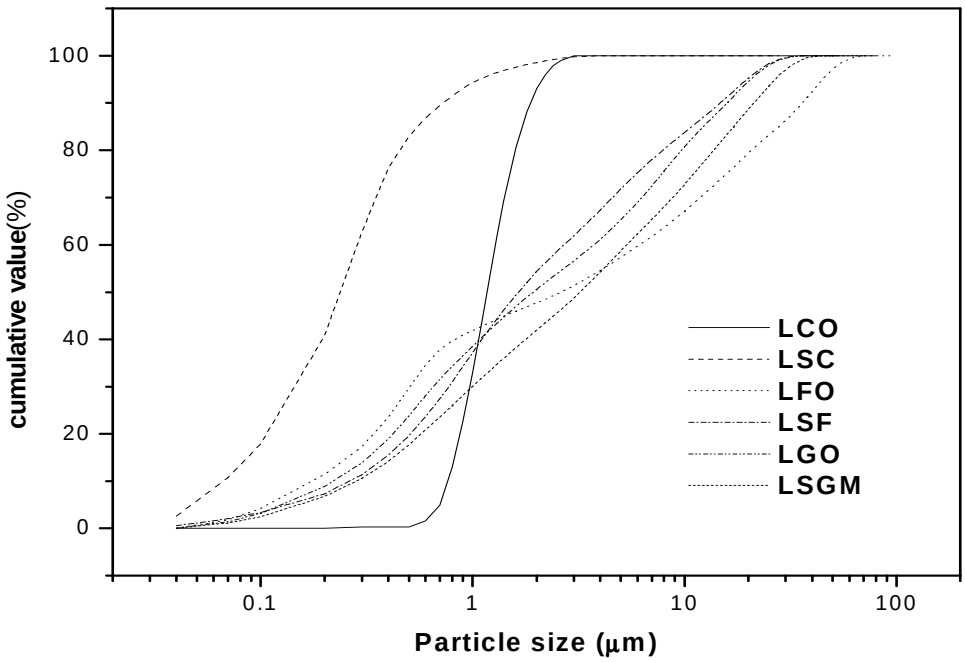

Fig.4.1.35 Particle size distribution of the different materials prepared by Pechini method

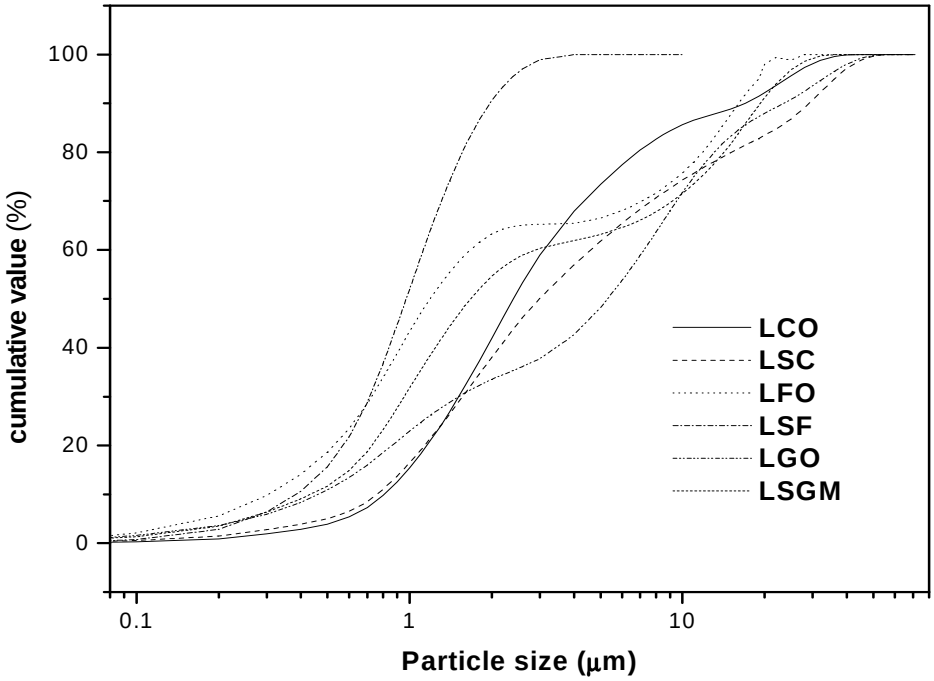

Fig. 4.1.36 Particle size distribution for the materials prepared by Co-precipitation method

The BET surface area obtained for the different crystalline single phases from combustion, co-precipitation and Pechini methods are given in Table 4.1.4. It was observed that the BET surface area of powders synthesized by Pechini method was higher than that of the other two methods. Further, the crystalline LSGM powders

synthesized both by combustion and citrate-gel methods yielded a much higher surface area (despite the larger particle size) than that achieved for the other phases. This might be attributed to a lower surface energy and thereby a lesser tendency for agglomeration or sintering of this phase. In general, the adsorption isotherm which shows the variation of adsorbate volume with relative pressure $0< P/P^o < 1$, contains information on the pore structure of materials. The pore size obtained from surface area measurement for the various powders synthesized in this study was in the range of 5-11 nm for the combustion method, 30-58 nm for the co-precipitation method and 7 to 37 nm for the citrate-gel method. Sing and co-workers [1985] also observed mesopores in the size range between 2 to 50 nm in the materials prepared by them using the sol-gel method. It could therefore be inferred that the powders prepared by the wet chemical routes adopted in this study especially the co-precipitation and Pechini routes were porous and had considerable internal pore surfaces. The internal surfaces of the pores also contributed to the specific surface area of samples measured by BET.

Table 4.1.4 Comparison of surface area and pore size of powders prepared by different synthetic routes

	Combustion method		**Co-Precipitation method**		**Citrate –gel method (Pechini)**	
Materials	**S_A (m^2/g)**	**Pore size (nm)**	**S_A (m^2/g)**	**Pore size (nm)**	**S_A (m^2/g)**	**Pore size (nm)**
LCO	0.75	7.6	1.29	57.6	2.48	7.7
LSC9010	1.80	8.0	1.98	31.2	3.53	18.1
LFO	1.47	5.2	-	-	3.45	12.6
LSF 9010	1.24	7.4	-	-	2.23	36.9
LGO	1.83	7.5	-	-	2.17	8.5
LSGM 9191	6.41	11.8	-	-	7.02	12.6

4.1.2.4. Morphology by Scanning Electron Microscopy

Back scattered electron images of the pure crystalline phases prepared by combustion, co-precipitation and Pechini methods are shown in Figs 4.1.37 to 4.1.39 respectively. The combustion synthesized pure phases (Fig. 4.1.37) had discrete particles with different morphologies and a porous and spongy appearance. The pure phases (LCO and LSC) synthesized by the co-precipitation method (Fig. 4.1.38)

showed high porosity and a tendency for agglomeration. In the case of co-precipitation, wherein a wet chemical processing using starting materials of oxides and nitrate salts was adopted, the powder morphology was significantly affected by the processing parameters. These include precipitation conditions, washing procedure and heating conditions in a static reactor. In the citrate-gel method, at the same calcination temperature, the powders were of finer size, exhibited a more uniform morphology and appeared porous in nature (Fig. 4.1.39). The powders from Pechini method appeared to be discrete and had a lesser tendency to agglomeration despite the finer size (Fig. 4.1.39). It was clear that the three methods exhibited varied microstructures in terms of particle size and morphology as shown in Figs 4.1.37 to 4.1.39. The agglomeration of particles depends on the processing condition and calcination temperatures.

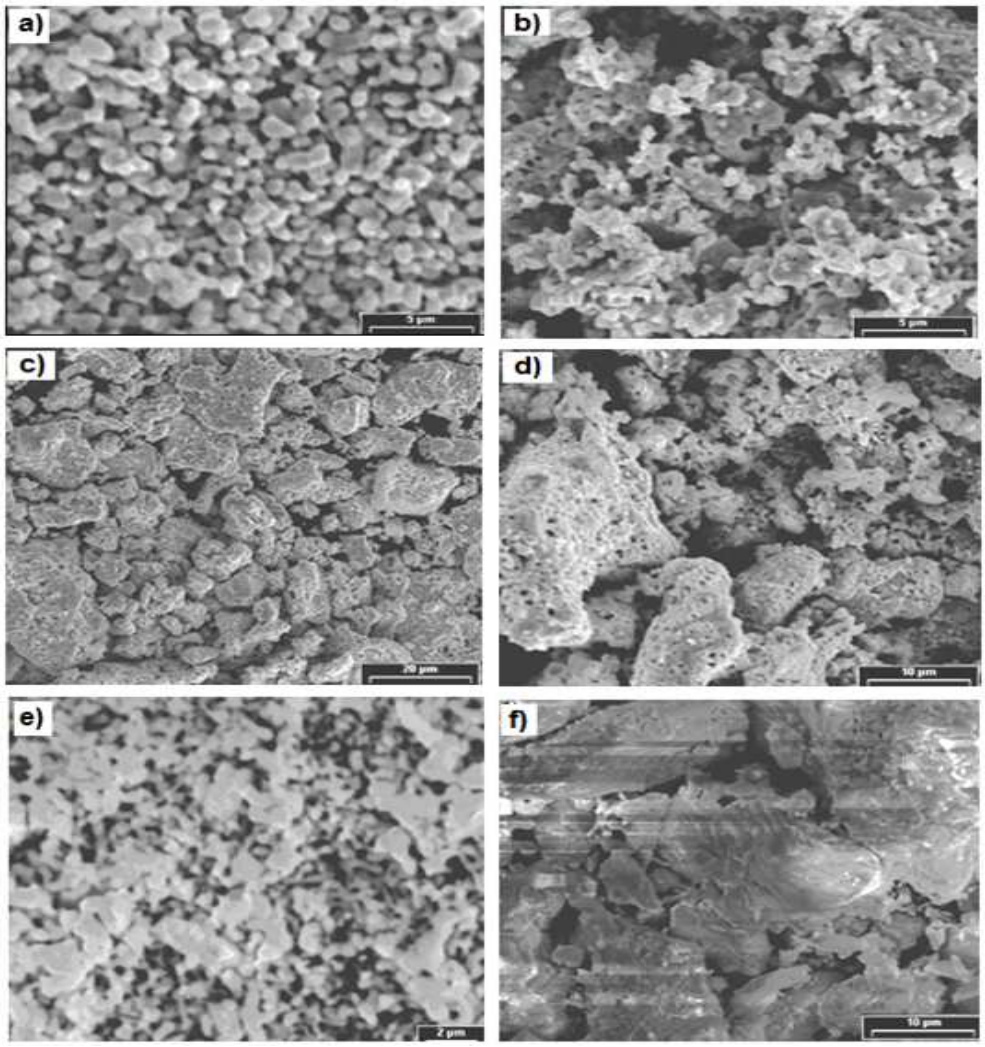

Fig. 4.1.37 Back-scattered electron images of a) LCO, b) LSC 9010, c) LFO, d) LSF9010, e) LGO and f) LSGM 9191 prepared by combustion method

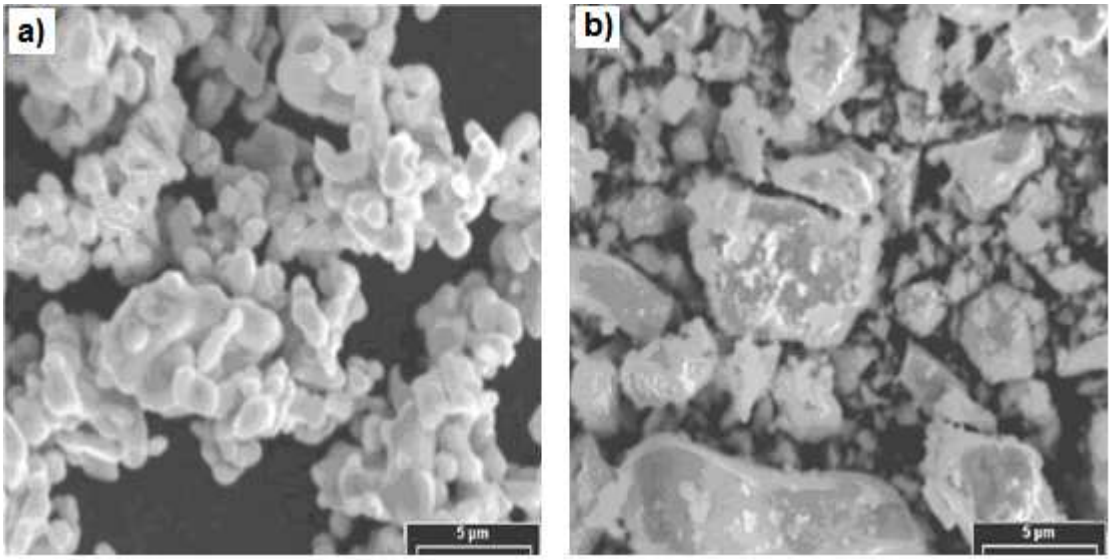

Fig. 4.1.38 Morphology of pure a) LCO and b) LSC 9010 prepared by Co-precipitation method as seen by back-scattered electron imaging.

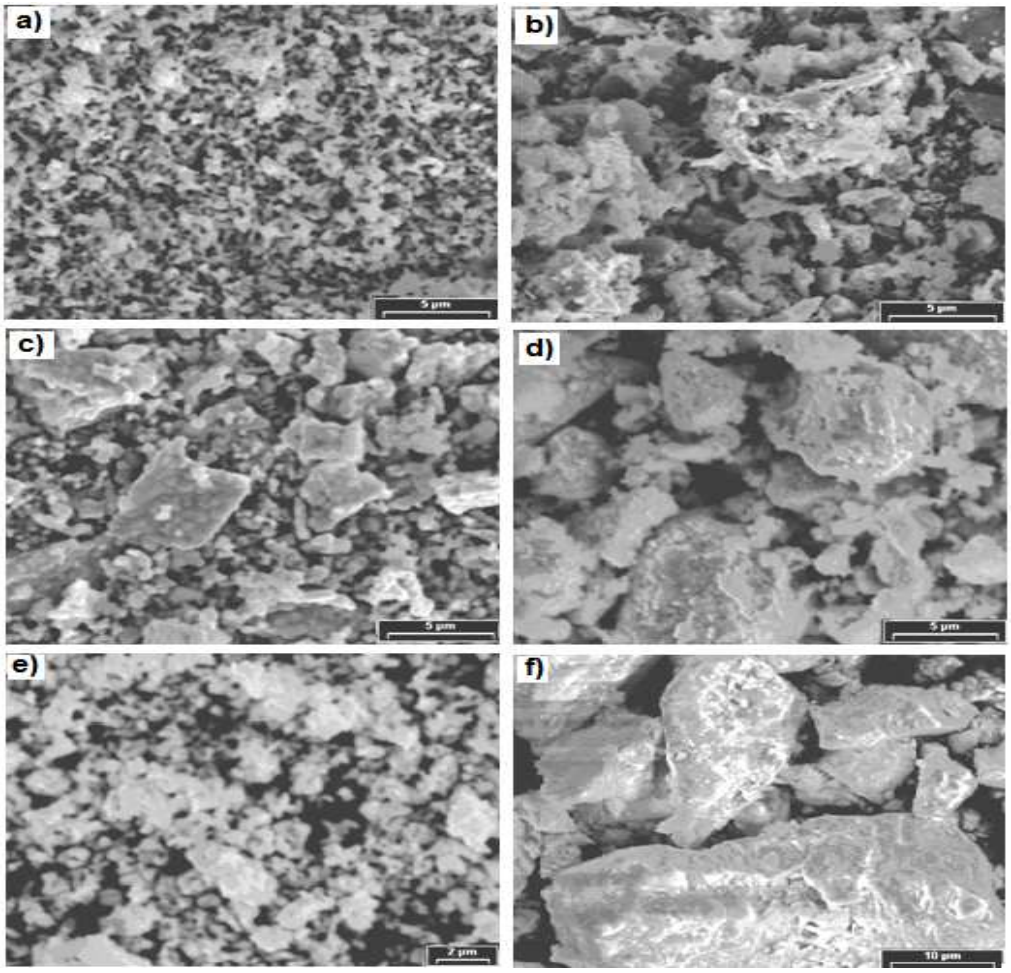

Fig. 4.1.39 SEM-BSE images of a) LCO, b) LSC 9010, c) LFO, d) LSF 9010, e) LGO and f) LSGM 9191 prepared by Pechini method

4.2. STABILITY RANGE AND PHASE EQUILIBRIUM OF Sr- AND Mg-DOPED LANTHANUM GALLATE

Since the literature reports on phase constitution in the La_2O_3-Ga_2O_3-SrO-MgO system at the $LaGaO_3$ rich end were not consistent with the topological rules for quaternary phase diagram construction and further phase equilibria at the operational temperature of Intermediate Temperature Solid Oxide Fuel Cells were also not available, this study was taken up with the objective of characterizing the complete compositional range of stability of $La_{1-x}Sr_xGa_{1-y}Sr_yO_{3-(x+y)/2}$ at 700 and 1500 ^oC respectively. Further, since the literature information on the ionic conductivity of LSGM as a function of Sr and Mg content was conflicting, detailed conductivity measurements as a function of Sr and Mg contents have also been carried out with the objective of identifying the window of optimum compositions that yield the highest ionic conductivity with the lowest activation energy.

4.2.1. Phase Purity and morphology of $La_{1-x}Sr_xGa_{1-y}Mg_yO_{3-\delta}$ at 1500^{o}C

Equilibration of the samples at 1500^{o}C was carried out for two different time periods, 8 and 24 h. The samples equilibrated at 1500^{o}C for 8 h were used to analyze the phase equilibrium because the samples equilibrated for 24 h showed significant Ga vaporization losses. The mass loss in the 8-hour equilibrated samples for all the compositions investigated ($La_{1-x}Sr_xGa_{1-y}Mg_yO_{3-\delta}$ x=0-0.3, y=0-0.3) was less than 0.3%. Similarly, for all compositions, in 8 hours of equilibration at 1500^{o}C, the Ga vaporization losses deduced from the bulk Ga concentration analyzed by EDAX was less than 0.5 at. %. The X-ray diffraction patterns of pure $LaGaO_3$, with varying Sr (x=0.01, 0.02, 0.03 and 0.04) and Mg content (y = 0, 0.02, 0.05, 0.10, 0.15, 0.20, 0.25 and 0.30) are shown in Figs. 4.2.1-4.2.4 and the corresponding back scattered electron images at a magnification of 500X (higher magnification pictures have been shown to represent the bulk microstructure) are shown in Figs. 4.2.5-4.2.7. It was seen from the XRD pattern that no secondary phases appeared for Mg concentrations up to 30 mol %. However, scanning electron images indicated that at 20, 25 and 30 mol % Mg, secondary phase of MgO (dark spherical precipitates at the grain boundary) precipitated from the solution. Traces of Ga_2MgO_4 were also detected by EDS in the SEM images of 20 and 25 mol% Mg samples. This indicated that the solubility of Mg in the pure perovskite phase is about 20 mol % at 1500^{o}C. The absence of MgO peaks in the XRD for the 20, 25 and 30 mol % samples might be because this phase was present at less

than 3 vol% or might have been amorphous in nature. However, samples sintered for 20 hrs clearly showed crystalline MgO peaks in the X-ray diffractogram.

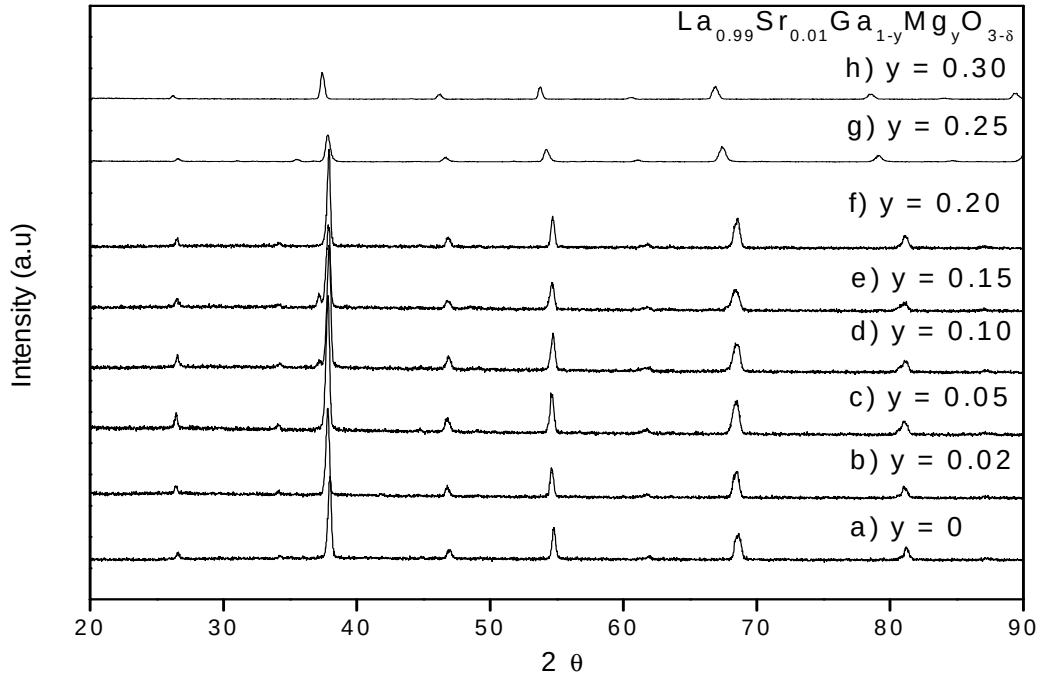

Fig.4.2.1 XRD pattern of $La_{0.99}Sr_{0.01}Ga_{1-y}Mg_yO_{3-\delta}$ (y= 0-0.30) equilibrated at 1500^oC

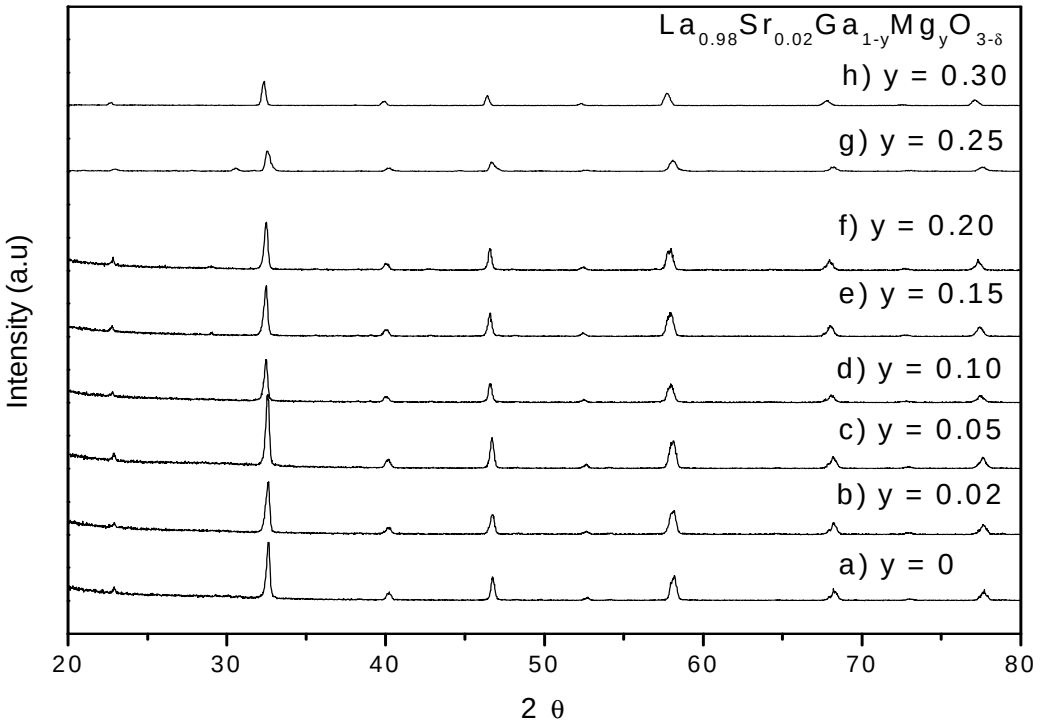

Fig.4.2.2 XRD pattern of $La_{0.98}Sr_{0.02}Ga_{1-y}Mg_yO_{3-\delta}$ (y= 0-0.30) equilibrated at 1500^oC

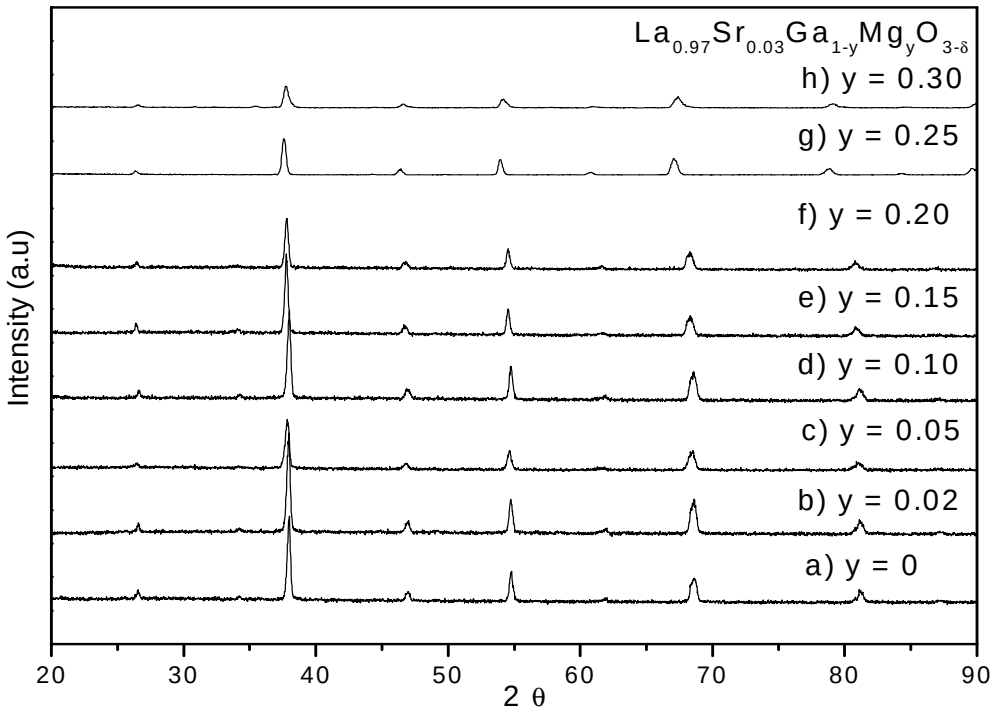

Fig.4.2.3 XRD pattern of $La_{0.97}Sr_{0.03}Ga_{1-y}Mg_yO_{3-\delta}$ (y= 0-0.30) equilibrated at 1500^oC

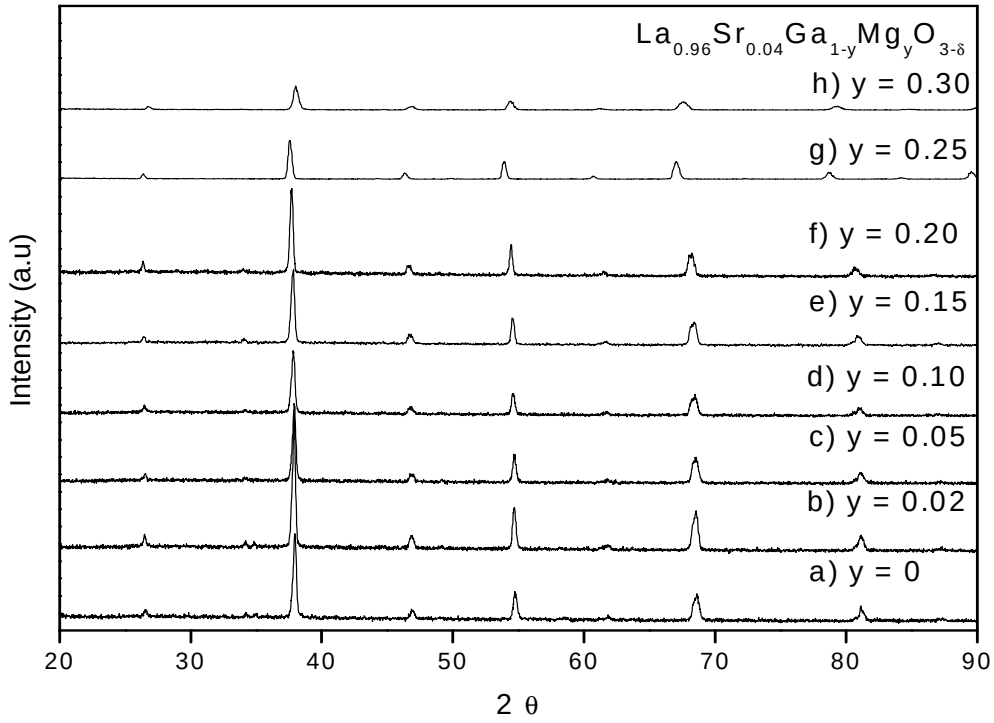

Fig.4.2.4 XRD pattern of $La_{0.94}Sr_{0.04}Ga_{1-y}Mg_yO_{3-\delta}$ (y= 0-0.30) equilibrated at 1500^oC

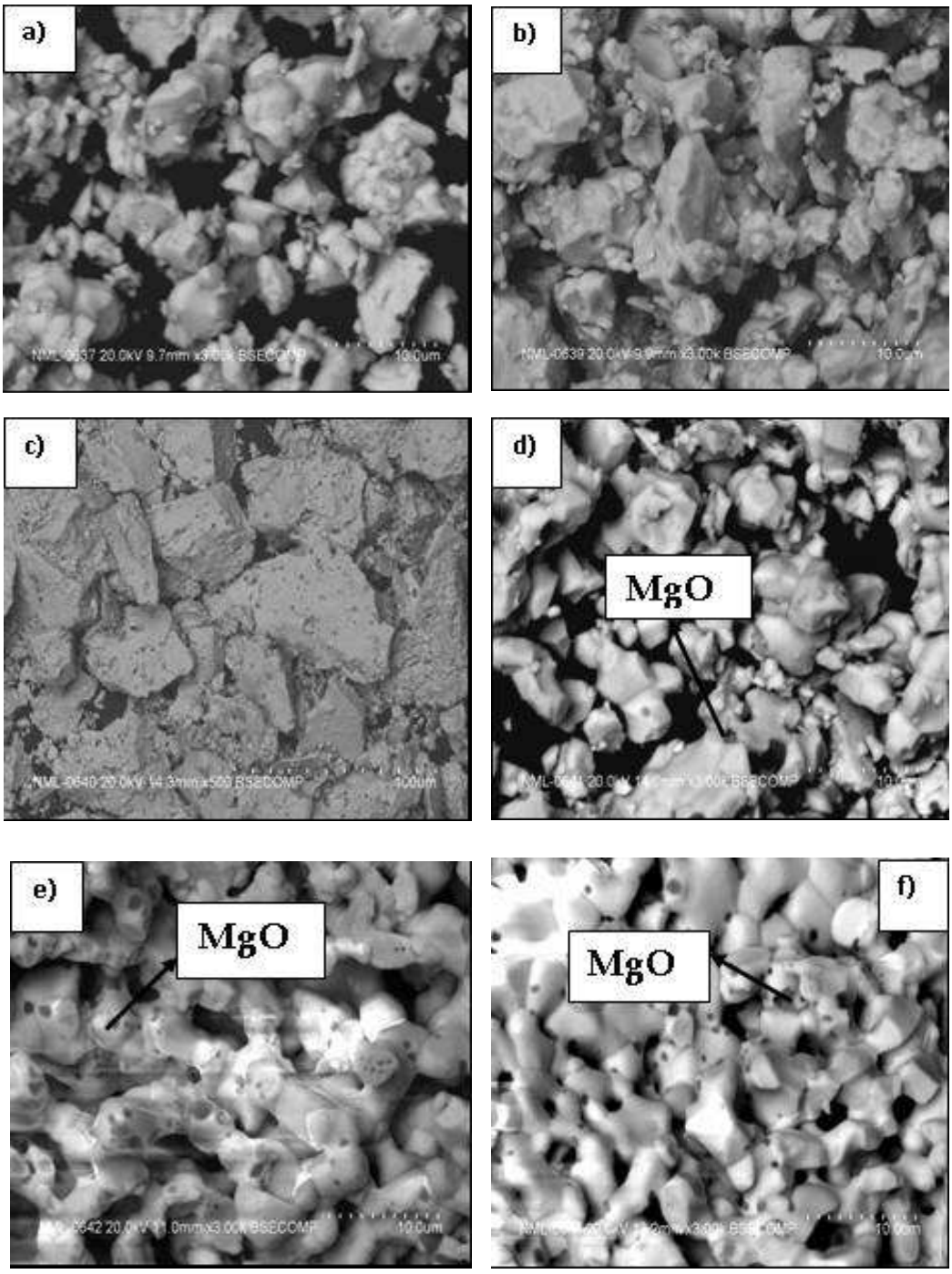

Fig.4.2.5 SEM-EDAX image of a) $La_{0.99}Sr_{0.01}GaO_{3-\delta}$, b) $La_{0.99}Sr_{0.01}Ga_{0.98}Mg_{0.02}O_{3-\delta}$, c) $La_{0.99}Sr_{0.01}Ga_{0.95}Mg_{0.05}O_{3-\delta}$, d) $La_{0.99}Sr_{0.01}Ga_{0.80}Mg_{0.20}O_{3-\delta}$, e) $La_{0.99}Sr_{0.01}Ga_{0.75}Mg_{0.25}O_{3-\delta}$, b) $La_{0.99}Sr_{0.01}Ga_{0.70}Mg_{0.30}O_{3-\delta}$, equilibrated at $1500^{o}C$

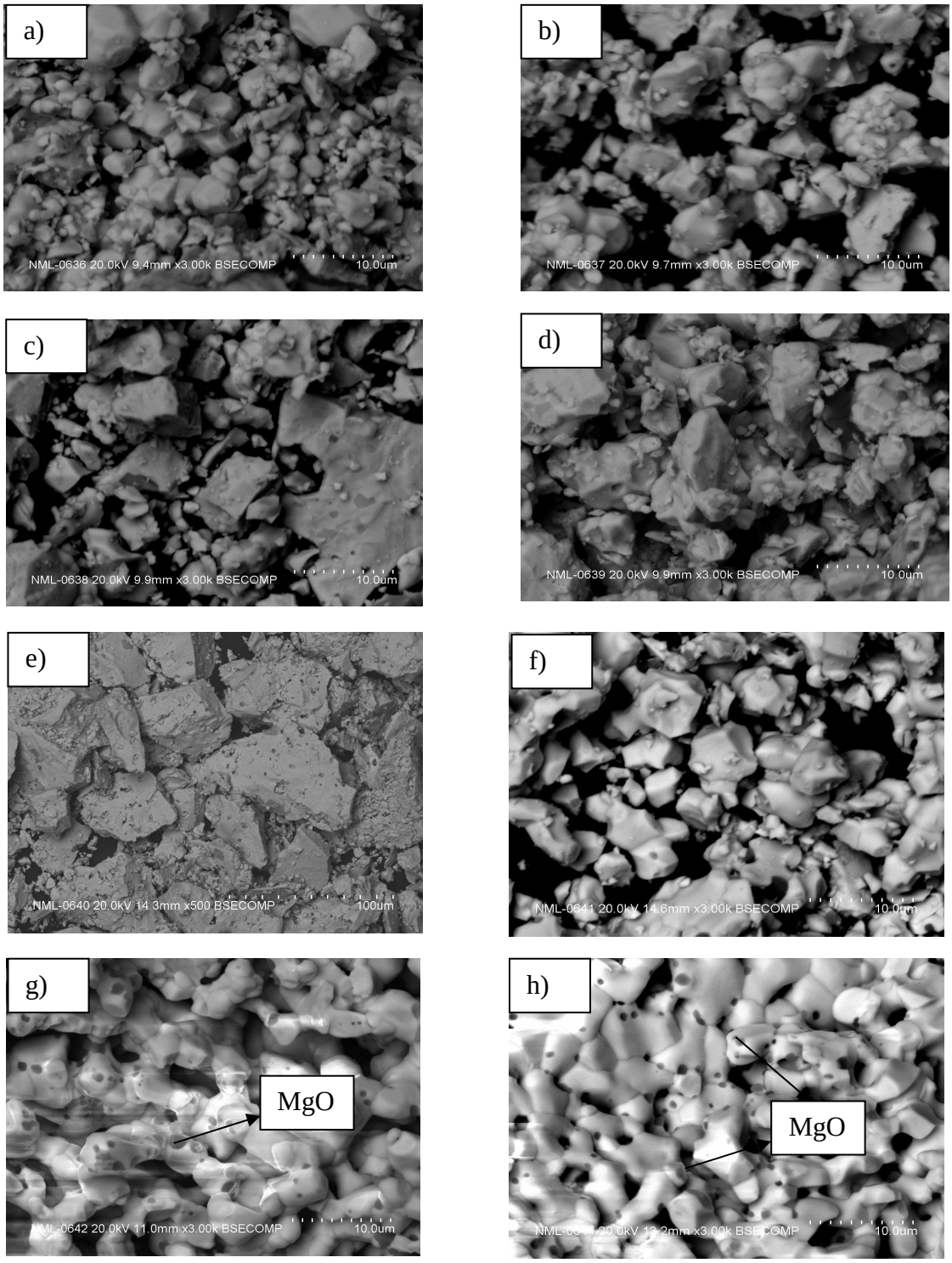

Fig.4.2.6 SEM-EDAX image of a) $La_{0.99}Sr_{0.02}GaO_{3-\delta}$, b) $La_{0.99}Sr_{0.02}Ga_{0.98}Mg_{0.02}O_{3-\delta}$, c) $La_{0.99}Sr_{0.02}Ga_{0.95}Mg_{0.05}O_{3-\delta}$, d) $La_{0.99}Sr_{0.02}Ga_{0.90}Mg_{0.10}O_{3-\delta}$, e) $La_{0.99}Sr_{0.02}Ga_{0.85}Mg_{0.15}O_{3-\delta}$, f) $La_{0.99}Sr_{0.02}Ga_{0.80}Mg_{0.20}O_{3-\delta}$, g) $La_{0.99}Sr_{0.02}Ga_{0.75}Mg_{0.25}O_{3-\delta}$, h) $La_{0.99}Sr_{0.02}Ga_{0.70}Mg_{0.30}O_{3-\delta}$, equilibrated at $1500^{o}C$

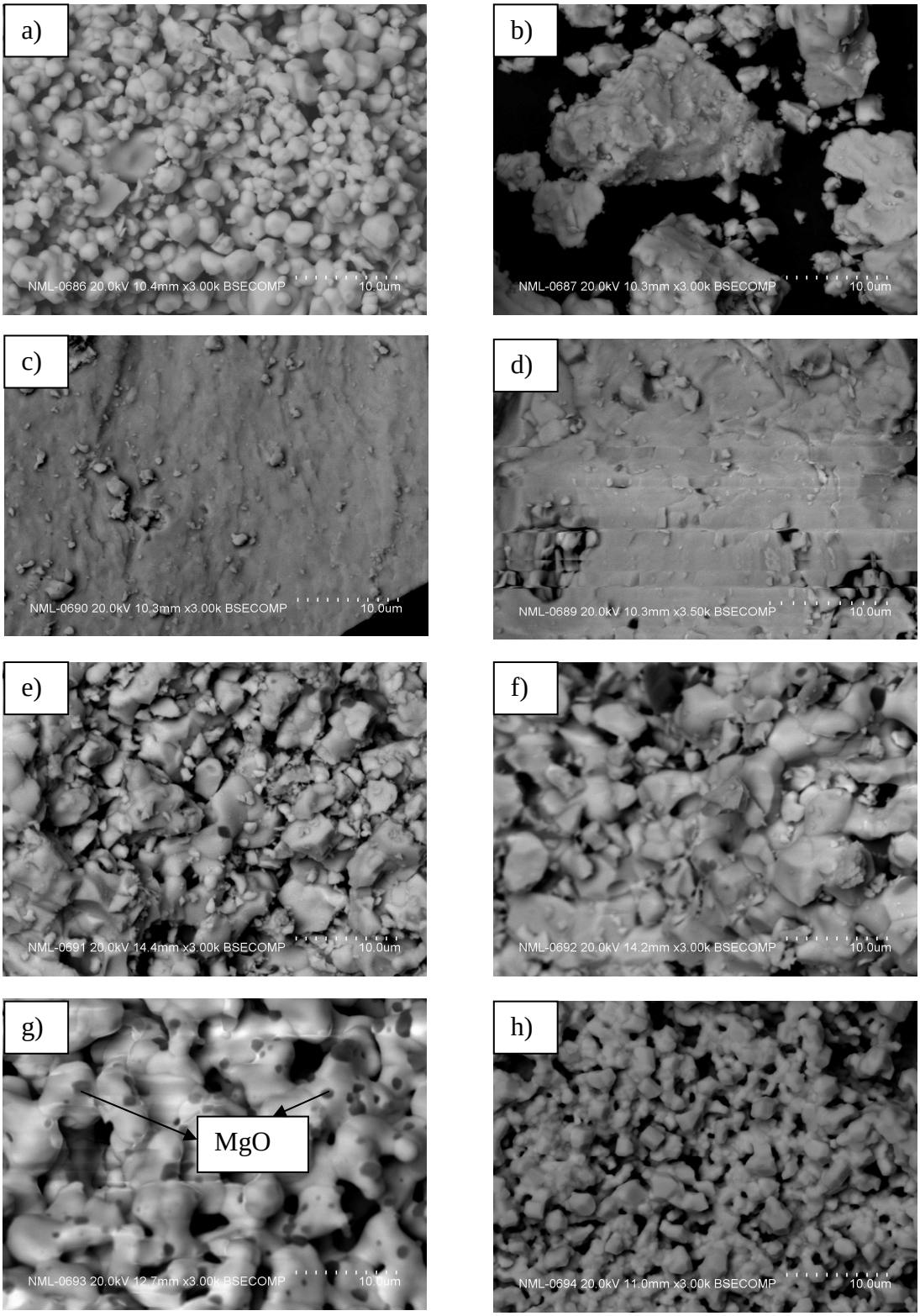

Fig.4.2.7 SEM-EDAX image of a) $La_{0.99}Sr_{0.03}GaO_{3-\delta}$, b) $La_{0.99}Sr_{0.03}Ga_{0.98}Mg_{0.02}O_{3-\delta}$, c) $La_{0.99}Sr_{0.03}Ga_{0.95}Mg_{0.05}O_{3-\delta}$, d) $La_{0.99}Sr_{0.03}Ga_{0.90}Mg_{0.10}O_{3-\delta}$, e) $La_{0.99}Sr_{0.03}Ga_{0.85}Mg_{0.15}O_{3-\delta}$, f) $La_{0.99}Sr_{0.03}Ga_{0.80}Mg_{0.20}O_{3-\delta}$, g) $La_{0.99}Sr_{0.03}Ga_{0.75}Mg_{0.25}O_{3-\delta}$, h) $La_{0.99}Sr_{0.03}Ga_{0.70}Mg_{0.30}O_{3-\delta}$ equilibrated at $1500^{o}C$

The XRD of pure $LaGaO_3$ with varying Sr content (x = 0.01, 0.02, 0.03, 0.04, 0.05, 0.10 and 0.15) is shown in Fig. 4.2.8 and the corresponding scanning electron images are depicted in Fig. 4.2.9. The X-ray diffractograms indicated that the solubility of Sr in pure $LaGaO_3$ appeared to be restricted to 4 mol %. At 5 mol % Sr, traces of the secondary phase $LaSrGa_3O_7$ were identified in the XRD. This was confirmed by scanning electron microscopy, wherein a single phase microstructure was observed up to 4 mol % Sr whereas traces of secondary phase $LaSrGa_3O_7$ (light grey contrast and present within the grains of the perovskite phase) was seen at 5 mol % Sr. The stoichiometry of $LaSrGa_3O_7$ was confirmed by EDAX analysis. $LaSrGa_3O_7$ has a range of stoichiometry varying from $La_{1.5}Sr_{0.5}Ga_3O_7$ to $La_{0.8}Sr_{1.2}Ga_3O_7$ [Majewski et al, b) 2001 and c) 2001]. It was also observed that no secondary phases other than $LaSrGa_3O_7$ appeared up to Sr concentrations of 20 mol % at 1500^{o}C.

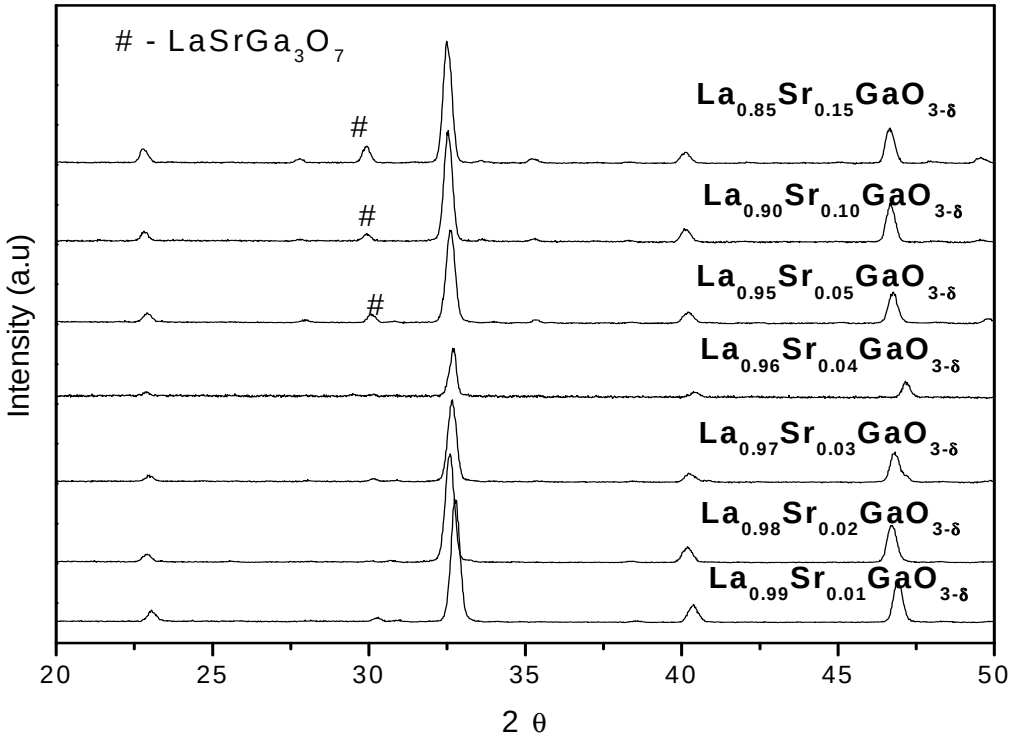

Fig.4.2.8 XRD pattern of $La_{1-x}Sr_xGaO_{3-\delta}$ (x= 0.01-0.15) equilibrated at 1500^{o}C

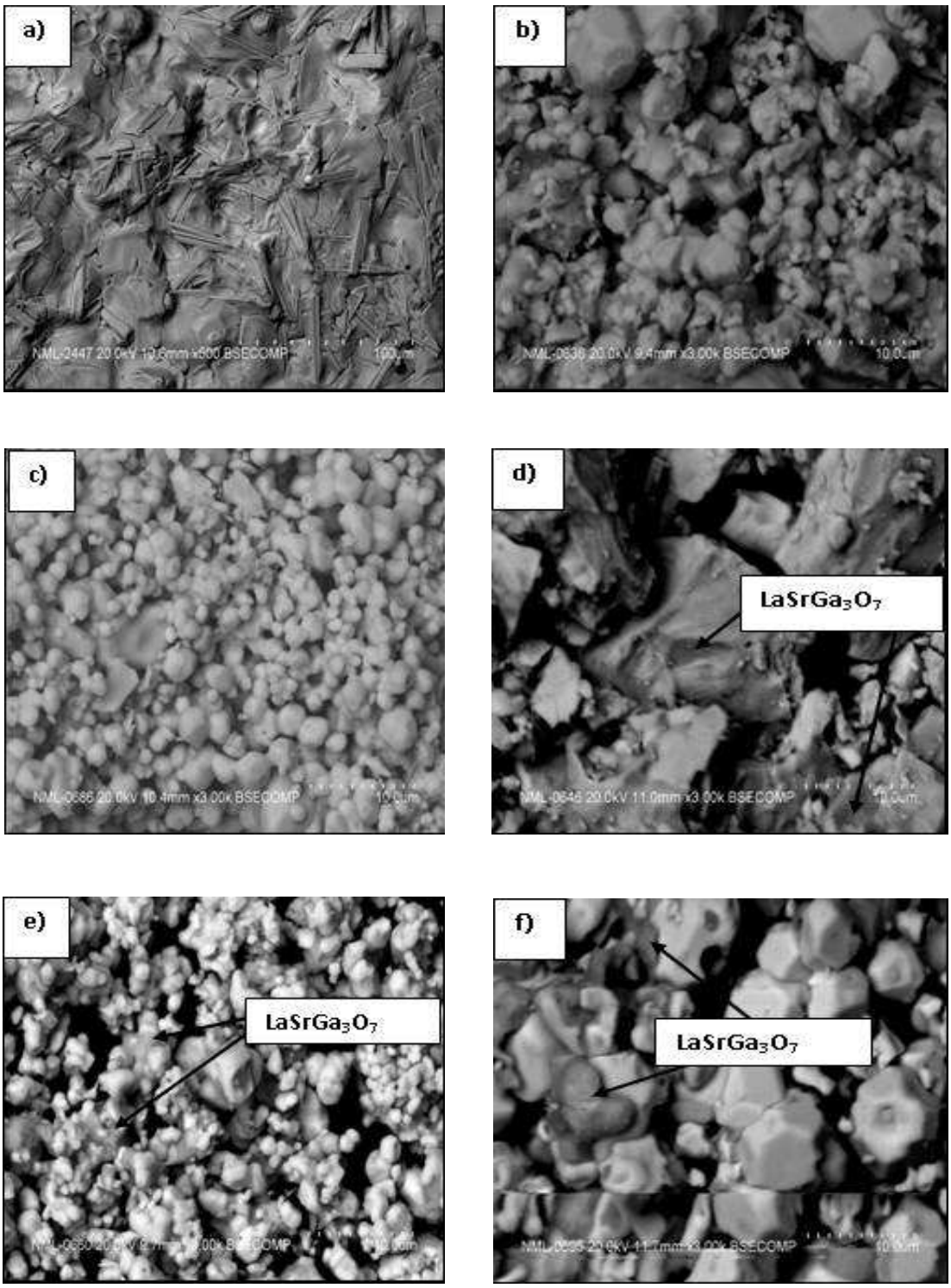

Fig.4.2.9 SEM-EDAX image of a) $La_{0.99}Sr_{0.01}GaO_{3-\delta}$, b) $La_{0.98}Sr_{0.02}GaO_{3-\delta}$, c) $La_{0.97}Sr_{0.03}GaO_{3-\delta}$, d) $La_{0.95}Sr_{0.05}GaO_{3-\delta}$, e) $La_{0.90}Sr_{0.10}GaO_{3-\delta}$, f) $La_{0.85}Sr_{0.15}GaO_{3-\delta}$ equilibrated at $1500^{o}C$

The XRD pattern of $La_{0.95}Sr_{0.05}Ga_{1-y}Mg_yO_{3-\delta}$ (y=0-0.3) as a function of concentration of Mg at the B-site is shown in Fig. 4.2.10 and the corresponding back

scattered electron images are shown in Fig. 4.2.11. It was seen from the XRD results that for a Sr content of 5 mol%, up to 15 mol % Mg, the secondary phase $LaSrGa_3O_7$ was present. However, beyond 15 mol % Mg, the XRD did not show any impurity phases for Mg concentrations of 20, 25 and 30 mol%. However, SEM results indicated that for the 5 mol % Sr sample, as Mg was increased, $LaSrGa_3O_7$ formed as the secondary phase up to 15 mol %Mg. For 20 mol % Mg it existed as pure phase and for 25 and 30 mol % Mg, the MgO phase precipitated. The absence of MgO reflections in the XRD was once again because of its low volume fraction.

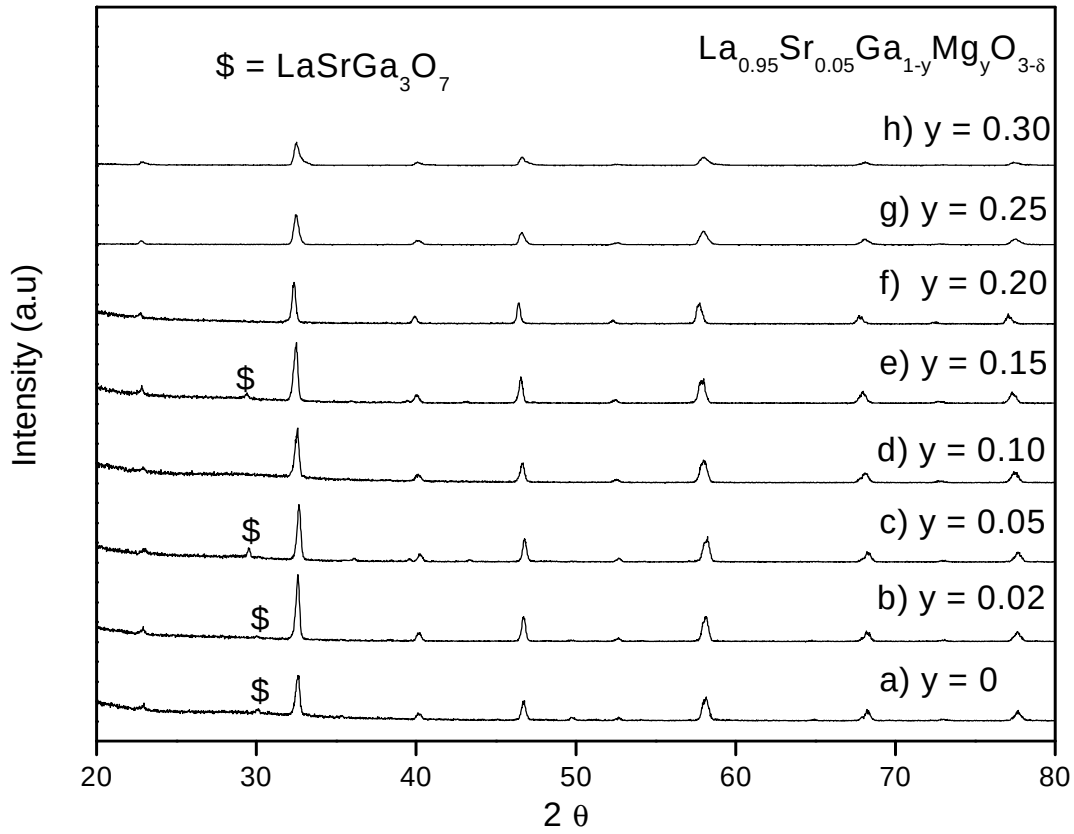

Fig.4.2.10 XRD pattern of $La_{0.95}Sr_{0.05}Ga_{1-y}Mg_yO_{3-\delta}$ (y= 0-0.30) equilibrated at 1500^oC

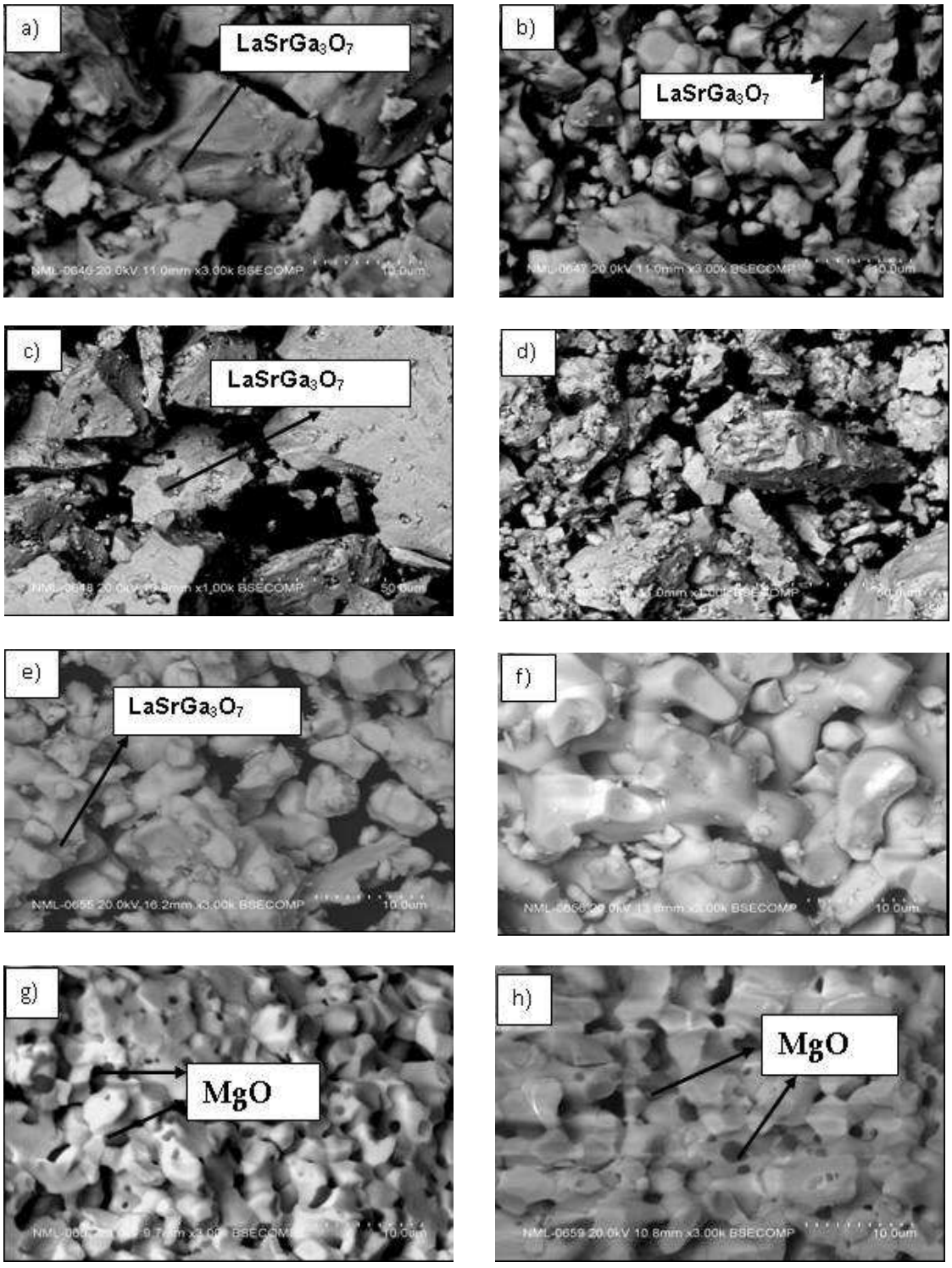

Fig.4.2.11 SEM-EDAX image of a) $La_{0.95}Sr_{0.05}GaO_{3-\delta}$, b) $La_{0.95}Sr_{0.05}Ga_{0.98}Mg_{0.02}O_{3-\delta}$, c) $La_{0.95}Sr_{0.05}Ga_{0.95}Mg_{0.05}O_{3-\delta}$, d) $La_{0.95}Sr_{0.05}Ga_{0.90}Mg_{0.10}O_{3-\delta}$, e) $La_{0.95}Sr_{0.05}Ga_{0.85}Mg_{0.15}O_{3-\delta}$, f) $La_{0.95}Sr_{0.05}Ga_{0.80}Mg_{0.20}O_{3-\delta}$, g) $La_{0.95}Sr_{0.05}Ga_{0.75}Mg_{0.25}O_{3-\delta}$, h) $La_{0.95}Sr_{0.05}Ga_{0.70}Mg_{0.30}O_{3-\delta}$ equilibrated at 1500^{o}C.

The X-ray diffractogram of $La_{0.90}Sr_{0.10}Ga_{1-y}Mg_yO_{3-\delta}$ (y=0-0.3) as a function of concentration of Mg at the B-site is shown in Fig. 4.2.12 and the corresponding scanning electron photographs are shown in Fig. 4.2.13. Here again for the 10 mol % Sr sample, it was seen that the secondary phase $LaSrGa_3O_7$ was present up to 20 mol % of Mg, it existed as a pure perovskite phase for 25 mol % Mg and for further additions of Mg, MgO was present as the second phase. The X-ray diffractogram of $La_{0.85}Sr_{0.15}Ga_{1-y}Mg_yO_{3-\delta}$ (y=0-0.3) as a function of concentration of Mg at the B-site is shown in Fig. 4.2.14 and the corresponding scanning electron micrographs are shown in Fig. 4.2.15.

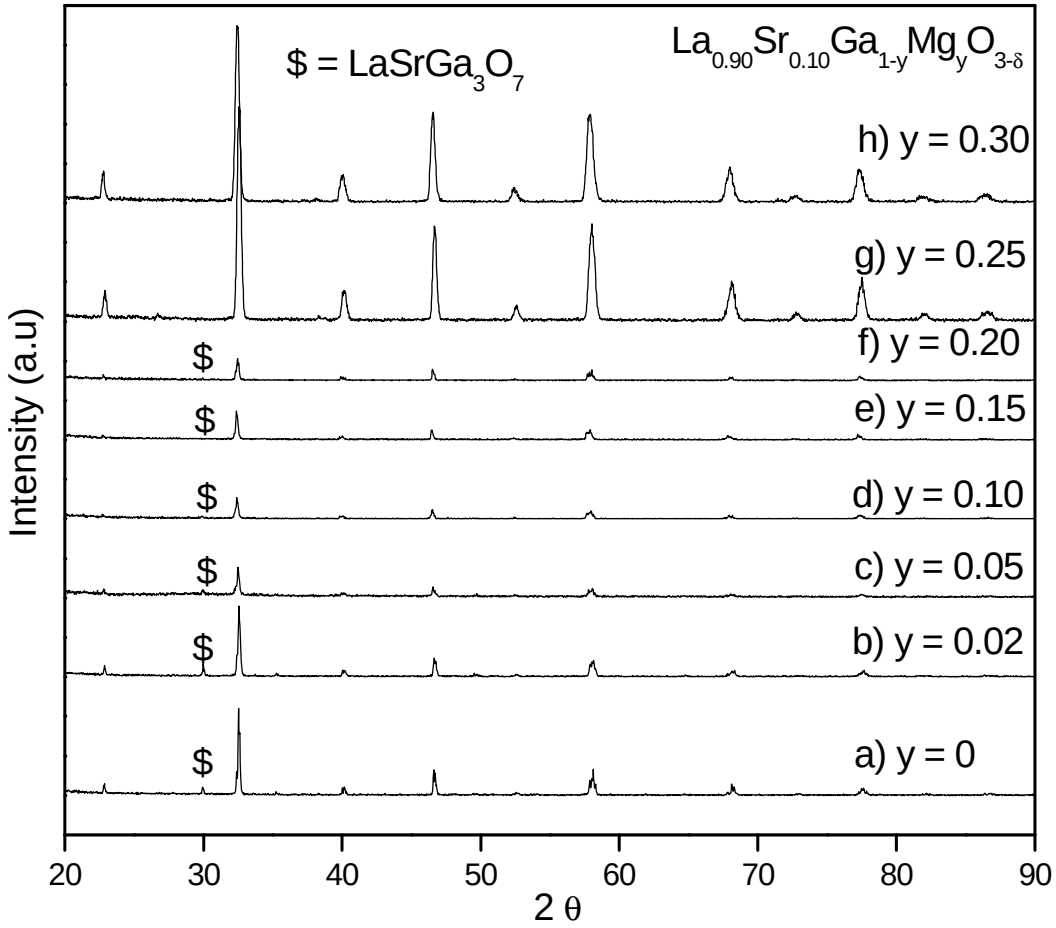

Fig.4.2.12 XRD pattern of $La_{0.90}Sr_{0.10}Ga_{1-y}Mg_yO_{3-\delta}$ (y= 0-0.30) equilibrated at 1500^oC.

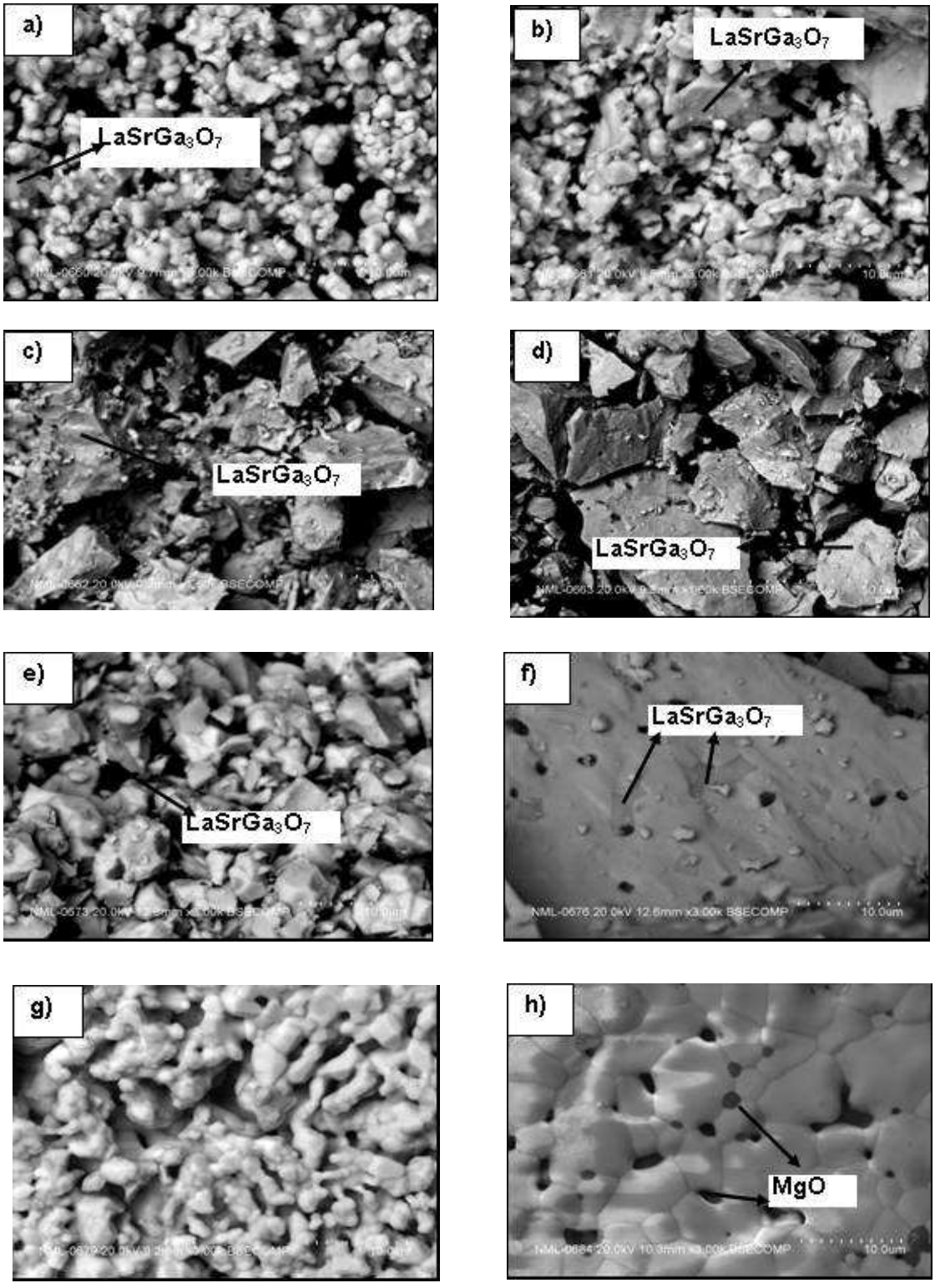

Fig.4.2.13 SEM-EDAX image of a) $La_{0.90}Sr_{0.10}GaO_{3-\delta}$, b) $La_{0.90}Sr_{0.10}Ga_{0.98}Mg_{0.02}O_{3-\delta}$, c) $La_{0.90}Sr_{0.10}Ga_{0.95}Mg_{0.05}O_{3-\delta}$, d) $La_{0.90}Sr_{0.10}Ga_{0.90}Mg_{0.10}O_{3-\delta}$, e) $La_{0.90}Sr_{0.10}Ga_{0.85}Mg_{0.15}O_{3-\delta}$, f) $La_{0.90}Sr_{0.10}Ga_{0.80}Mg_{0.20}O_{3-\delta}$, g) $La_{0.90}Sr_{0.10}Ga_{0.75}Mg_{0.25}O_{3-\delta}$, h) $La_{0.90}Sr_{0.10}Ga_{0.70}Mg_{0.30}O_{3-\delta}$ equilibrated at $1500^{o}C$

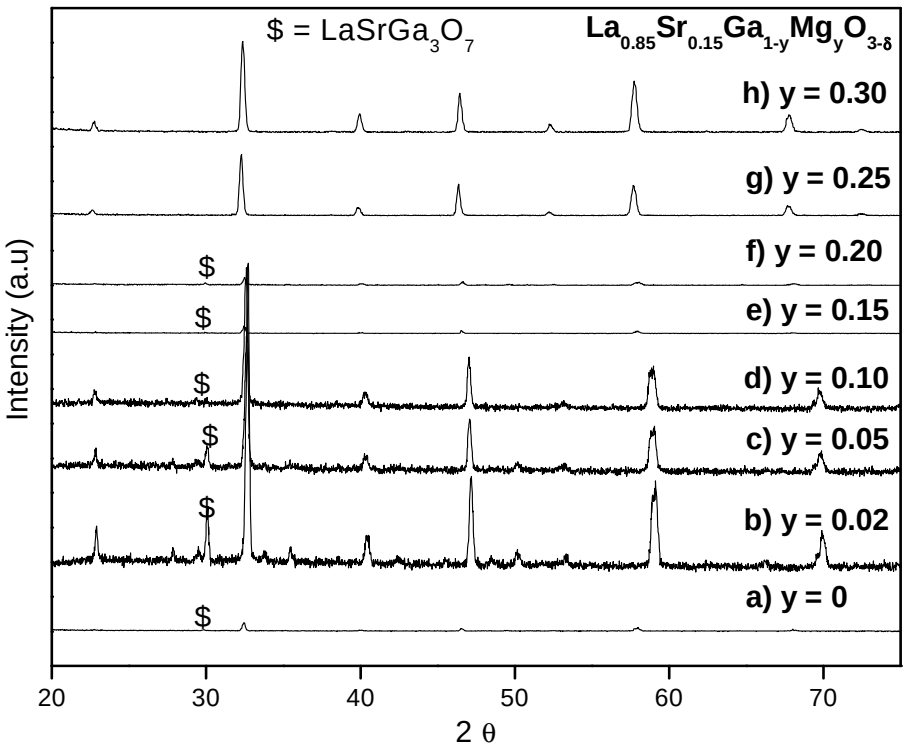

Fig.4.2.14 XRD pattern of $La_{0.85}Sr_{0.15}Ga_{1-y}Mg_yO_{3-\delta}$ (y= 0-0.30) equilibrated at 1500^{o}C.

For the 15 mol % Sr sample, it was seen that the secondary phase $LaSrGa_3O_7$ was present up to 20 mol % of Mg, it existed as a pure perovskite phase for 25 mol % Mg and for further additions of Mg, MgO was present as the second phase. As seen in the SEM micrograph, for Sr content of 15 mol %, the phase $MgGa_2O_4$ was found to be present in addition to MgO at Mg concentration of 30 mol%. For the 20 mol % Sr samples, the perovskite phase was not present as a single phase at any of the Mg compositions from 0 to 30 mol% as shown in Fig. 4.2.16. Up to 25 mol % Mg, the impurity phase $LaSrGa_3O_7$ was present, beyond which for the first time the $LaSrGaO_4$ phase was detected along with the perovskite and MgO phases for the 30 mol % Mg composition.

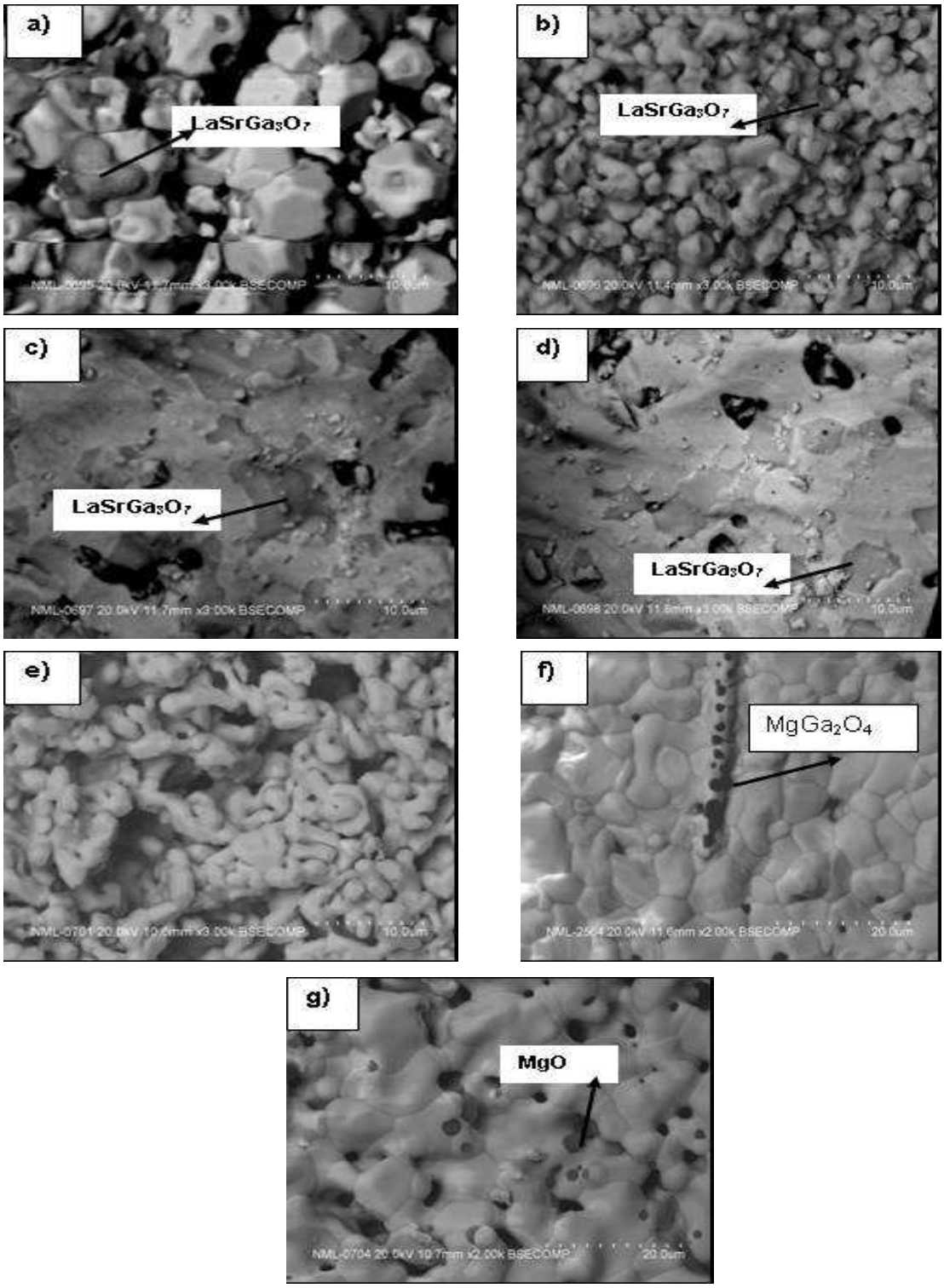

Fig.4.2.15 SEM-EDAX image of a) $La_{0.85}Sr_{0.15}GaO_{3-\delta}$, b) $La_{0.85}Sr_{0.15}Ga_{0.98}Mg_{0.02}O_{3-\delta}$, c) $La_{0.85}Sr_{0.15}Ga_{0.95}Mg_{0.05}O_{3-\delta}$, d) $La_{0.85}Sr_{0.15}Ga_{0.90}Mg_{0.10}O_{3-\delta}$, e) $La_{0.90}Sr_{0.10}Ga_{0.80}Mg_{0.20}O_{3-\delta}$, f) $La_{0.90}Sr_{0.10}Ga_{0.75}Mg_{0.25}O_{3-\delta}$ and g) $La_{0.90}Sr_{0.10}Ga_{0.70}Mg_{0.30}O_{3-\delta}$ equilibrated at 1500^{o}C

$La_{0.85}Sr_{0.15}Ga_{1-y}Mg_{y}O_{3-\delta}$ (y= 0-0.30) equilibrated at 1500^{o}C

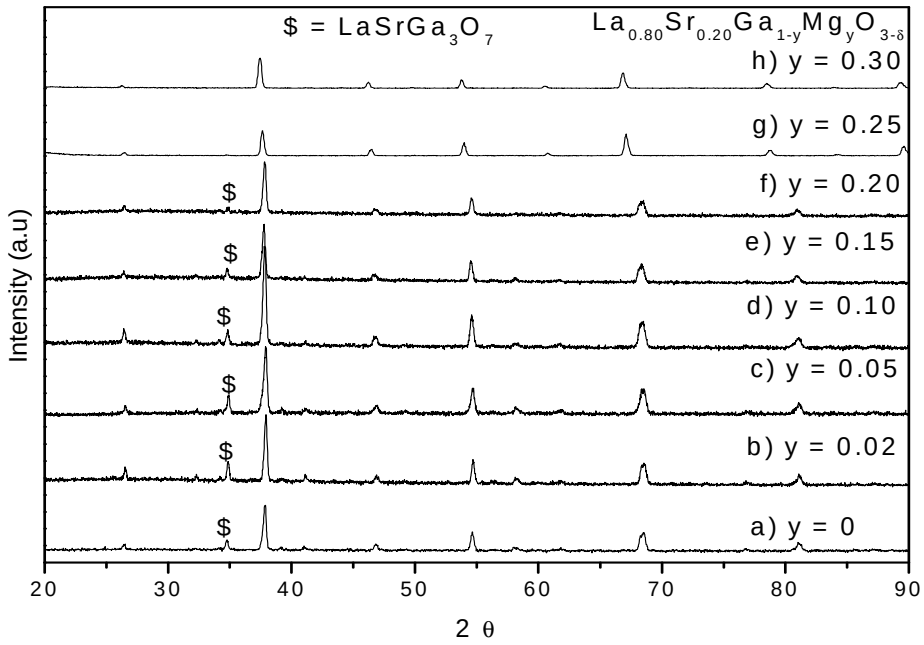

Fig.4.2.16 XRD pattern of $La_{0.80}Sr_{0.20}Ga_{1-y}Mg_yO_{3-\delta}$ (y= 0-0.30) equilibrated at 1500^{o}C.

The lattice parameters (indexed for a cubic perovskite phase) at 1500^{o}C was calculated for all the dopant concentrations. These results are plotted in Fig. 4.2.17 as a function of Mg concentration at the B-sites. It was seen that the lattice parameter increased up to 15 mol % Sr and remained constant or decreased thereafter indicating that the saturation solubility of Sr was around 15 mol %. Similarly, at lower Sr concentrations, the lattice parameter increased with Mg content up to 20 mol % and thereafter remained constant or decreased.

The samples of all the compositions of $La_{1-x}Sr_xGa_{1-y}Mg_yO_{3-(x+y)/2}$ (x=0-0.2, y=0-0.3) were also equilibrated for 24 hours at 1500^{o}C and characterized by XRD, SEM and EDS. These samples after equilibration for 24 h showed extensive mass loss (up to 5 wt %) and Ga vaporization (up to 7 at. % as determined by EDAX bulk analysis). The secondary phases identified by X-ray diffraction and SEM with EDAX is given in Table 4.2.1.

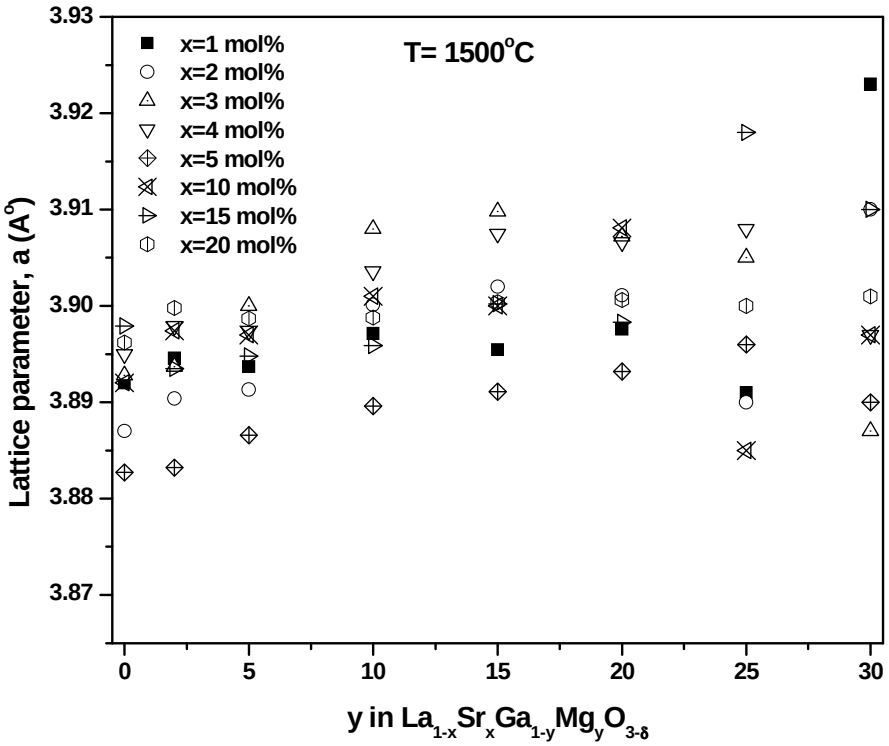

Fig.4.2.17 The lattice parameter of $La_{1-x}Sr_xGa_{1-y}Mg_yO_{3-\delta}$ (where x=0-20 and y= 0-30 mol%) was plotted against Mg content (equilibrated at 1500°C for 8 hrs)

Various impurity phases such as $La_4Ga_2O_9$, $LaSrGaO_4$, $LaSrGa_3O_7$, $MgGa_2O_4$ and MgO were detected along with the perovskite phase. As Sr content increased, the secondary phase $La_4Ga_2O_9$ formed initially and increased in quantity along with the $LaSrGa_3O_7$. However as Sr content increased further, the amount of $La_4Ga_2O_9$ decreased whereas the volume fraction of $LaSrGaO_4$ increased. Similarly, when the Mg content increased, the amount of the secondary phase Ga_2MgO_4 increased and further increase in Mg contents resulted in increasing volume fractions of MgO at the expense of Ga_2MgO_4. The scanning electron micrographs of the evolution of Ga_2MgO_4 and then MgO as the Mg content is increased for a 10 mol % Sr sample sintered for 24 h is shown in Fig. 4.2.18.

Table 4.2.1 The secondary phases identified in $La_{1-x}Sr_xGa_{1-y}Mg_yO_{3-\delta}$ (x=0-0.20 and y=0-0.30) at 1500^oC at 24 hrs.

Compositions	**1500 ^oC, 24 hrs**
	Phases identified by SEM-EDAX
$La_{0.99}Sr_{0.01}GaO_3$	Pure LSGM
$La_{0.99}Sr_{0.01}Ga_{0.98}Mg_{0.02}O_3$	Pure LSGM
$La_{0.99}Sr_{0.01}Ga_{0.95}Mg_{0.05}O_3$	Pure LSGM+ $MgGa_2O_4$
$La_{0.99}Sr_{0.01}Ga_{0.90}Mg_{0.10}O_3$	Pure LSGM+ $MgGa_2O_4$
$La_{0.99}Sr_{0.01}Ga_{0.85}Mg_{0.15}O_3$	Pure LSGM+ $MgGa_2O_4$
$La_{0.99}Sr_{0.01}Ga_{0.80}Mg_{0.20}O_3$	Pure LSGM+ $MgGa_2O_4$
$La_{0.99}Sr_{0.01}Ga_{0.75}Mg_{0.25}O_3$	Pure LSGM+ MgO
$La_{0.99}Sr_{0.01}Ga_{0.70}Mg_{0.30}O_3$	Pure LSGM+ MgO
$La_{0.98}Sr_{0.02}GaO_3$	Pure LSGM+ $LaSrGa_3O_7$
$La_{0.98}Sr_{0.02}Ga_{0.98}Mg_{0.02}O_3$	Pure LSGM+ $LaSrGa_3O_7$+ $MgGa_2O_4$
$La_{0.98}Sr_{0.02}Ga_{0.95}Mg_{0.05}O_3$	Pure LSGM + $MgGa_2O_4$
$La_{0.98}Sr_{0.02}Ga_{0.90}Mg_{0.10}O_3$	Pure LSGM+ $MgGa_2O_4$
$La_{0.98}Sr_{0.02}Ga_{0.85}Mg_{0.15}O_3$	Pure LSGM+ MgO
$La_{0.98}Sr_{0.02}Ga_{0.80}Mg_{0.20}O_3$	Pure LSGM+ MgO
$La_{0.98}Sr_{0.02}Ga_{0.75}Mg_{0.25}O_3$	Pure LSGM+ MgO
$La_{0.98}Sr_{0.02}Ga_{0.70}Mg_{0.30}O_3$	Pure LSGM+ MgO
$La_{0.97}Sr_{0.03}GaO_3$	Pure LSGM
$La_{0.97}Sr_{0.03}Ga_{0.98}Mg_{0.02}O_3$	Pure LSGM+ $LaSrGa_3O_7$+ $MgGa_2O_4$
$La_{0.97}Sr_{0.03}Ga_{0.95}Mg_{0.05}O_3$	Pure LSGM+ $MgGa_2O_4$
$La_{0.97}Sr_{0.03}Ga_{0.90}Mg_{0.10}O_3$	Pure LSGM+ $MgGa_2O_4$
$La_{0.97}Sr_{0.03}Ga_{0.85}Mg_{0.15}O_3$	Pure LSGM+ $MgGa_2O_4$+ MgO
$La_{0.97}Sr_{0.03}Ga_{0.80}Mg_{0.20}O_3$	Pure LSGM+ MgO
$La_{0.97}Sr_{0.03}Ga_{0.75}Mg_{0.25}O_3$	Pure LSGM+ MgO
$La_{0.97}Sr_{0.03}Ga_{0.70}Mg_{0.30}O_3$	Pure LSGM+ MgO
$La_{0.95}Sr_{0.05}GaO_3$	Pure LSGM
$La_{0.95}Sr_{0.05}Ga_{0.98}Mg_{0.02}O_3$	Pure LSGM
$La_{0.95}Sr_{0.05}Ga_{0.95}Mg_{0.05}O_3$	Pure LSGM+ $MgGa_2O_4$
$La_{0.95}Sr_{0.05}Ga_{0.90}Mg_{0.10}O_3$	Pure LSGM
$La_{0.95}Sr_{0.05}Ga_{0.85}Mg_{0.15}O_3$	Pure LSGM+ $MgGa_2O_4$
$La_{0.95}Sr_{0.05}Ga_{0.80}Mg_{0.20}O_3$	Pure LSGM+ MgO
$La_{0.95}Sr_{0.05}Ga_{0.75}Mg_{0.25}O_3$	Pure LSGM+ MgO

$La_{0.95}Sr_{0.05}Ga_{0.70}Mg_{0.30}O_3$	Pure LSGM
$La_{0.90}Sr_{0.10}GaO_3$	Pure LSGM
$La_{0.90}Sr_{0.10}Ga_{0.98}Mg_{0.02}O_3$	Pure LSGM
$La_{0.90}Sr_{0.10}Ga_{0.95}Mg_{0.05}O_3$	Pure LSGM+ $MgGa_2O_4$
$La_{0.90}Sr_{0.10}Ga_{0.90}Mg_{0.10}O_3$	Pure LSGM+ $MgGa_2O_4$
$La_{0.90}Sr_{0.10}Ga_{0.85}Mg_{0.15}O_3$	Pure LSGM+ MgO
$La_{0.90}Sr_{0.10}Ga_{0.80}Mg_{0.20}O_3$	Pure LSGM+ $LaSrGa_3O_7$+ MgO
$La_{0.90}Sr_{0.10}Ga_{0.75}Mg_{0.25}O_3$	Pure LSGM+ MgO
$La_{0.90}Sr_{0.10}Ga_{0.70}Mg_{0.30}O_3$	Pure LSGM+ MgO
$La_{0.85}Sr_{0.15}GaO_3$	Pure LSGM
$La_{0.85}Sr_{0.15}Ga_{0.98}Mg_{0.02}O_3$	Pure LSGM+ $LaSrGa_3O_7$
$La_{0.85}Sr_{0.15}Ga_{0.95}Mg_{0.05}O_3$	Pure LSGM+ $LaSrGa_3O_7$
$La_{0.85}Sr_{0.15}Ga_{0.90}Mg_{0.10}O_3$	Pure LSGM+ $LaSrGa_3O_7$
$La_{0.85}Sr_{0.15}Ga_{0.85}Mg_{0.15}O_3$	Pure LSGM+ $MgGa_2O_4$
$La_{0.85}Sr_{0.15}Ga_{0.80}Mg_{0.20}O_3$	Pure LSGM+ MgO
$La_{0.85}Sr_{0.15}Ga_{0.75}Mg_{0.25}O_3$	Pure LSGM+ MgO
$La_{0.85}Sr_{0.15}Ga_{0.70}Mg_{0.30}O_3$	Pure LSGM+ MgO

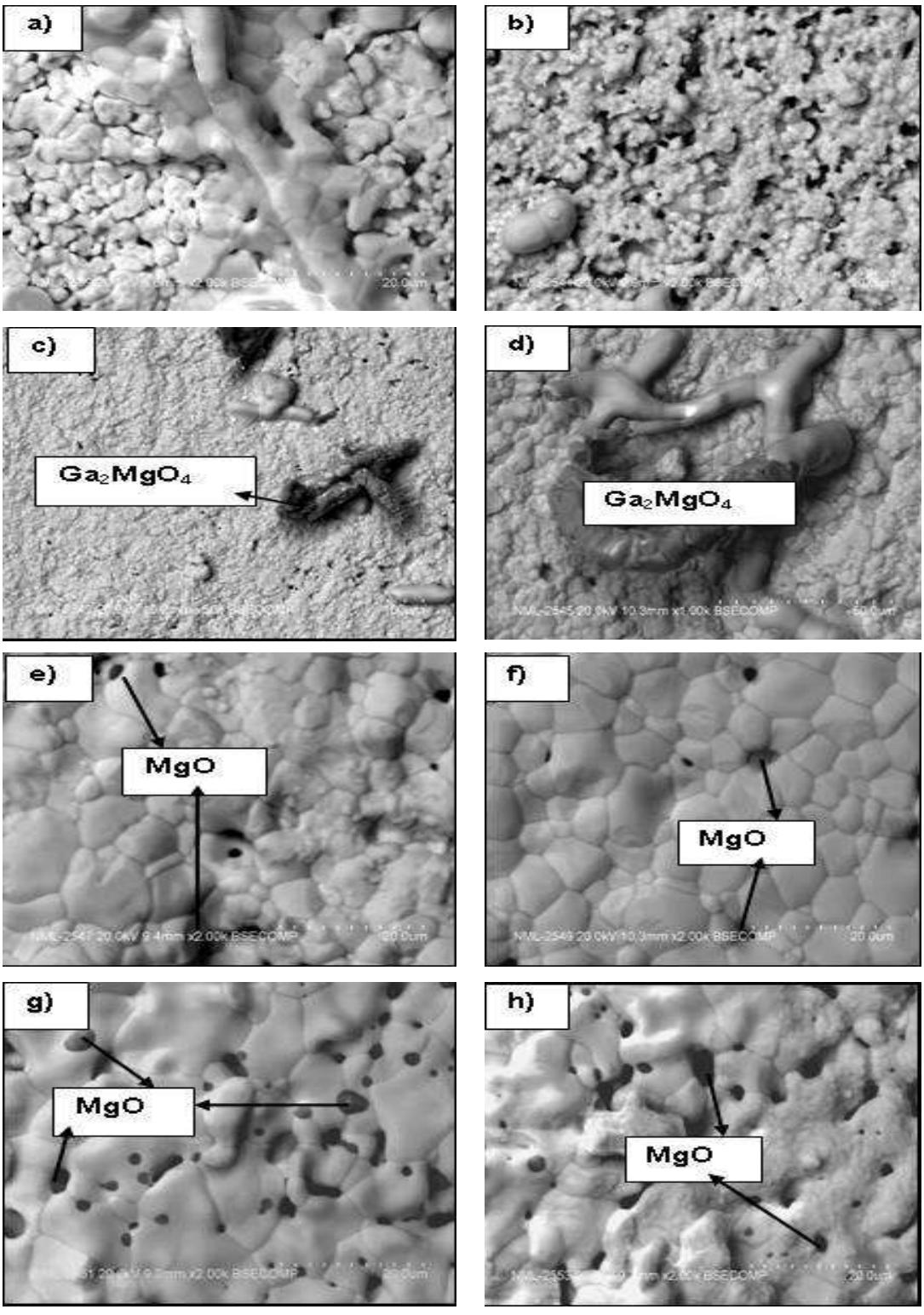

Fig.4.2.18 The scanning electron micrographs showing the evolution of Ga_2MgO_4 and then MgO as the Mg content is increased for a 10 mol % Sr sample sintered at 1500^{o}C for 24 h; a) $La_{0.90}Sr_{0.10}GaO_{3-\delta}$, b) $La_{0.90}Sr_{0.10}Ga_{0.98}Mg_{0.02}O_{3-\delta}$, c) $La_{0.90}Sr_{0.10}Ga_{0.95}Mg_{0.05}O_{3-\delta}$, d) $La_{0.90}Sr_{0.10}Ga_{0.90}Mg_{0.10}O_{3-\delta}$, e) $La_{0.90}Sr_{0.10}Ga_{0.85}Mg_{0.15}O_{3-\delta}$, f) $La_{0.90}Sr_{0.10}Ga_{0.80}Mg_{0.20}O_{3-\delta}$, g) $La_{0.90}Sr_{0.10}Ga_{0.75}Mg_{0.25}O_{3-\delta}$, h) $La_{0.90}Sr_{0.10}Ga_{0.70}Mg_{0.30}O_{3-\delta}$

4.2.2. Phase equilibrium in $La_{1-x}Sr_xGa_{1-y}Mg_yO_{3-\delta}$ at 1500°C

The phase diagram at 1500°C of the hypothetical $LaGaO_3$-$LaSrO_{2.5}$-$LaMgO_{2.5}$ system at the LGO rich corner was constructed based on the phase equilibrium results and is shown in Fig. 4.2.19. Three phase regions of perovskite+$LaSrGa_3O_7$+ $LaSrGaO_4$, perovskite+$LaSrGaO_4$+MgO, perovskite+$La_4Ga_2O_9$+$LaSrGa_3O_7$, perovskite+Ga_2MgO_4+$LaSrGa_3O_7$ and 4-phase regions of perovskite+Ga_2MgO_4 +$LaSrGa_3O_7$ +$LaSrGaO_4$, perovskite+$La_4Ga_2O_9$+$LaSrGa_3O_7$+$LaSrGaO_4$, perovskite +Ga_2MgO_4+$LaSrGa_3O_7$+$LaSrGaO_4$, perovskite+Ga_2MgO_4+$LaSrGa_3O_7$+MgO were also detected. Some of these might correspond to metastable equilibria because of partial Ga vaporization and the consequent change in bulk composition.

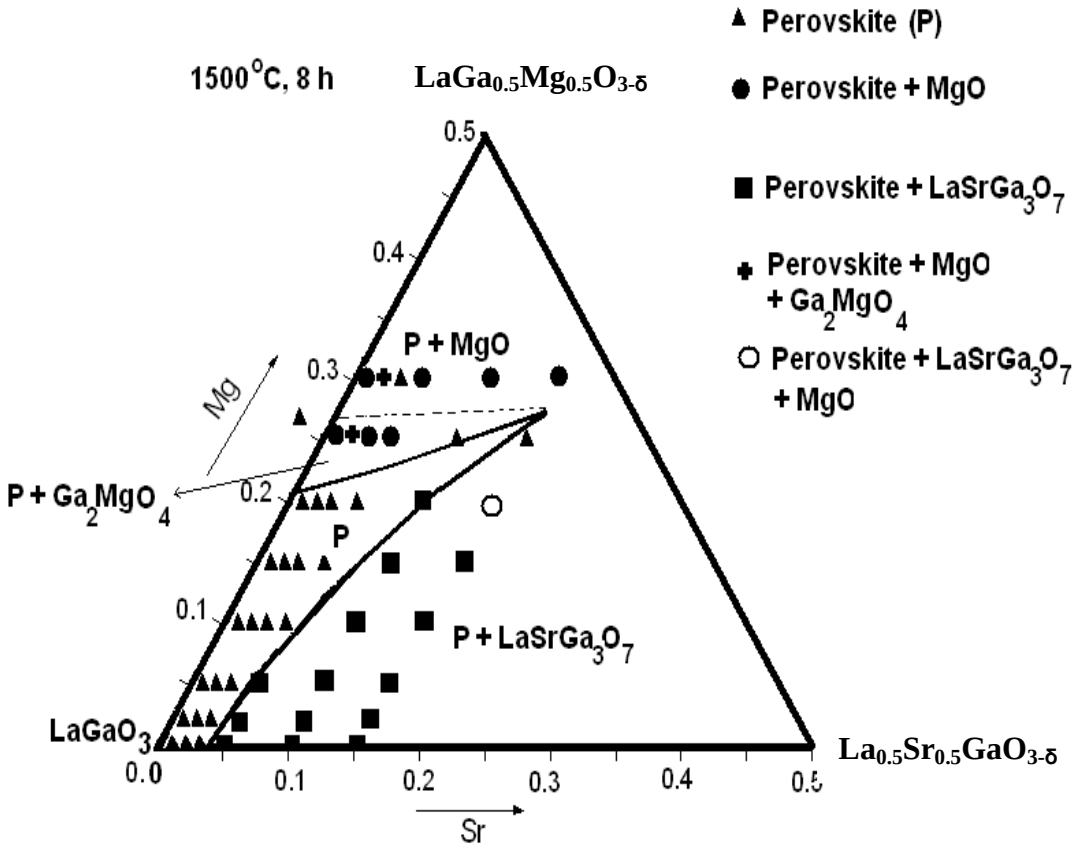

Fig.4.2.19 Range of stability of Sr and Mg-doped lanthanum gallate equilibrated at 1500°C for 8 hours

It was seen that the pure perovskite phase existed over a reasonably large compositional domain in the ternary system. The solubility of Sr at the A-site was found to depend strongly upon the extent of Mg- in the B-site. With an increase in Mg-content, the solubility limit of Sr at 1500°C in the perovskite phase increased from less than 4 mol % in the absence of Mg to about 15 mol % when 25 mol % Mg was present at the B-

site. Conversely, the amount of Sr at the A-site had only a small effect on the solubility limit of Mg in the B-site. The solubility of Mg in the perovskite phase increased marginally from 20 to 25 mol % with the addition of 15 mol % of Sr. With increasing Sr-content, the impurity phases $LaSrGa_3O_7$ and subsequently $LaSrGaO_4$ were found to form whereas with increasing Mg-content, initially Ga_2MgO_4 and later MgO was found to co-exist with the perovskite phase. The range of compositions over which the 2-phase equilibrium perovskite+$LaSrGa_3O_7$ existed as Sr content was increased was broad (up to 20 mol%). However, the two phase region of perovskite+$MgGa_2O_4$ towards the $LaMgO_{2.5}$ end was very narrow. In fact, in many of the cases, the perovskite phase was found to be in equilibrium with MgO.

The phase equilibrium observed in our study at 1500^{o}C is very different from that reported in the literature [Matraszek et al, 2004; Zheng et al, 2004; Huang et al, 1998; Majewski et al, 2001; Rozumek et al, 2003 and Liu et al, 2006]. Firstly, the solubility limits of Sr and Mg were found to be different compared to the earlier reports. Whereas the Sr solubility in pure $LaGaO_3$ reported by Majewski and co-workers [2001] (4-6 mol %) and Matraszek and co-workers [2004] (2 mol%) at 1400^{o}C was somewhat close to that obtained in the present study, the Mg solubility in pure $LaGaO_3$ reported to be only 4-5 mol % by Majewski and co-workers was much lower than that obtained in the present study. However, Matraszek and co-workers [2004] found that the solubility of MgO in pure $LaGaO_3$ at 1400^{o}C was far higher (20 mol %). Sammes et al [1998] reported a maximum solubility of up to 20 mol % Sr and 5 mol % MgO at 1500^{o}C in pure $LaGaO_3$, whereas Chen and Fung reported saturation solubility of ~10% SrO and in excess of 20 mol % MgO. However, when Sr and Mg were simultaneously doped, the solubility limit was reported to be considerably enhanced. Huang et al [1998] reported a solubility of 20 mol % each of Sr and Mg when doubly doped between 800-1500^{o}C. Zheng and co-workers [2004] reported a saturation solubility of 10 mol % SrO and 20 mol % MgO whereas Liu et al [2006] determined a saturation solubility of 25 mol % SrO and more than 28 mol % MgO at 1500^{o}C when doubly doped. When simultaneously doped, the maximum solubility obtained in this study was 15 mol% for SrO and 25 mol% for MgO. These results were in reasonable agreement with that of Huang et al [1998] and Majewski and co-workers [2001] but differ from that of Liu et al [2006].

Huang et al [1998] have shown the perovskite phase to be in equilibrium with $LaSrGa_3O_7$ and $LaSrGaO_4$ between 800-1500^{o}C without the existence of any 2-phase

equilibrium. As seen from the ternary phase diagram of the La_2O_3-Ga_2O_3-SrO system [Rozumek et al, 2003], $LaSrGaO_4$ cannot be in thermodynamic equilibrium with the perovskite phase. This phase possibly formed in their study because of the depletion of Ga shifting the bulk composition to Sr rich regions. The phase equilibria at 1400^{o}C depicted by Majewski and co-workers [2001] and Matraszek et al [2004] are also in disagreement with the present study and were not consistent with phase rules. The 3-phase and 4-phase regions bounding the perovskite phase and the absence of 2-phase regions separating the 3-phase and 4-phase regions shown by them were irreconcilable with the topological rules for quaternary phase diagram construction. Liu et al [2006] depicted the single phase perovskite region to be interrupted by two 2-phase regions LSGM+$LaSrGaO_4$ and LSGM+$LaSaGa_3O_7$ as the Sr content was increased. This was again in contradiction to established rules for phase equilibria. In most of the literature reports on phase equilibria in the $LaGaO_3$-$LaSrO_{2.5}$-$LaMgO_{2.5}$ system, the equilibrium co-existence of $LaSrGaO_4$ with the perovskite phase was projected which was again not consistent with the constituent ternary systems. Our observation was that both, $La_4Ga_2O_9$ as well $LaSrGaO_4$ phases formed when Ga evaporated and the bulk composition shifted to the Sr rich region. It was observed from the ternary La_2O_3-Ga_2O_3-SrO system [Majewski et al 2001] that as Sr was doped to the perovskite phase, the first secondary phase to form would be $LaSrGa_3O_7$ and as Sr content increased further, a 3-phase equilibrium of perovskite+$LaSrGa_3O_7$+$La_4Ga_2O_9$ would result. Further increase of Sr concentration or depletion of Ga below 40-50% would result in the formation of $LaSrGaO_4$ at the expense of the perovskite phase. Similarly, we are of the opinion that the formation of the Ga_2MgO_4 and MgO phases at much lower Mg solubility in the 24 h sintered samples was promoted by the vaporization of Ga from the perovskite phase. It was seen from the phase diagram for the La_2O_3-Ga_2O_3-MgO system [Majewski et al 2001] that as Ga was depleted at close to the perovskite phase composition, the equilibrium shifted towards the perovskite+$MgGa_2O_4$+MgO three phase equilibrium, followed by a small composition range in which the perovskite+MgO equilibrium existed and thereafter to the perovskite+MgO+$La_4Ga_2O_9$ equilibrium. All the 2, 3 and 4 phase combinations obtained for 24 hours of equilibration at 1500^{o}C conformed to the sequence of phase evolution that would result from Ga evaporation. A plot of the mass loss and Ga loss determined from EDAX bulk analysis for LSGM9182 subjected to various times of equilibration at 1500^{o}C is shown

in Fig. 4.2.20. It was seen that for times of equilibration beyond 8 hours, substantial Ga vaporization and consequent mass loss occurred.

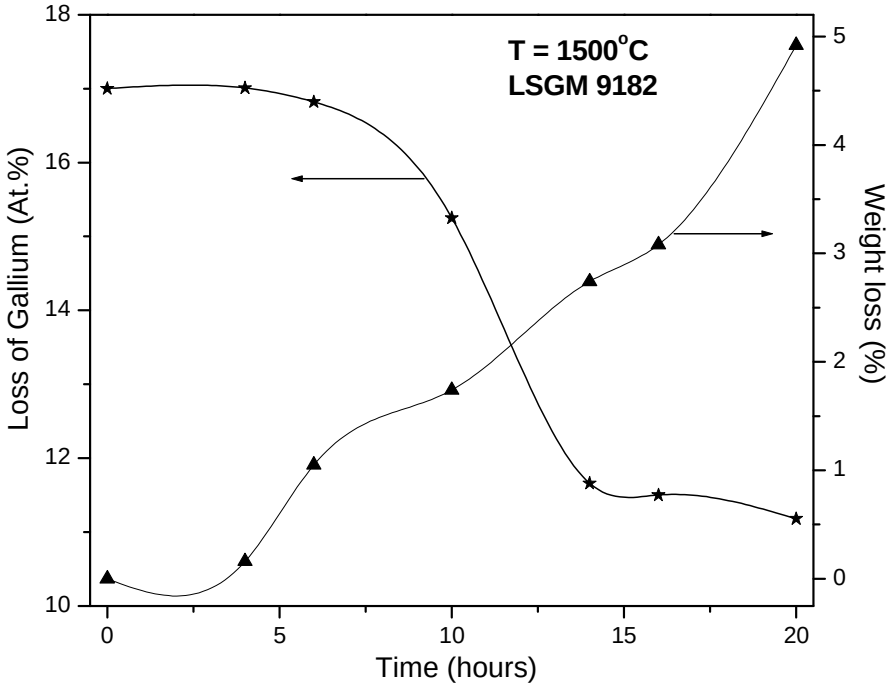

Fig.4.2.20 A plot of the mass loss and Ga loss determined from EDAX bulk analysis for LSGM9182 subjected to various times of equilibration at 1500°C

4.2.3. Phase purity, Morphology and Phase equilibrium in $La_{1-x}Sr_xGa_{1-y}Mg_yO_{3-\delta}$ at 700°C

The results of the XRD and the corresponding back scattered electron images for pure $LaGaO_3$ with varying Sr concentration and with varying Mg concentrations are given in Figs. 4.2.21 - 4.2.24. It was seen that the solubility of Sr and Mg in pure $LaGaO_3$ had reduced at 700°C compared to that observed at 1500°C. At 700°C, the saturation solubility of Sr and Mg in the perovskite phase was found to be 4 mol % and 15 mol % respectively. The X-ray diffractograms and the corresponding microstructures for $La_{0.98}Sr_{0.02}Ga_{1-y}Mg_yO_{3-\delta}$ $La_{0.97}Sr_{0.03}Ga_{1-y}Mg_yO_{3-\delta}$, $La_{0.96}Sr_{0.04}Ga_{1-y}Mg_yO_{3-\delta}$, $La_{0.95}Sr_{0.05}Ga_{1-y}Mg_yO_{3-\delta}$, $La_{0.90}Sr_{0.1`0}Ga_{1-y}Mg_yO_{3-\delta}$, $La_{0.85}Sr_{0.15}Ga_{1-y}Mg_yO_{3-\delta}$ and $La_{0.95}Sr_{0.05}Ga_{1-y}Mg_yO_{3-\delta}$ are depicted in Figs.4.2.25 - 4.2.38 respectively. No secondary phase formation was observed for varying Sr-content up to 4 mol% with varying Mg content in the B-site. While increasing the Sr-content, a similar trend in the solubility of Sr varying with Mg content was also observed at lower temperatures, the overall solubility limits were found to decrease with temperature. The combined maximum solubility of Sr and Mg were found to be 10 and 15 mol % respectively at 700°C when simultaneously doped. Other than the solubility getting restricted in the

ternary compositions, the overall phase relations at 700°C was similar to that observed at 1500°C. With increasing Sr-content, the impurity phases $LaSrGa_3O_7$ was found to form whereas with increasing Mg-content, initially $MgGa_2O_4$ and later MgO were found to co-exist with the perovskite phase.

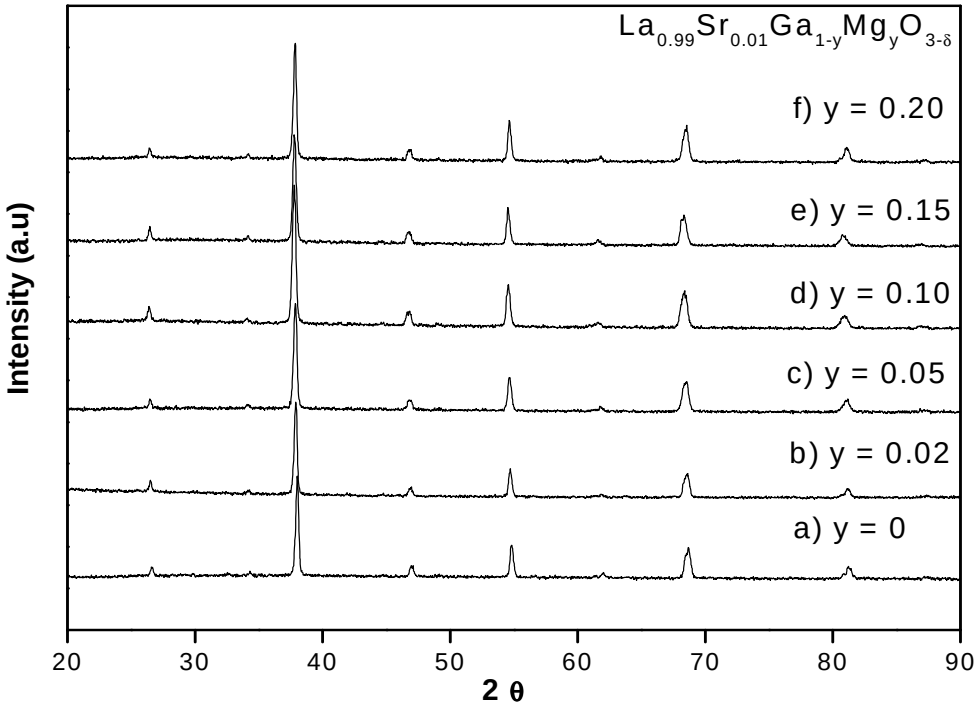

Fig.4.2.21 XRD pattern of $La_{0.99}Sr_{0.01}Ga_{1-y}Mg_yO_{3-\delta}$ (y= 0-0.20) equilibrated at 700°C for 720 hrs.

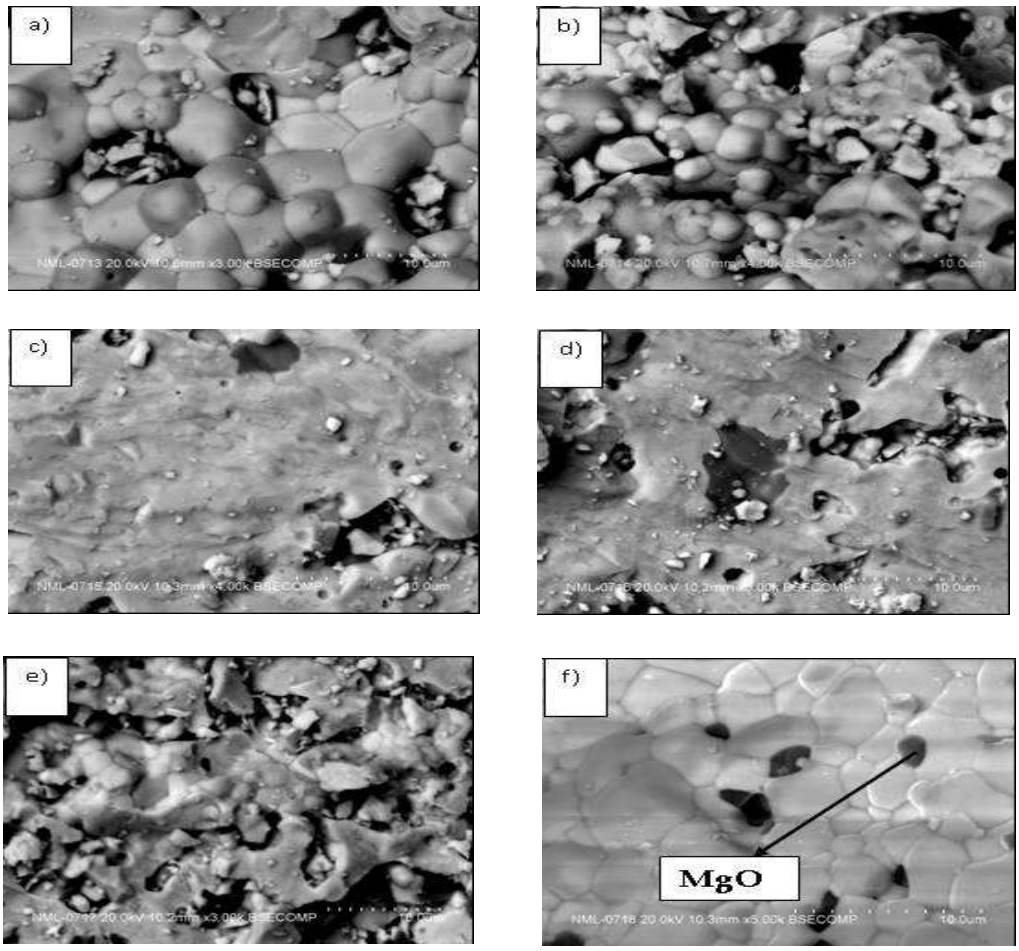

Fig.4.2.22 SEM-EDAX image of a) $La_{0.99}Sr_{0.01}GaO_{3-\delta}$, b) $La_{0.99}Sr_{0.01}Ga_{0.98}Mg_{0.02}O_{3-\delta}$, c) $La_{0.99}Sr_{0.01}Ga_{0.95}Mg_yO_{3-\delta}$, d) $La_{0.99}Sr_{0.01}Ga_{0.90}Mg_{0.10}O_{3-\delta}$, e) $La_{0.99}Sr_{0.01}Ga_{0.85}Mg_{y0.15}O_{3-\delta}$, f) $La_{0.99}Sr_{0.01}Ga_{0.80}Mg_{0.20}O_{3-\delta}$ equilibrated at 700^{o}C for 720 hrs

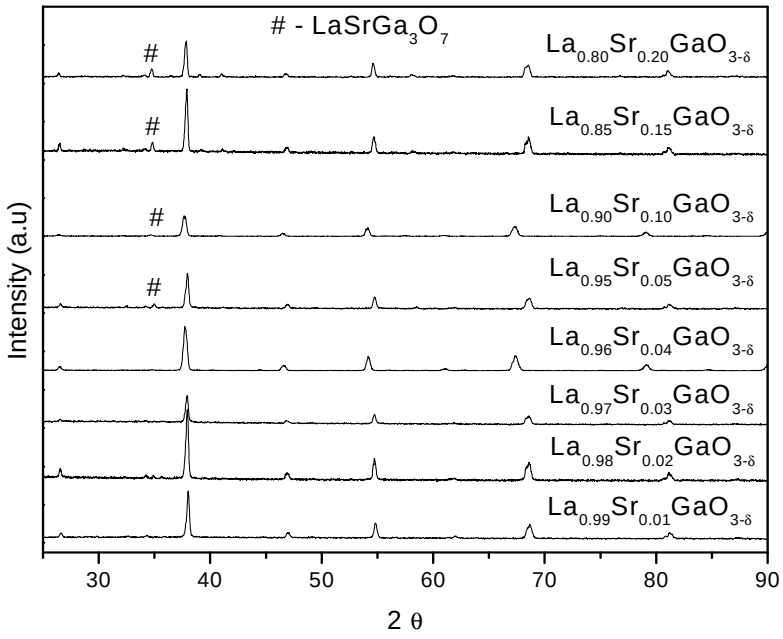

Fig.4.2.23 XRD pattern of $La_{1-x}Sr_xGaO_{3-\delta}$ (x= 0-0.15) equilibrated at 700^{o}C for 720 hrs

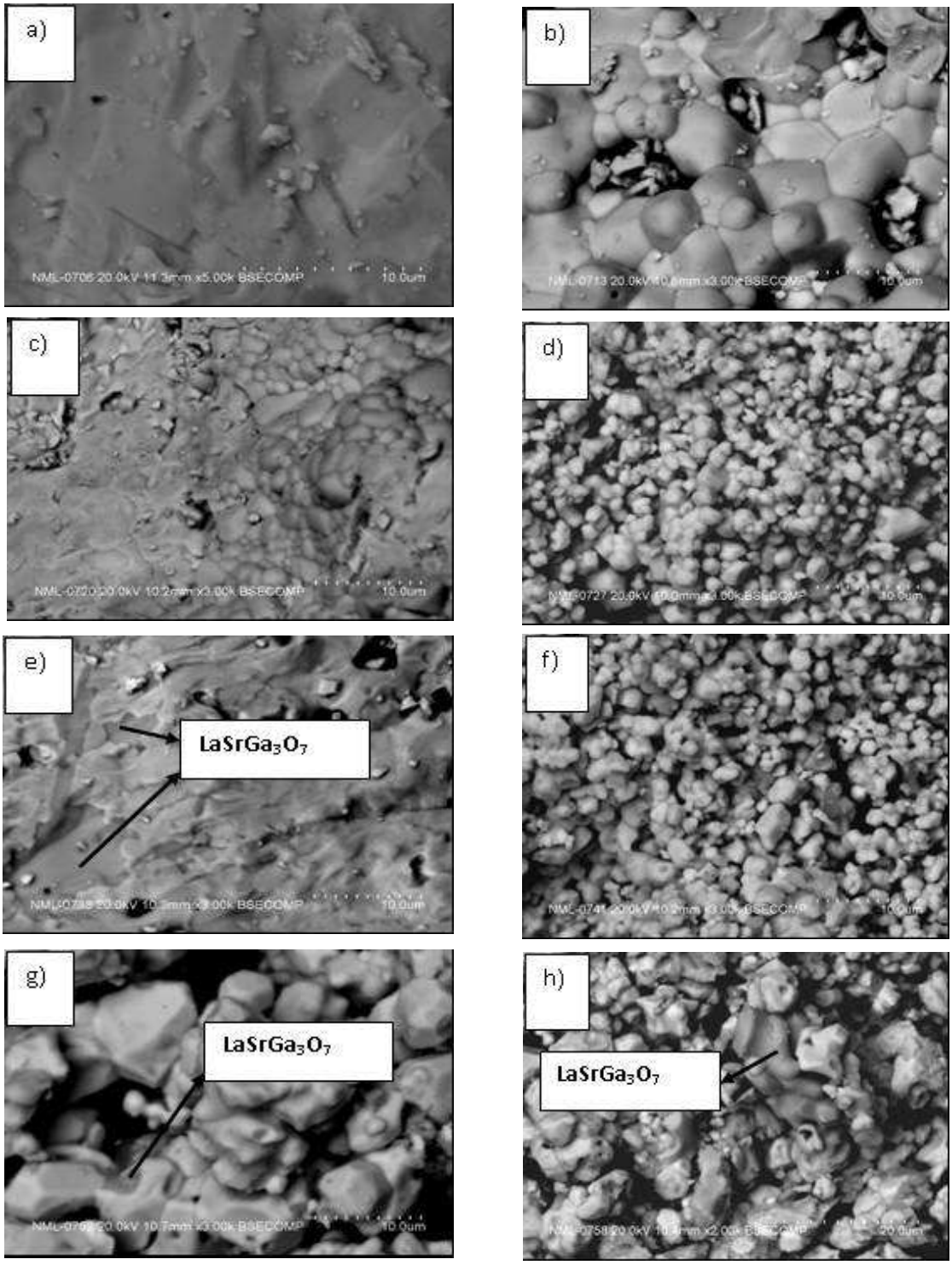

Fig.4.2.24 SEM-EDAX image of a) $La_{0.99}Sr_{0.01}GaO_{3-\delta}$, b) $La_{0.98}Sr_{0.02}GaO_{3-\delta}$, c) $La_{0.97}Sr_{0.03}GaO_{3-\delta}$, d) $La_{0.96}Sr_{0.04}GaO_{3-\delta}$, e) $La_{0.95}Sr_{0.05}GaO_{3-\delta}$, f) $La_{0.90}Sr_{0.10}GaO_{3-\delta}$, g) $La_{0.85}Sr_{0.15}GaO_{3-\delta}$ and g) $La_{0.80}Sr_{0.20}GaO_{3-\delta}$ equilibrated at 700^{o}C for 720 hrs.

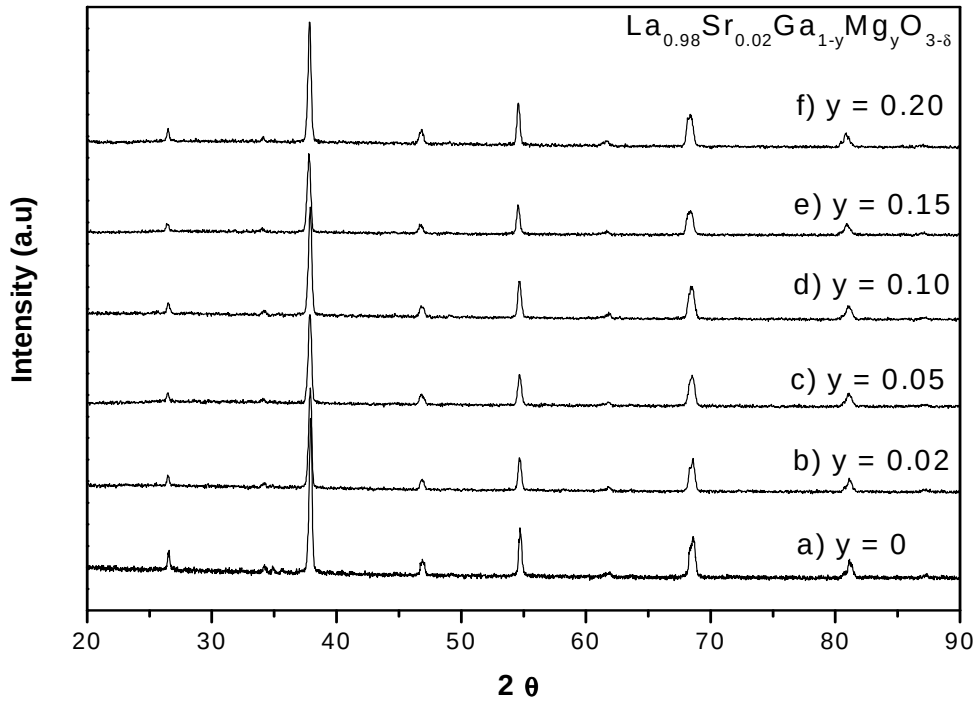

Fig.4.2.25 XRD pattern of $La_{0.98}Sr_{0.02}Ga_{1-y}Mg_yO_{3-\delta}$ (y= 0-0.20) equilibrated at 700^oC for 720 hrs.

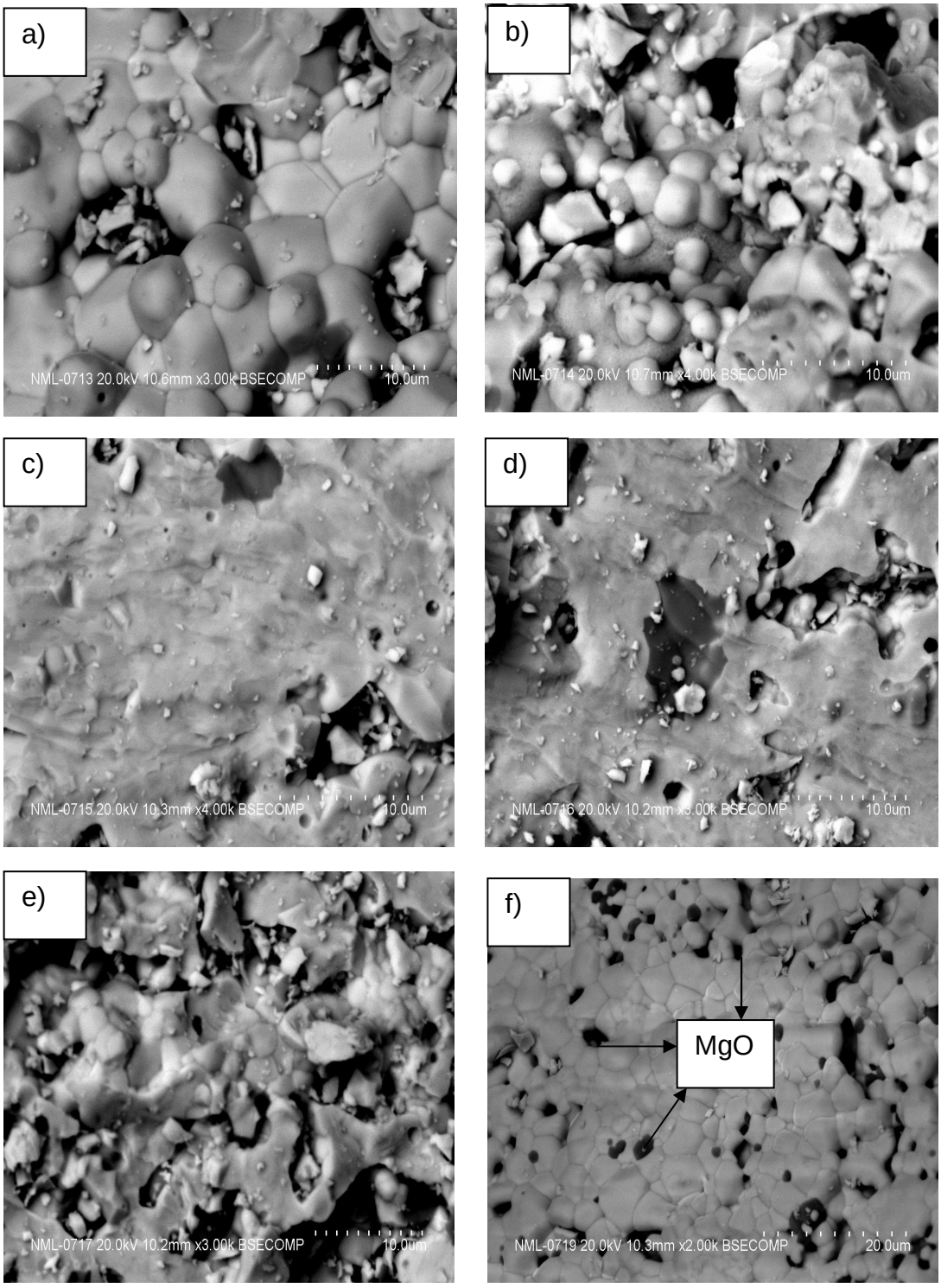

Fig.4.2.26 SEM-EDAX image of a) $La_{0.98}Sr_{0.02}GaO_{3-\delta}$, b) $La_{0.98}Sr_{0.02}Ga_{0.98}Mg_{0.02}O_{3-\delta}$, c) $La_{0.98}Sr_{0.02}Ga_{0.95}Mg_{y}O_{3-\delta}$, d) $La_{0.98}Sr_{0.02}Ga_{0.90}Mg_{0.10}O_{3-\delta}$, e) $La_{0.98}Sr_{0.02}Ga_{0.85}Mg_{y0.15}O_{3-\delta}$, f) $La_{0.98}Sr_{0.02}Ga_{0.80}Mg_{0.20}O_{3-\delta}$ equilibrated at $700^{o}C$ for 720 hrs.

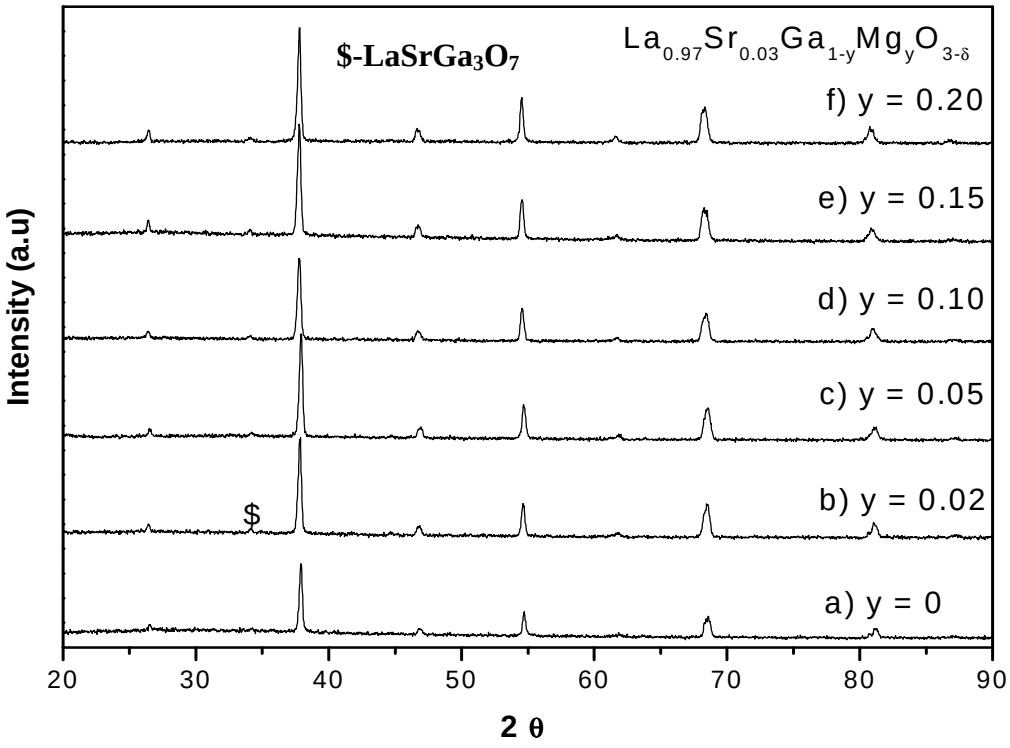

Fig. 4.2.27 XRD pattern of $La_{0.97}Sr_{0.03}Ga_{1-y}Mg_yO_{3-\delta}$ (y= 0-0.20) equilibrated at 700^oC for 720 hrs.

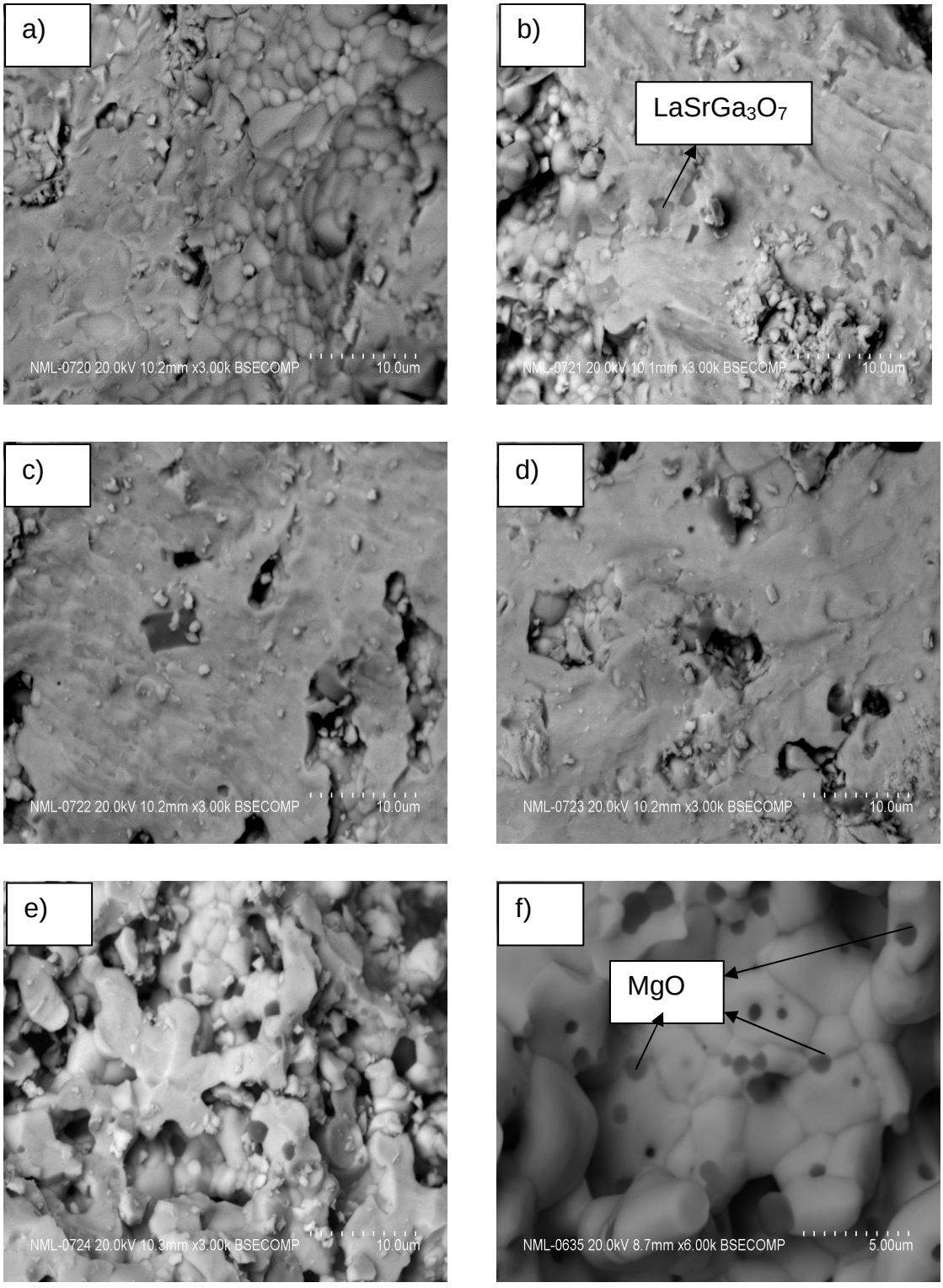

Fig.4.2.28 SEM-EDAX image of a) $La_{0.97}Sr_{0.03}GaO_{3-\delta}$, b) $La_{0.97}Sr_{0.03}Ga_{0.98}Mg_{0.02}O_{3-\delta}$, c) $La_{0.97}Sr_{0.03}Ga_{0.95}Mg_{y}O_{3-\delta}$, d) $La_{0.97}Sr_{0.03}Ga_{0.90}Mg_{0.10}O_{3-\delta}$, e) $La_{0.97}Sr_{0.03}Ga_{0.85}Mg_{y0.15}O_{3-\delta}$, f) $La_{0.97}Sr_{0.03}Ga_{0.80}Mg_{0.20}O_{3-\delta}$ equilibrated at 700^{o}C for 720 hrs.

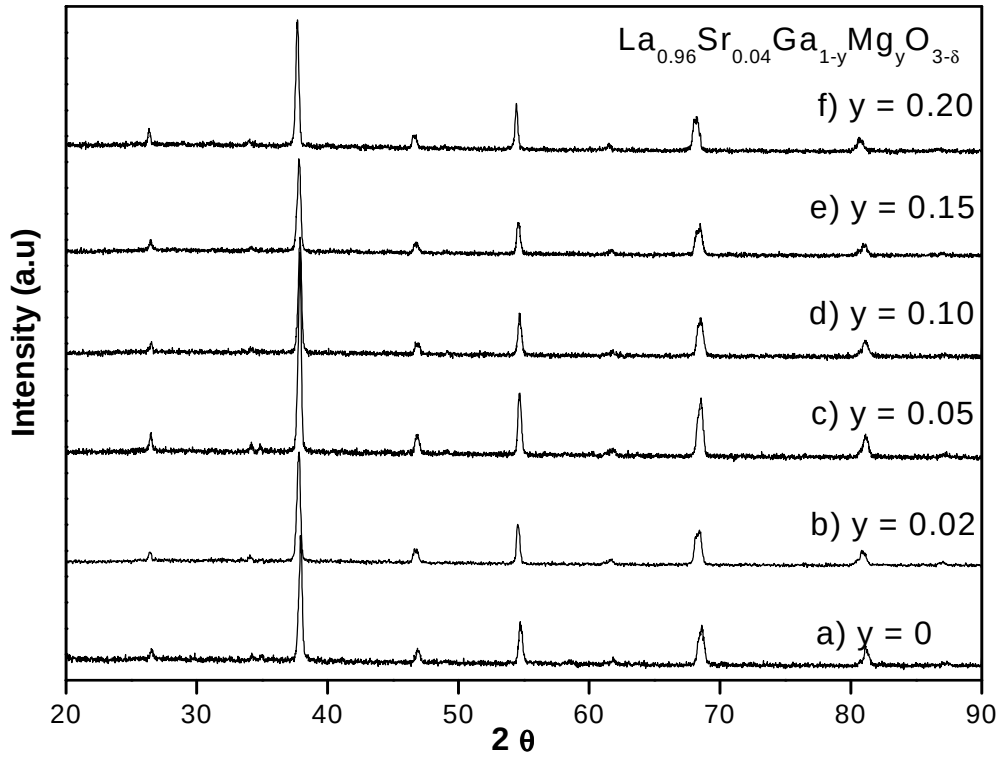

Fig.4.2.29 XRD pattern of $La_{0.96}Sr_{0.04}Ga_{1-y}Mg_yO_{3-\delta}$ (y= 0-0.20) equilibrated at 700^oC for 720 hrs

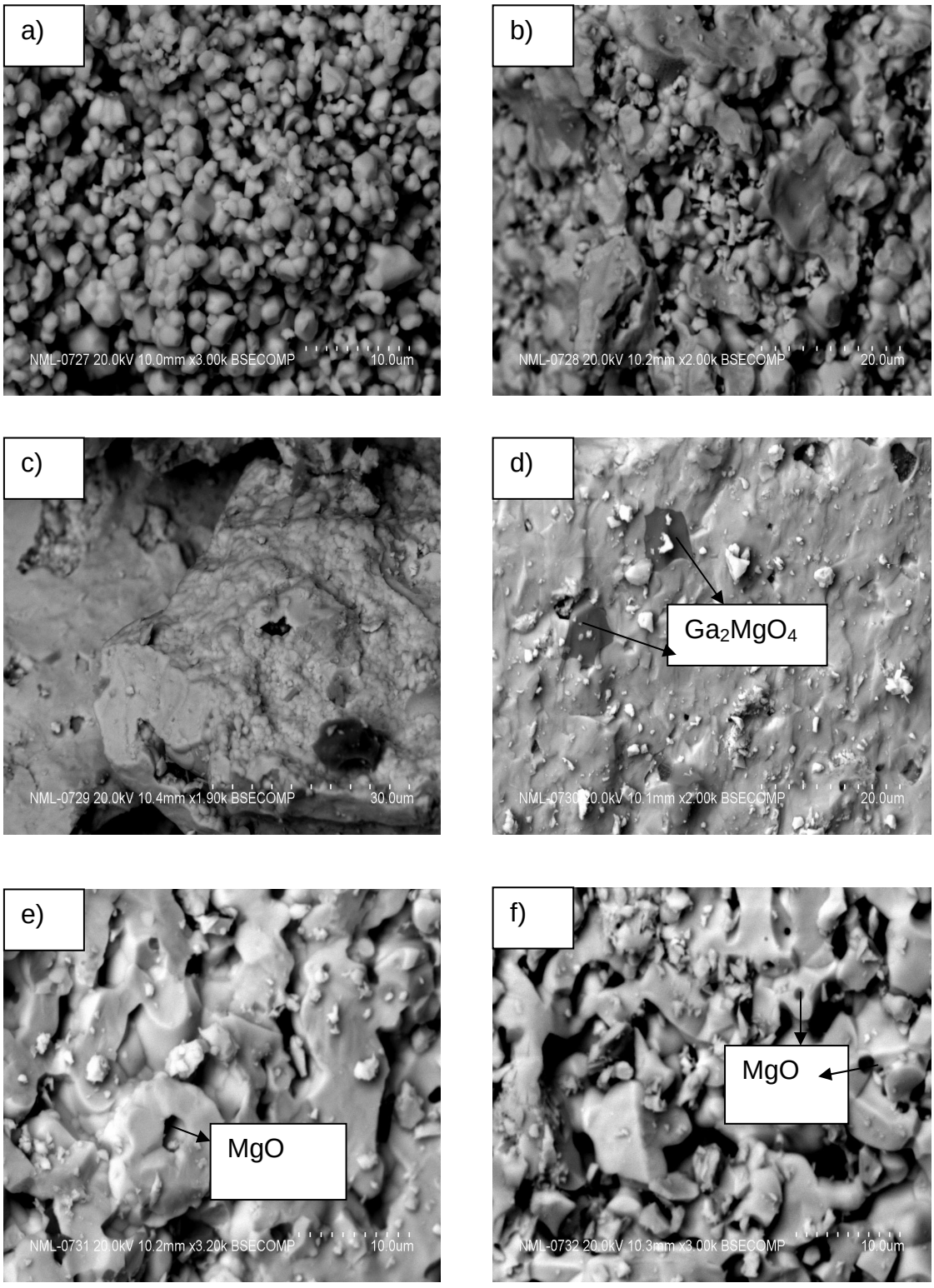

Fig.4.2.30 SEM-EDAX image of a) $La_{0.96}Sr_{0.04}GaO_{3-\delta}$, b) $La_{0.96}Sr_{0.04}Ga_{0.98}Mg_{0.02}O_{3-\delta}$, c) $La_{0.96}Sr_{0.04}Ga_{0.95}Mg_{y}O_{3-\delta}$, d) $La_{0.96}Sr_{0.04}Ga_{0.90}Mg_{0.10}O_{3-\delta}$, e) $La_{0.96}Sr_{0.04}Ga_{0.85}Mg_{y0.15}O_{3-\delta}$, f) $La_{0.96}Sr_{0.04}Ga_{0.80}Mg_{0.20}O_{3-\delta}$ equilibrated at $700^{o}C$ for 720 hrs.

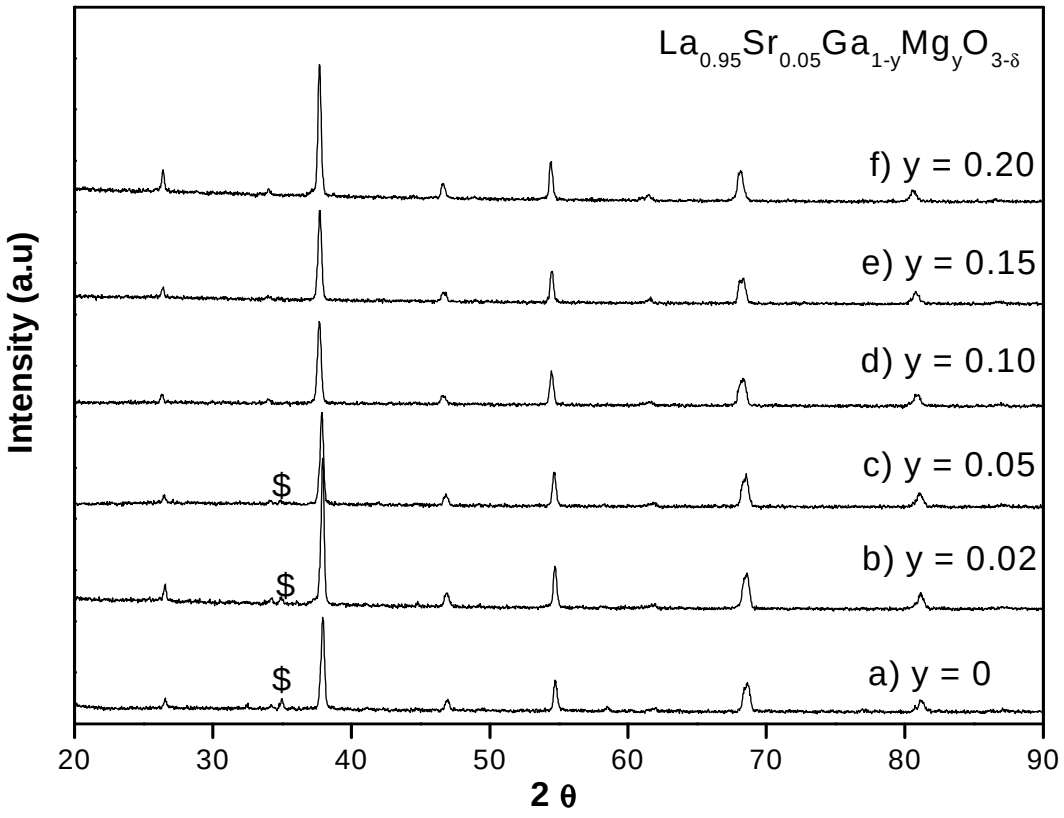

Fig.4.2.31 XRD pattern of $La_{0.95}Sr_{0.05}Ga_{1-y}Mg_yO_{3-\delta}$ (y= 0-0.20) equilibrated at 700^oC for 720 hrs

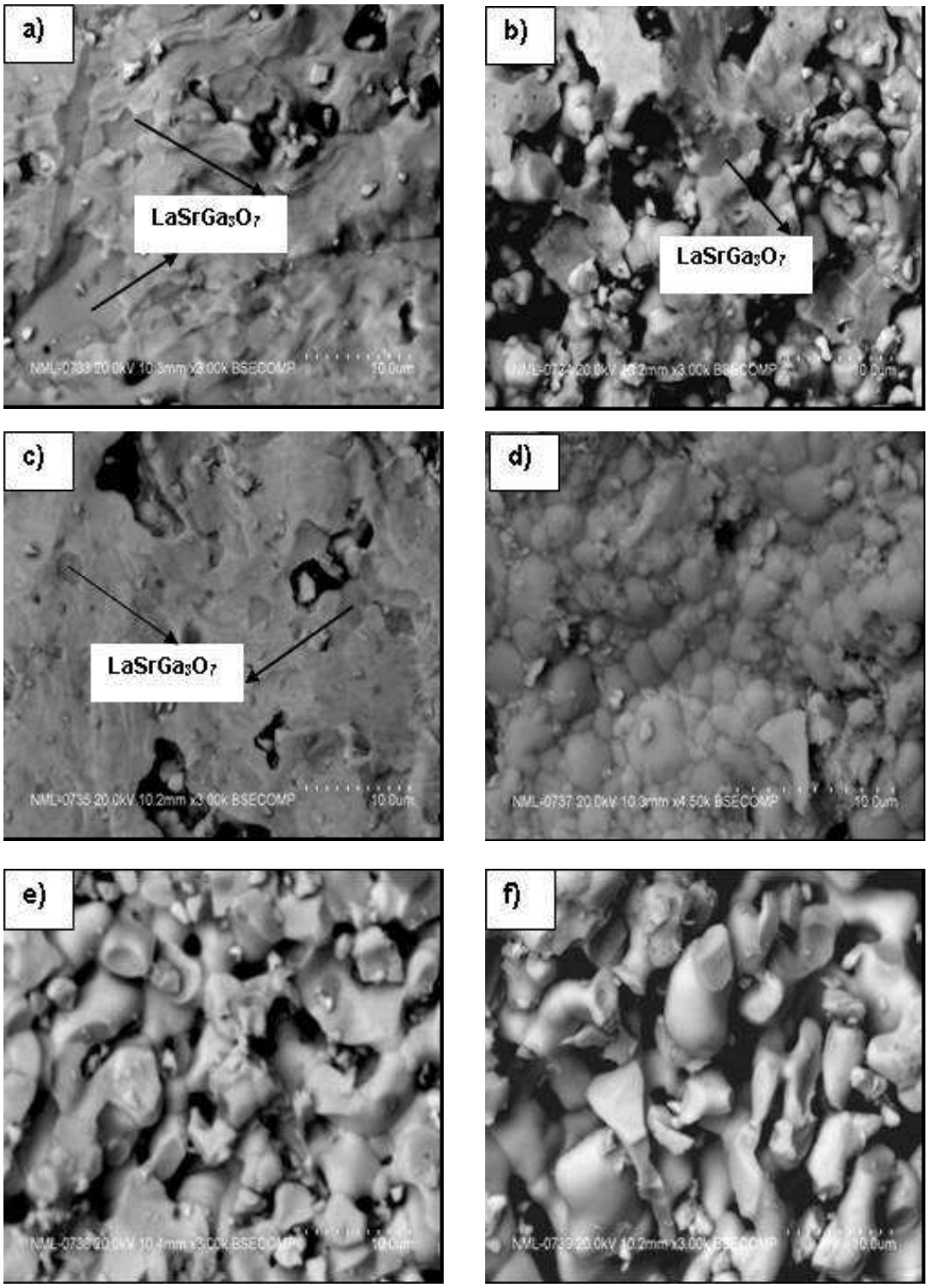

Fig.4.2.32 SEM-EDAX image of a) $La_{0.95}Sr_{0.05}GaO_{3-\delta}$, b) $La_{0.95}Sr_{0.05}Ga_{0.98}Mg_{0.02}O_{3-\delta}$, c) $La_{0.95}Sr_{0.05}Ga_{0.95}Mg_{y}O_{3-\delta}$, d) $La_{0.95}Sr_{0.05}Ga_{0.90}Mg_{0.10}O_{3-\delta}$, e) $La_{0.95}Sr_{0.05}Ga_{0.85}Mg_{y0.15}O_{3-\delta}$, f) $La_{0.95}Sr_{0.05}Ga_{0.80}Mg_{0.20}O_{3-\delta}$ equilibrated at 700^{o}C for 720 hrs

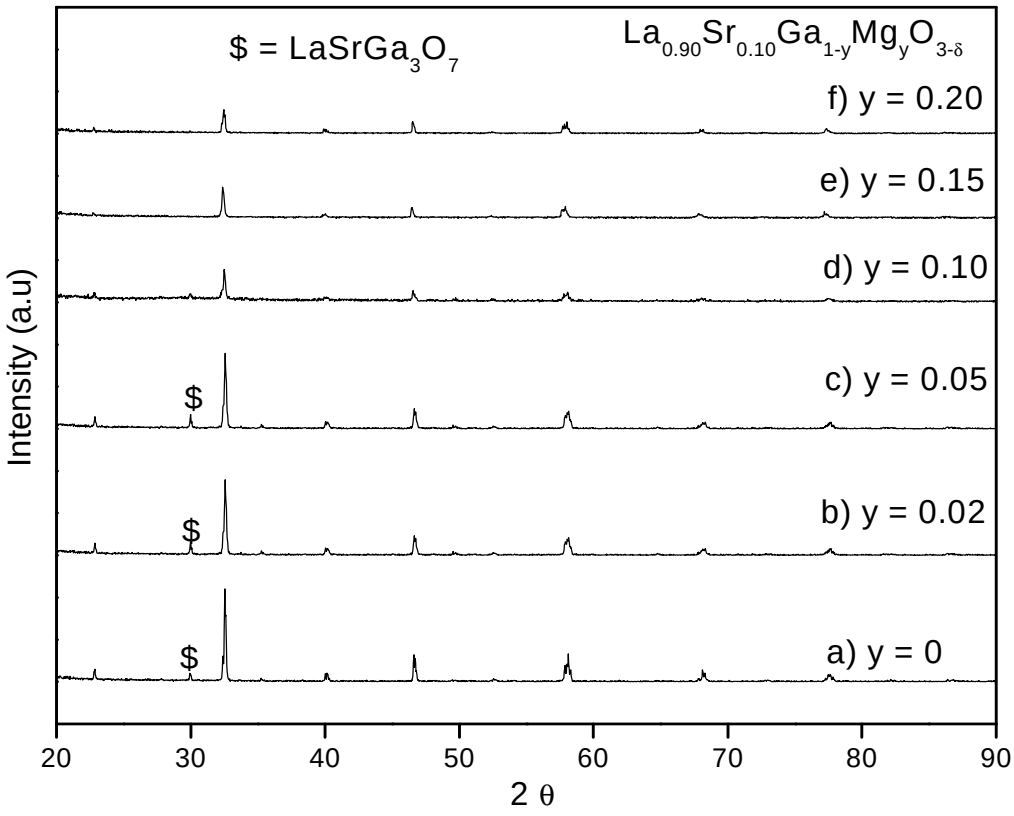

Fig.4.2.33 XRD pattern of $La_{0.90}Sr_{0.10}Ga_{1-y}Mg_yO_{3-\delta}$ (y= 0-0.20) equilibrated at 700^oC for 720 hrs.

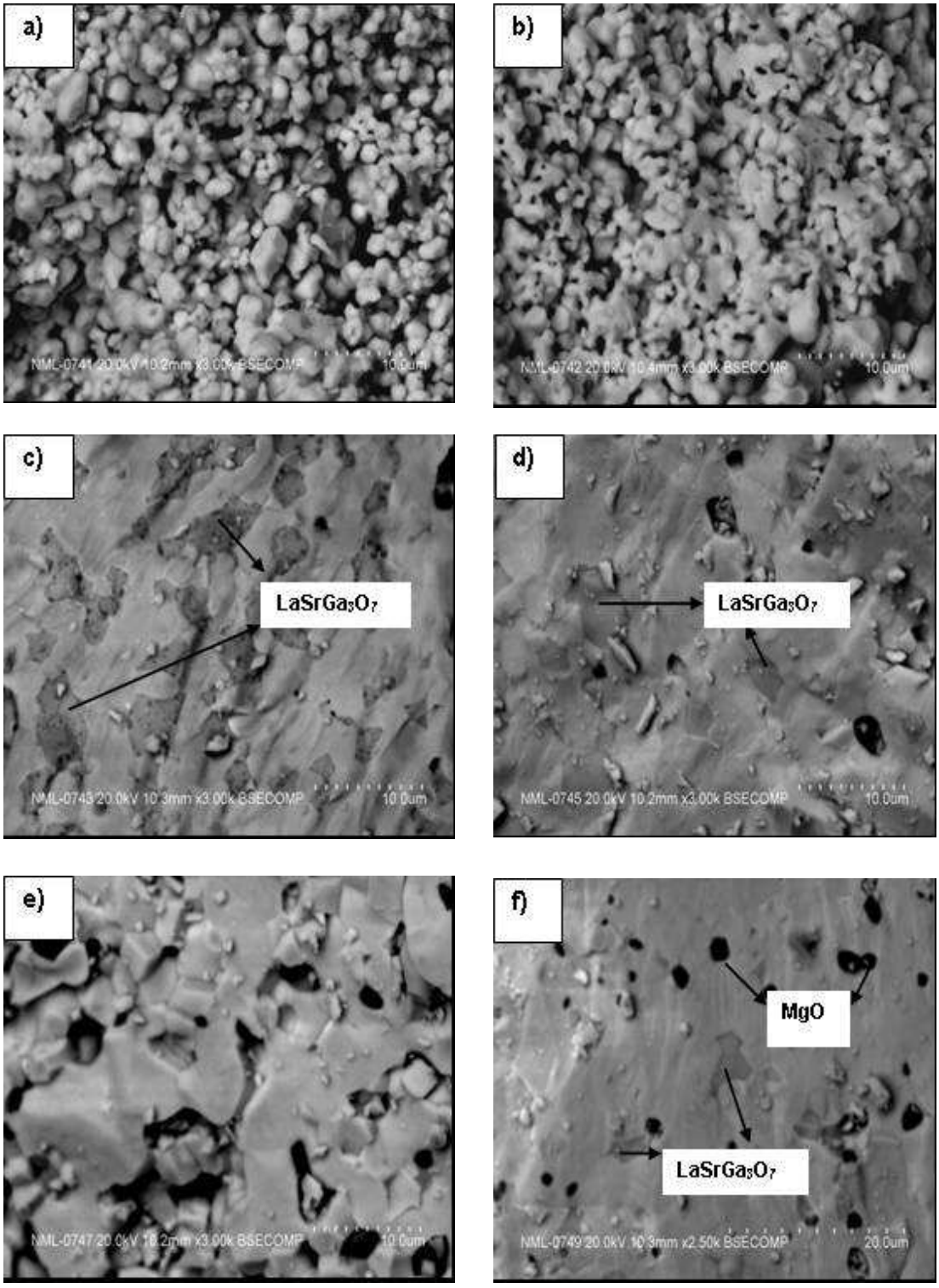

Fig.4.2.34 SEM-EDAX image of a) $La_{0.90}Sr_{0.10}GaO_{3-\delta}$, b) $La_{0.90}Sr_{0.10}Ga_{0.98}Mg_{0.02}O_{3-\delta}$, c) $La_{0.90}Sr_{0.10}Ga_{0.95}Mg_{y}O_{3-\delta}$, d) $La_{0.90}Sr_{0.10}Ga_{0.90}Mg_{0.10}O_{3-\delta}$, e) $La_{0.90}Sr_{0.10}Ga_{0.85}Mg_{y0.15}O_{3-\delta}$, f) $La_{0.90}Sr_{0.10}Ga_{0.80}Mg_{0.20}O_{3-\delta}$ equilibrated at 700^{o}C for 720 hrs

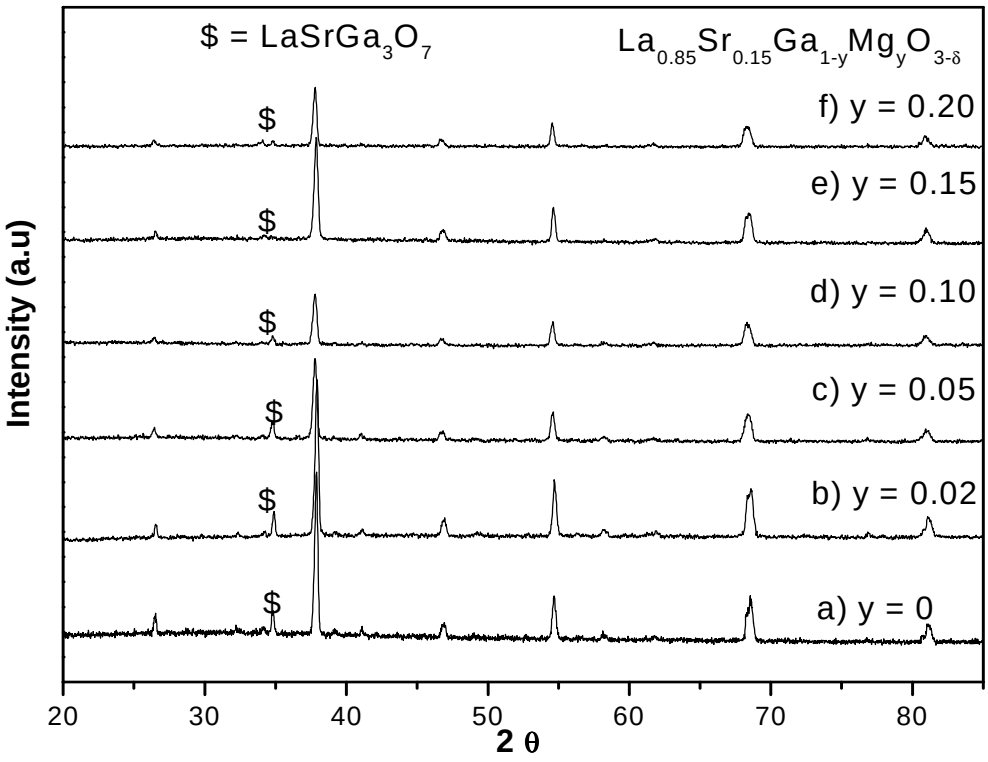

Fig.4.2.35 XRD pattern of $La_{0.85}Sr_{0.15}Ga_{1-y}Mg_yO_{3-\delta}$ (y= 0-0.20) equilibrated at 700^oC for 720 hrs

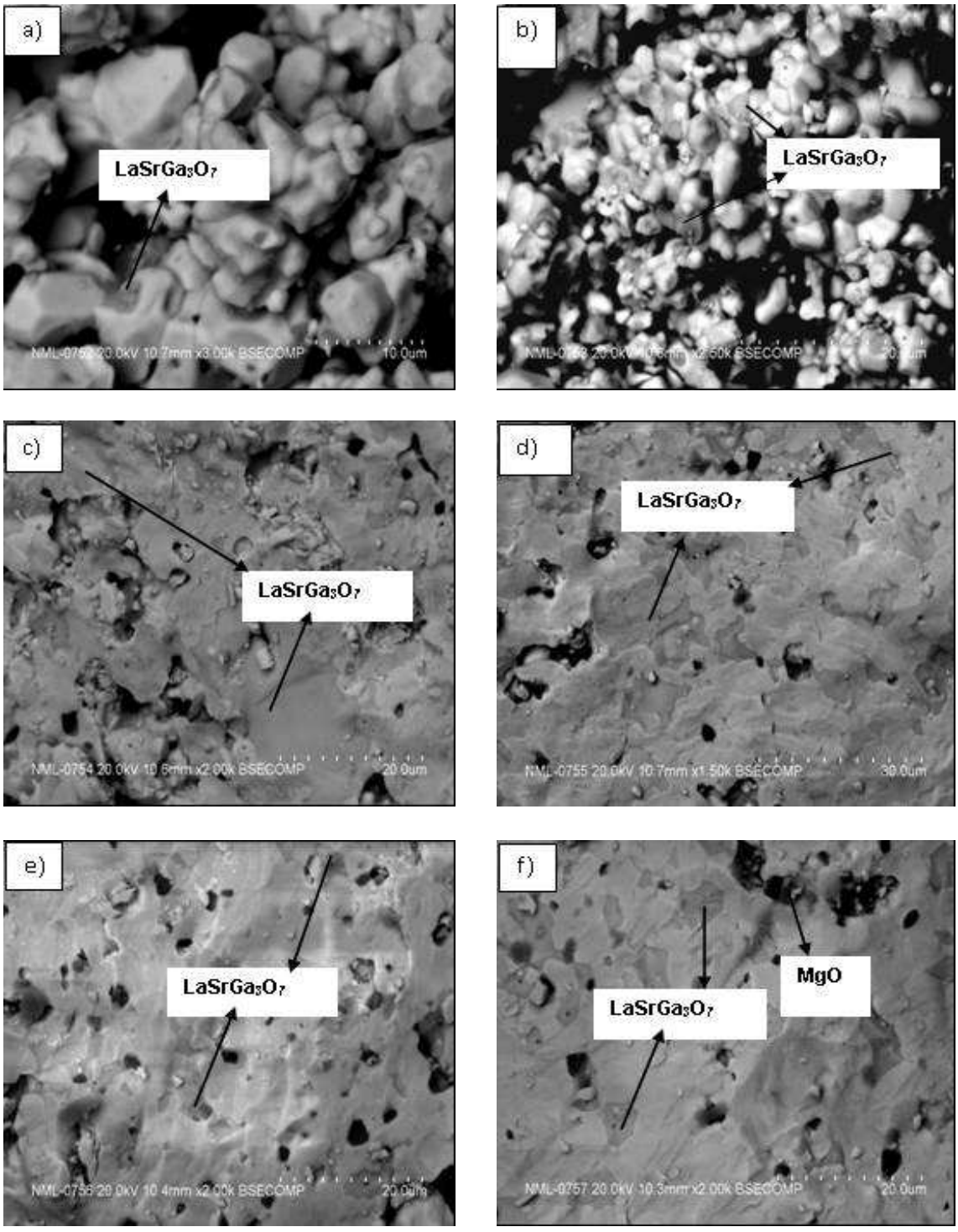

Fig.4.2.36 SEM-EDAX image of a) $La_{0.85}Sr_{0.15}GaO_{3-\delta}$, b) $La_{0.85}Sr_{0.15}Ga_{0.98}Mg_{0.02}O_{3-\delta}$, c) $La_{0.85}Sr_{0.15}Ga_{0.95}Mg_{y}O_{3-\delta}$, d) $La_{0.85}Sr_{0.15}Ga_{0.90}Mg_{0.10}O_{3-\delta}$, e) $La_{0.85}Sr_{0.15}Ga_{0.85}Mg_{y0.15}O_{3-\delta}$, f) $La_{0.85}Sr_{0.15}Ga_{0.80}Mg_{0.20}O_{3-\delta}$ equilibrated at 700^{o}C for 720 hrs

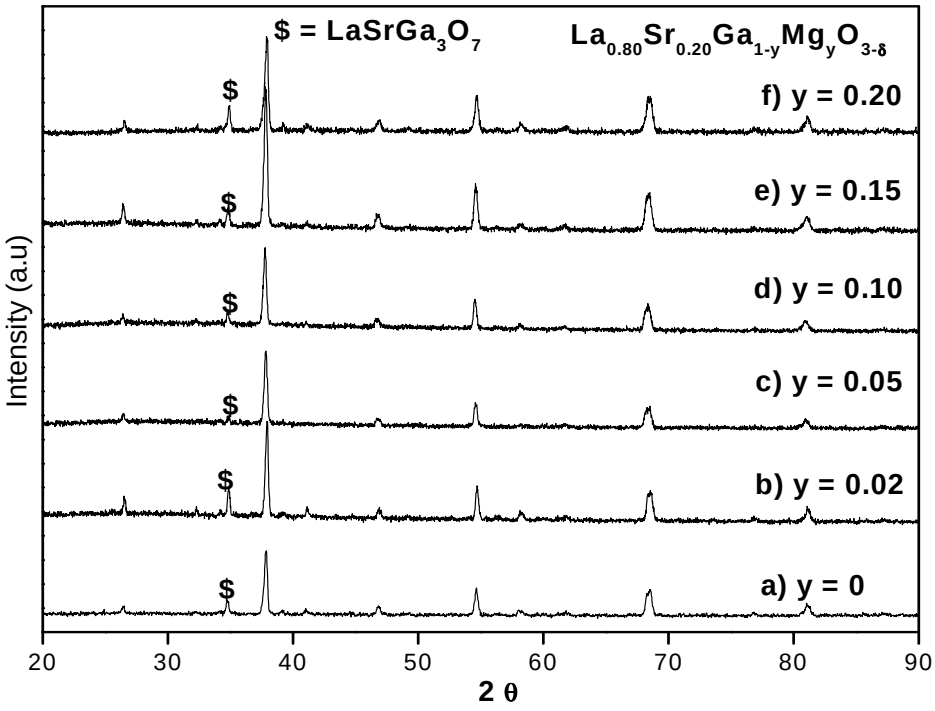

Fig.4.2.37 XRD pattern of $La_{0.80}Sr_{0.20}Ga_{1-y}Mg_yO_{3-\delta}$ (y= 0-0.20) equilibrated at 700^oC for 720 hrs

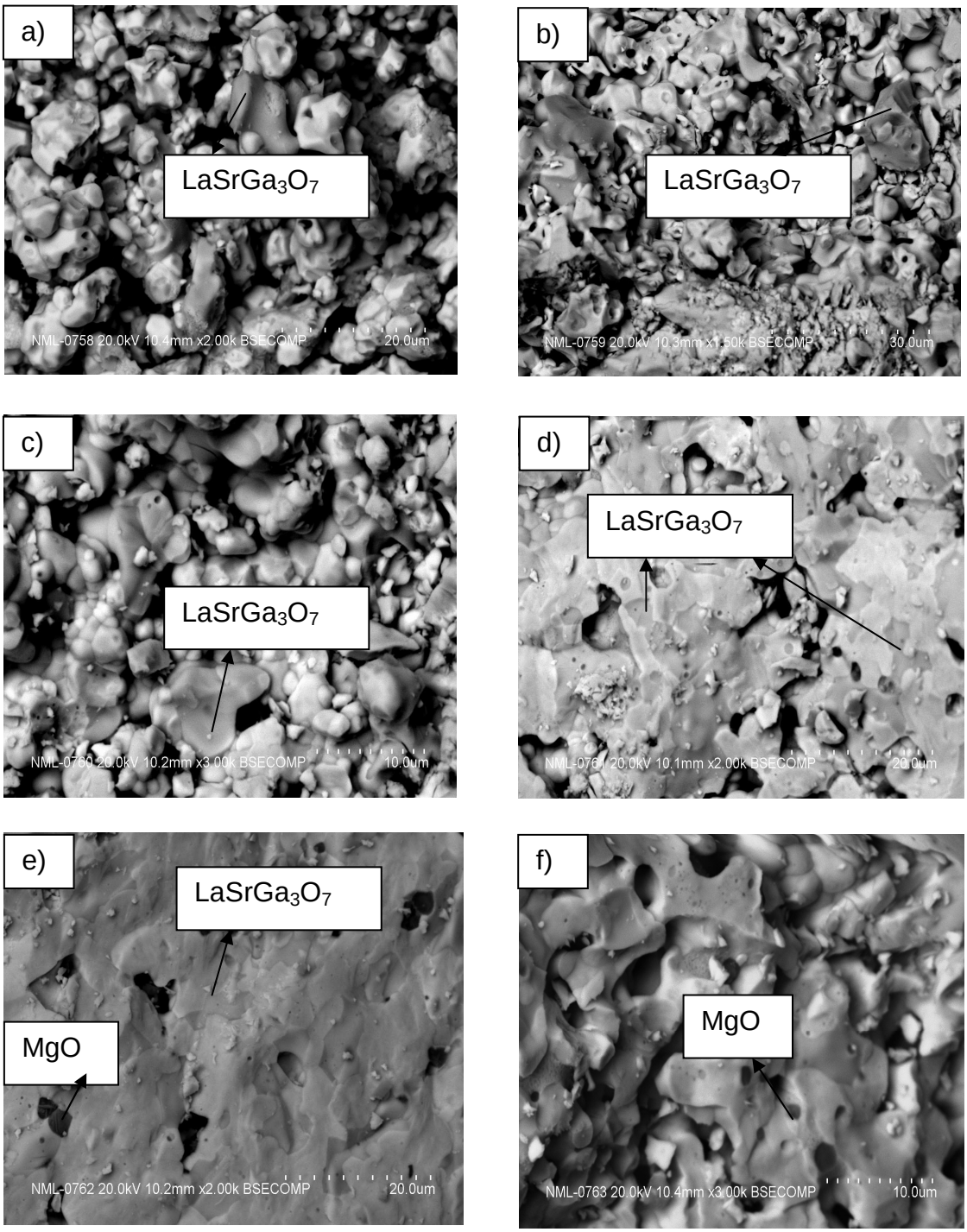

Fig.4.2.38 SEM-EDAX image of a) $La_{0.80}Sr_{0.20}GaO_{3-\delta}$, b) $La_{0.80}Sr_{0.20}Ga_{0.98}Mg_{0.02}O_{3-\delta}$, c) $La_{0.80}Sr_{0.20}Ga_{0.95}Mg_{y}O_{3-\delta}$, d) $La_{0.80}Sr_{0.20}Ga_{0.90}Mg_{0.10}O_{3-\delta}$, e) $La_{0.80}Sr_{0.20}Ga_{0.85}Mg_{y0.15}O_{3-\delta}$, f) $La_{0.80}Sr_{0.20}Ga_{0.80}Mg_{0.20}O_{3-\delta}$ equilibrated at 700^{o}C for 720 hrs

The variation of lattice parameter at 700^{o}C with Mg concentrations at the B sites of the perovskite phase is shown in Fig. 4.2.39. The point of inflection in the lattice parameter plot corresponds to the saturation solubility of the dopants. The phase

diagram of the $LaGaO_3$-$LaSrO_{2.5}$-$LaMgO_{2.5}$ at 700^{o}C was constructed from the XRD and SEM-EDS results and is shown in Fig. 4.2.40. The secondary phases identified for both 1500^{o}C and 700^{o}C by XRD and SEM-EDAX are given in Table 4.2.2 & 4.2.3 respectively.

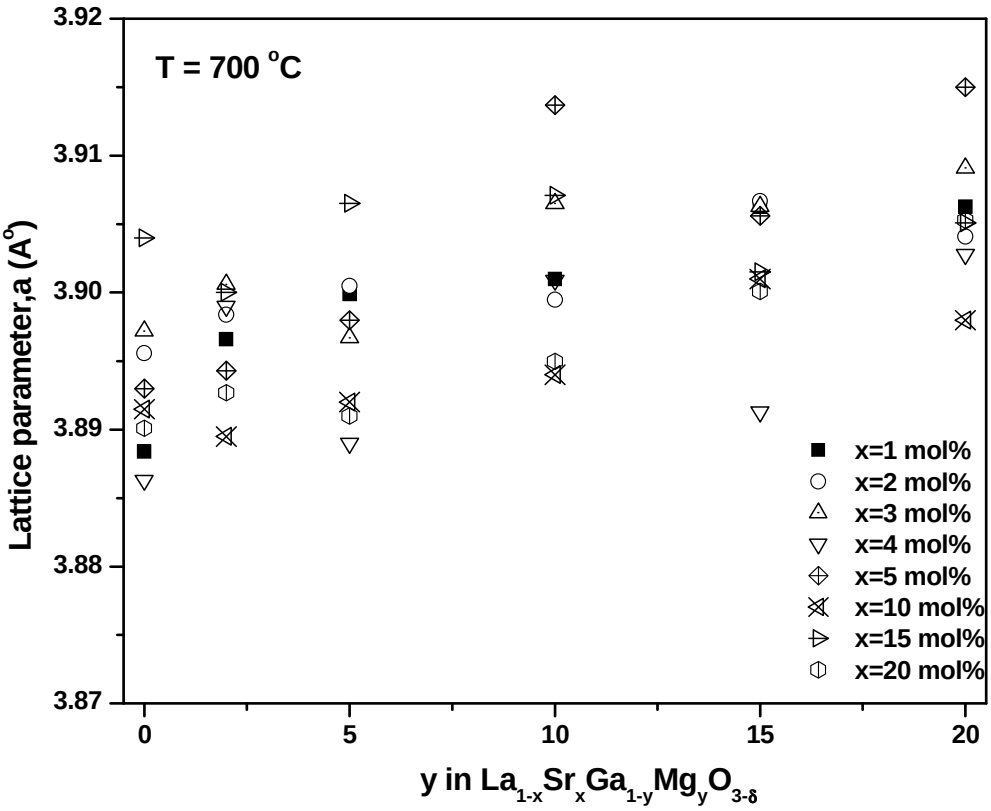

Fig.4.2.39 The lattice parameter of $La_{1-x}Sr_xGa_{1-y}Mg_yO_{3-\delta}$ (where x=0-20 and y= 0-20) is plotted against Mg content (equilibrated at 700^{o}C for 720 hrs)

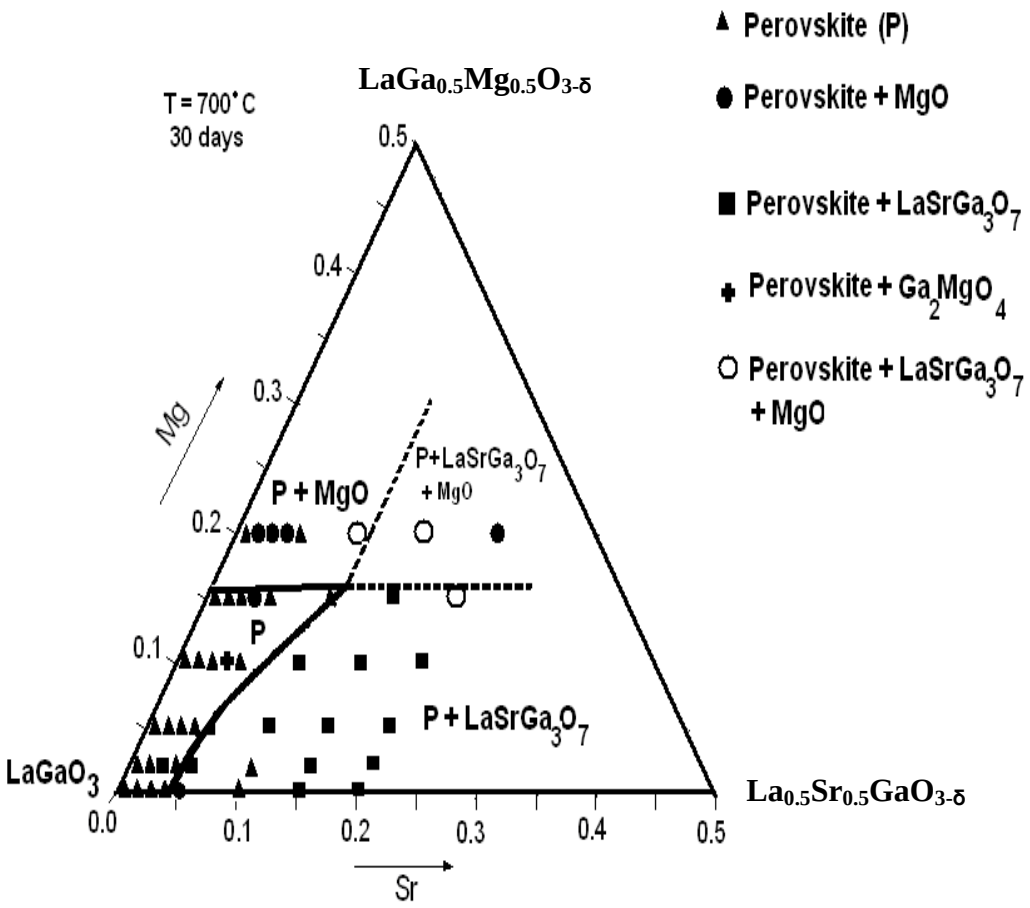

Fig.4.2.40 Range of stability of Sr and Mg-doped lanthanum gallate equilibrated at 700^{o}C for 720 hours

Table 4.2.2 The identified secondary phases in LSGM as a function of dopant concentration equilibrated at 1500^{o}C for 8 hours.

Compositions	**1500 ^{o}C, 8 h**						
	Phases identified by XRD	**Phases identified by SEM-EDAX**					
		Impurity phase	**Elemental composition of impurity phase (atomic percent)**				
			La	Sr	Ga	Mg	O
$La_{0.99}Sr_{0.01}GaO_{3-\delta}$	Pure LSGM	Pure LSGM	-	-	-	-	-
$La_{0.99}Sr_{0.01}Ga_{0.98}Mg_{0.02}O_{3-\delta}$	Pure LSGM	Pure LSGM	-	-	-	-	-
$La_{0.99}Sr_{0.01}Ga_{0.95}Mg_{0.05}O_{3-\delta}$	Pure LSGM	Pure LSGM	-	-	-	-	-
$La_{0.99}Sr_{0.01}Ga_{0.90}Mg_{0.10}O_{3-\delta}$	Pure LSGM	Pure LSGM	-	-	-	-	-
$La_{0.99}Sr_{0.01}Ga_{0.85}Mg_{0.15}O_{3-\delta}$	Pure LSGM	Pure LSGM	-	-	-	-	-
$La_{0.99}Sr_{0.01}Ga_{0.80}Mg_{0.20}O_{3-\delta}$	Pure LSGM	Pure LSGM	-	-	-	-	-
$La_{0.99}Sr_{0.01}Ga_{0.75}Mg_{0.25}O_{3-\delta}$	Pure LSGM	Pure LSGM + MgO	-	-	-	43.12	49.88
$La_{0.99}Sr_{0.01}Ga_{0.70}Mg_{0.30}O_{3-\delta}$	Pure LSGM	Pure LSGM + MgO	-	-	-	39.92	55.17
$La_{0.98}Sr_{0.02}GaO_{3-\delta}$	Pure LSGM	Pure LSGM	-	-	-	-	-
$La_{0.98}Sr_{0.02}Ga_{0.98}Mg_{0.02}O_{3-\delta}$	Pure LSGM	Pure LSGM	-	-	-	-	-
$La_{0.98}Sr_{0.02}Ga_{0.95}Mg_{0.05}O_{3-\delta}$	Pure LSGM	Pure LSGM	-	-	-	-	-
$La_{0.98}Sr_{0.02}Ga_{0.90}Mg_{0.10}O_{3-\delta}$	Pure LSGM	Pure LSGM	-	-	-	-	-
$La_{0.98}Sr_{0.02}Ga_{0.85}Mg_{0.15}O_{3-\delta}$	Pure LSGM	Pure LSGM	-	-	-	-	-

$La_{0.98}Sr_{0.02}Ga_{0.80}Mg_{0.20}O_{3-\delta}$	Pure LSGM	Pure LSGM	-	-	-	-	-
$La_{0.98}Sr_{0.02}Ga_{0.75}Mg_{0.25}O_{3-\delta}$	Pure LSGM	Pure LSGM + MgO+ $MgGa_2O_4$	-	-	-	33.93	59.15
			9.04	-	9.05	10.17	71.73
$La_{0.98}Sr_{0.02}Ga_{0.70}Mg_{0.30}O_{3-\delta}$	Pure LSGM	Pure LSGM + MgO + $MgGa_2O_4$	-	-	-	45.52	50.38
			9.93	-	9.12	5.68	75.27
$La_{0.97}Sr_{0.03}GaO_{3-\delta}$	Pure LSGM	Pure LSGM	-	-	-	-	-
$La_{0.97}Sr_{0.03}Ga_{0.98}Mg_{0.02}O_{3-\delta}$	Pure LSGM	Pure LSGM	-	-	-	-	-
$La_{0.97}Sr_{0.03}Ga_{0.95}Mg_{0.05}O_{3-\delta}$	Pure LSGM	Pure LSGM	-	-	-	-	-
$La_{0.97}Sr_{0.03}Ga_{0.90}Mg_{0.10}O_{3-\delta}$	Pure LSGM	Pure LSGM	-	-	-	-	-
$La_{0.97}Sr_{0.03}Ga_{0.85}Mg_{0.15}O_{3-\delta}$	Pure LSGM	Pure LSGM	-	-	-	-	-
$La_{0.97}Sr_{0.03}Ga_{0.80}Mg_{0.20}O_{3-\delta}$	Pure LSGM	Pure LSGM	-	-	-	-	-
$La_{0.97}Sr_{0.03}Ga_{0.75}Mg_{0.25}O_{3-\delta}$	Pure LSGM	Pure LSGM + MgO	-	-	-	41.09	54.46
$La_{0.97}Sr_{0.03}Ga_{0.70}Mg_{0.30}O_{3-\delta}$	Pure LSGM	Pure LSGM	-	-	-	-	-
$La_{0.95}Sr_{0.05}GaO_{3-\delta}$	Pure LSGM + $LaSrGa_3O_7$	Pure LSGM + $LaSrGa_3O_7$	24.16	0.21	37.42	-	38.21
$La_{0.95}Sr_{0.05}Ga_{0.98}Mg_{0.02}O_{3-\delta}$	Pure LSGM + $LaSrGa_3O_7$	Pure LSGM + $LaSrGa_3O_7$	14.65	1.67	38.02	-	45.67
$La_{0.95}Sr_{0.05}Ga_{0.95}Mg_{0.05}O_{3-\delta}$	Pure LSGM + $LaSrGa_3O_7$	Pure LSGM + $MgGa_2O_4$	1.19	-	21.18	13.10	64.53

$La_{0.95}Sr_{0.05}Ga_{0.90}Mg_{0.10}O_{3-\delta}$	Pure LSGM	Pure LSGM	-	-	-	-	-
$La_{0.95}Sr_{0.05}Ga_{0.85}Mg_{0.15}O_{3-\delta}$	Pure LSGM + $LaSrGa_3O_7$	Pure LSGM	-	-	-	-	-
$La_{0.95}Sr_{0.05}Ga_{0.80}Mg_{0.20}O_{3-\delta}$	Pure LSGM	Pure LSGM	-	-	-	-	-
$La_{0.95}Sr_{0.05}Ga_{0.75}Mg_{0.25}O_{3-\delta}$	Pure LSGM	Pure LSGM + MgO	-	-	-	46.46	53.43
$La_{0.95}Sr_{0.05}Ga_{0.70}Mg_{0.30}O_{3-\delta}$	Pure LSGM	Pure LSGM + MgO	-	-	-	43.01	54.52
$La_{0.90}Sr_{0.10}GaO_{3-\delta}$	Pure LSGM + $LaSrGa_3O_7$	Pure LSGM + $LaSrGa_3O_7$	6.81	2.30	14.51	-	78.38
$La_{0.90}Sr_{0.10}Ga_{0.98}Mg_{0.02}O_{3-\delta}$	Pure LSGM + $LaSrGa_3O_7$	Pure LSGM + $LaSrGa_3O_7$	26.24	-	48.43	-	25.34
$La_{0.90}Sr_{0.10}Ga_{0.95}Mg_{0.05}O_{3-\delta}$	Pure LSGM + $LaSrGa_3O_7$	Pure LSGM + $LaSrGa_3O_7$	18.06	3.51	43.75	0.52	34.16
$La_{0.90}Sr_{0.10}Ga_{0.90}Mg_{0.10}O_{3-\delta}$	Pure LSGM + $LaSrGa_3O_7$	Pure LSGM + $LaSrGa_3O_7$	24.96	0.79	33.67	1.45	39.13
$La_{0.90}Sr_{0.10}Ga_{0.85}Mg_{0.15}O_{3-\delta}$	Pure LSGM + $LaSrGa_3O_7$	Pure LSGM + $LaSrGa_3O_7$	3.20	-	2.97	36.97	56.86
$La_{0.90}Sr_{0.10}Ga_{0.80}Mg_{0.20}O_{3-\delta}$	Pure LSGM + $LaSrGa_3O_7$	Pure LSGM + $LaSrGa_3O_7$	6.25	5.53	15.79	-	72.43
$La_{0.90}Sr_{0.10}Ga_{0.75}Mg_{0.25}O_{3-\delta}$	Pure LSGM	Pure LSGM	-	-	-	-	-
$La_{0.90}Sr_{0.10}Ga_{0.70}Mg_{0.30}O_{3-\delta}$	Pure LSGM	Pure LSGM + MgO	-	-	-	39.86	60.14

$La_{0.85}Sr_{0.15}GaO_{3-\delta}$	$LaSrGa_3O_7$	Pure LSGM + $LaSrGa_3O_7$	4.50	5.82	16.24	-	73.44
$La_{0.85}Sr_{0.15}Ga_{0.98}Mg_{0.02}O_{3-\delta}$	$LaSrGa_3O_7$	Pure LSGM + $LaSrGa_3O_7$	19.14	1.02	31.41	0.30	48.13
$La_{0.85}Sr_{0.15}Ga_{0.95}Mg_{0.05}O_{3-\delta}$	$LaSrGa_3O_7$	Pure LSGM + $LaSrGa_3O_7$	6.91	6.31	18.13	1.14	67.51
$La_{0.85}Sr_{0.15}Ga_{0.90}Mg_{0.10}O_{3-\delta}$	$LaSrGa_3O_7$	Pure LSGM + $LaSrGa_3O_7$	7.13	6.00	19.66	1.27	65.93
$La_{0.85}Sr_{0.15}Ga_{0.85}Mg_{0.15}O_{3-\delta}$	$LaSrGa_3O_7$	Pure LSGM + $LaSrGa_3O_7$+ MgO	6.11	6.70	15.40	1.40	70.38
			-	-	-	42.54	55.01
$La_{0.85}Sr_{0.15}Ga_{0.80}Mg_{0.20}O_{3-\delta}$	$LaSrGa_3O_7$	Pure LSGM + $LaSrGa_3O_7$+ MgO	6.17	5.69	15.90	2.56	69.67
			-	-	-	38.59	57.20
$La_{0.85}Sr_{0.15}Ga_{0.75}Mg_{0.25}O_{3-\delta}$	Nil	Pure LSGM	-	-	-	-	-
$La_{0.85}Sr_{0.15}Ga_{0.70}Mg_{0.30}O_{3-\delta}$	Nil	Pure LSGM + MgO	-	-	-	41.73	57.86

Table 4.2.3 The identified secondary phases in LSGM as a function of composition for equilibration at 700^{o}C for 720 h

Compositions	**700 ^{o}C, 720 h**						
	Phases identified by XRD	**Phases identified by SEM-EDAX**					
		Impurity phase	**Elemental composition of impurity phase (atomic percent)**				
			La	Sr	Ga	Mg	O
$La_{0.99}Sr_{0.01}GaO_{3-\delta}$	Pure LSGM	Pure LSGM	-	-	-	-	-
$La_{0.99}Sr_{0.01}Ga_{0.98}Mg_{0.02}O_{3-\delta}$	Pure LSGM	Pure LSGM	-	-	-	-	-
$La_{0.99}Sr_{0.01}Ga_{0.95}Mg_{0.05}O_{3-\delta}$	Pure LSGM	Pure LSGM	-	-	-	-	-
$La_{0.99}Sr_{0.01}Ga_{0.90}Mg_{0.10}O_{3-\delta}$	Pure LSGM	Pure LSGM	-	-	-	-	-
$La_{0.99}Sr_{0.01}Ga_{0.85}Mg_{0.15}O_{3-\delta}$	Pure LSGM	Pure LSGM	-	-	-	-	-
$La_{0.99}Sr_{0.01}Ga_{0.80}Mg_{0.20}O_{3-\delta}$	Pure LSGM	Pure LSGM	-	-	-	-	-
$La_{0.98}Sr_{0.02}GaO_{3-\delta}$	Pure LSGM	Pure LSGM	-	-	-	-	-
$La_{0.98}Sr_{0.02}Ga_{0.98}Mg_{0.02}O_{3-\delta}$	Pure LSGM	Pure LSGM	-	-	-	-	-
$La_{0.98}Sr_{0.02}Ga_{0.95}Mg_{0.05}O_{3-\delta}$	Pure LSGM	Pure LSGM	-	-	-	-	-
$La_{0.98}Sr_{0.02}Ga_{0.90}Mg_{0.10}O_{3-\delta}$	Pure LSGM	Pure LSGM	-	-	-	-	-
$La_{0.98}Sr_{0.02}Ga_{0.85}Mg_{0.15}O_{3-\delta}$	Pure LSGM	Pure LSGM	-	-	-	-	-
$La_{0.98}Sr_{0.02}Ga_{0.80}Mg_{0.20}O_{3-\delta}$	Pure LSGM	Pure LSGM + MgO	-	-	-	39.79	58.15
$La_{0.97}Sr_{0.03}GaO_{3-\delta}$	Pure LSGM	Pure LSGM	-	-	-	-	-
$La_{0.97}Sr_{0.03}Ga_{0.98}Mg_{0.02}O_{3-\delta}$	Pure LSGM	Pure LSGM+	9.10	5.16	19.93	1.03	64.78

		$LaSrGa_3O_7$					
$La_{0.97}Sr_{0.03}Ga_{0.95}Mg_{0.05}O_{3-\delta}$	Pure LSGM	Pure LSGM	-	-	-	-	-
$La_{0.97}Sr_{0.03}Ga_{0.90}Mg_{0.10}O_{3-\delta}$	Pure LSGM	Pure LSGM	-	-	-	-	-
$La_{0.97}Sr_{0.03}Ga_{0.85}Mg_{0.15}O_{3-\delta}$	Pure LSGM	Pure LSGM	-	-	-	-	-
$La_{0.97}Sr_{0.03}Ga_{0.80}Mg_{0.20}O_{3-\delta}$	Pure LSGM	Pure LSGM + MgO	-	-	-	40.37	55.90
$La_{0.96}Sr_{0.04}GaO_{3-\delta}$	Pure LSGM	Pure LSGM	-	-	-	-	-
$La_{0.96}Sr_{0.04}Ga_{0.98}Mg_{0.02}O_{3-\delta}$	Pure LSGM	Pure LSGM	-	-	-	-	-
$La_{0.96}Sr_{0.04}Ga_{0.95}Mg_{0.05}O_{3-\delta}$	Pure LSGM	Pure LSGM	-	-	-	-	-
$La_{0.96}Sr_{0.04}Ga_{0.90}Mg_{0.10}O_{3-\delta}$	Pure LSGM	Pure LSGM + $MgGa_2O_4$	0.24	0.02	35.27	11.79	52.68
$La_{0.96}Sr_{0.04}Ga_{0.85}Mg_{0.15}O_{3-\delta}$	Pure LSGM	Pure LSGM + MgO	-	-	-	41.56	57.91
$La_{0.96}Sr_{0.04}Ga_{0.80}Mg_{0.20}O_{3-\delta}$	Pure LSGM	Pure LSGM + MgO					
$La_{0.95}Sr_{0.05}GaO_{3-\delta}$	Pure LSGM + $LaSrGa_3O_7$	Pure LSGM + $LaSrGa_3O_7$	24.16	0.21	37.42	-	38.21
$La_{0.95}Sr_{0.05}Ga_{0.98}Mg_{0.02}O_{3-\delta}$	Pure LSGM + $LaSrGa_3O_7$	Pure LSGM + $LaSrGa_3O_7$	14.65	1.67	38.02	-	45.67
$La_{0.95}Sr_{0.05}Ga_{0.95}Mg_{0.05}O_{3-\delta}$	Pure LSGM + $LaSrGa_3O_7$	Pure LSGM + $MgGa_2O_4$	1.19	-	21.18	13.10	64.53
$La_{0.95}Sr_{0.05}Ga_{0.90}Mg_{0.10}O_{3-\delta}$	Pure LSGM	Pure LSGM	-	-	-	-	-
$La_{0.95}Sr_{0.05}Ga_{0.85}Mg_{0.15}O_{3-\delta}$	Pure LSGM	Pure LSGM	-	-	-	-	-
$La_{0.95}Sr_{0.05}Ga_{0.80}Mg_{0.20}O_{3-\delta}$	Pure LSGM	Pure LSGM	-	-	-	-	-

$La_{0.90}Sr_{0.10}GaO_{3-\delta}$	Pure LSGM + $LaSrGa_3O_7$	Pure LSGM	-	-	-	-	-
$La_{0.90}Sr_{0.10}Ga_{0.98}Mg_{0.02}O_{3-\delta}$	Pure LSGM + $LaSrGa_3O_7$	Pure LSGM	-	-	-	-	-
$La_{0.90}Sr_{0.10}Ga_{0.95}Mg_{0.05}O_{3-\delta}$	Pure LSGM + $LaSrGa_3O_7$	Pure LSGM + $LaSrGa_3O_7$	5.35	6.09	15.64	1.37	71.55
$La_{0.90}Sr_{0.10}Ga_{0.90}Mg_{0.10}O_{3-\delta}$	Pure LSGM	Pure LSGM + $LaSrGa_3O_7$	10.67	6.25	28.24	0.52	54.32
$La_{0.90}Sr_{0.10}Ga_{0.85}Mg_{0.15}O_{3-\delta}$	Pure LSGM	Pure LSGM	-	-	-	-	-
$La_{0.90}Sr_{0.10}Ga_{0.80}Mg_{0.20}O_{3-\delta}$	Pure LSGM	Pure LSGM + $LaSrGa_3O_7$+ MgO	5.88	6.65	18.08	1.55	67.84
			-	-	-	38.05	54.30
$La_{0.85}Sr_{0.15}GaO_{3-\delta}$	$LaSrGa_3O_7$	Pure LSGM + $LaSrGa_3O_7$	8.76	4.15	14.88	-	72.20
$La_{0.85}Sr_{0.15}Ga_{0.98}Mg_{0.02}O_{3-\delta}$	$LaSrGa_3O_7$	Pure LSGM + $LaSrGa_3O_7$	7.74	6.20	23.24	0.73	62.09
$La_{0.85}Sr_{0.15}Ga_{0.95}Mg_{0.05}O_{3-\delta}$	$LaSrGa_3O_7$	Pure LSGM + $LaSrGa_3O_7$	8.43	6.31	24.90	1.17	59.20
$La_{0.85}Sr_{0.15}Ga_{0.90}Mg_{0.10}O_{3-\delta}$	$LaSrGa_3O_7$	Pure LSGM + $LaSrGa_3O_7$	7.37	6.32	19.10	1.36	65.84

$La_{0.85}Sr_{0.15}Ga_{0.85}Mg_{0.15}O_{3-\delta}$	$LaSrGa_3O_7$	Pure LSGM + MgO	-	-	-	36.56	57.88
$La_{0.85}Sr_{0.15}Ga_{0.80}Mg_{0.20}O_{3-\delta}$	$LaSrGa_3O_7$	Pure LSGM + $LaSrGa_3O_7$+ MgO	7.46	6.25	22.38	1.80	62.03
			-	-	-	41.48	55.66
$La_{0.80}Sr_{0.20}GaO_{3-\delta}$	$LaSrGa_3O_7$	Pure LSGM + $LaSrGa_3O_7$	7.31	8.86	23.76	-	60.08
$La_{0.80}Sr_{0.20}Ga_{0.98}Mg_{0.02}O_{3-\delta}$	$LaSrGa_3O_7$	Pure LSGM + $LaSrGa_3O_7$	4.89	6.77	15.14	0.58	72.62
$La_{0.80}Sr_{0.20}Ga_{0.95}Mg_{0.05}O_{3-\delta}$	$LaSrGa_3O_7$	Pure LSGM + $LaSrGa_3O_7$	5.25	6.44	15.26	2.49	70.56
$La_{0.80}Sr_{0.20}Ga_{0.90}Mg_{0.10}O_{3-\delta}$	$LaSrGa_3O_7$	Pure LSGM + $LaSrGa_3O_7$	8.95	5.85	22.48	2.03	60.70
$La_{0.80}Sr_{0.20}Ga_{0.85}Mg_{0.15}O_{3-\delta}$	$LaSrGa_3O_7$	Pure LSGM + $LaSrGa_3O_7$+ MgO	10.06	6.26	29.71	1.76	52.21
			-	-	-	43.47	52.19
$La_{0.80}Sr_{0.20}Ga_{0.80}Mg_{0.20}O_{3-\delta}$	$LaSrGa_3O_7$	Pure LSGM + MgO	-	-	-	40.38	51.04

4.2.4. Electrical Conductivity of $La_{1-x}Sr_xGa_{1-y}Mg_yO_{3-\delta}$

The electrical conductivity of $La_{1-x}Sr_xGa_{1-y}Mg_yO_{3-\delta}$ as a function of Sr- and Mg-concentrations at the A- and B- sites was investigated by two probe ac electrochemical impedance (EIS) method in the temperature range 500-1000^{o}C at an interval of 100^{o}C. For the EIS measurements, AC amplitude used was 100 mV and the scan was carried out in the frequency range of 10 Hz-10 MHz. The bulk conductivity of $La_{1-x}Sr_xGa_{1-y}Mg_yO_{3-\delta}$ compositions was deduced from the measured bulk resistance and the dimensions (area and thickness) of the pellet. It was calculated using the following equation:

$$\sigma_{bulk} = \frac{L}{R\,A} \qquad [4.4]$$

where σ is the bulk conductivity (S/cm), L is the thickness of the sample (cm), R is the bulk resistance measured from the abscissa of the Nyquist plot (Ω) and A is the area of the sample (cm^2). The calculated bulk conductivities of $La_{1-x}Sr_xGa_{1-y}Mg_yO_{3-\delta}$ (x=0.0-0.30 and y= 0.0-0.30mol) at different temperatures are given in Table 4.2.4.

AC impedance analysis over a wide range of frequencies can resolve the resistances and capacitances associated with the bulk, grain boundary and electrode processes in ceramic samples in a complex plane. The high frequency semi-circle corresponds to the bulk capacitance and conductance, the low frequency semi-circle is because of the ion and electron transfer at the electrode-electrolyte interface and the intermediate frequency semicircle results from the grain boundary resistance and dielectric processes. All these three contributions vary with temperature and need not be always present. At higher temperatures, since the grain boundary resistance is considerably lower, the intermediate frequency semicircle is not present. Since all the impedance analysis measurements in the present thesis were carried out above 500^{o}C, the characteristic 3-semi circle plot was not obtained. Typical impedance plots obtained in this study are shown in Fig. 4.2.41. Since, a maximum frequency up to 10 MHz was used, the bulk resistance semicircle became inaccessible as a result of the high oxygen ion conductivity. Therefore, we have taken the real resistance obtained at the highest frequency of measurement to correspond to the bulk resistivity. This value was in excellent agreement (within 3-5%) with the bulk resistance measured by the DC method. The iso-conductivity contours as a function of Sr and Mg doping at the A- and B- sites at 600, 800 and 1000^{o}C are shown in Figs. 4.2.42a-c. It was

seen that the highest conductivities at all these three temperatures occurred in the concentration range of 10-15 mol % Sr and 20-25 mol % Mg. The variation of conductivity with Sr and Mg content at 800^{o}C is depicted in Fig. 4.2.43**.**

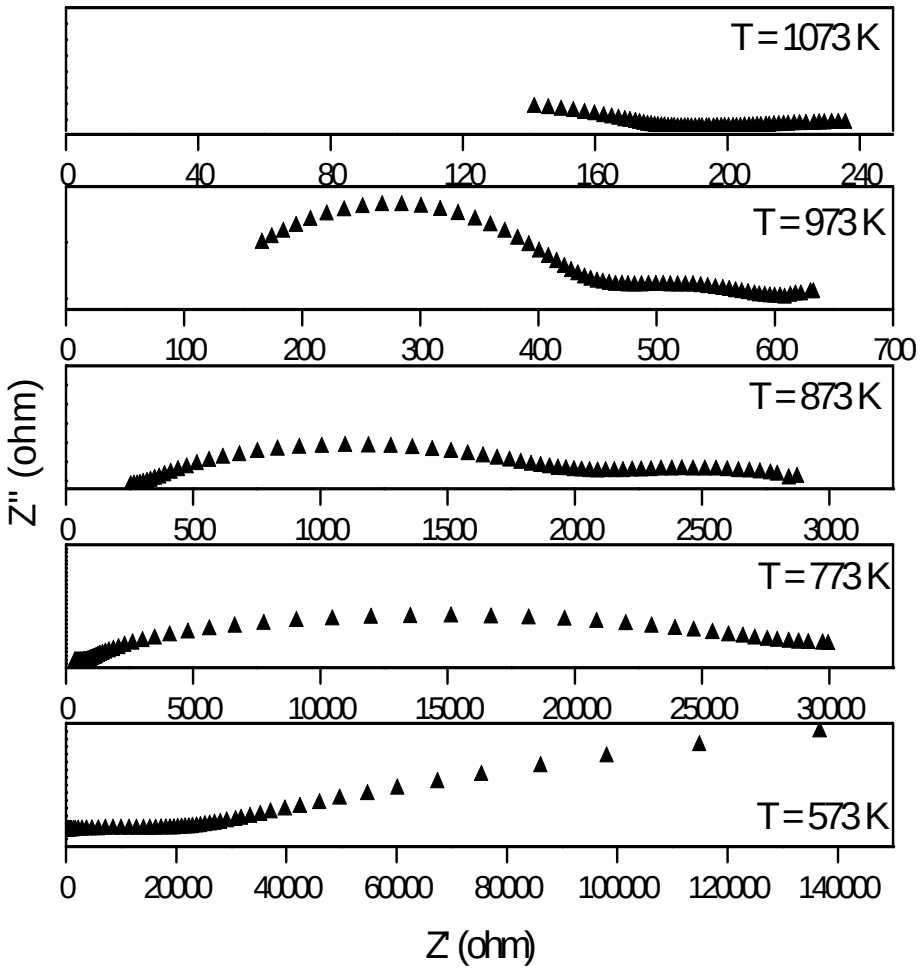

Fig. 4.2.41 Nyquist plot for $La_{0.98}Sr_{0.02}Ga_{0.98}Mg_{0.02}O_{3-\delta}$ at different temperatures

Table 4.2.4 Bulk conductivity of $La_{1-x}Sr_xGa_{1-y}Mg_yO_{3-\delta}$ at different temperatures

Sr mol%	Mg mol%	Conductivity (S/cm)					
		500° C	600° C	700° C	800° C	900° C	1000° C
1	0	5.02×10^{-4}	1.57×10^{-3}	3.86×10^{-3}	7.37×10^{-3}	8.32×10^{-3}	1.23×10^{-2}
2		3.88×10^{-4}	6.08×10^{-4}	7.52×10^{-4}	2.36×10^{-3}	4.56×10^{-3}	7.54×10^{-3}
3		5.27×10^{-5}	1.97×10^{-4}	4.98×10^{-4}	1.24×10^{-3}	2.29×10^{-3}	3.99×10^{-2}
5		1.75×10^{-4}	1×10^{-3}	3.59×10^{-3}	9.21×10^{-3}	1.82×10^{-2}	2.87×10^{-2}
10		4.74×10^{-4}	1.78×10^{-3}	4.98×10^{-3}	1.03×10^{-2}	1.78×10^{-2}	2.64×10^{-2}
15		6.38×10^{-4}	2.52×10^{-4}	7.18×10^{-4}	1.52×10^{-3}	2.80×10^{-3}	4.14×10^{-3}
1	02	6.74×10^{-4}	3.06×10^{-3}	8.32×10^{-3}	9.98×10^{-3}	1.31×10^{-2}	1.90×10^{-2}
2		1.17×10^{-3}	4.30×10^{-3}	7.70×10^{-3}	8.64×10^{-3}	9.64×10^{-3}	1.62×10^{-2}
3		3.46×10^{-3}	7.28×10^{-3}	1.23×10^{-2}	2.62×10^{-2}	4.26×10^{-2}	6.16×10^{-2}
5		1.86×10^{-3}	8.94×10^{-3}	2.21×10^{-2}	4.55×10^{-2}	7.20×10^{-2}	9.78×10^{-2}
10		1.95×10^{-3}	7.42×10^{-3}	1.90×10^{-2}	3.65×10^{-2}	5.70×10^{-2}	7.70×10^{-2}
15		4.30×10^{-4}	2.16×10^{-3}	6.21×10^{-3}	1.30×10^{-2}	2.21×10^{-2}	3.28×10^{-2}
1	05	7.14×10^{-4}	3.90×10^{-3}	6.98×10^{-3}	8.51×10^{-3}	1.37×10^{-2}	1.88×10^{-2}
2		8.41×10^{-4}	4.38×10^{-3}	7.03×10^{-3}	1.37×10^{-2}	2.20×10^{-2}	3.02×10^{-2}
3		4.60×10^{-3}	1.18×10^{-2}	2.86×10^{-2}	4.82×10^{-2}	7.02×10^{-2}	9.22×10^{-2}
5		4.66×10^{-3}	1.63×10^{-2}	3.64×10^{-2}	6.33×10^{-2}	9.16×10^{-2}	0.117
10		4.24×10^{-3}	1.41×10^{-2}	3.30×10^{-2}	5.98×10^{-2}	8.54×10^{-2}	1.11×10^{-1}
15		2.15×10^{-3}	9.00×10^{-3}	2.20×10^{-2}	4.10×10^{-2}	6.50×10^{-2}	8.84×10^{-2}
1	10	4.85×10^{-3}	1.17×10^{-2}	2.04×10^{-2}	3.38×10^{-2}	3.86×10^{-2}	4.34×10^{-2}
2		4.75×10^{-3}	8.38×10^{-3}	2.76×10^{-2}	4.82×10^{-2}	7.00×10^{-2}	9.08×10^{-2}
3		4.40×10^{-3}	1.32×10^{-2}	4.20×10^{-2}	8.00×10^{-2}	1.17×10^{-1}	1.48×10^{-1}
5		5.23×10^{-3}	1.65×10^{-2}	4.75×10^{-2}	8.55×10^{-2}	0.119	0.147
10		8.90×10^{-3}	2.60×10^{-2}	6.28×10^{-2}	1.01×10^{-1}	1.37×10^{-1}	1.64×10^{-1}
15		4.36×10^{-3}	1.75×10^{-2}	4.06×10^{-2}	7.41×10^{-2}	1.09×10^{-1}	1.46×10^{-1}
1	15	6.35×10^{-3}	1.13×10^{-2}	2.12×10^{-2}	3.28×10^{-2}	4.21×10^{-2}	4.78×10^{-2}
2		9.88×10^{-3}	1.96×10^{-2}	4.56×10^{-2}	7.66×10^{-2}	1.09×10^{-1}	1.28×10^{-1}
3		3.86×10^{-3}	2.90×10^{-2}	6.94×10^{-2}	1.13×10^{-1}	1.16×10^{-1}	1.89×10^{-1}
5		7.20×10^{-3}	2.60×10^{-2}	3.79×10^{-2}	8.90×10^{-2}	0.122	9.31×10^{-2}
10		5.26×10^{-3}	2.56×10^{-2}	6.74×10^{-2}	1.18×10^{-1}	1.77×10^{-1}	2.28×10^{-1}
15		7.84×10^{-3}	3.21×10^{-2}	7.47×10^{-2}	1.26×10^{-1}	1.73×10^{-1}	2.08×10^{-1}
1	20	1.03×10^{-2}	1.59×10^{-2}	3.14×10^{-2}	4.58×10^{-2}	5.44×10^{-2}	5.98×10^{-2}
2		6.38×10^{-3}	2.66×10^{-2}	5.72×10^{-2}	9.66×10^{-2}	1.38×10^{-1}	1.68×10^{-1}
3		1.73×10^{-3}	1.60×10^{-2}	6.20×10^{-2}	1.16×10^{-1}	1.62×10^{-1}	1.96×10^{-1}
5		5.33×10^{-4}	6.08×10^{-3}	1.33×10^{-2}	2.70×10^{-2}	0.13	0.159
10		5.40×10^{-3}	2.40×10^{-2}	7.51×10^{-2}	1.10×10^{-1}	1.57×10^{-1}	1.93×10^{-1}
15		5.17×10^{-3}	1.97×10^{-2}	5.42×10^{-2}	9.25×10^{-2}	1.32×10^{-1}	1.74×10^{-1}
1	25	3.60×10^{-3}	1.67×10^{-2}	3.26×10^{-2}	4.44×10^{-2}	5.46×10^{-2}	5.84×10^{-2}
2		$3.18v10^{-3}$	1.73×10^{-2}	6.92×10^{-2}	1.24×10^{-1}	1.70×10^{-1}	2.06×10^{-1}
3		1.68×10^{-3}	9.54×10^{-3}	5.08×10^{-2}	1.11×10^{-1}	1.66×10^{-1}	2.04×10^{-1}
5		1.73×10^{-3}	1.30×10^{-2}	5.68×10^{-2}	0.1185	0.1729	0.2154
10		5.09×10^{-3}	2.76×10^{-2}	7.17×10^{-2}	1.28×10^{-1}	1.82×10^{-1}	2.25×10^{-1}

15		2.59×10^{-3}	1.49×10^{-2}	3.94×10^{-2}	7.68×10^{-2}	1.16×10^{-1}	1.53×10^{-1}
1		2.90×10^{-3}	1.30×10^{-2}	2.86×10^{-2}	4.50×10^{-2}	5.10×10^{-2}	5.34×10^{-2}
2		7.58×10^{-4}	4.86×10^{-3}	4.18×10^{-2}	8.86×10^{-2}	1.28×10^{-1}	1.57×10^{-1}
3	30	5.36×10^{-4}	3.84×10^{-3}	2.44×10^{-2}	6.26×10^{-2}	1.08×10^{-1}	1.52×10^{-1}
5		1.56×10^{-3}	6.96×10^{-3}	4.36×10^{-2}	9.82×10^{-2}	0.1544	0.199
10		2.31×10^{-3}	1.63×10^{-2}	5.74×10^{-2}	1.11×10^{-1}	1.68×10^{-1}	0.212
15		6.78×10^{-4}	4.52×10^{-3}	2.46×10^{-2}	6.16×10^{-2}	9.96×10^{-2}	1.35×10^{-1}

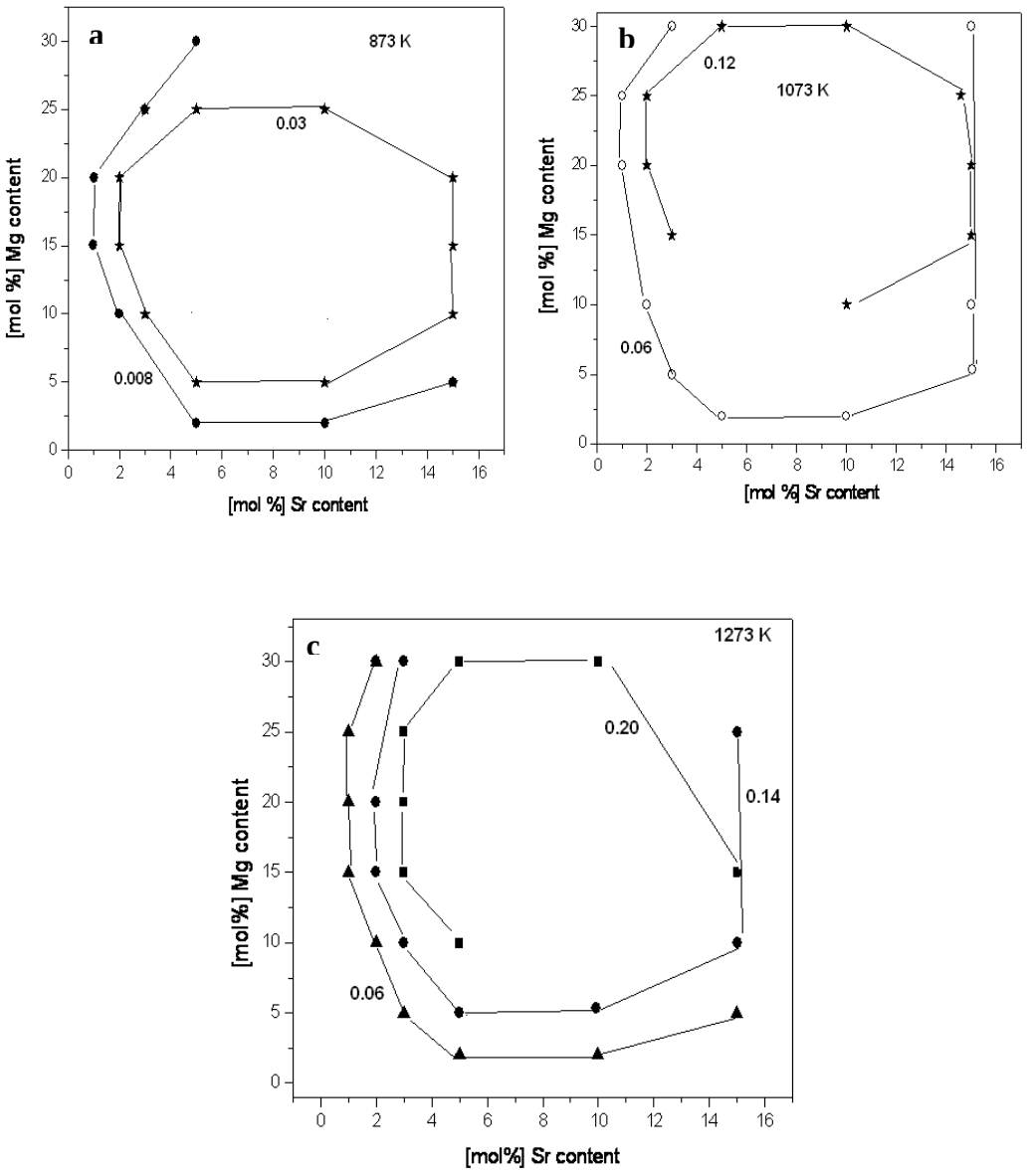

Fig. 4.2.42 Isoconductivity contours for $La_{1-x}Sr_xGa_{1-y}Mg_yO_{3-\delta}$ (where x=0-20 and y= 0-30 mol%) constructed at a) 600 ^oC, b) 800 ^oC and c) 1000^oC

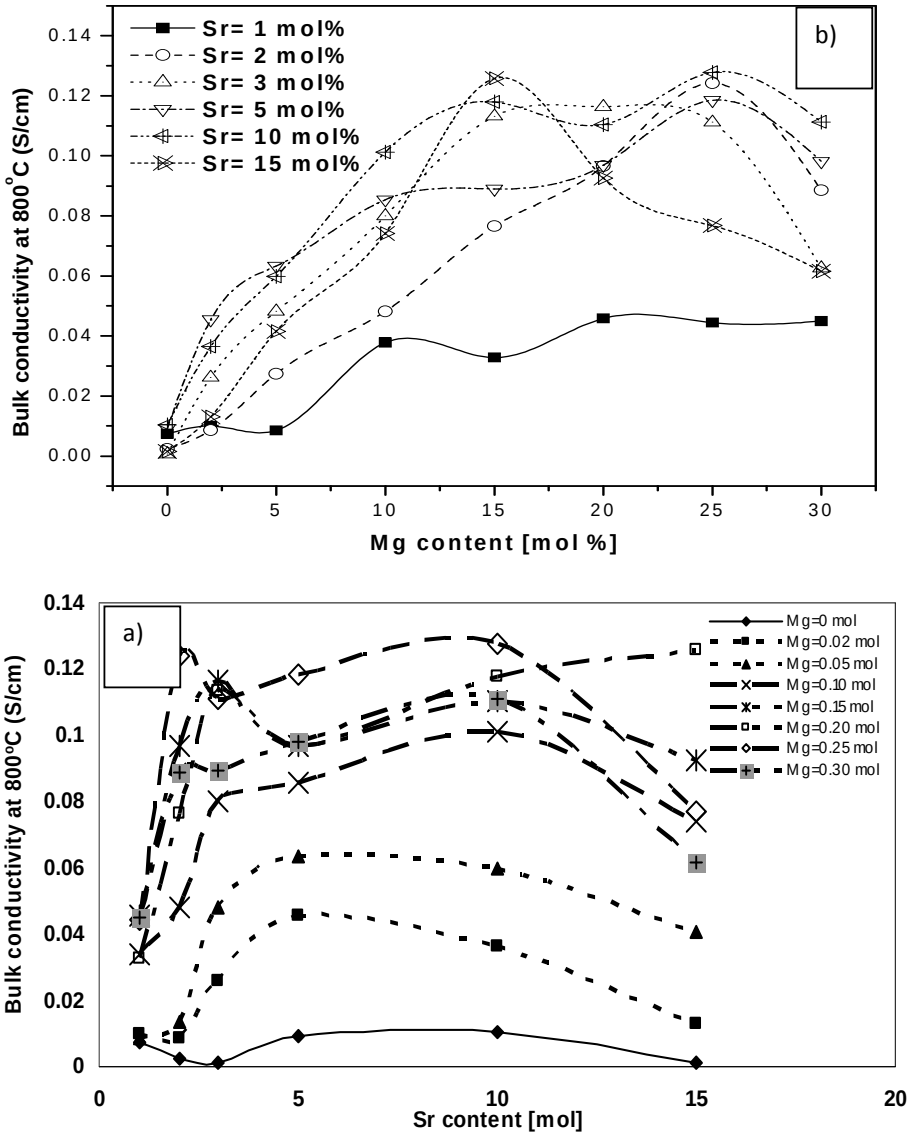

Fig. 4.2.43 The bulk conductivity of $La_{1-x}Sr_xGa_{1-y}Mg_yO_{3-\delta}$ is plotted against a) Sr content and b) Mg content in the A and B-sites

The variation of conductivity showed a trend similar to solubility. The conductivity increased with increase in dopant concentration both at the A- and B-sites until the formation of the second phase, after which it decreased with concentration. The highest bulk conductivity at 600, 800 and 1000°C of 0.028, 0.128 and 0.225 S/cm respectively was found for the compositions $La_{0.90}Sr_{0.10}Ga_{0.75}Mg_{0.25}O_{3-\delta}$ almost tallying with the highest

concentration of doping at the A- and B-sites. The Arrhenius plots for several compositions of Sr and Mg are displayed in Fig. 4.2.44. The Arrhenius plots did not yield a single straight line over the measured temperature range. The Arrhenius slopes showed different behavior in the two different temperature ranges 500-700^{o}C and 700-1000^{o}C. The slope was slightly higher in the low temperature than the high temperature range. At the low temperature range, the activation energy corresponded to the trapping of oxygen vacancies by the dopant cations and vacancy clustering whereas in the high temperature range, it corresponded to oxygen ion migration. The variation of activation energy for oxygen ion migration as a function of Sr and Mg concentrations are also given in Fig. 4.2.45. The activation energies for vacancy trapping by cations (E_1) as well as for oxygen ion migration (E_2) calculated for all the compositions in this study are summarized in Table 4.2.5.

Although in terms of maximum conductivities at different temperatures, the results obtained in the present study were in agreement with that reported in the literature, the behaviour of the activation energy with Sr and Mg concentrations at the A- and B- sites showed some differences with the literature [Huang et al, 1998; 2000; Liu et al, 2006; and Gorelov et al, 2001]. Further, the activation energies obtained in the present study was somewhat lower than the values reported in the literature. Although Huang et al [1998] observed the maximum in conductivity for Sr and Mg concentrations in the range of 12.5-25 mol %, the activation energy for both vacancy trapping and oxygen ion migration showed a minimum at 15-20 mol % Sr and 5 mol % Mg. They justified this observation pointing out that the superior oxygen ion conductivity in LSGM is associated with the Ga^{3+} and not the La^{3+} ion, and that the oxygen vacancy is more strongly trapped by a Ga-O-Mg bond than by a La-Sr-O bond. Chen and Fung [2004] also observed a similar trend i.e., the activation energy for oxygen ion migration decreased with increasing Sr content and decreasing Mg content. They attributed this to the large size difference between the gallium and magnesium ions. The large size difference would be expected to restrict the solubility of Mg at the Ga site. However, it was seen that the solubility of Mg in the perovskite phase was quite large (20-25 mol % at 1500^{o}C). In the studies of Liu et al [2006], the minimum in activation energy coincided with the maximum solubility range both for Sr and Mg as observed in the present study.

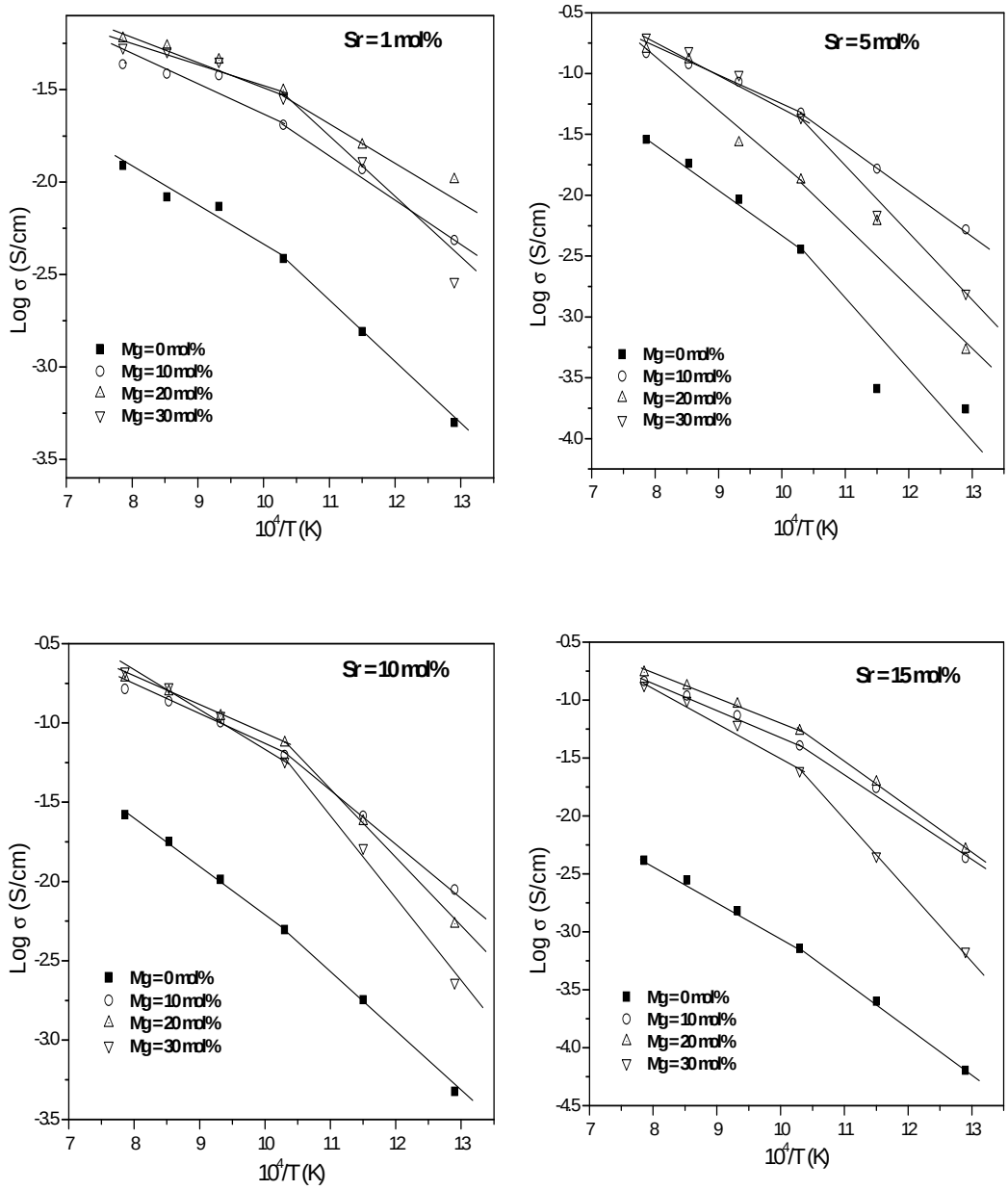

Fig.4.2.44 Arrhenius plot of $La_{1-x}Sr_xGa_{1-y}Mg_yO_{3-\delta}$ (where x=0-15 and y=0-30)

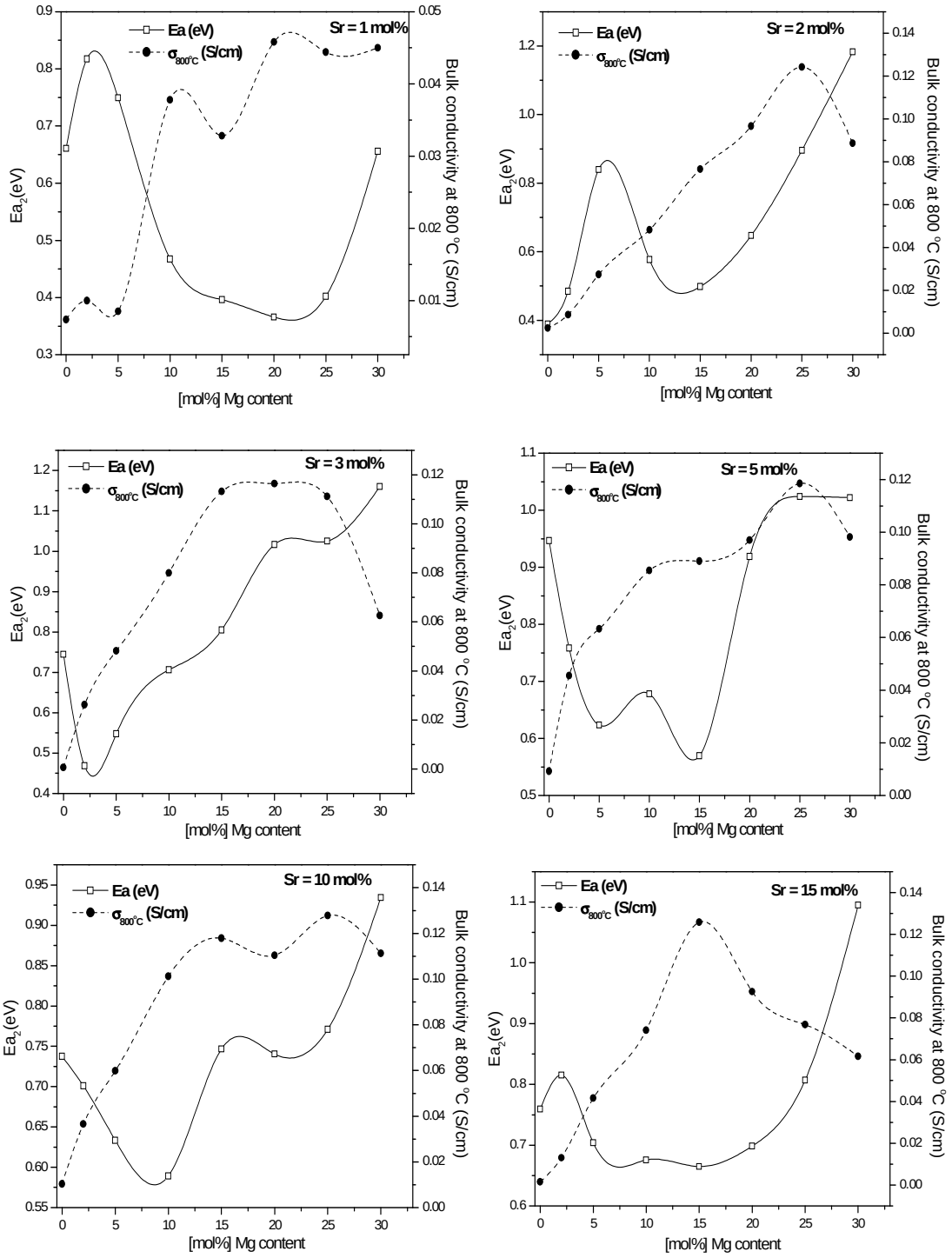

Fig.4.2.45 The variation of activation energy for oxygen ion migration as a function of Mg concentration at various concentration of Sr content

Table 4.2.5 The energy of activation of $La_{1-x}Sr_xGa_{1-y}Mg_yO_{3-\delta}$ at the low and high temperature ranges

Composition	Ea = slope x k (k = 8.62 x10^{-5} (eV/K)		Composition	Ea = slope x k (k = 8.62 x10^{-5} (eV/K)	
	500-700^{o}C	800-1000^{o}C		500-700^{o}C	800-1000^{o}C
LSG 01	0.66	0.39	LSG 05	0.95	0.74
LSGM 0102	0.81	0.29	LSGM 0502	0.76	0.53
LSGM 0105	0.75	0.36	LSGM 0505	0.62	0.42
LSGM 0110	0.47	0.25	LSGM 0510	0.68	0.40
LSGM 0115	0.40	0.29	LSGM 0515	0.57	0.32
LSGM 0120	0.37	0.23	LSGM 0520	0.92	0.96
LSGM 0125	0.40	0.21	LSGM 0525	1.02	0.47
LSGM 0130	0.66	0.22	LSGM 0530	1.02	0.54
LSG 02	0.39	0.82	LSG 10	0.74	0.60
LSGM 0202	0.48	0.24	LSGM 1002	0.70	0.50
LSGM 0205	0.84	0.52	LSGM 1005	0.63	0.43
LSGM 0210	0.58	0.42	LSGM 1010	0.59	0.34
LSGM 0215	0.50	0.37	LSGM 1015	0.75	0.44
LSGM 0220	0.65	0.39	LSGM 1020	0.74	0.34
LSGM 0225	0.89	0.39	LSGM 1025	0.77	0.41
LSGM 0230	1.18	0.47	LSGM 1030	0.93	0.47
LSG 03	0.74	0.74	LSG 15	0.76	0.63
LSGM 0302	0.47	0.57	LSGM 1502	0.81	0.59
LSGM 0305	0.55	0.42	LSGM 1505	0.70	0.50
LSGM 0310	0.71	0.45	LSGM 1510	0.67	0.45
LSGM 0315	0.80	0.32	LSGM 1515	0.66	0.37
LSGM 0320	1.02	0.41	LSGM 1520	0.70	0.41
LSGM 0325	1.02	0.50	LSGM 1525	0.80	0.48
LSGM 0330	1.16	0.67	LSGM 1530	1.09	0.60

4.3. CHARACTERIZATION AND ELECTRICAL PROPERTIES OF SECONDARY PHASES $La_4Ga_2O_9$, $LaSrGaO_4$, $LaSrGa_3O_7$ and $MgGa_2O_4$

Since no data was available on the electrical properties of the common impurity phases associated with LSGM i.e., $La_4Ga_2O_9$, $LaSrGaO_4$, $LaSrGa_3O_7$ and $MgGa_2O_4$, and since this information was necessary to ascertain the long term degradation behavior of solid oxide fuel cells based on lanthanum gallate, pure phases of $La_4Ga_2O_9$, $LaSrGaO_4$, $LaSrGa_3O_7$ and $MgGa_2O_4$ were synthesized and the electrical conductivities of these phases measured in the relevant temperature range.

4.3.1. Phase purity by X-ray diffraction

The powders synthesized by the Pechiney method were calcined at 900-1600^oC to get pure oxide powders.

The X-ray diffraction patterns of $LaSrGaO_4$, $La_4Ga_2O_9$, $LaSrGa_3O_7$ and Ga_2MgO_4 powders after calcination and sintering respectively are shown in Figs. 4.3.1- 4.3.4. It was observed (see Fig.4.3.1**)** that a small amount of impurity phases in addition to the $LaSrGaO_4$ were present in the calcined powder. The impurity phases were identified to be LaOCl (JCPDS file No. 34-1494) which might have formed because of the use of small amounts of hydrochloric acid for accelerating the gallium dissolution in nitric acid, $LaSrGa_3O_7$ (JCPDS file No.86-1839) and $SrGa_{12}O_{19}$ (JCPDS No. 26-0983). However, sintering the calcined product at 1300^oC for 6 h resulted in the elimination of the impurities and the formation of pure $LaSrGaO_4$. The XRD's of $La_4Ga_2O_9$ in the calcined and sintered states respectively are shown in Fig. 4.3.2. It was seen that for this phase also, calcination at 900^oC was not sufficient for the pure phase to form and secondary phases of $LaGaO_3$ and La_2O_3 were observed. However, sintering at 1100^oC for 4 hours yielded pure $La_4Ga_2O_9$. Figure 4.3.3 shows the X-ray diffraction patterns of $LaSrGa_3O_7$ powders calcined at 900 and sintered at 1500^oC. It was observed that in the calcined state, a small quantity of $SrGa_2O_4$ phase (JCPDS file No.22-0905) was present in addition to pure $LaSrGa_3O_7$. This phase disappeared upon heating at 1500^oC for 6 h and only pure $LaSrGa_3O_7$ (JCPDS file No.86-1839) was present in the product. The X ray diffraction patterns of $MgGa_2O_4$ powders after calcination at 900 and sintering at 1500^oC respectively are shown in Fig. 4.3.4. Traces of the impurity phase α-$GaCl_2$ (JCPDS file No. 39-1223) was detected which

might have formed because of the use of small amounts of hydrochloric acid for accelerating the gallium dissolution in nitric acid.

The synthesized pure oxides were indexed and its corresponding interplanar-spacings were used for lattice parameter calculations. $LaSrGaO_4$, $La_4Ga_2O_9$ oxides crystallized in the tetragonal structure whereas $LaSrGa_3O_7$ and Ga_2MgO_4 crystallized with a monoclinic and cubic symmetry respectively. The lattice parameter of the pure phases were calculated using the following equations,

For tetragonal,

$$\frac{1}{d^2} = \left(\frac{h^2 + k^2}{a^2} \right) + \frac{l^2}{c^2} \qquad [4.5]$$

For cubic,

$$\frac{1}{d^2} = \frac{h^2 + k^2 + l^2}{a^2} \qquad [4.6]$$

For monoclinic

$$\frac{1}{d^2} = \frac{1}{\sin^2 \beta} \left(\frac{h^2}{a^2} + \frac{k^2 \sin^2 \beta}{b^2} + \frac{l^2}{c^2} - \frac{2hl \cos \beta}{ac} \right) \qquad [4.7]$$

The crystallite size of the pure phases was calculated using Scherrer's equation (neglecting lattice strain and stacking fault effects):

$$d = \frac{0.9\lambda}{\beta \cos \theta} \qquad [4.8]$$

where d is the average size of the crystallite, 0.9 is the Scherrer's constant, λ is wave length of the X-ray radiation, β is the peak width at half-height (FWHM) in radians and θ corresponds to the peak position. The X ray density of the sintered pure phases was calculated from the lattice parameters using the equation:

$$\rho = \frac{z\,M}{N\,V} \qquad [4.9]$$

where ρ is the density of the sample, z is the number of unit cells, M is the molecular weight of the sample, N is the Avogadro's number and V is the volume of the unit cell. The calculated lattice parameters and crystallite sizes from the XRD data are summarized in Table 4.3.1.

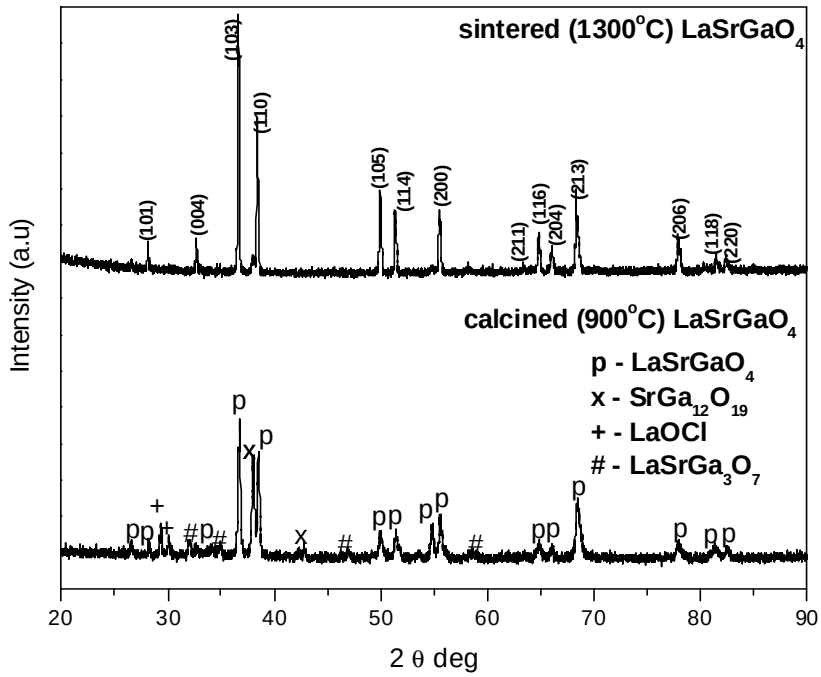

Fig.4.3.1 XRD pattern of calcined and sintered powders of $LaSrGaO_4$

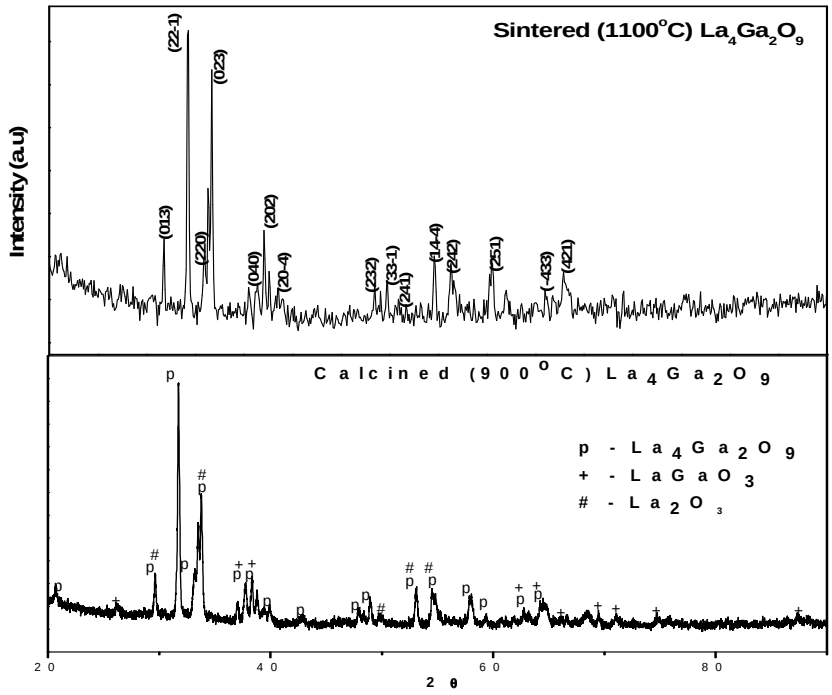

Fig. 4.3.2 XRD pattern of calcined and sintered powders of $La_4Ga_2O_9$

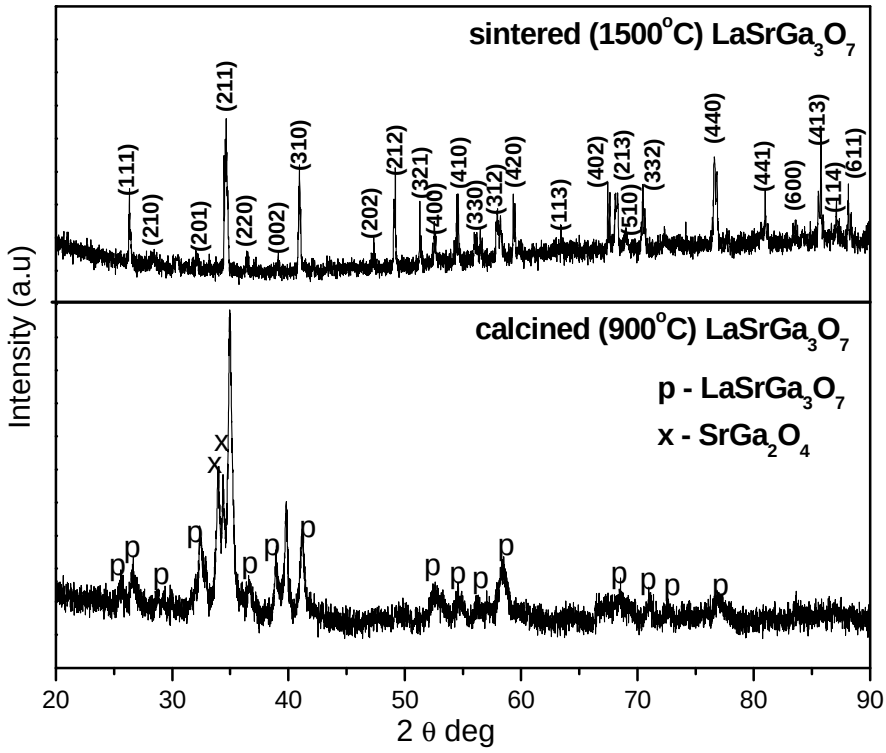

Fig. 4.3.3 XRD pattern of calcined and sintered powders of $LaSrGa_3O_7$

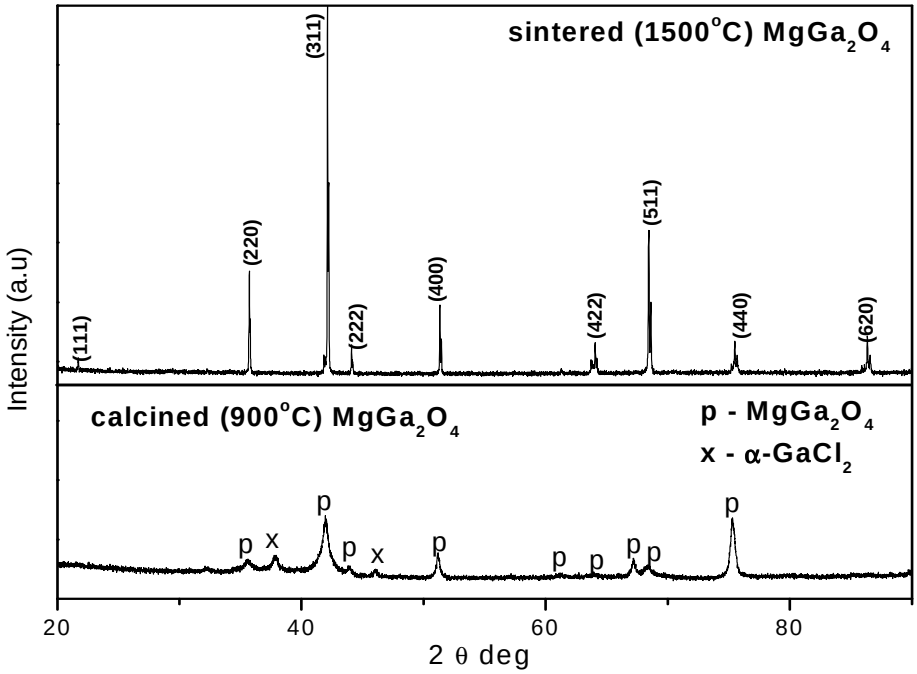

Fig. 4.3.4 XRD pattern of calcined and sintered powders of $MgGa_2O_4$

Table 4.3.1 Crystallographic data, conductivity values and energy of activation of $LaSrGaO_4$, $La_4Ga_2O_9$, $LaSrGa_3O_7$ and $MgGa_2O_4$

Materials	**Crystal structure**	**Lattice parameter (A˚)**	**Crystallite size (nm)**	**X-ray density (g/cc)**	**Bulk conductivity (S/cm)**					**Ea (eV)**
					600°C	**700 °C**	**800 °C**	**900 °C**	**1000 °C**	
$LaSrGaO_4$	Tetragonal	a = 3.835 c = 12.740	56	6.38	4.5E-7	3.0E-6	1.2E-5	3.3E-5	5.9E-5	1.09
$La_4Ga_2O_9$	Monoclinic	a = 8.040 b = 11.062 c = 11.719	106	5.63	3.7E-6	1.3E-5	3.0E-5	7.2E-5	1.5E-4	0.89
$LaSrGa_3O_7$	Tetragonal	a = 8.086 c = 5.405	31	5.16	1.9E-7	1.0E-6	3.9E-6	1.0E-5	2.5E-5	0.77
$MgGa_2O_4$	Cubic	8.249	154	5.39	1.2E-7	6.7E-7	3.0E-6	2.7E-5	2.2E-4	1.43

4.3.2. Thermogravimetric and Differential Thermal Analysis

The TG/DTA results (from ambient temperature to 1325^{o}C).of $LaSrGaO_4$, $La_4Ga_2O_9$, $LaSrGa_3O_7$ and Ga_2MgO_4 precursors obtained after calcination and the pure phases obtained after sintering at a higher temperature are given in Figs. 4.3.5-4.3.8. $LaSrGaO_4$ powders shows an endothermic phase transformation at ~800^{o}C with about 10% mass loss for the calcined sample (Fig. 4.3.5**)** whereas other phases show only a small mass loss (< 5%). However, $LaSrGaO_4$, $La_4Ga_2O_9$, $LaSrGa_3O_7$ and Ga_2MgO_4 phases sintered at high temperatures shows no subsequent mass loss or heat effects in TGA and DTA.

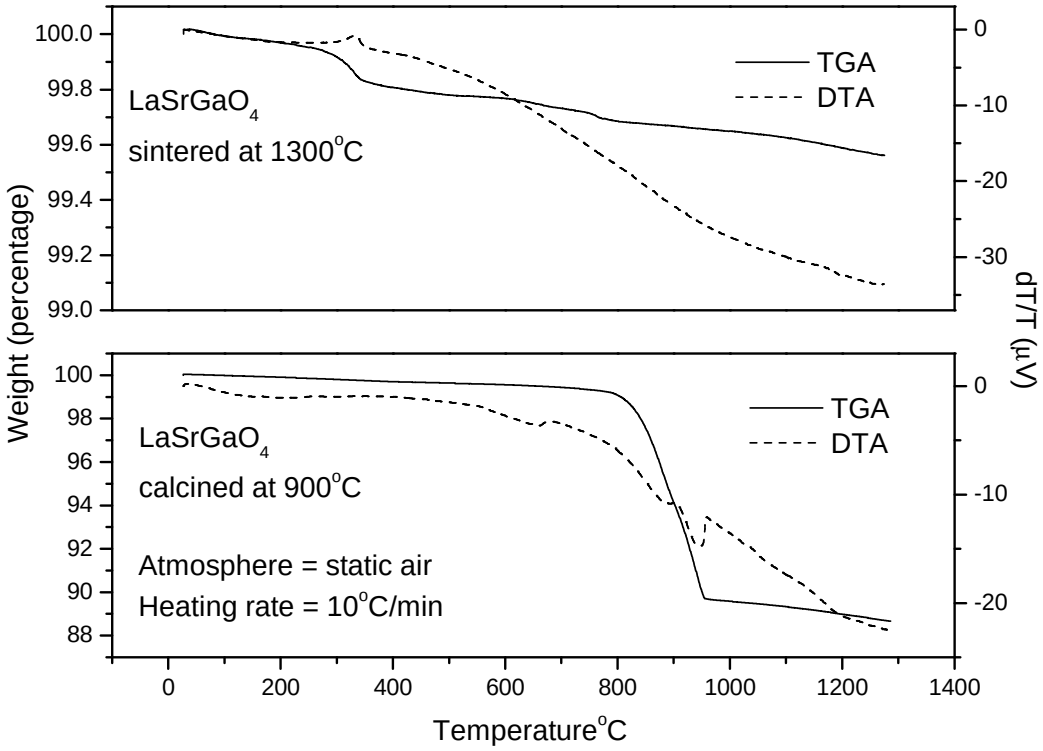

Fig. 4.3.5 TGA and DTA pattern of calcined and sintered powders of $LaSrGaO_4$

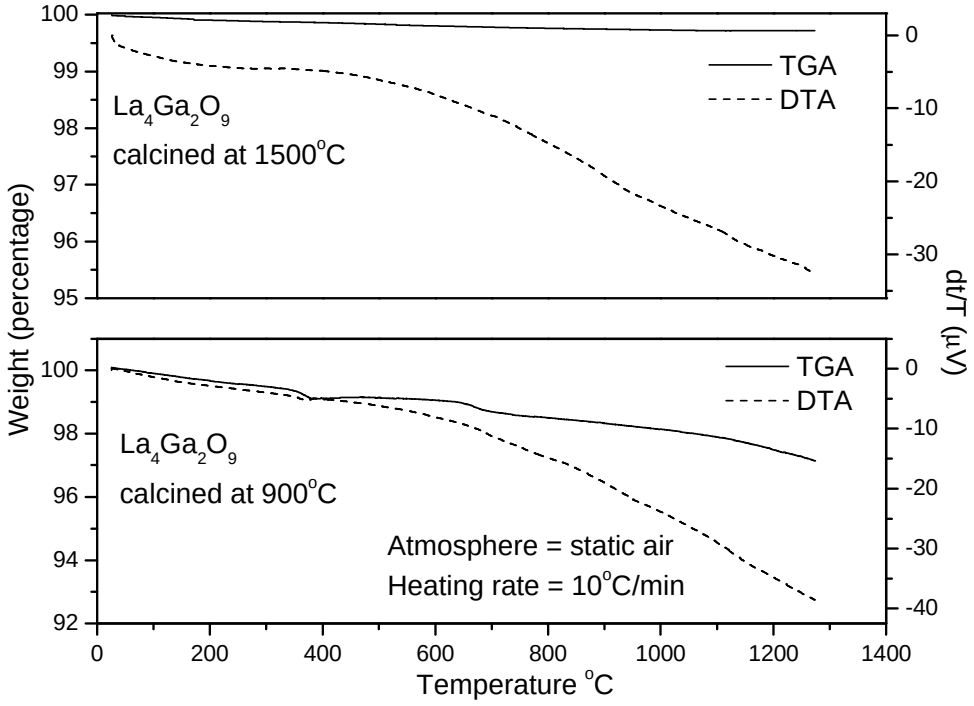

Fig. 4.3.6 TGA and DTA pattern of calcined and sintered powders of $La_4Ga_2O_9$

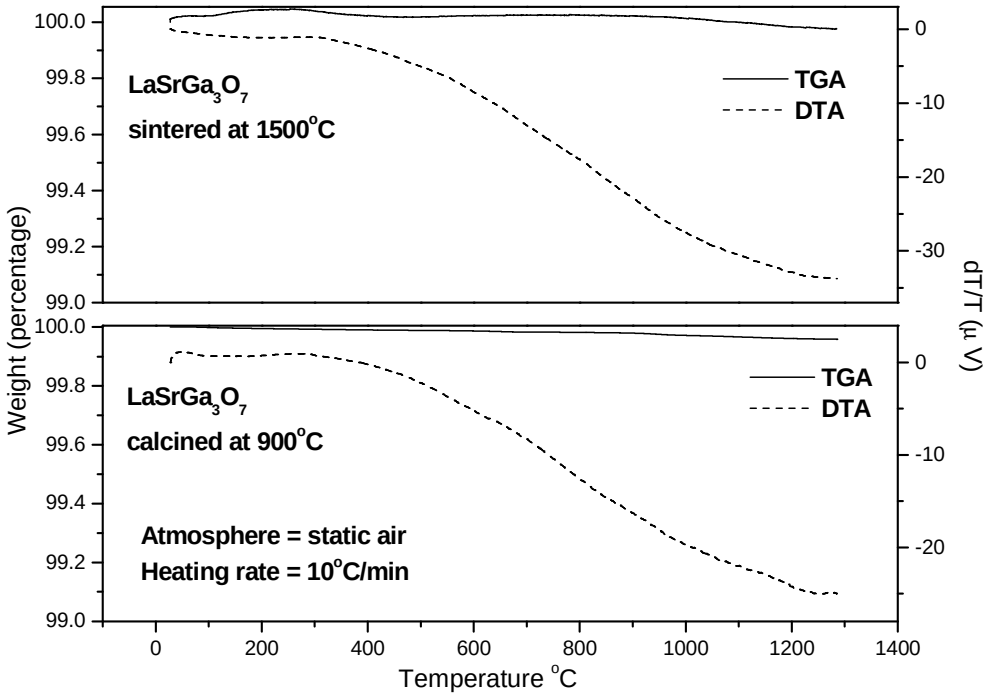

Fig. 4.3.7 TGA and DTA pattern of calcined and sintered powders of $LaSrGa_3O_7$

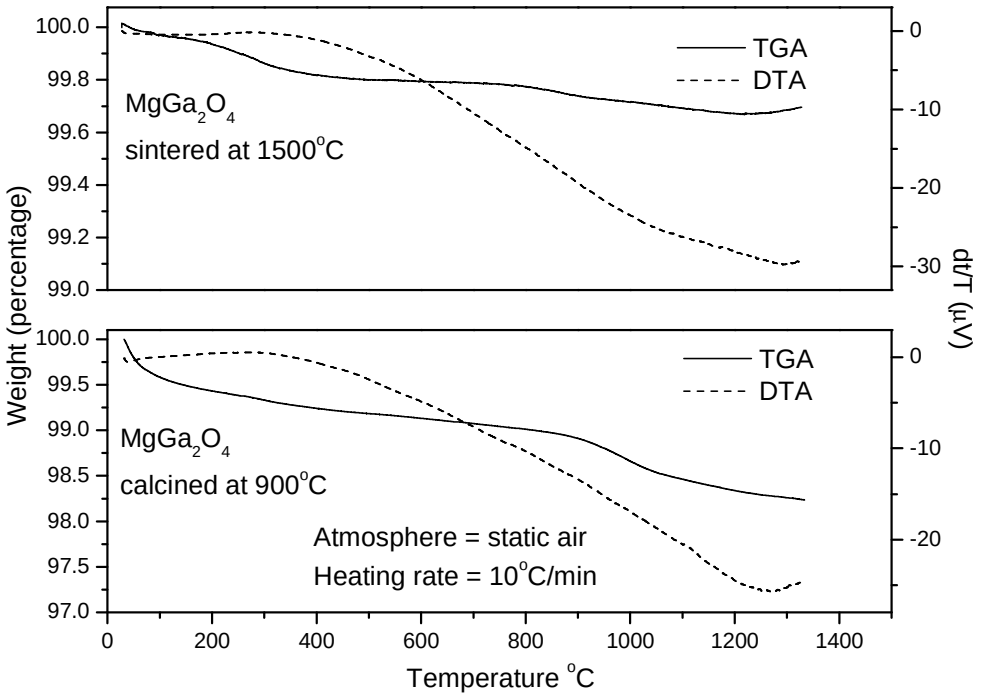

Fig. 4.3.8 TGA and DTA pattern of calcined and sintered powders of $MgGa_2O_4$

4.3.3. Scanning electron microscopy with EDAX

The back scattered electron images of pure $LaSrGaO_4$, $La_4Ga_2O_9$, $LaSrG_3O_7$ and Ga_2MgO_4 phases are shown in Fig.4.3.9a-c. It was seen that for all the phases synthesized the microstructure corresponded to that of a dense single phase except for $La_4Ga_2O_9$ which revealed a single phase microstructure with pores (Fig.4.3.9b). The bulk analysis of the synthesized pure phases was carried out by EDAX and is summarized in Table 4.3.2. Bulk analysis by EDAX especially of oxygen is only semi-quantitative and has large uncertainties.

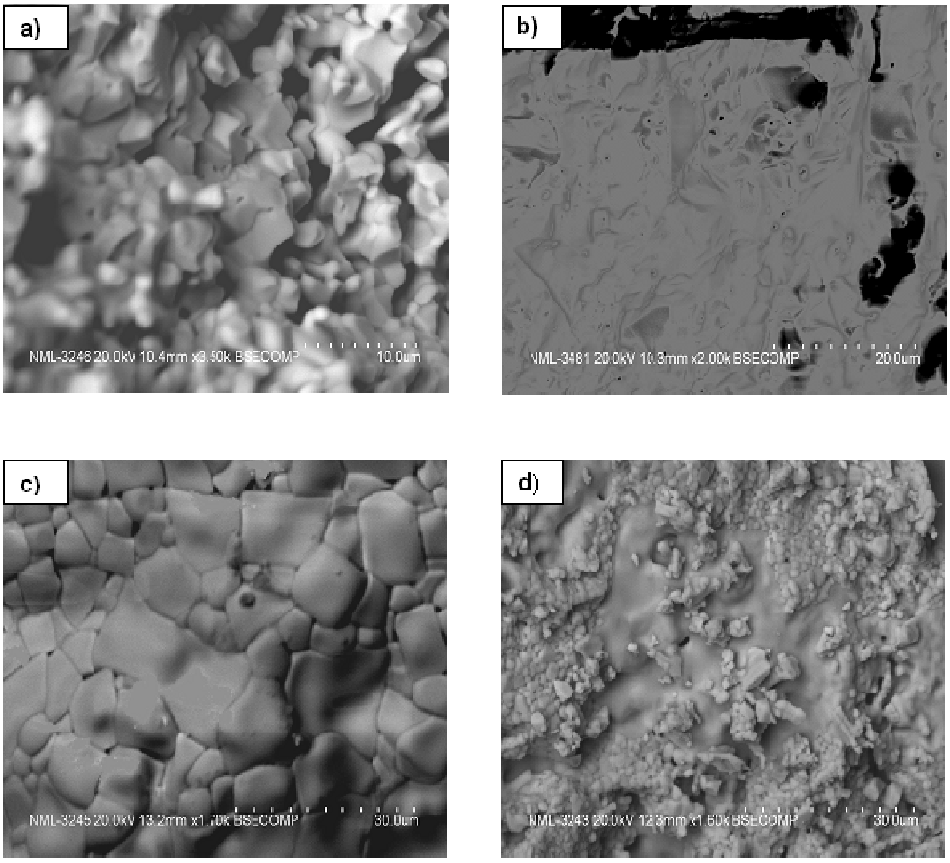

Fig. 4.3.9 Scanning electron images of a) $LaSrGaO_4$ b) $La_4Ga_2O_9$, c) $LaSrGa_3O_7$ and d) $MgGa_2O_4$

Table 4.3.2 EDAX results of synthesized $LaSrGaO_4$, $La_4Ga_2O_9$, $LaSrGa_3O_7$ and $MgGa_2O_4$ compounds

Atomic ratio (%)	**Materials**					
	$LaSrGaO_4$	**$La_4Ga_2O_9$**	**$LaSrGa_3O_7$**	**$MgGa_2O_4$**		
	1300°C	**1200°C**	**1500°C**	**1300°C**		**1500°C**
	Matrix	**Matrix**	**Matrix**	**Matrix**	**Secondary phase**	**Matrix**
La	10.68	29.79	8.05	-	-	-
Sr	15.72	-	8.55	-	-	-
Ga	13.91	16.60	21.87	23.33	60.73	24.08
Mg	-	-	-	15.15	-	14.47
O	59.69	53.19	61.53	61.52	32.45	61.45

4.3.4. Conductivity measurements

The impedance plots at different temperatures between 700-1000°C of the pure phases $LaSrGaO_4$, $La_4Ga_2O_9$, $LaSrGa_3O_7$ and $MgGa_2O_4$ are shown in Figs. 4.3.10-4.3.14. Since the impedance analysis measurements were at high temperatures, a typical 3-semi circle plot was not obtained. It showed only one semi-circle corresponding to the

bulk resistance of the sample. The Arrhenius plot of the variation of conductivity with reciprocal temperature is displayed in Fig. 4.3.15. The measured conductivities at different temperatures and the calculated activation energies are also tabulated in Table 4.3.1. The total electrical conductivity for these compounds vary in the range of 10^{-4} to 10^{-7} in the temperature range 600-1000^{o}C.

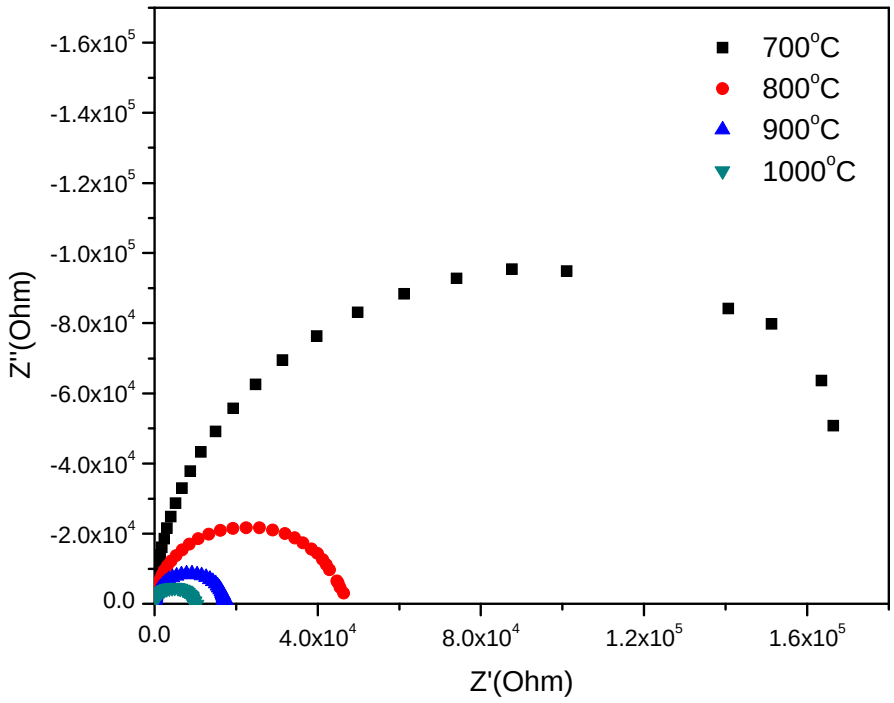

Fig. 4.3.10 Nyquist plot for $LaSrGaO_4$ at different temperatures

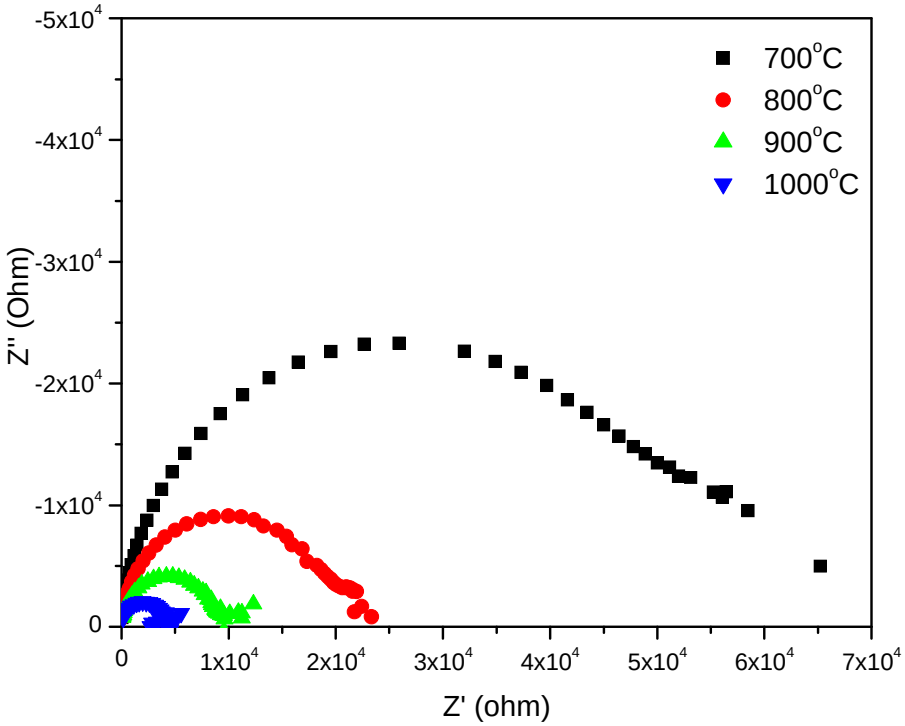

Fig. 4.3.11 Nyquist plot for $La_4Ga_2O_9$ at different temperatures

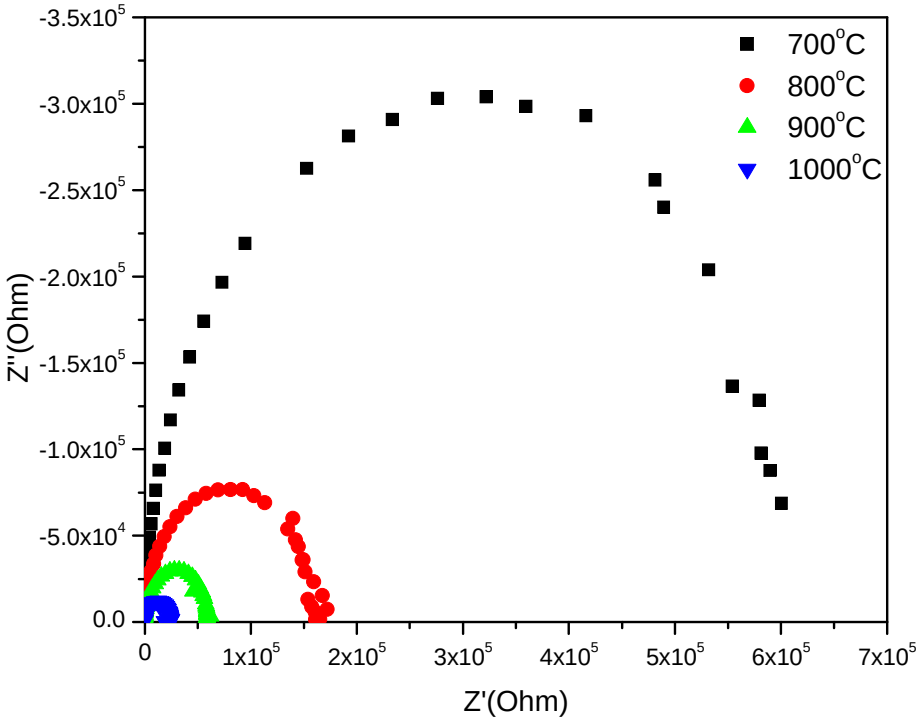

Fig. 4.3.12 Nyquist plot for $LaSrGa_3O_7$ at different temperatures

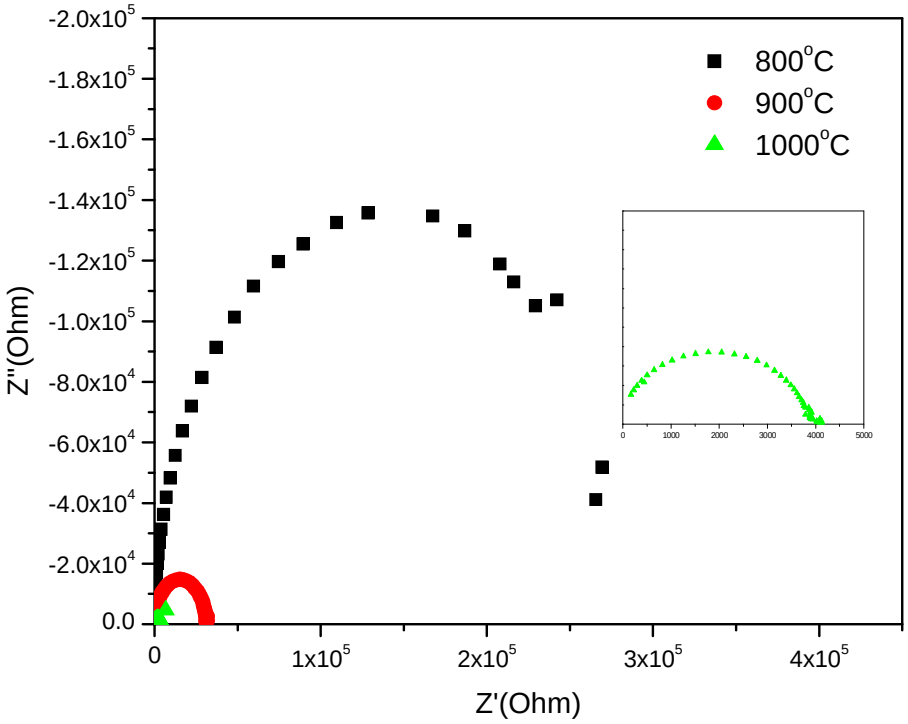

Fig. 4.3.13 Nyquist plot for Ga_2MgO_4 at different temperatures

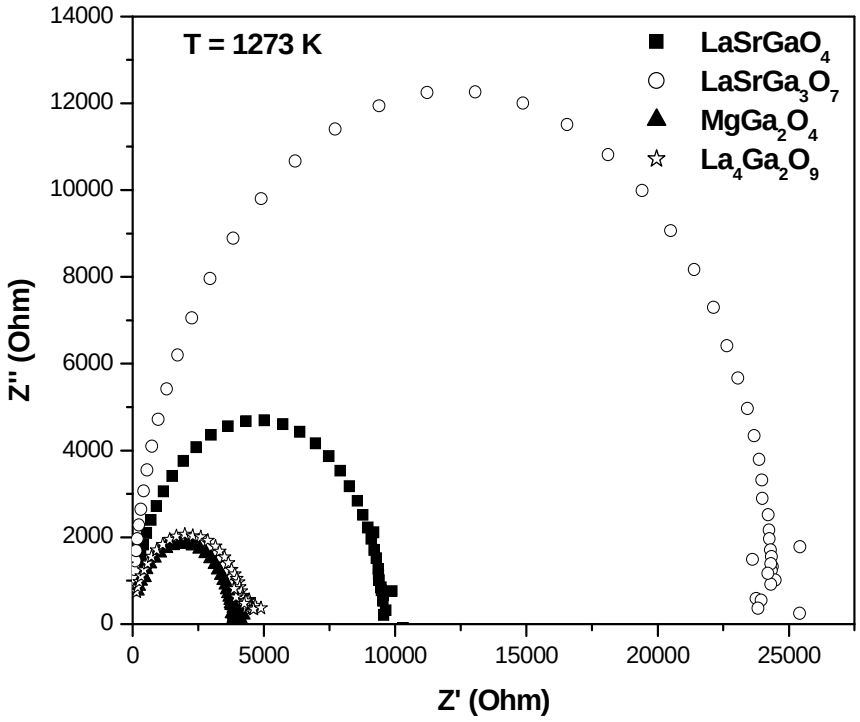

Fig. 4.3.14 Nyquist plot for a) $LaSrGaO_4$ b) $La_4Ga_2O_9$, c) $LaSrGa_3O_7$ and d) $MgGa_2O_4$ at 1000°C

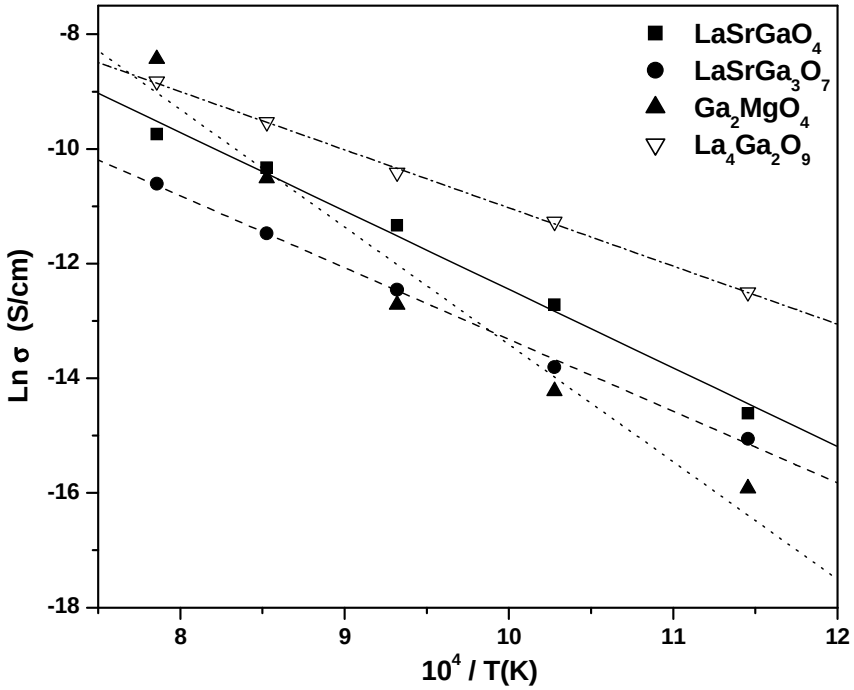

Fig. 4.3.15 Arrhenius plot of $LaSrGaO_4$, $La_4Ga_2O_9$, $LaSrGa_3O_7$ and $MgGa_2O_4$

4.3.5. Transport number measurements

Transport number measurements on the pure phases $LaSrGaO_4$, $La_4Ga_2O_9$, $LaSrGa_3O_7$ and $MgGa_2O_4$ were carried out using the EMF technique. The open circuit potential (OCP) of the electrochemical cells: O_2,Pt/$LaSrGaO_4$/Pt,H_2; O_2/$La_4Ga_2O_9$/Pt,H_2,Pt, O_2/$LaSrGa_3O_7$/Pt,H_2 and O_2,Pt/Ga_2MgO_4/Pt,H_2 were measured in the temperature range of 800-1000^oC at an interval of 100^oC. The open circuit voltages were recorded as a function of time (up to 8 hours) using the potentiostat.

The open circuit potentials (OCP/OCV) of these cells as a function of time at different temperatures with a flow of 30ml/min of hydrogen (pH_2=1 atm) and 10ml/min of oxygen (pO_2= 1 atm) are shown in Figs. 4.3.16-4.3.18. The open circuit voltage for all the cells remained constant for periods in excess of four hours and gave the same value on temperature recycling. The flow rates of hydrogen and oxygen did not have any effect on the OCV. For the Ga_2MgO_4 based cell, the open circuit potential was close to zero in the temperature range 800-1000^oC. The maximum OCP of 0.22 V was observed for $LaSrGa_3O_7$ based cell at 1000 ^oC whereas other cells yielded a maximum open circuit voltage of less than 0.15 V at the same temperature.

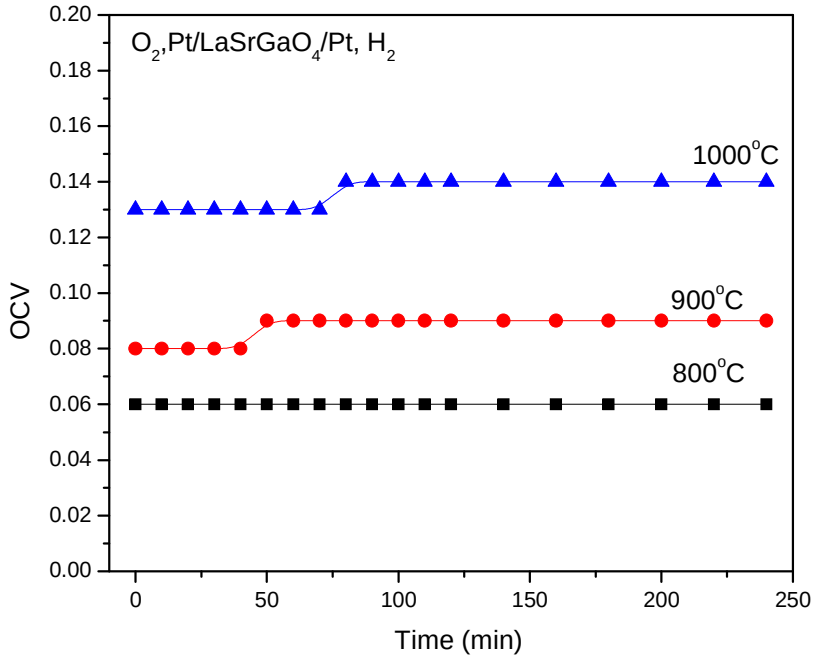

Fig. 4.3.16 The OCP of O_2,Pt/$LaSrGaO_4$/Pt,H_2 cell as a function of time

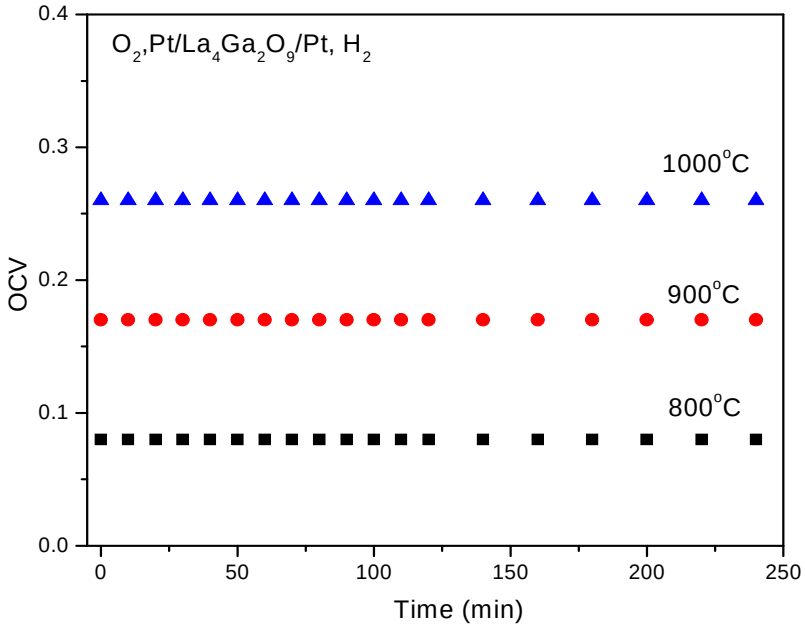

Fig. 4.3.17 The OCP of O_2, Pt/$La_4Ga_2O_9$/Pt, H_2 symmetric cell as a function of time

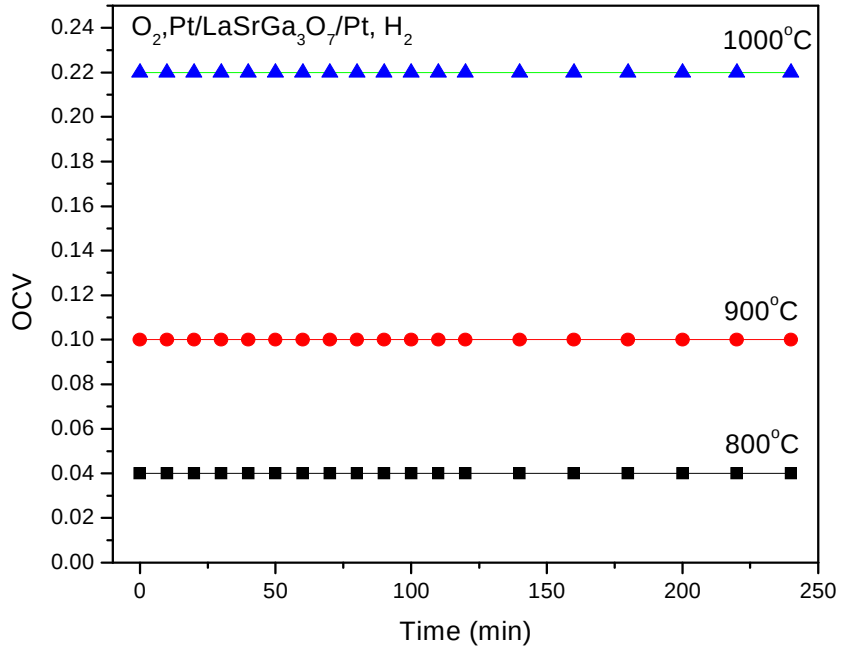

Fig. 4.3.18 The OCP of O_2, Pt/$LaSrGa_3O_7$/Pt, H_2 symmetric cell as a function of time

The measured open circuit potentials were used for the calculation of transport numbers for the respective oxides using the following equation,

$$t_{ion} = \frac{E_{measured}}{E_{Nernstian}} \qquad [4.10]$$

where t_{ion} is the transport number of the oxide ions, E_{meas} is the OCP measured experimentally and $E_{Nernstian}$ is the thermodynamic Nernstian potential. The transport number of $LaSrGaO_4$, $La_4Ga_2O_9$, $LaSrGa_3O_7$ and $MgGa_2O_4$ oxides at different temperatures is given in Table 4.3.3. As expected, the ionic transport number for all these oxides are small indicating the insulating nature of the $LaSrGaO_4$, $La_4Ga_2O_9$, $LaSrGa_3O_7$ and $MgGa_2O_4$ oxides.

Table 4.3.3 Transport number $LaSrGaO_4$, $La_4Ga_2O_9$, $LaSrGa_3O_7$ and $MgGa_2O_4$ oxides obtained by EMF method

	Transport number (t_{ion})		
Materials	**800°C**	**900°C**	**1000°C**
$LaSrGaO_4$	0.05	0.06	0.11
$La_4Ga_2O_9$	0.06	0.14	0.21
$LaSrGa_3O_7$	0.03	0.08	0.18
Ga_2MgO_4	0	0	0

4.4. AREA SPECIFIC RESISTANCE (ASR) MEASUREMENTS AND POLARIZATION STUDIES OF ELECTROLYTE SUPPORTED SINGLE CELLS

This section deals with the results on fabrication, area specific resistance measurements (ASR) and testing of single cells based on the materials synthesized. (i.e., $La_{0.90}Sr_{0.10}Ga_{0.80}Mg_{0.20}O_{3-\delta}$ (LSGM 9182) as electrolyte; $La_{0.6}Sr_{0.4}Co_{0.2}Fe_{0.80}O_{3-\delta}$ (LSCF6428) as cathode; NiO+$La_{0.90}Sr_{0.10}Ga_{0.80}Mg_{0.20}O_{3-\delta}$ and NiO+$Ce_{0.9}Gd_{0.1}O_{2-\delta}$ as anodes).

4.4.1. Area Specific Resistance Measurements

Area specific resistances of symmetric cathode based cells (using LSF, LSC and LSCF) under pure oxygen atmosphere and anode based cells (using NiO+LSGM and GDC+NiO) under pure hydrogen atmosphere with LSGM9182 as electrolyte and for the complete cells Pt,H_2,NiO+LSGM/LSGM/LSCF,O_2,Pt and Pt,H_2,NiO+GDC/LSGM/LSCF,O_2,Pt were measured as a function of temperature by AC two-probe electrochemical impedance spectroscopy. ASR measurements were also carried out as a function of gas flow rates.

4.4.1.1. ASR of Cathode/LSGM9182 based cells

LSF 9010, LSC 9010 and LSCF6428 cathode materials were used for ASR measurements. The Nyquist plots for the symmetric cells: Pt,LSF/LSGM9182/LSF,Pt; Pt,LSC/LSGM9182/LSC,Pt and Pt,LSCF/LSGM9182/LSCF, Pt are shown in Figs. 4.4.1-4.4.3. The high frequency intercept of the Nyquist plot gave the ohmic resistance of the cell (R_s), which included the resistive contributions of the electrolyte, the two electrodes, the current collectors and the lead wires. The low frequency intercept gave the total resistance (R_s+R_e), which included the total ohmic resistance of the cell (R_s), and the effective interfacial polarization resistance at the electrodes (R_e). The total polarization resistance of the cell was extracted from the impedance plot. For most samples measured in this investigation, a single depressed arc was observed. The area specific resistance was determined from the impedance results using the following equation:

$$\text{ASR } (\Omega.cm^2) = \text{Area x polarization resistance}$$

The measured area specific resistance of the LSF-, LSC- and LSCF-based symmetric cells was 0.09, 0.62 and 0.03 $\Omega.cm^2$ respectively at 800^oC. The ASR value for the LSC

cell was much higher than that for the LSF-cell which was higher than the LSCF cell. Gong and co-workers [2004] studied the ASR measurement of different cathode materials with LSGM electrolyte. Their reported interfacial resistance values were 0.21Ω. The ASR value for the Pt,O_2,LSCF/LSGM/lSCF,O_2,Pt cell obtained in this study was much smaller than that reported by Gong and co-workers [2004]. The ASR of the symmetric cells Pt,O_2,LSCF/LSGM/LSCF,O_2,Pt; Pt,O_2,LSF/LSGM/LSF,O_2,Pt and Pt,O_2,LSC/LSGM/LSC,O_2,Pt as a function of temperature are shown in Figs. 4.4.4 – 4.4.6. As expected, the measured ASR values decreased with increasing temperature.

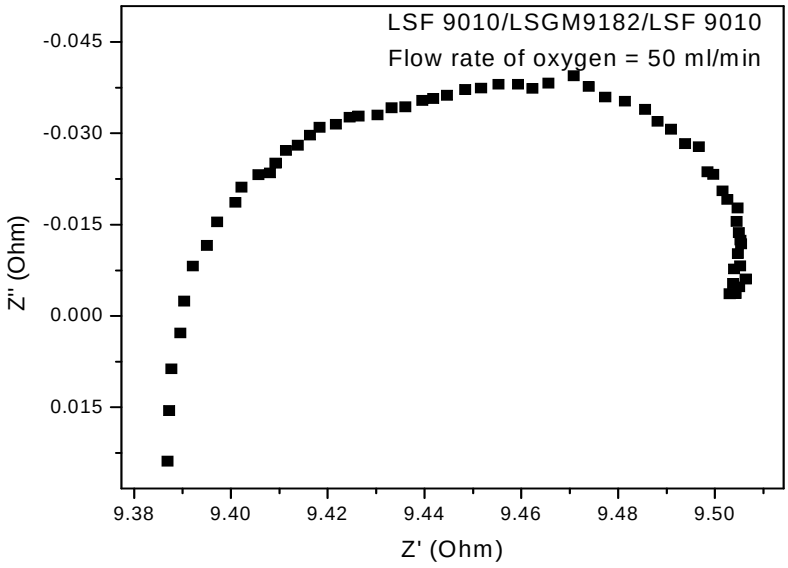

Fig.4.4.1 Nyquist plot of Pt, LSF/LSGM/LSF,O_2,Pt at 800 ^oC

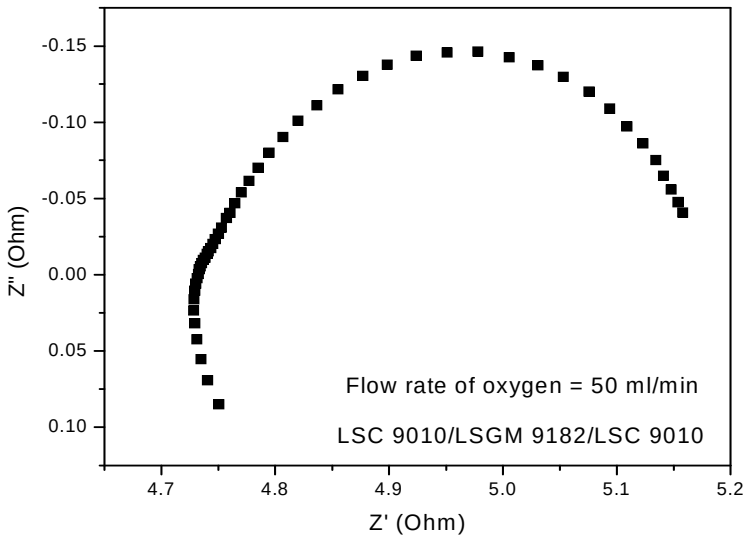

Fig.4.4.2 Nyquist plot of Pt,O_2,LSC/LSGM/LSC,O_2,Pt at 800 ^oC

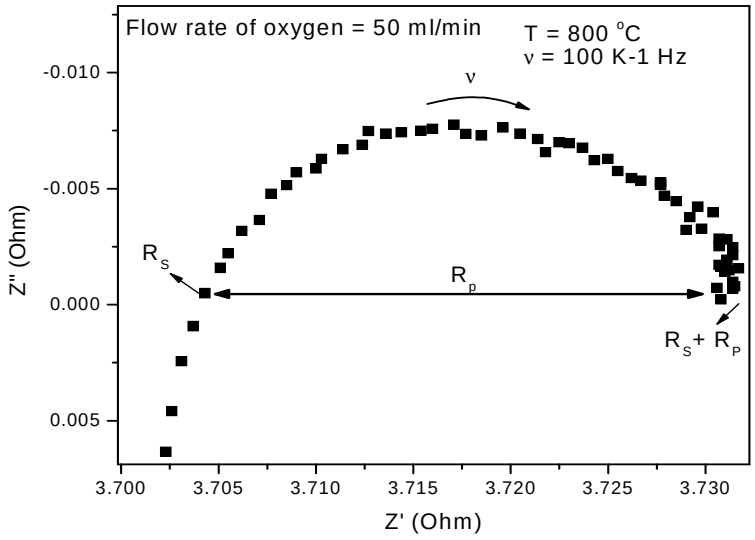

Fig.4.4.3 Nyquist plot of Pt,O_2,LSCF/LSGM/LSCF,O_2,Pt at 800 ^oC

The variation of ASR at 800^oC with flow rate of oxygen for the symmetric cells with different cathode materials is shown in Figs. 4.4.7-4.4.9. The ASR value of the cell Pt,O_2,LSCF/LSGM/LSCF,O_2,Pt at 800^oC decreased with increasing flow rate of oxygen up to 160 ml/min and thereafter increased. In the case of Pt,O_2,LSF/LSGM/LSF,O_2,Pt and Pt,O_2,LSC/LSGM/LSC,O_2,Pt cells, the ASR value increased marginally with increasing gas flow rate.

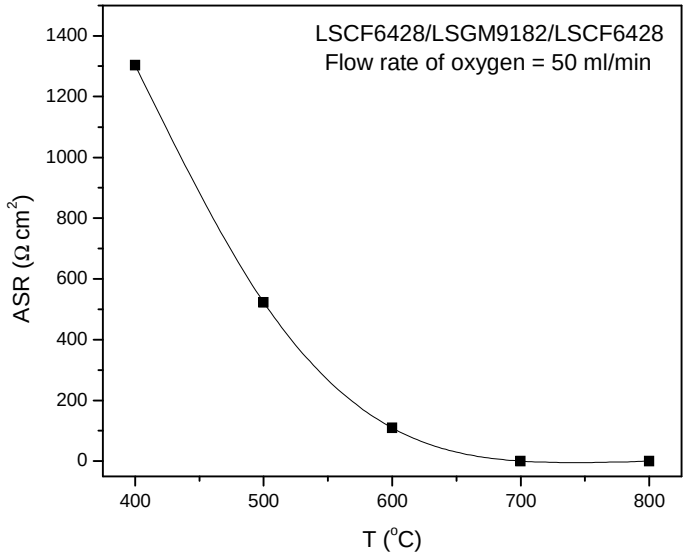

Fig.4.4.4 ASR of Pt,O_2,LSCF/LSGM/LSCF,O_2,Pt is plotted as a function of temperature at constant oxygen flow rate.

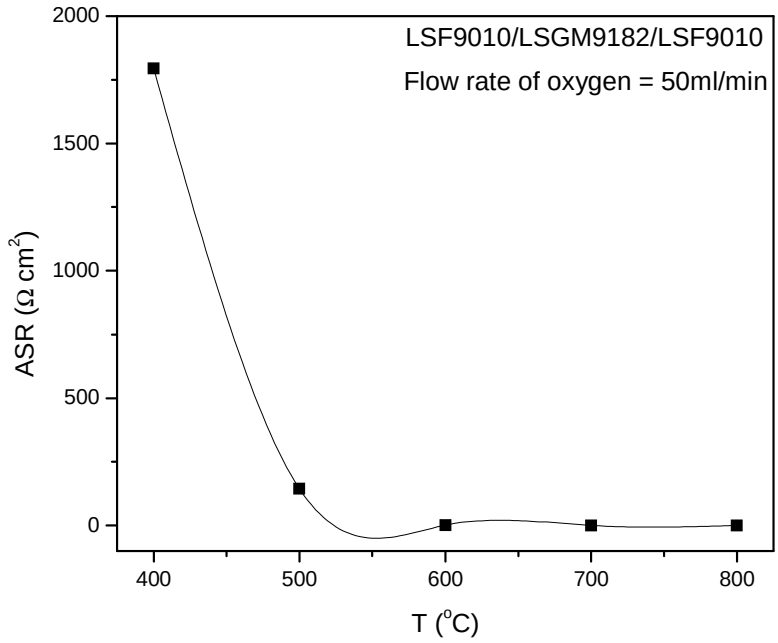

Fig.4.4.5 ASR of Pt,O_2,LSF/LSGM/LSF,O_2,Pt is plotted as a function of temperature at constant oxygen flow rate.

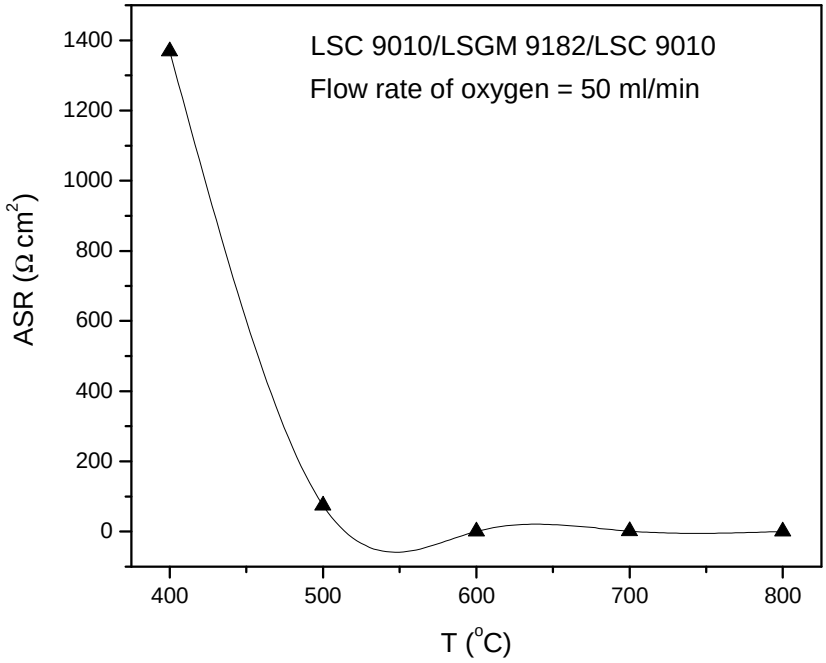

Fig.4.4.6 ASR of Pt,O_2,LSC/LSGM/LSC,O_2,Pt is plotted as a function of temperature at constant oxygen flow rate.

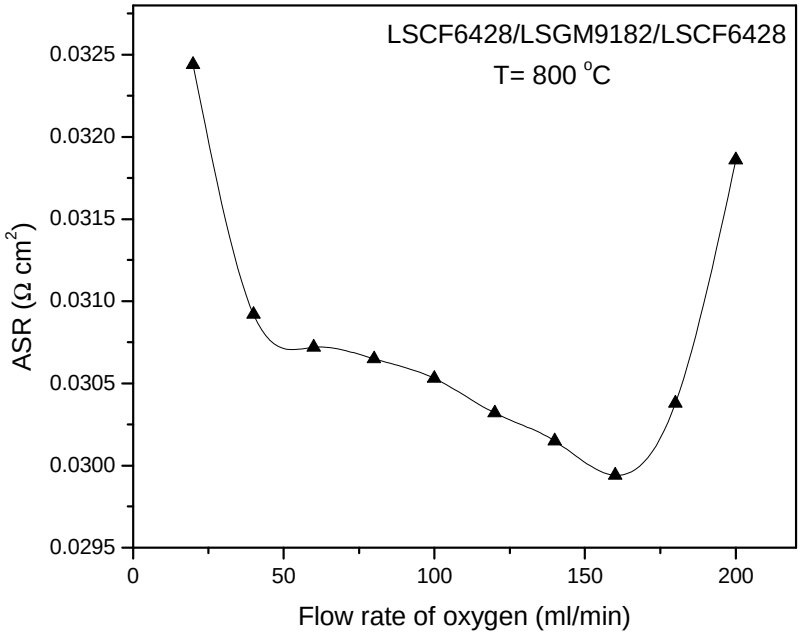

Fig.4.4.7 ASR of Pt,O_2,LSCF /LSGM/LSCF,O_2,Pt is plotted as a function of different flow rate of oxygen gas at 800^{o}C.

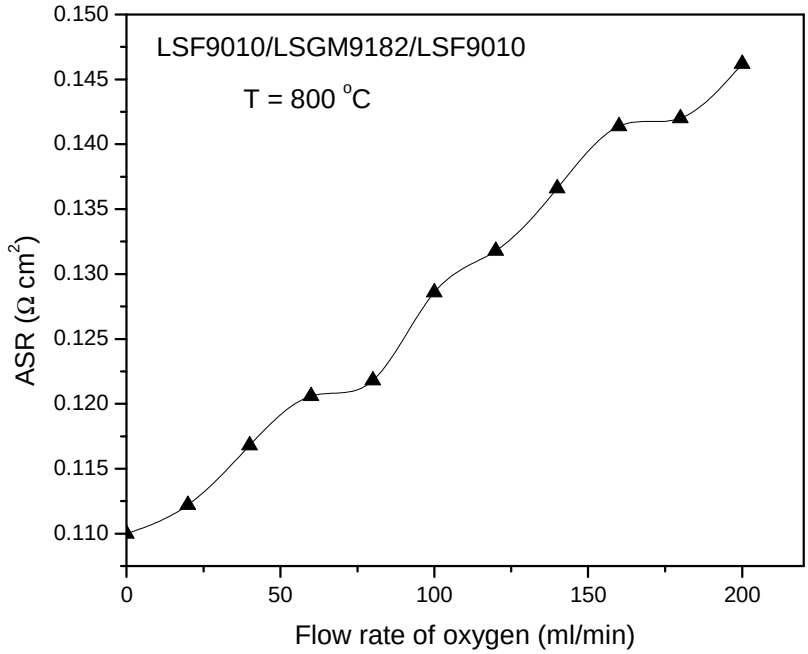

Fig.4.4.8 ASR of Pt,O_2,LSF/LSGM/LSF,O_2,Pt is plotted as a function of different flow rate of oxygen gas at 800^{o}C.

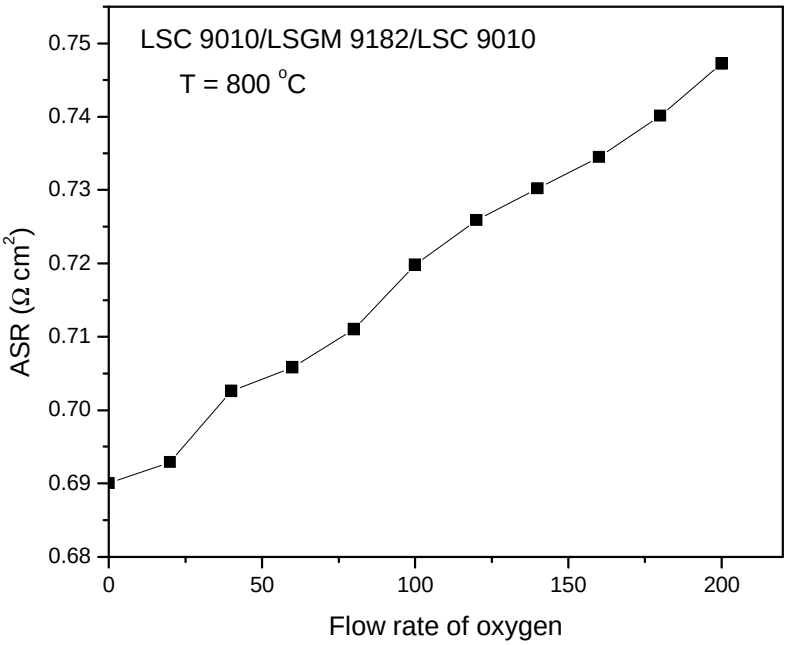

Fig.4.4.9 ASR of Pt,O_2,LSC /LSGM/LSC,O_2,Pt is plotted as a function of different flow rate of oxygen gas at 800^{o}C.

4.4.1.2. ASR of Anode/LSGM based cells

NiO+LSGM and NiO+GDC were used in conjunction with LSGM9182 electrolyte for constructing the single cells. The ASR measurements on Pt,H_2,NiO+LSGM/LSGM/NiO+LSGM,H_2,Pt and Pt,H_2,NiO +GDC/ LSGM/ NiO +GDC,H_2,Pt symmetric cells as a function of temperature and hydrogen gas flow rates were carried out by electrochemical impedance spectroscopy. A typical Nyquist plot of the cell; Pt,H_2,NiO+LSGM/LSGM/NiO+LSGM,H_2,Pt at 800^{o}C is shown in Fig. 4.4.10. The variation of ASR values of the symmetric cell Pt,H_2,NiO+LSGM/LSGM/NiO+LSGM,H_2,Pt with temperature and hydrogen flow rate are shown in Figs.4.4.11-4.4.12 respectively**.** The ASR value of this cell decreased from 85 Ωcm^2 at 500^{o}C to 11 Ωcm^2 at 800^{o}C. The resistance of this cell was much higher than the desired value for application in SOFC. The high area specific cell resistance was attributed to the interfacial reaction of nickel with LSGM to form lanthanum nickelate [Huang and Goodenough, 2000]. They reported that use of a thin interlayer (samarium doped ceria) at the anode-electrolyte interface prevented the formation of

this insulating phase. With increasing flow rate of hydrogen, the ASR value also increased.

A typical Nyquist plot of the Pt,H_2,NiO+GDC/LSGM/NiO+GDC,H_2,Pt symmetric cell at at 800^{o}C and a hydrogen flow rate of 50ml/min is shown in Fig. 4.4.13. The variation of ASR for the symmetric cell Pt,H_2,NiO+LSGM/LSGM/NiO+LSGM,H_2,Pt with temperature and hydrogen flow rate are shown in Figs.4.4.14-4.4.15 respectively. The ASR values of NiO+GDC anode were much smaller when compared to that of the symmetric cells using NiO+LSGM. When the flow rate of hydrogen was increased, the ASR value decreased up to a flow rate of 60ml/min of hydrogen and thereafter increased. Since GDC is an excellent oxygen ion conductor in the temperature range of interest and is chemically and mechanically compatible with the LSGM electrolyte, the use of NiO+GDC as anode is preferable for use in intermediate temperature solid oxide fuel cells.

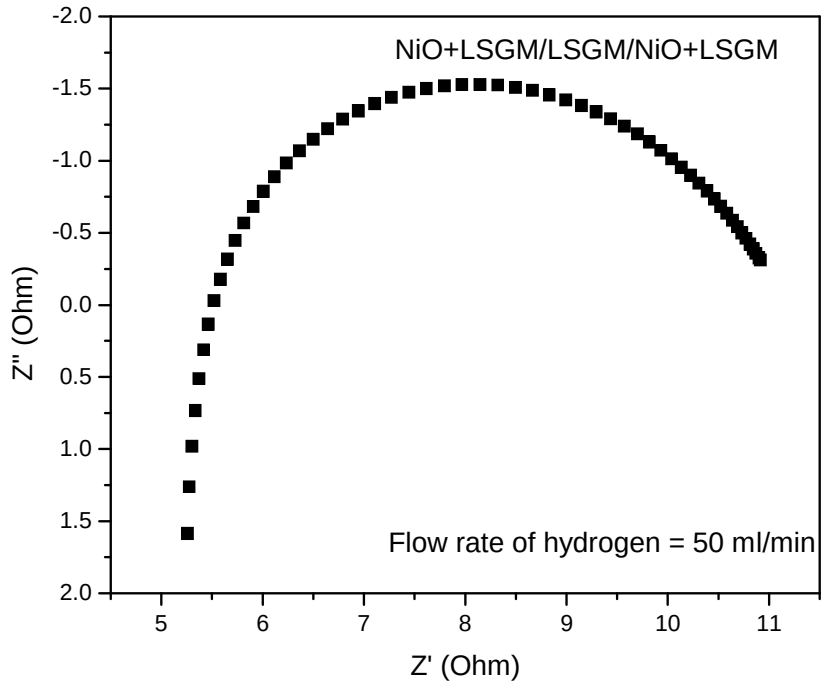

Fig.4.4.10 Nyquist plot of Pt,H_2,NiO+LSGM/LSGM/NiO+LSGM,H_2,Pt at 800 ^{o}C

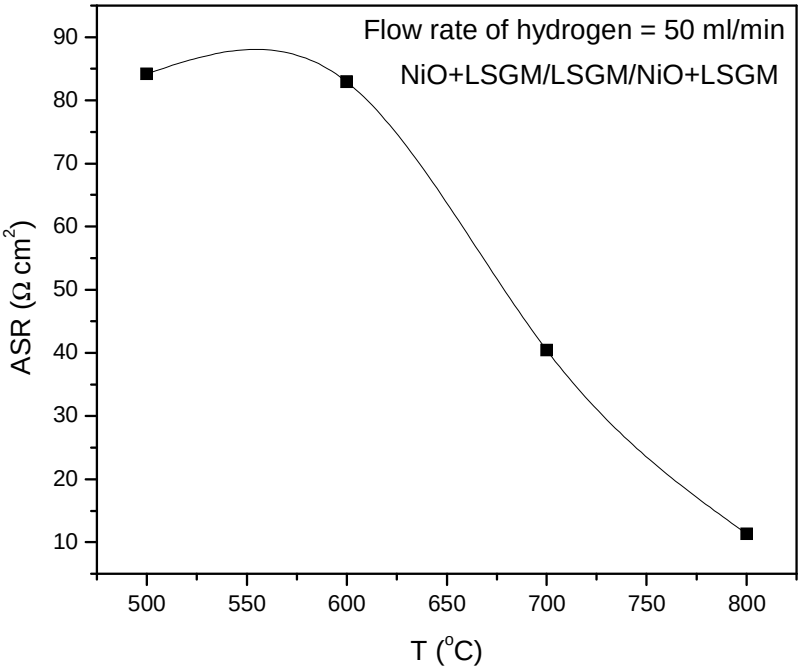

Fig.4.4.11 ASR of Pt,H_2,NiO+LSGM/LSGM/NiO+LSGM,H_2,Pt as a function of temperature.

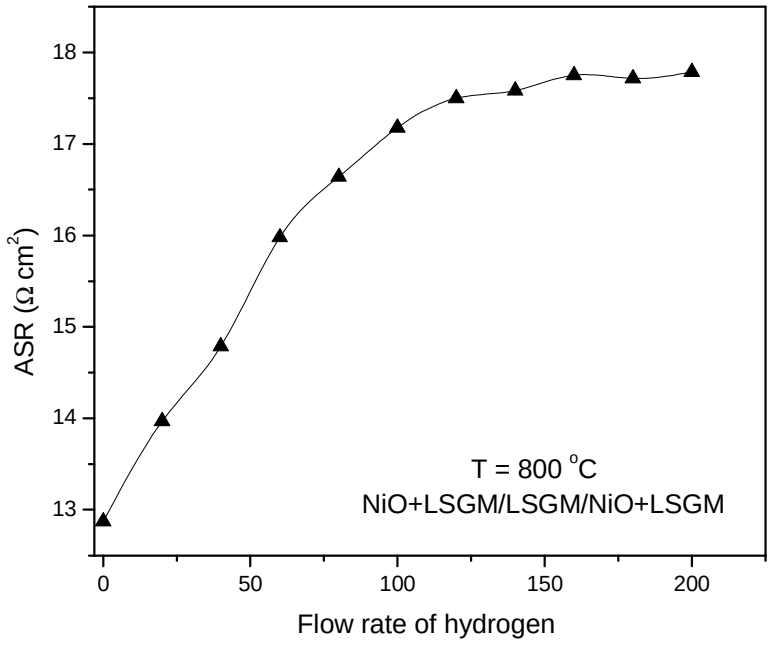

Fig.4.4.12 ASR of Pt,H_2,NiO+LSGM/LSGM/NiO+LSGM,H_2,Pt as a function of hydrogen flow rate 800°C.

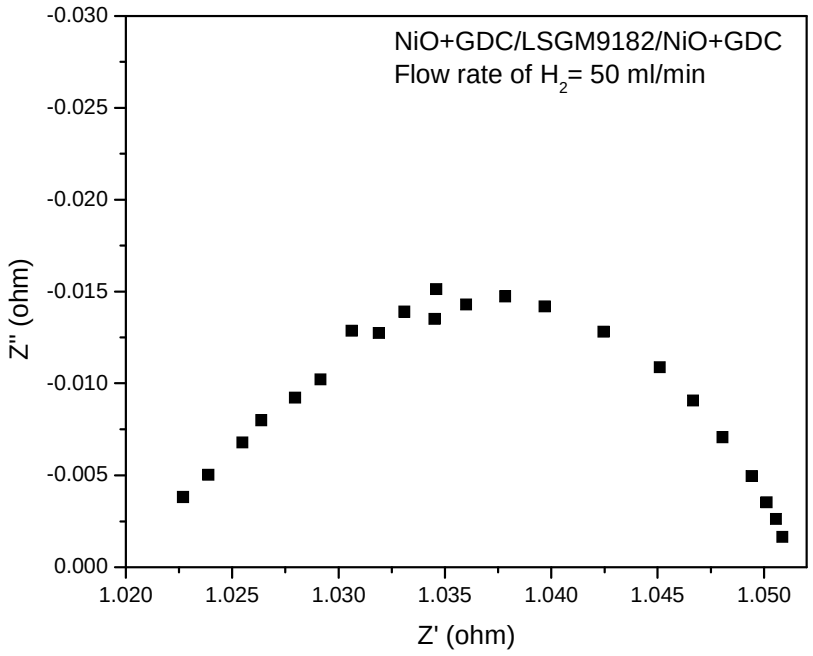

Fig.4.4.13 Nyquist plot of Pt,H_2,NiO+GDC/LSGM/NiO+GDC,H_2,Pt at 800 ^oC

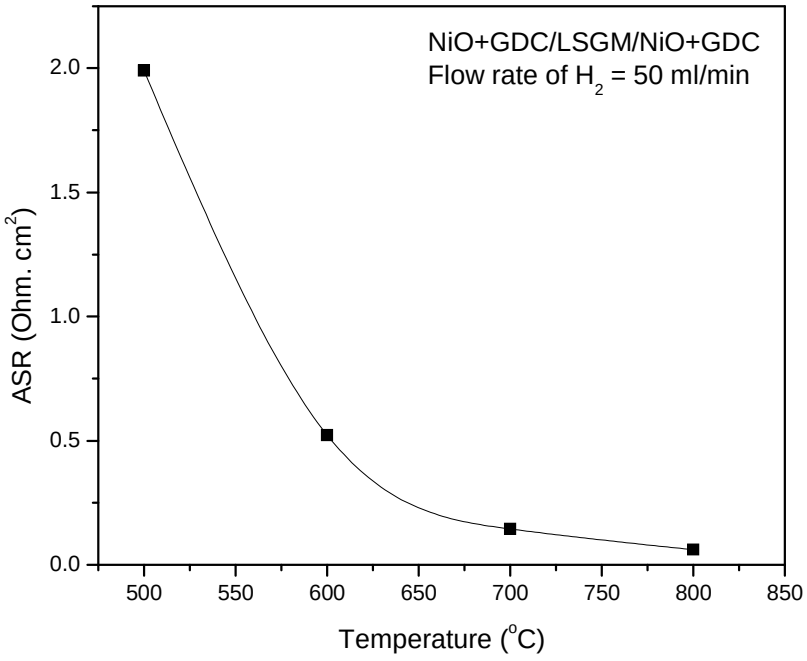

Fig.4.4.14 ASR of Pt,H_2,NiO+GDC/LSGM/NiO+GDC,H_2,Pt as a function of temperature.

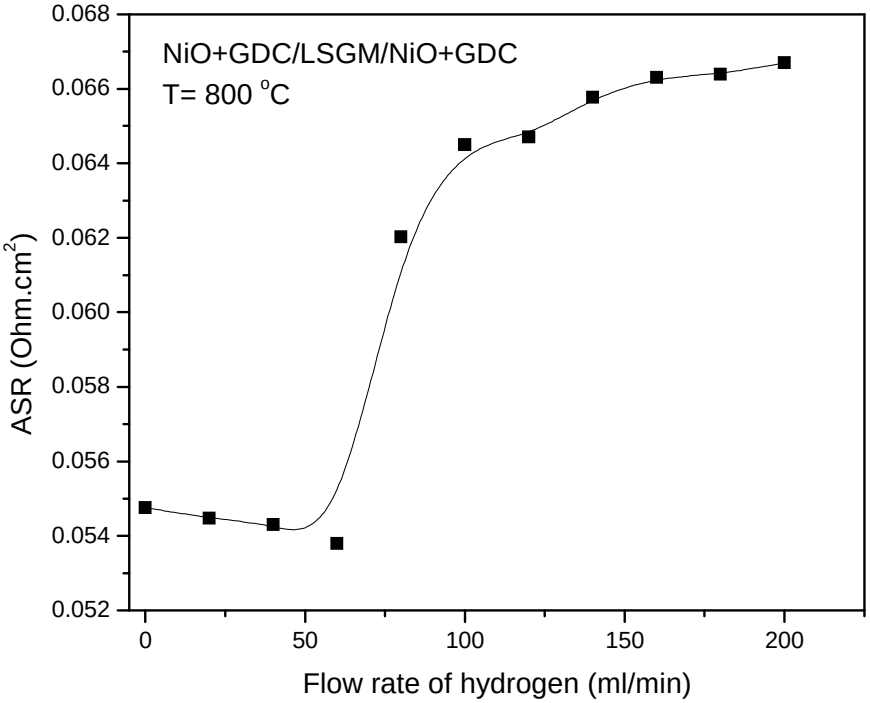

Fig.4.4.15 ASR of Pt,H_2,NiO+GDC/LSGM/NiO+GDC,H_2,Pt as a function of hydrogen flow rate at 800^{o}C.

4.4.2. Single Cell Performance

4.4.2.1. Single Cell Pt,H_2,NiO+LSGM/LSGM9182/LSCF6428,O_2,Pt

The open circuit potential at 800^{o}C of Pt,H_2,NiO+LSGM/LSGM/LSCF,O_2,Pt single cell with time (measured using a potentiostat) is shown in Fig. 4.4.16. Initially, silver foil was used as the sealant for the cell. The open circuit potential of the single cell was 0.65V at 800^{o}C at a flow rate of 50 ml/min of hydrogen and oxygen respectively at the anode and cathode compartments. The open circuit potential remained constant for periods in excess of 3 hours. It was clear from Fig. 4.4.16 that the open circuit potential in this test was much lower than the theoretical value (1.02 V at 800^{o}C). OCP's lower than the theoretical value might be because of physical permeability of the gases between the anode and cathode compartments i.e., leakage through the silver sealing or significant electronic conductivity in the electrolyte, side reactions at the electrode/electrolyte interface or poor catalytic activity of the electrodes. When the same cell was tested using Aremco ceramic sealant, it showed the same OCP of 0.65 at 800^{o}C. Since the ionic conductivity of LSGM9182 measured at

800^{o}C showed negligible electronic or hole conductivity, it was concluded that the lower OCP was because of the formation of the insulating lanthanum nickelate phase at the anode. The high ASR values measured earlier for NiO+LSGM based symmetric cells supported this argument. Simultaneously, the area specific resistance (ASR) of the complete cell was also measured in the temperature range of 500-1000^{o}C by ac impedance spectroscopy. The Nyquist plots of Pt,H_2,NiO+LSGM/LSGM/LSCF,O_2,Pt at 500 and 800^{o}C are shown in Figs. 4.4.17-4.4.18**.** The variation of the ASR values with temperature for this cell is plotted as a function of temperature in Fig.4.4.19. The ASR value of the complete cell was observed to be very high at all the temperatures. Fig. 4.4.20 shows the polarization (I-V and I-P) curves for the single cell Pt,H_2,NiO+LSGM/LSGM/LSCF,O_2,Pt at 800^{o}C. The peak power density achieved for this single cell operating at 800^{o}C was 40 mW/cm^2.

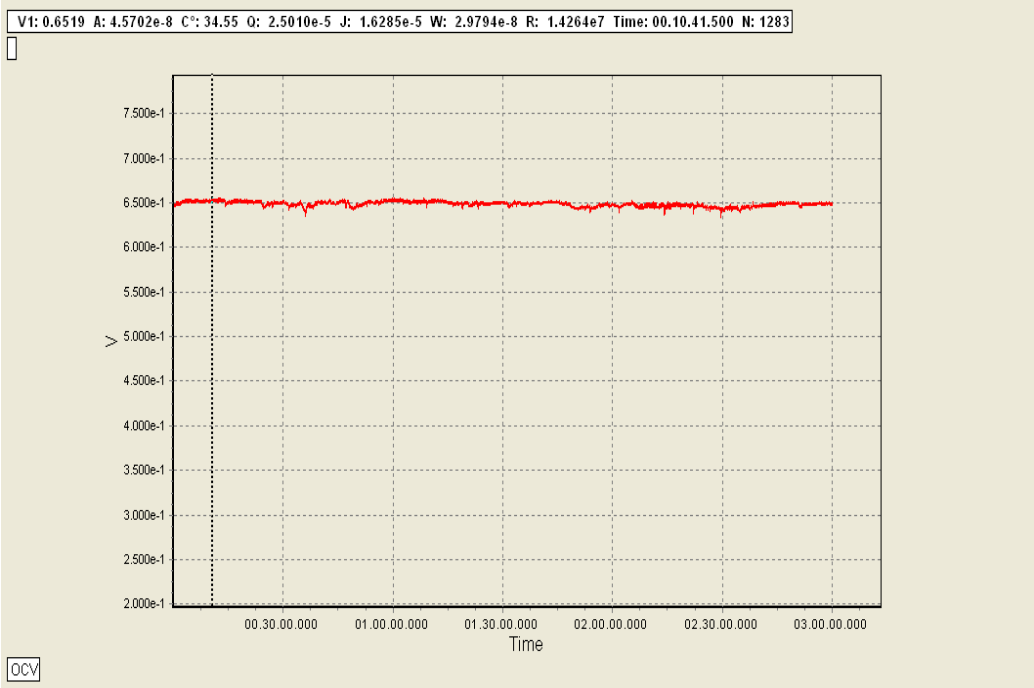

Fig. 4.4.16 The open circuit potential of Pt,H_2,NiO+LSGM/LSGM/LSCF,O_2,Pt as a function of time at 800^{o}C

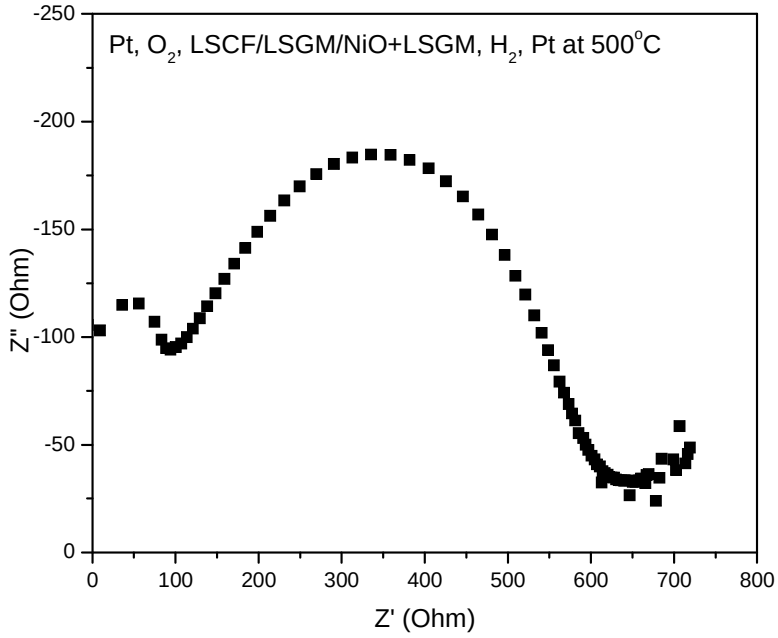

Fig.4.4.17 Nyquist plot of Pt,H_2,NiO+LSGM/LSGM/LSCF,O_2,Pt at 500^{o}C

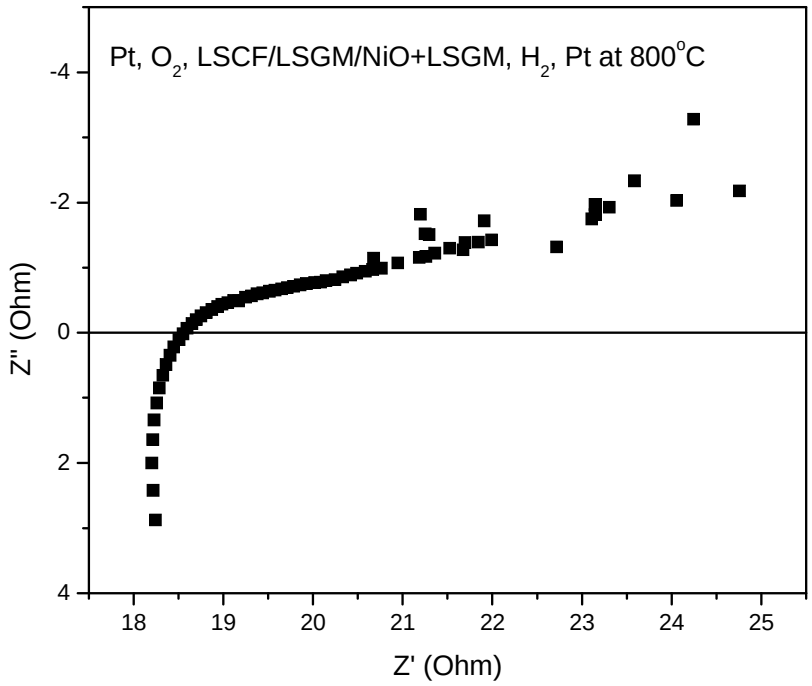

Fig.4.4.18 Nyquist plot of Pt,H_2,NiO+LSGM/LSGM/LSCF,O_2,Pt at 800^{o}C

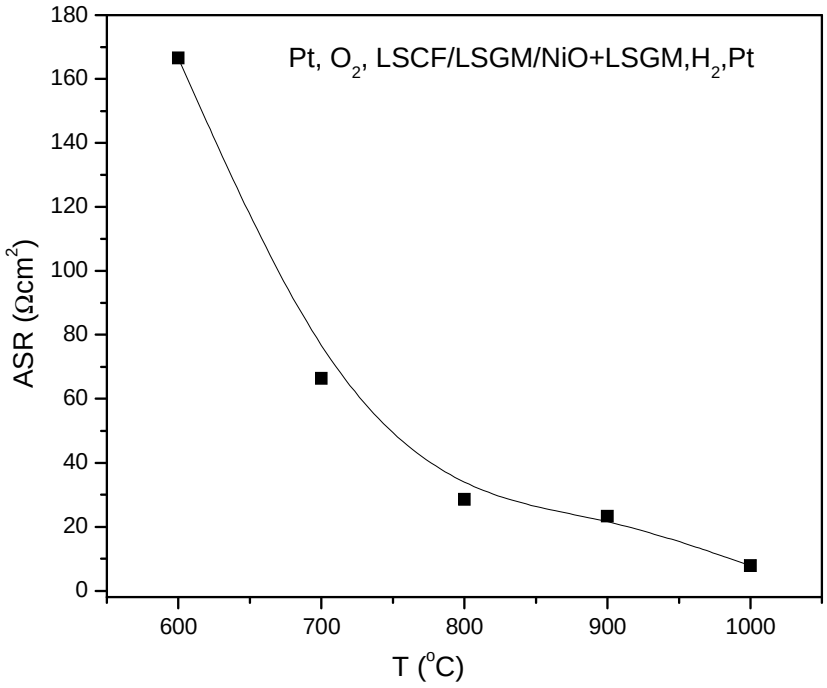

Fig.4.4.19 The total area specific resistance of the Pt,H_2,NiO+LSGM/LSGM/LSCF,O_2, Pt as a function of temperatures

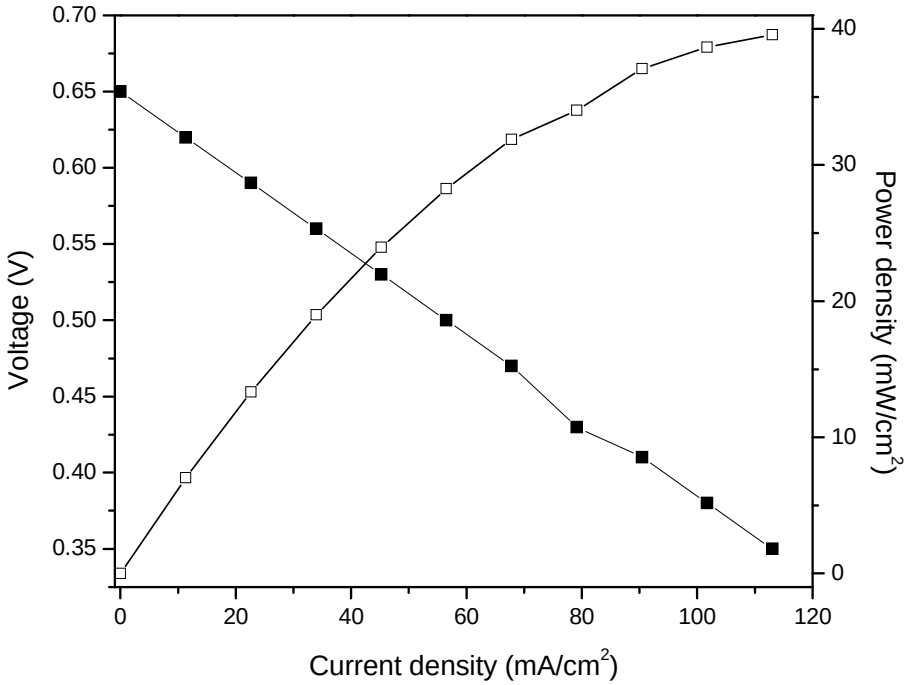

Fig. 4.4.20 Polarization (I-V & I-P) plot of Pt,H_2,NiO+LSGM/LSGM/LSCF,O_2,Pt at 800^{o}C

4.4.2.2. Single Cell Pt,H_2,NiO+GDC/LSGM9182/LSCF6428,O_2,Pt

The fabricated Pt,H_2,NiO+GDC/LSGM/LSCF,O_2,Pt single cell was operated in the temperature range of 500-800^{o}C with a flow rate of 40 ml/min of hydrogen and 10 ml/min of oxygen at anode and cathode compartments respectively. The commercial Aremco ceramic sealant was used for this cell. This cell gave an open circuit potential of 1.00-1.02 V in the temperature of 500-800^{o}C, which is almost equal to the thermodynamic Nernstian potential. The open circuit potentials of this single cell at different temperatures between 500-800^{o}C are depicted in Figs. 4.4.21 - 4.4.24. The OCP's at all the measured temperatures remained constant for time periods in excess of 3 hours. The polarization plots for this cell in the temperature range 600-800^{o}C are shown in Figs. 4.4.25. The current density and power density achieved at 800^{o}C were 190 (mA/cm^2) and 50 (mW/cm^2) respectively. The observed current density and power density were somewhat lower at lower temperatures (600 and 700^{o}C). The performance of this cell was much superior to that of Pt,H_2,NiO+LSGM/LSGM/LSCF,O_2,Pt, indicating that the NiO-GDC anode had much superior catalytic properties compared to NiO-LSGM. The ASR measurement of the corresponding cell was measured in the temperature range of 500-1000^{o}C using impedance spectroscopy. The Nyquist plots of Pt, H_2, NiO+GDC/LSGM/LSCF,O_2, Pt symmetric cell at 500 and 800^{o}C are shown in Figs.4.4.26 and 4.4.27. The variation of ASR for the complete cell as a function of temperature is shown in Fig.4.4.28. The ASR values for this cell were low; much lower than that of the NiO+LSGM anode based cells.

The ASR values for the electrochemical cell with LSCF and NiO+GDC as cathode and anode respectively observed in this study are lower than that reported in the literature [Gong, 2004]. They observed that the LSCF cathodes had a small polarization resistance compared to the other cathodes and also that with the use of NiO+GDC anode, the ASR values increased with time when directly used in LSGM electrolyte. Therefore, they recommended the use of a dense inter layer of lanthanum doped ceria (LDC) between the anode and electrolyte.

The electrolyte supported cell configurations used in this thesis i.e., Pt, H_2,NiO+LSGM/LSGM/LSCF,O_2,Pt and Pt, H_2,NiO+GDC/LSGM/LSCF,O_2,Pt have not been tested and reported in the literature. Maffei and Kuriakose [1998] have developed LSGM supported single cells with Ca doped lanthanum cobalt ferrite as cathode and NiO-CeO_2 as anode. They reported a power density of 9 mW/cm^2 at 800^{o}C

for this cell with the use of H_2 and O_2. This is much lower than the power density achieved in the present thesis with the use of LSCF and NiO+GDC as cathode and anode. Gong et al [2004] have developed a LSGM supported single cell with LSCF-LSGM cathode, NiO+LDC (lanthanum doped ceria) anode and LDC as barrier between anode and electrolyte, which yielded a maximum power density of 192 mW/cm^2 at with the use of H_2 and O_2. This is much higher than the power density obtained in this study. Huang and Goodenough [2000] developed a single cell (electrolyte supported) using $La_{0.6}Sr_{0.4}CoO_3$ cathode, NiO+LSGM and NiO+SDC (samaria doped ceria) anodes with a power density of 550mW/cm^2 for SDC/SDC+Ni, 440mW/cm2 for Ni+SDC and 270 mW/cm^2 for NiO+LSGM. Hwang et al [2008] achieved output power densities of 440 mW/ cm^2 at 800 °C, 275 mW/cm^2 at 750 °C and 170 mW/ cm^2 at 700 °C for LSCF/LSGM/Ni+YSZ single cells. LSGM supported single cells using LSCF as cathode and Ni+LDC as anode with and without buffer yielded a power density of 780 and 150mW/cm^2 respectively with the use of H_2 and O_2 [Bozza etal, 2009]. The power density achieved in the present study is in general lower to that reported in the literature for various other electrolyte supported cell configurations. However, most of these studies employed one or more inter-layers between the anode and electrolyte to prevent the formation of insulating phases at the interface. The use of an interlayer might have improved the power density for the present cell configurations also.

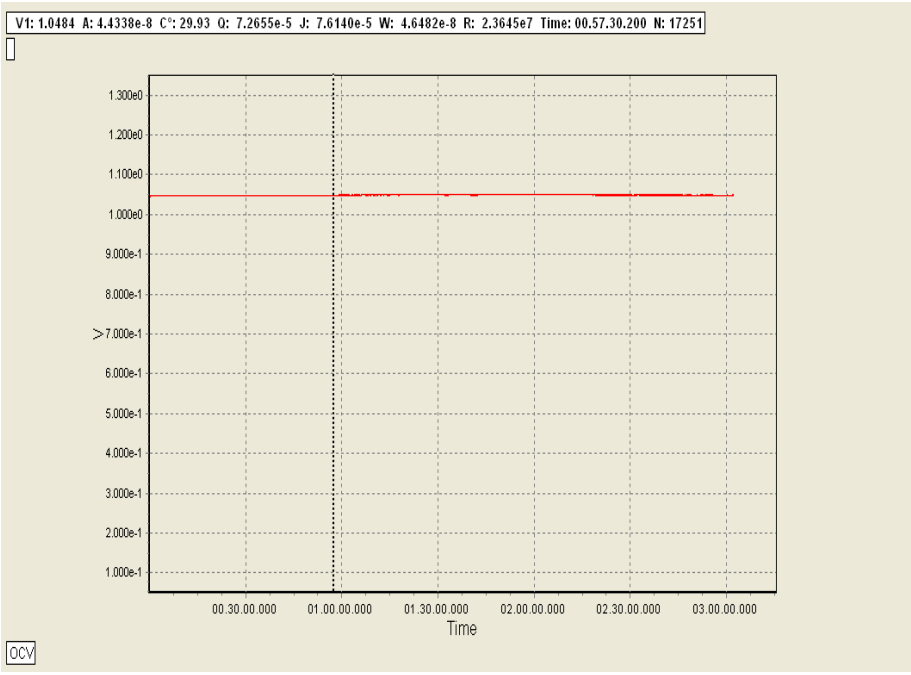

Fig. 4.4.21 The open circuit potential of Pt,H_2,NiO+GDC/LSGM/LSCF,O_2,Pt as a function of time at 500^{o}C

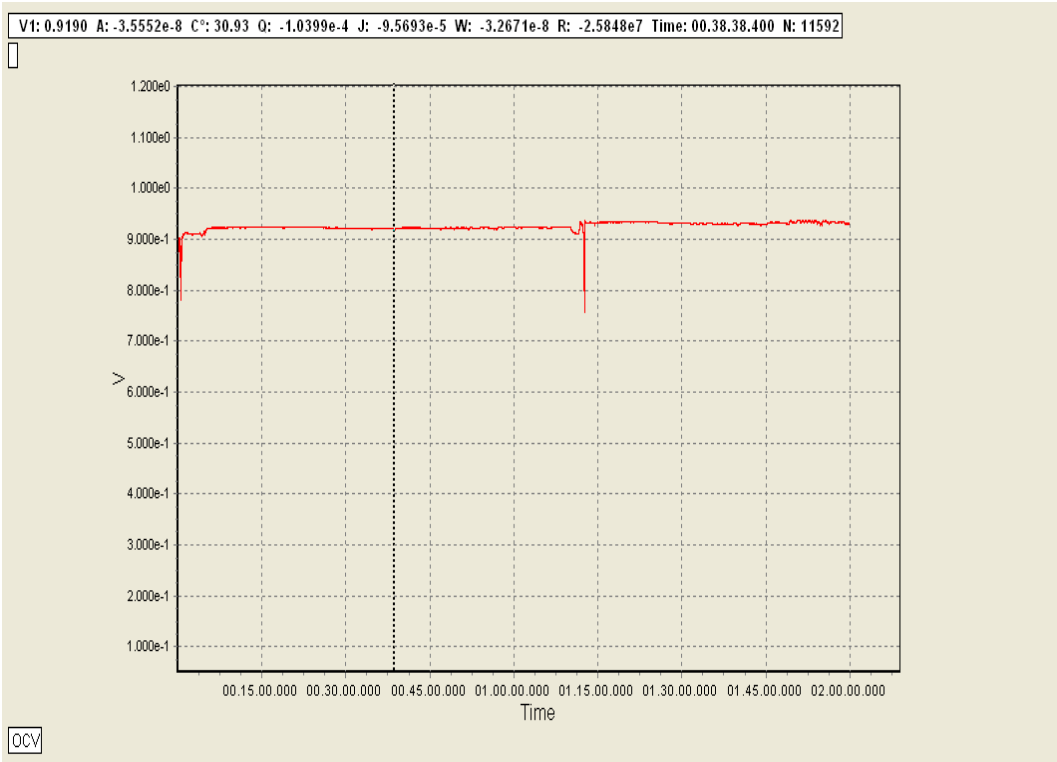

Fig. 4.4.22 The open circuit potential of Pt,H_2,NiO+GDC/LSGM/LSCF,O_2,Pt as a function of time at 600^{o}C

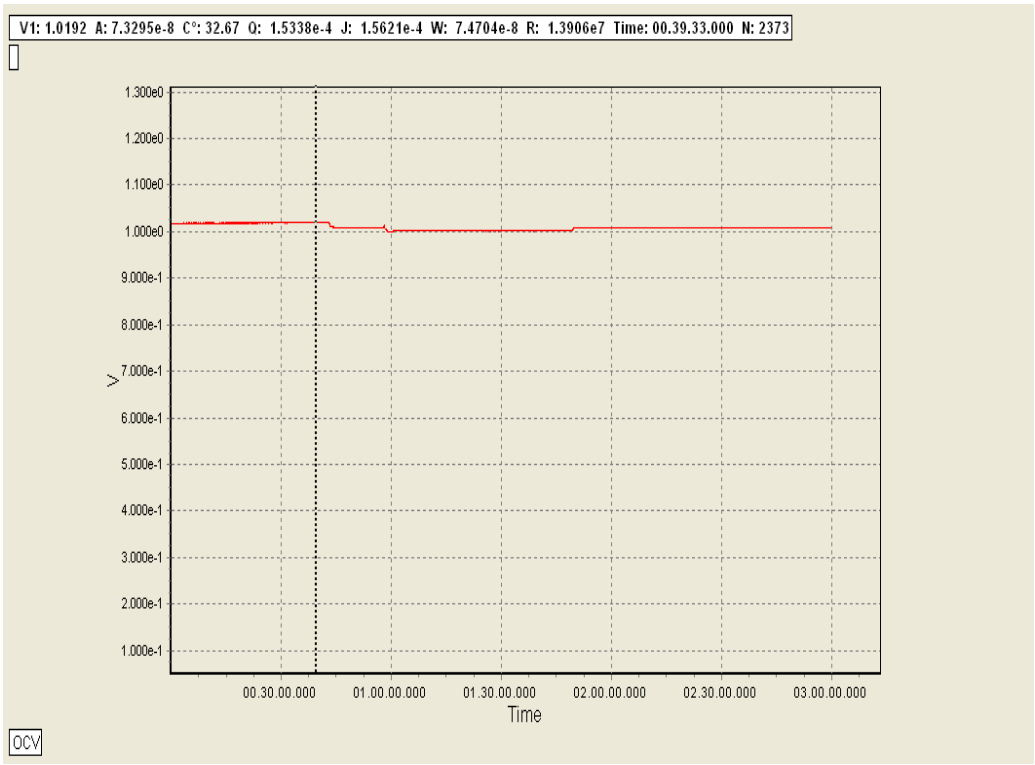

Fig. 4.4.23 The open circuit potential of Pt,H_2,NiO+GDC/LSGM/LSCF,O_2,Pt as a function of time at 700^{o}C

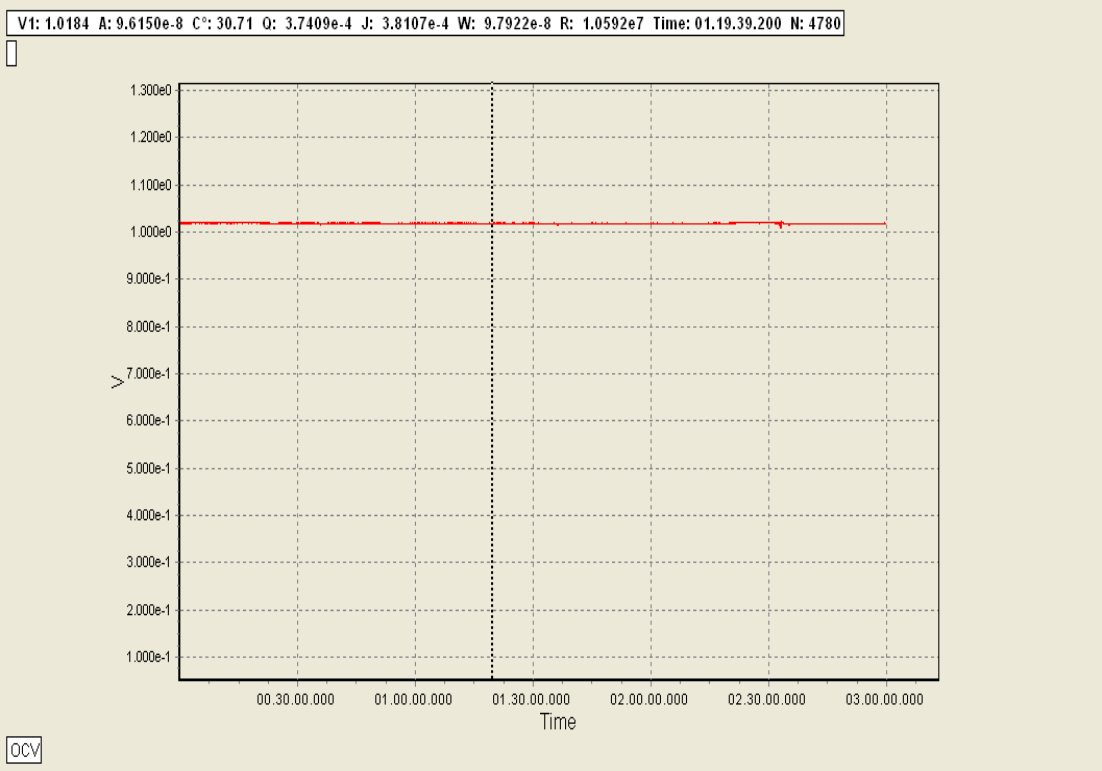

Fig. 4.4.24 The open circuit potential of Pt, H_2,NiO+GDC/LSGM/LSCF,O_2,Pt as a function of time at 800^{o}C

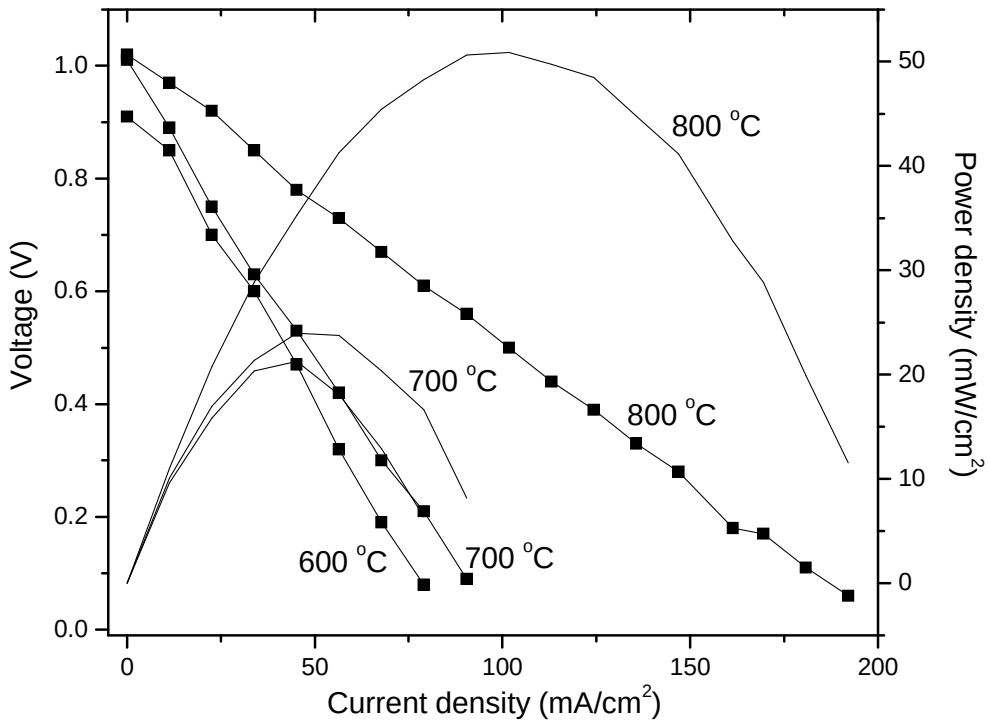

Fig. 4.4.25 Polarization plot of Pt,H_2,NiO+GDC/LSGM/LSCF,O_2,Pt at different temperatures

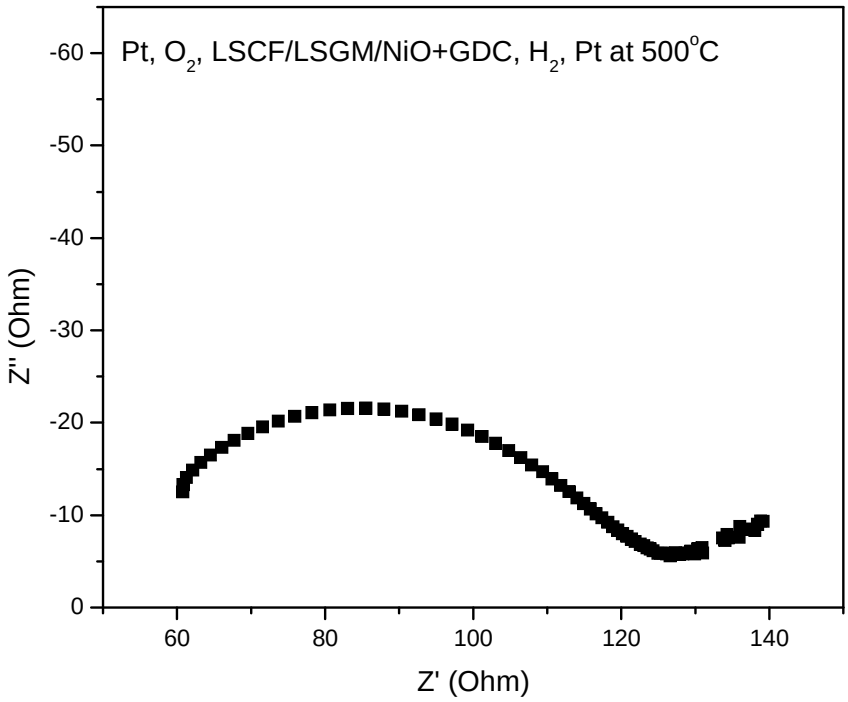

Fig.4.4.26 Nyquist of Pt,H_2,NiO+GDC/LSGM/LSCF,O_2 at 500^{o}C

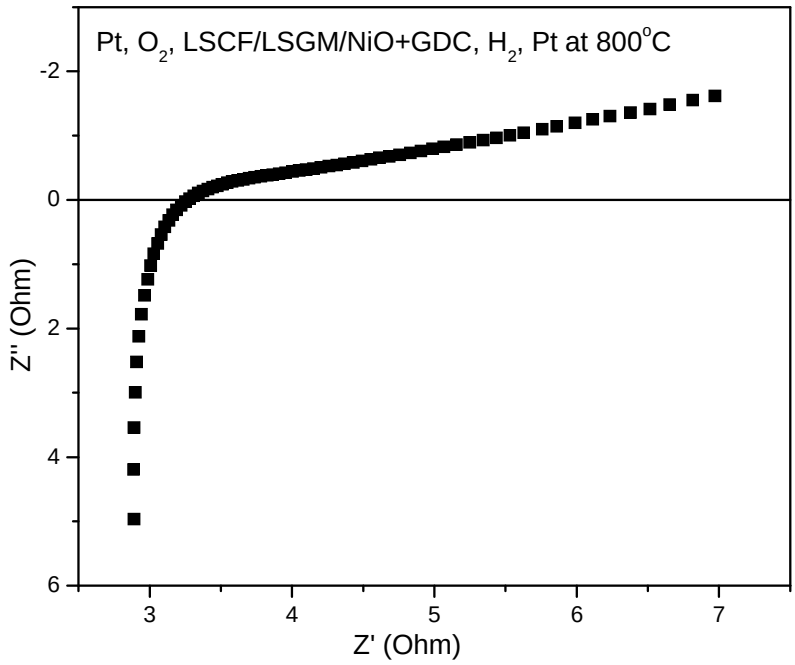

Fig.4.4.27 Nyquist of Pt,H_2,NiO+GDC/LSGM/LSCF,O_2,Pt at 800^{o}C

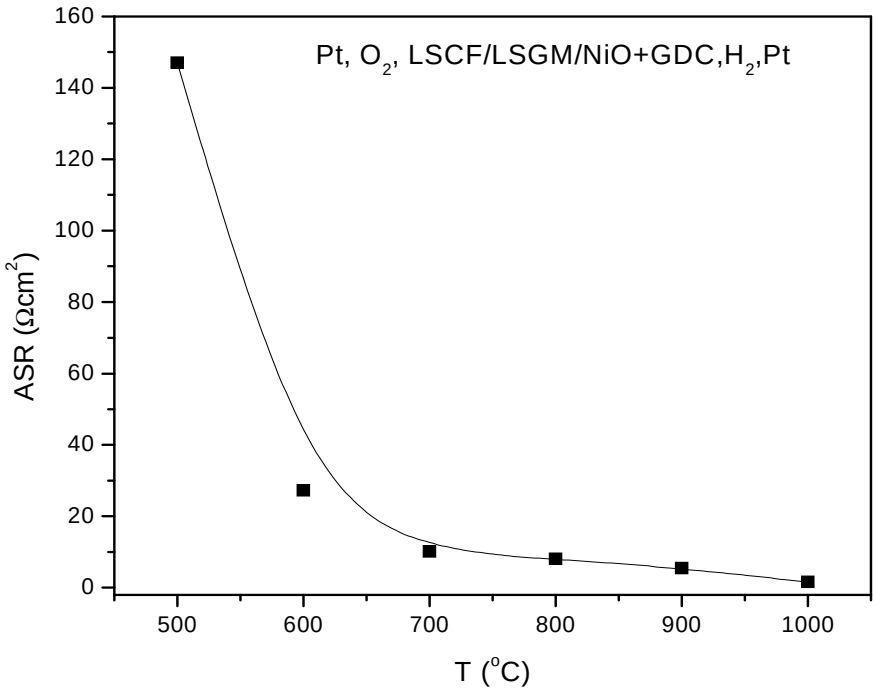

Fig.4.4.28 The total ASR of Pt,H_2,NiO+GDC/LSGM/LSCF,O_2,Pt cell as a function of temperature

After completion of single cell testing, the interface between anode and electrolyte was examined by x-ray diffraction. It was found that the first layer of the interface between the anode (NiO+LSGM) and electrolyte (LSGM) showed a pure perovskite phase associated with significant amounts of secondary phases namely lanthanum oxide, La_2O_3, (JCPDS Card No. 22-0641) and lanthanum nickelate, La_2NiO_4 (JCPDS Card No.70-0509 whereas second layer of the interface revealed substantial formation of La_2NiO_4 (JCPDS Card No. 70-0509) and $LaSrGa_3O_7$ (JCPDS Card No. 45-0637) along with a pure lanthanum gallate phase. The x-ray diffraction pattern of the interface layer is shown in Fig.4.4.29. When NiO+LSGM anode was replaced by NiO+GDC in the cell configuration, the first and second layer of the interface showed a minor quantity of La_2NiO_4 and $LaSrGa_3O_7$ along with a pure lanthanum gallate phase. The XRD pattern of NiO+GDC/LSGM interface is shown in Fig. 4.4.30. The minor amounts of the impurity phases in this case did not affect the area specific resistance of the cell and its polarization behavior. **T**he formation of insulating phase, lanthanum nickelate at the anode-electrolyte interface for NiO+LSGM based anode has earlier been reported in the literature [Huang et al, 2008 and Gong et al, 2004].

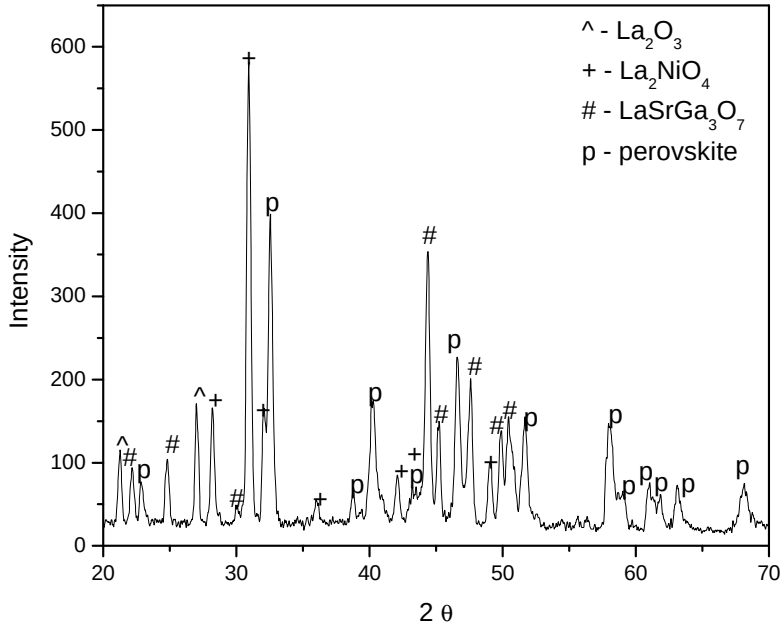

Fig. 4.4.29 X-ray diffraction pattern of NiO+LSGM/LSGM interface

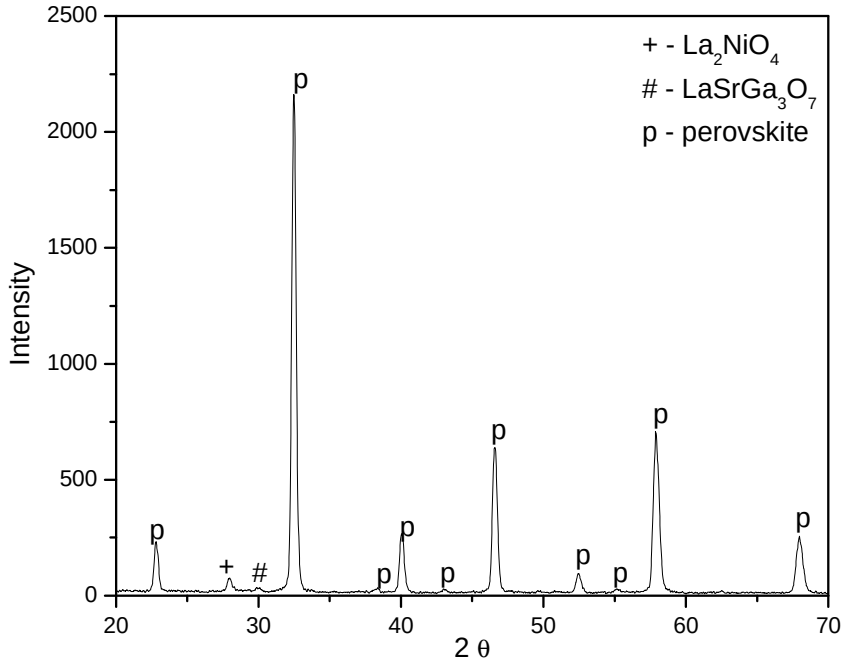

Fig. 4.4.30 XRD pattern of NiO+GDC/LSGM interface

CHAPTER V

CONCLUSIONS AND SCOPE FOR FUTURE WORK

1. Various pure perovskite oxide phases relevant for ITSOFC applications i.e., lanthanum cobaltite ($LaCoO_3$), lanthanum ferrite ($LaFeO_3$), lanthanum gallate ($LaGaO_3$), Sr-doped lanthanum cobaltite ($La_{0.90}Sr_{0.10}CoO_{3-\delta}$), lanthanum ferrite ($La_{0.90}Sr_{0.10}FeO_{3-\delta}$), and Sr- and Mg- doped lanthanum gallate ($La_{0.90}Sr_{0.10}Ga_{0.90}Mg_{0.10}O_{3-\delta}$ and $La_{0.90}Sr_{0.10}Ga_{0.80}Mg_{0.20}O_{3-\delta}$) powders could be prepared by combustion and Pechini methods. Co-precipitation method yielded pure phases only for lanthanum cobaltite and Sr-doped lanthanum cobaltite.
2. Powders of LCO, LSC 9010, LFO, LSF 9010, LGO, LSGM 9191 and LSGM9182 prepared by combustion and Pechini methods were discrete whereas pure phases synthesized by co-precipitation had a tendency to agglomerate.
3. Powders synthesized by the Pechini method were found to be superior in terms of phase purity, particle size and BET surface area.
4. All these pure phases were stable in oxidizing atmosphere, whereas, both lanthanum cobaltite ($LaCoO_3$) as well as Sr-doped $LaCoO_3$ were partially reduced to Co^{+2} form in reducing atmosphere.
5. The solubility of Sr at the A-site was found to depend strongly upon the extent of Mg- in the B-site. In the absence of Mg at the B-site, the solubility limit of Sr at 1500^{o}C was less than 4 mol % whereas the solubility of Sr increased to 15 mol % when 25 mol % Mg was present at the B-site. The solubility of Mg in the perovskite phase increased marginally from 20 to 25 mol % with the addition of 15 mol % of Sr.
6. The overall solubility limits of Sr and Mg in the perovskite lanthanum gallate phase were found to decrease at lower temperatures. The combined maximum solubility of Sr and Mg were found to be 10 and 15 mol % respectively at 700^{o}C.
7. With increasing Sr-content, the impurity phases $LaSrGa_3O_7$ and subsequently $LaSrGaO_4$ were found to form whereas with increasing Mg-content, initially Ga_2MgO_4 and later MgO were found to co-exist with the perovskite phase.
8. Equilibration at 1500^{o}C for periods exceeding 8 hours led to extensive Ga vaporization which resulted in the formation of several secondary phases ($LaSrGa_3O_7$, $LaSrGaO_4$, $La_4Ga_2O_9$, Ga_2MgO_4 and MgO) co-existing with the perovskite LSGM phase.

9. The conductivity of LSGM increased with increase in dopant concentration both at the A- and B-sites until the formation of the second phase, after which it decreased with concentration. The highest bulk conductivity at 800^{o}C of 0.13 S/cm was found for the composition $La_{0.90}Sr_{0.10}Ga_{0.75}Mg_{0.25}O_{3-\delta}$. The lowest activation energy for oxygen ion migration achieved was also for this composition and was 0.31 eV.
10. Pure phases of $LaSrGaO_4$, $La_4Ga_2O_9$, $LaSrGa_3O_7$ and $MgGa_2O_4$ could be synthesized in bulk by Pechini method. Electrochemical impedance measurements on all these phases indicated that their conductivity is about three to four orders of magnitude lower than the perovskite LSGM phase. Transport number measurements on these phases indicated that these pure phases are poor oxygen ion conductors.
11. The area specific resistance of the symmetric cells using $La_{0.6}Sr_{0.4}Co_{0.2}Fe_{0.8}O_{3-\delta}$, $La_{0.9}Sr_{0.1}CoO_{3-\delta}$, and $La_{0.9}Sr_{0.1}FeO_{3-\delta}$ and $La_{0.9}Sr_{0.1}Ga_{0.8}Mg_{0.2}O_{3-\delta}$ electrolyte under flowing oxygen atmosphere measured at 800^{o}C was 0.032, 0.62 and 0.09 respectively.
12. ASR measurements on symmetric cells employing $NiO+Ce_{0.9}Gd_{0.1}O_{2-\delta}$ with LSGM electrolyte in flowing H_2 atmosphere was lower compared to the symmetric cell using $NiO+ La_{0.9}Sr_{0.1}Ga_{0.8}Mg_{0.2}O_{3-\delta}$. This was attributed to interfacial reaction between Ni and LSGM.
13. The ASR values of the complete cell, Pt, H_2,NiO+GDC/LSGM/LSCF, O_2, Pt is lower compared to that of Pt, H_2,NiO+LSGM/LSGM/LSCF, O_2, Pt. This was attributed to the significant formation of La_2NiO_4 at the anode/electrolyte interface.
14. The single cell Pt, O_2, LSCF/LSGM/NiO+LSGM, H_2, Pt yielded an open circuit potential of only 0.65 V at 800^{o}C because of the formation of the impurity phase at the anode/electrolyte interface.
15. The single cell Pt, O_2, LSCF/LSGM/NiO+GDC, H_2, Pt showed an open circuit potential of 0.91 and 1.02 V at 600 and 800^{o}C respectively and yielded a maximum current density of 80mA/cm^2 and 190 mA/cm^2 at 600 and 800^{o}C respectively.

Scope for Future Work

- Study phase equilibria in the systems LGO-LFO-LCO, LSGM-LSF-LSC, LSGM-Ni, LSGM-GDC-Ni in the relevant temperature and oxygen partial pressure range.
- Reduce the electrolyte and cathode thickness further to minimize polarization losses.
- Explore the use of different mixed ionic-electronic conductors at the anode/electrolyte interface.
- Development of anode supported cells with the same anode, cathode and electrolyte materials. Explore the use of electrophoretic deposition to obtain thin films of LSGM on the porous anode substrate.
- Explore new candidate materials for anodes and cathodes chemically and thermally compatible with Sr- and Mg doped lanthanum gallate electrolyte to achieve higher power densities in intermediate temperature solid oxide fuel cells.
- Test these cells with the use of $CO+H_2$, natural gas and other hydrocarbons as fuel.

BIBILOGRAPHY

Amow, C., Whitfield, P.S., Davidson, J.J., Hammond, R.P., Munnings, C.N., Skinner, S.J., Structural and sintering characteristics of the $La_2Ni_{1-x}Co_xO_{4+\delta}$ series, Ceram. Intl., 30 (2004) 1635-1639.

Anderson, M. D., Stevenson, J.M., Simner, S.P., Reactivity of lanthanide ferrite SOFC cathodes with YSZ electrolyte, J. Power Sources, 129 (2004) 188-192.

Arai, H., in Proceedings of the International Symposium on Solid Oxide Fuel Cells, November 13-14, 1989, Nagoya, Japan. O.Yamamoto, M. Dokiya and I Tagawa (eds.), Science House, Tokyo, Japan, 1989, p.12.

Aruna, S. T., Muthuraman, M and Patil, K.C., Combustion synthesis and properties of strontium substituted lanthanum manganites $La_{1-x}Sr_xMnO_3$ ($0 \leq x \leq 0.3$), J. Mater. Chem., 7 (1997) 2499-2503.

Atkinson, A., Barnett, S., Gorte, R.J., Irvine, J.T.S., Mcevoy, A.J., Mogensen, M. Singhal, S.C and Vohs, J., Advanced anodes for high-temperature fuel cells Nature Mater., 3 (2004) 17-27.

Augustin, C.O., Kalai Selvan, R., Nagaraj, R., Berchmans, L.J., Effect of La^{3+} substitution on the structural, electrical and electrochemical properties of strontium ferrite by citrate combustion method, Mater. Chem. Phys., 89 (2005) 406-411.

Azad, A-M. & Er, L. F., Microstructural evolution in B-site Mg-substituted $La_{0.9}Sr_{0.1}GaO_{3-\delta}$ oxide solid solutions, J. Alloys Compds., 306 (2000) 103-112.

Bae, J-M., Steele, B.C.H., Properties of $La_{0.6}Sr_{0.4}Co_{0.2}Fe_{0.8}O_{3-\delta}$ (LSCF) double layer

cathodes on gadolinium-doped ceria oxide (CGO) electrolytes I. Role of SiO_2, Solid State Ionics, 106 (1998) 247-253.

Bagger, C., in 1992 Fuel Cell Seminar Abstracts, November 29- December 2, 1992, Tucson, AZ, Courtesy Associates, Washington, DC 1992, p.241

Bard, A.J and Faulkner, L.R., Electrochemical methods. Fundamentals and applications. John wiley & sons, 1980 Edition, 1980.

Basu, R.N., Tietz, F., Wessel, E., Buchkremer, H.P., Stover, D., Microstructure and electrical conductivity of $LaNi_{0.6}Fe_{0.4}O_3$ prepared by combustion synthesis routes, Mater. Res. Bull., 39 (2004) 1335-1345.

Basu, R.N., Günter Blass, Hans Peter Buchkremer, Detlev Stöver, Frank Tietz, Egber Wessel, Izaak C. Vinke, Simplified processing of anode-supported thin film planar solid oxide fuel cells, J. Euro. Ceram. Soc., 25 (2005) 463–471.

Baur, E. and Preis, H.Z.., U¨ ber Brennstoff-Ketten mit Festleitern. Z. Elektrochem., 43 (1937) 727-732.

Baythoun, M.S.G and Sale, F.R., Production of strontium-substituted lanthanum manganite perovskite powder by the amorphous citrate process, J. Mater. Sci., 17 (1982) 2757-2769.

Berger, D., Landschoot, N.V., Ionica, C., Papa, F., Fruth, V., Synthesis of pure and doped lanthanum cobaltite by the combustion method, J. Optoelectron. Adv. Mater., 5 (2003) 719-724.

Berkowski, M., $SrLaGaO_4$---$SrLaAlO_4$ solid solutions: new promising substrate materials for HTSc, J. Alloys Compds., 251 (1997) 1-6.

Bockris, J.O'M and Reddy, A.K.N., Modern Electrochemistry, volume 1&2. Plenum press, 1977 edition, Third Printing-July 1977.

Boehm, E., Bassat, J.-M., Steil, M.C., Dordor, P., Mauvy, F., Greiner, J.-C., Oxygen transport properties of $La_2Ni_{1-x}Cu_xO_{4+\delta}$ mixed conducting oxides, Solid State Sci., 5 (2003) 973-981.

Boivin, J-C., Structural and electrochemical features of fast oxide ion conductors, Int. J. Inorg. Mater., 3 (2001) 1261–1266.

Bossel, U.G., Comparative evaluation of the performance potentials of the ten prominent SOFC configurations. In S.C. Singhal and H. Iwahara, editors, Proceedings of the Third International Symposium on Solid Oxide Fuel Cells, 1993 Hawaii, pp 833–840. The Electrochemical Society, Pennington, NJ, 1993.

Bozza, F., Polini, R., Traversa, E., High performance anode-supported intermediate temperature solid oxide fuel cells (IT-SOFCs) with $La_{0.8}Sr_{0.2}Ga_{0.8}Mg_{0.2}O_{3-\delta}$ electrolyte films prepared by electrophoretic deposition, Electrochem. Commun., 11 (2009) 1680-1683.

Brunauer, S., Emmett, P.H. & Teller, E., Adsorption of gases in multimolecular layers. J. Am. Chem. Soc., 60 (1938) 309–319.

Bucher, E., Jantscher, W., Benisek, A., Sitte, W., Preis, W., Rom, I., Hofer, F., Transport properties of $La_{0.4}Sr_{0.6}CoO_{3-\delta}$ Solid State Ionics, 141-142 (2001) 375-380.

Buchler,O., Serra, J.M., Meulenberg, W.A., Sebold, D., Buchkremer,H.P., Preparation and properties of thin $La_{1-x}Sr_xCo_{1-y}Fe_yO_{3-\delta}$ perovskitic membranes supported on tailored ceramic substrates, Solid State Ionics, 178 (2007) 91–99.

Burggraaf, A.J., Van Dijk, T., Verkerk, M.J., Structure and conductivity of pyrochlore and fluorite type solid solutions, Solid State Ionics, 5 (1981) 519-522.

Chae, N.S., Park, K.S., Yoon, Y.S., Yoo, I.S., Kim, J.S. and Yoon, H.H., Sr- and Mg-doped $LaGaO_3$ powder synthesis by carbonate co-precipitation, Colloids Surf., A, 313-314 (2008) 154-157.

Charojrochkul, S., Choy, K.-L., Steele, B.C.H., Cathode/electrolyte systems for solid oxide fuel cells fabricated using flame assisted vapour deposition technique, Solid State Ionics, 121 (1999) 107-113.

Chen, F., Liu, M., Study of transition metal oxide doped $LaGaO_3$ as electrode materials for LSGM based solid oxide fuel cells, J. Solid State Electrochem.,3 (1998) 7-14.

Chen, T-Y. & Fung, K-Z., Comparison of dissolution behavior and ionic conduction between Sr and/or Mg doped $LaGaO_3$ and $LaAlO_3$, J. Power Sources, 132 (2004) 1-10.

Cheng, J. & Navrotsky, A., Energetics of magnesium, strontium, and barium doped lanthanum gallate perovskites, J. Solid State Chem., 177 (2004) 126-133.

Chiang, Y.M., Lavik, E.B., Blom, D.A., Defect thermodynamics and electrical properties of nanocrystalline oxides: Pure and doped CeO_2, Nanostruct.Mater., 9 (1997) 633-642.

Coffey, G.W., Hardy, J., Pederson, L.R., Rieke, P.C., Thomsen, E.C., Walpole, M., Electrochemical properties of lanthanum strontium aluminum ferrites for the oxygen reduction reaction Solid State Ionics, 158 (2003) 1-9.

Cong, L., He, T., Ji, Y., Guan, P., Huang, Y. & Su, W., Synthesis and characterization of IT-electrolyte with perovskite structure $La_{0.8}Sr_{0.2}Ga_{0.85}Mg_{0.15}O_{3-\delta}$ by glycine-nitrate combustion method, J. Alloys Compds., 348 (2003) 325-331.

Cottis, R., Turgoose, S., Syrett, B. C., Cottis, B., Corrosion Testing Made Easy: Electrochemical Impedance and Noise, National Association of Corrosion Engineers (NACE), 1999.

Cullity, B.D and Stock, R., Elements of X-ray diffraction, Third edition, Prentice Hall, Inc, New Jersey, 2001.

Datta, P., Majewski, P. & Aldinger, F., Synthesis and Microstructural characterization of Sr- and Mg-substituted $LaGaO_3$ solid electrolyte, Mater. Chem. Phys., 102 (2007) 240-244.

De Boer, B., Gonzales, M., Bouwmeester, H.J.M., Verweij, H., The effect of the presence of fine YSZ particles on the performance of porous nickel electrodes, Solid State Ionics, 127 (2000), 269-276.

De Haart, L.G.J., Lin, Y.S., De Vries. K.J., Burggraaf, A.J., Modified CVD of nanoscale structures in and EVD of thin layers on porous ceramic membranes, J. Eur. Ceram. Soc., 8 (1991) 59-70.

De Souza, S., Visco, S. J., De Jonghe, L. C., Thin-film solid oxide fuel cell with high performance at low-temperature, Solid State Ionics, 98 (1997) 57-61.

De Souza, M.A.F., Candeia, R.A., Ssouza, S.C., Chaves, A.C., Lima, S.J.G., Longo, E., Soledade, L.E.B., Santos, I.M.G., Souza, A.G., Synthesis and characterization of $Sr_{1-}xMgxTiO_3$ obtained by the polymeric precursor method, Mater. Lett., 59 (2005) 549-553.

Ding, J., Liu, J., Novel design and performance of cone-shaped tubular anode-supported segmented-in-series solid oxide fuel cell stack, J. Power Sources, 193 (2009) 769-773.

Djurado, E. & Labeau, M., Second phases in doped lanthanum gallate perovskites, J. Eur. Ceram. Soc., 18 (1998) 1397-1404.

Dongare, M.K., Dongare, A. M., Tare, V.B., Kemnitz, E., Synthesis and characterization of copper-stabilized zirconia as an anode material for SOFC, Solid State Ionics, 152-153 (2002) 455-462.

Doshi, R., Richards, V.L., Carter, J.D., Wang, X., Krumpelt, M., Development of solid-oxide fuel cells that operate at 500°C, J. Electrochem. Soc., 146 (1999) 1273-1278.

Du, Y., Sammes, N.M., Fabrication of tubular electrolytes for solid oxide fuel cells using strontium- and magnesium-doped $LaGaO_3$ materials J. Euro. Ceram. Soc., 21 (2001) 727-735.

Duquette, J., Petric, A., Silver wire seal design for planar solid oxide fuel cell stack, J. Power Sources, 137 (2004) 71–75.

Elshof, J.E. ten., Bouwmeester, H.J.M., Verweij, H., Oxygen transport through $La_{1-x}Sr_xFeO_{3-\delta}$ membranes. I. Permeation in air/He gradients, Solid State Ionics, 81 (1995) 97-109.

Elshof, J.E. ten., Bouwmeester, H.J.M., Verweij, H., Oxygen transport through $La_{1-x}Sr_xFeO_{3-\delta}$ membranes II. Permeation in air/CO, CO_2 gradients, Solid State Ionics, 89 (1996) 81-92.

Figueiredo, F.M., Frade, J.R., Marques, F.M.B., Performance of composite $LaCoO_3 - La_2(Zr,Y)_2O_7$ cathodes, Solid State Ionics, 135 (2000) 463-467.

Fleig, J., Kreuer, K.D., Maier, J., Handbook of Advanced Ceramics, Materials, Applications, and Processing, Academic Press, 1-60 (2001).

Fleig, J., On the width of the electrochemically active region in mixed conducting solid oxide fuel cell cathodes, J. Power Sources, 105 (2002) 228-238.

Fu, Q., Xu, X., Peng, D., Liu, X., Meng, G., Preparation and electrochemical characterization of Sr- and Mn-doped $LaGaO_3$ as anode materials for LSGM-based SOFCs, J. Mat. Sci., 38 (2003) 2901-2906.

Fukui, T., Ohara, S., Murata, K., Yoshida, H., Miura, K and Inagaki, T., Performance of intermediate temperature solid oxide fuel cells with $La(Sr)Ga(Mg)O_3$ electrolyte film, J. Power Sources, 106 (2002) 142-145.

Ganguly, P. and Vasanthacharrya, Y., Infrared and Mössbauer spectroscopic study of the metal-insulator transition in some oxides of perovskite structure, J. Solid State chem., 61 (1986) 164-167.

Gao, J., Liu, X., Peng, D., Meng, G., Electrochemical behavior of Ln0.6Sr0.4Co0.2Fe0.8O3-δ (Ln = Ce, Gd, Sm, Dy) materials used as cathode of IT-SOFC, Catal. Today, 82 (2003) 207-211.

Gong, W., Gopalan, S and Pal, U.B., Cathodic polarization study on doped lanthanum gallate electrolyte using impedance spectroscopy, J. Electrocerm., 13 (2004) 653-661.

Gong, W., Gopalan, S and Pal, U.B., Polarization study on doped lanthanum gallate electrolyte using impedance spectroscopy, J. Mater. Eng. Perform., 13 (2004) 274-281.

Gong, W., Gopalan, S and Pal, U.B., Performance of intermediate temperature (600-800^oC) solid oxide fuel cell based on Sr and Mg doped lanthanum gallate electrolyte, J. Power Sources, 160 (2006) 305-315.

Gonzalez, A., Tamayo, E.M., Porter, A.B., Corberan, V.C., Synthesis of high surface area perovskite catalysts by non-conventional routes, Catal. Today, 33 (1997) 361-369.

Goodenough, J.B., Ceramic solid electrolytes, Solid State Ionics, 94 (1997) 17-25.

Goodenough, J.B., Oxide-ion electrolytes, Annu. Rev. Mater. Res., 33 (2003) 91-128.

Gorelov, V.P., Bronin, D.I., Sokolova, Ju.V., Nafe, H. & Aldinger, F., The effect of doping and processing conditions on properties of $La_{1-x}Sr_xGa_{1-y}Mg_yO_{3-\delta}$, J. Eur. Ceram. Soc., 21 (2001) 2311-2317.

Hart, N.T., Brandon, N.P., Day, M.J., Lapena-Rey, N., Functionally graded composite cathodes for solid oxide fuel cells, J. Power Sources, 106 (2002) 42-50.

Hartley, A., Sahibzada, M., Weston, M., Metcalfe, I.S., Mantzavinos, D., $La_{0.6}Sr_{0.4}Co_{0.2}Fe_{0.8}O_3$ as the anode and cathode for intermediate temperature solid oxide fuel cells, Catal. Today, 55 (2004) 197-204.

Hoshina, T., Yoshida, T., Sakurada, S., in 1990 Fuel Cell Seminar Abstracts, November 25-28, 1990, Phoenix, AZ, Courtesy Associates, Washington, DC 1990, p.516.

Horita, T., Yamaji, K., Sakai, N., Yokokawa, H., Weber, A., Ivers-Tiffée, E., Oxygen reduction mechanism at porous $La_{1-x}Sr_xCoO_{3-\delta}$ cathodes/$La_{0.8}Sr_{0.2}Ga_{0.8}Mg_{0.2}O_{2.8}$ electrolyte interface for solid oxide fuel cells, Electrochim. Acta, 46 (2001) 1837-1845.

Huang, K. and Goodenough, J.B., Wet Chemical synthesis of Sr- and Mg-doped LaGaO3, a perovskite-type oxide-ion conductor, Solid State Chem., 136 (1994) 274-283.

Huang, K., Feng, M. & Goodenough, J.B., Sol-gel synthesis of a new oxide-ion conductor Sr and mg-doped $LaGaO_3$ perovskite, J. Am. Ceram. Soc., 79 (1996) 1100-1104.

Huang, K., Tichy, R.S. & Goodenough, J.B., Superior perovskite oxide–ion conductor; Strontium-and magnesium-doped $LaGaO_3$: I, Phase relationships and electrical properties, J. Am. Ceram. Soc., 81 (1998) 2565-75.

Huang, K. and Goodenough, J. B., Wet Chemical Synthesis of Sr- and Mg-Doped $LaGaO_3$, a Perovskite-Type Oxide-Ion Conductor, J. Solid State Chem., 136 (1998) 274-283.

Huang, K. & Goodenough, J.B., A solid oxide fuel cell based on Sr- and Mg-doped $LaGaO_3$ electrolyte: the role of a rare-earth oxide buffer, J. Alloys Compds., 303-304 (2000) 454-464.

Huang, B., Wang, S.R., Liu, R.Z., Ye, X.F., Nie, H.W., Sun, X.F., Wen, T.L., Performance of La0.75Sr0.25Cr0.5Mn0.5O3-δ perovskite-structure anode material at lanthanum gallate electrolyte for IT-SOFC running on ethanol fuel, J. Power Sources, 167 (2007) 39-46.

Huijsmans, J.P.P., Ceramics in solid oxide fuel cells, Curr. Opin. Solid St. Mater. Sci., 5 (2001) 317-323.

Hwang, J.J., Chen, C.K., Lai, D.Y., Detailed characteristic comparison between planar and MOLB-type SOFCs, J. Power Sources, 143 (2005) 75–83.

Hwang, C., Tsai, C-H., Lo, C-H., Sun, C-H., Plasma sprayed metal supported YSZ/Ni–LSGM–LSCF ITSOFC with nanostructured anode, J. Power Sources, 180 (2008) 132-142 .

Inagaki, T., Miura, K., Yoshida, H., Maric, R., Ohara, S., Zhang, X., Mukai, K., Fukui, T., High-performance electrodes for reduced temperature solid oxide fuel cells with doped lanthanum gallate electrolyte: II. $La(Sr)CoO_3$ cathode, J. Power Source, 86 (2000) 347-351.

Inaba, H. & Tagawa, H., Ceria based solid electrolytes, Solid State Ionics, 83 (1996) 1-16.

Irvine, J.T.S., Fagg, D.P., Labrincha, J., Marques, F.M.B., Development of novel anodes for solid oxide fuel cells, Catal. Today, 38 (1997) 467-472.

Ishihara,T, Matsuda, H and Takita, Y., Doped $LaGaO_3$ perovskite type oxide as a new oxide ionic conductor, J. Am. Chem. Soc., 116 (1994) 3081-3803.

Ishihara, T., Shibayama, T., Ishikawa, S., Hosoi, K., Nishiguchi, H., Takita, Y., Novel fast oxide ion conductor and application for the electrolyte of solid oxide fuel cell, J.Euro.Ceram.Soc., 24 (2004) 1329–1335

Ishikawa, H., Enoki, M., Ishihara, T & Akiyama, T., Self-propagating high-temperature synthesis of $La(Sr)Ga(Mg)O_{3-\delta}$ for electrolyte of solid oxide fuel cells, J. Alloys Compds., 430 (2007) 246-251.

Jang, J.H. and Choi, G.M., Partial electronic conductivity of Sr and Mg doped $LaGaO_3$, Solid State Ionics, 154-155, (2002) 481-486.

Jang,W.S., Hyun, S. H., Kim, S.G., Preparation of YSZ/YDC and YSZ/GDC composite electrolytes by the tape casting and sol-gel dip-drawing coating method for low-temperature SOFC, J. Mater. Sci., 37 (2002) 2535 – 2541.

Ji, Y., Liu, J., He, T., Cong, L., Wang, J., Su, W., Single intermediate-temperature SOFC prepared by glycine-nitrate process, J. Alloys Compds, 353 (2003) 257-262.

Jiang, S.P., Issues on development of (La,Sr)MnO_3 cathode for solid oxide fuel cells, J. Power Sources, 124 (2003) 390-402.

Jiang, S.P and Love, J.G., Observation of structural change induced by cathodic polarization on (La,Sr)MnO_3 electrodes of solid oxide fuel cells, Solid State Ionics, 158 (2003) 45-53.

Johnson, D.W., Gallagher, P.K., Schrey, F and Rhodes, W.W., Preparation of high surface area substituted $LaMnO_3$ catalysts, Am. Ceram. Soc. Bull., 55 (1976) 520-523.

Kenjo, T., Kanehira, Y., Influence of the local variation of the polarization resistance on SOFC cathodes, Solid State Ionics, 148 (2002) 1-14.

Kawada T., and Yokokawa, H., Materials and characterization of solid oxide fuel cell, Key Eng. Mater., 125-126 (1997) 187-248.

Kesapragada, S.V., Bhaduri, S.B., Bhaduri, S., Densification of LSGM electrolytes using activated microwave sintering, J. Power Source, 124 (2003) 499-504.

Khanlou, A.A., Tietz, F. & Stover, D., Material properties of $La_{0.8}Sr_{0.2}Ga_{0.9+x}Mg_{0.1}O_{3-\delta}$ as a function of Ga content, Solid State Ionics, 135 (2000) 543-547.

Kharton, V.V., Viskup, A.P., Naumovich, E.N and Tikhonorich, V.N., Oxygen permeability of $LaFe_{1-x}Ni_xO_{3-\delta}$ solid solutions, Mater. Res. Bull., 34 (1999) 1311-1317.

Kharton, V.V., Figueiredo, F.M., Kovalevsky, A.V., Viskup, A.D., Naumovich, E.N., Bashmakov, A.V., Marques, F.M.B., Processing, microstructure and properties of $LaCoO_{3-\delta}$ ceramics, J. Euro. Ceram, Soc., 21 (2001) 2301-2309.

Kharton, V.V., Shaula, A.L., Vyshatoko, N.P. & Marques, F.M.B., Electron-hole transport in $(La_{0.9}Sr_{0.1})_{0.98}Ga_{0.8}Mg_{0.2}O_{3-\square}$ electrolyte: effects of ceramic microstructure, Electrochim. Acta., 48 (2003) 1817-1828.

Kharton, V.V., Marques, F.M.B., Atkinson, A., Transport properties of solid oxide electrolyte ceramics: a brief review, Solid State Ionics, 174 (2004) 135-149.

Kilner, J.A., Fast oxygen transport in acceptor doped oxides, Solid State Ionics, 129 (2000) 13-23.

Kim, J.H and Yoo, H-I., Partial electronic conductivity and electrolytic domain of $La_{0.9}Sr_{0.1}Ga_{0.8}Mg_{0.2}O_{3-\delta}$, Solid State Ionics, 140 (2001) 105-113.

Kiukkola, K and Wagner, C., Measurements on galvanic cells involving solid electrolytes, J. Electrochem. Soc., 104 (1957) 379-387.

Kordesch, K., The Advancement of Fuel Cell Systems and Spin-off Battery Technology. Ber. Bunsenges.Phys.Chem., 94 (1990) 902-912.

Kostogloudis, G.Ch., Ftikos, Ch., Khanlou, A.A, Naoumidis, A., Stöver, D., Chemical compatibility of alternative perovskite oxide SOFC cathodes with doped lanthanum gallate solid electrolyte, Solid State Ionics, 134 (2000) 127-138.

Kostogloudis, G. Ch and Ftikos, Ch., Properties of A-site-deficient $La_{0.6}Sr_{0.4}Co_{0.2}Fe_{0.8}O_{3-\delta}$ based perovskite oxides, Solid State Ionics, 126 (1999) 143-151.

Kramer, S., Spears, M., Tuller, H.L., Conduction in titanate pyrochlores: role of dopants, Solid State Ionics, 72 (1994) 59-66

Kruger, H.G., Knote, A., Schindler, U., Kern, H., Composite ceramic metal coatings by means of combined electrophoretic deposition and galvanic method, J. Mat. Sci., 39 ((2004) 839-844.

Krumpelt, M., Ralph, J., Cruse, T., Bae, J.M., Materials for low-temperature solid oxide fuel cells, 5th European SOFC Forum, July 1-5, 2002, Lucerne, Switzerland.

Kuroda, K., Hashimoto, I., Adachi, K., Akikusa, J., Tamou, Y., Komada, N., Ishihara, T., Takita, Y., Characterization of solid oxide fuel cell using doped lanthanum gallate, Solid State Ionics, 132 (2000) 199-208.

Kurumada, M., Hara, H., Munakata, F., Iguchi, E., Electric conductions in $La_{0.9}Sr_{0.1}GaO_{3-\delta}$ and $La_{0.9}Sr_{0.1}Ga_{0.9}Mg_{0.1}O_{3-\delta}$, Solid State Ionics, 176 (2005) 245-251.

Lecarpentier, F., Tuller, H.L., Long, N., Performance of La0.9Sr0.1Ga0.5Ni0.5O3 as a cathode for lanthanum gallate fuel cell, J, Electroceram., 5:3 (2000) 225-229.

Li, Y., Xie, Y., Gong, J., Chen, Y., Zhang, Z., Preparation of Ni/YSZ materials for SOFC anodes by buffer-solution method, Mater. Sci. Eng., B86 (2001) 119-122.

Lin, Y.S., De Haart, L.G.J., De Vries. K.J., Burggraaf, A.J., in Proceedings of the first International Symposium on Solid Oxide Fuel Cells, October 16-18, 1989, Hollywood. S.C. Singhal (ed.) Electrochemical Society, Pennington, Nj, 1989, p. 67.

Liu, N., Shi, M., Wang, C., Yuan, Y.P., Majewski, P. & Aldinger, F., Microstructure and ionic conductivity of Sr- and Mg-doped $LaGaO_3$, J. Mater. Sci., 41 (2006) 4205-4213.

Livermore, S.J.A., Cotton, J. W., Mark Ormerod, R. Fuel reforming and electrical performance studies in intermediate temperature ceria-gadolinia based SOFCs, J. Power Sources, 86 (2000) 411-416.

Lu, C., An, S., Worrell, W.L., Vohs, J.M and Gorte, R.J., Development of intermediate-temperature solid oxide fuel cells for direct utilization of hydrocarbon fuels, Solid State Ionics, 175 (2004) 47-50.

Ma, X.Q., Zhang, H.,Dal, J., Roth, J., Hul, R., Xiao, T.D., Reisner, D.E., Intermediate temperature solid oxide fuel cell based on fully integrated plasma-sprayed components, J. Therm. Spray Technol., 14 (2005) 61-66.

Maffei, N and Kuriakose, A.K., Performance of planar single cell lanthanum gallate based solid oxide fuel cells, J. Power Sources, 75 (1998) 162-166.

Maguire, E., Gharbage, B., Marques, F.M.B., Labrincha, J.A., Cathode materials for intermediate temperature SOFCs, Solid State Ionics, 127 (2000) 329-335.

Mai, A., Tietz, F., Stover, D., Partial reduction and re-oxidation of iron-and cobalt-containing perovskites using catalyst characterization measurements, Solid State Ionics, 174 (2004) 35-40.

Majewski, P., Rozumek, M. & Aldinger, F., Phase diagram studies in the systems La_2O_3-SrO-MgO-Ga_2O_3 at 1350-1673 K in air with emphasis on Sr and Mg substituted $LaGaO_3$, J. Alloys Compds., 329 (2001) 253-258.

Majewski, P., Rozumek, M., Schluckwerder, H. & Aldinger, F., Phase diagram studies in the systems La_2O_3-SrO-Ga_2O_3 and La_2O_3-MgO-Ga_2O_3 at 1673 K in air, Int. J. Inorg. Mater., 3 (2001) 1343-1344.

Majewski, P., Rozumek, M., Schluckwerder, H. & Aldinger, F., Phase diagram studies in the systems La_2O_3-SrO-Ga_2O_3, La_2O_3-MgO-Ga_2O_3, and SrO-MgO-Ga_2O_3 at 1673 K in air, J. Am. Ceram.Soc., 84 (2001) 1093-96.

Majewski, P., Rozumek, M., Tas, A.C. & Aldinger, F., Processing of (La,Sr)(Ga,Mg)O_3 solid electrolyte, J. Elecroceram., 8 (2002) 65-73.

Malinowski, M., Pracka, I., Surma, B., Luksiewicz, T., Wolinski, W., Wolski, R., Spectroscopic and laser properties of SrLaGa3O7:Pr3+, Opt. Mater., 6 (1996) 305.

Marina, O.A, Canfield, N.L., Stevenson, J.W, Thermal, electrical, and electrocatalytical properties of lanthanum-doped strontium titanate, Solid State Ionics, 149 (2002) 21-28.

Martinez, J.P., Tarancon, A., Lopez, D.M., Ruiz-Morales, J.C., Evaluation of GdBaCo2O5+δ as cathode material for doped lanthanum gallate electrolyte IT-SOFCs, Fuel Cells, 08 (2008) 351-359.

Matraszek, A., Singhesiser, L., Kobertz, D., Hilpert, K., Miller, M., Schulez, O. & Martin, M., Phase diagram study in the La_2O_3-Ga_2O_3-MgO-SrO system in air, Solid State Ionics, 166 (2004) 343-350.

Matsuda, M., Ihara, K., Miyake, M., Influences of Ga doping on lattice parameter, microstructure, thermal expansion coefficient and electrical conductivity of $La_{0.6}Sr_{0.4}CoO_{3-y}$, Solid State Ionics, 172 (2004) 57-61.

Matsuzaki, Y., Yasuda, I., Electrochemical properties of reduced-temperature SOFCs with mixed ionic-electronic conductors in electrodes and/or interlayers, Solid State Ionics, 152-153 (2002) 463-468.

Matsuzaki, Y., Yasuda, I., Electrochemical properties of a SOFC cathode in contact a chromium-containing alloy separator, Solid State Ionics, 132 (2000) 271-278.

McPheethers,C.C., Claar, T.D., in 1986 Fuel Cell Seminar Abstracts, October 26-291986, Tucson, AZ, Courtesy Associates, Washington, DC 1986, p.64.

Miao, J.P., Li, L.P., Song, Y.B., Xu, D.P., Lu, Z., Su, W.H., High-pressure and-temperature synthesis and characterization of mixed valence perovskite oxides $LaTi_{1-x}Mg_xO_3$, Mater. Chem. Phys., 62 (2000) 226-229.

Minh, N. Q. Ceramic Fuel Cells**,** J. Am. Ceram. Soc., 76 (1993) 563-589.

Minh, N.G and Takahashi, T., Science and Technology of Ceramic Fuel Cells, Elsevier science, Amsterdam, 1995.

Mizuno, M., Yamada, T. and Ohtake, T., Phase diagram of the system Ga_2O_3–La_2O_3 at high temperatures, Yogyo Kyokaishi, 93 (1985) 295-300.

Moon, P.K., Tuller, H.L., in: Subhash C. Singhal (Ed.), Proceedings of the First International Symposium on Solid Oxide Fuel Cells, The Electrochemical Society Inc., NJ, Proc, vol. 89–11, 1989, p. 30.

Moriga, T., Yoshiasa, A., Kanamaru, F., Koto, K., Crystal structure analyses of the pyrochlore and fluorite-type $Zr_2Gd_2O_7$ and anti-phase domain structure, Solid State Ionics, 31 (1989) 319-328.

Moriga, T., Sakamoto, T., Sato, Y., Suenari, R., Nakabayashi, I., Crystal Structures and Electrical and Optical Properties of $MgIn_{2-x}Ga_xO_4$ Solid Solutions, J. Solid State Chem., 142 (1999) 206-213.

Murakami, S., Akiyama, Y., Ishida. N., Yasuo, T., Saito, T., Furukaw, N., in Proceedings of the second International Symposium on Solid Oxide Fuel Cells, July 2-5, 1991, Athens, Greece. F. Gorosz, P. Zegers, S.C. Singhal and O.Yamamoto (eds.) Commission of European Communities, Luxembourg, 1991, p.59.

Naiqing, Z., Kening, S., Derui, Z and Dechang, J., Study on properties of LSGM electrolyte made by tape casting method and applications in SOFC, J. Rare Earths, 24 (2006) 90-92.

Nakayama, S., Okazaki, M., Aung, Y.L., Sakamoto, M., Preparations of perovskite-type oxides $LaCoO_3$ from three different methods and their evaluation by homogeneity, sinterability and conductivity, Solid State Ionics, 158 (2003) 133-139.

Negishi, H., Yamaji, K., Sakai, N., Horita, T., Yanagishita, H., Yokokawa, H., Electrophoretic deposition of YSZ powders for solid oxide fuel cells, J. Mat. Sci., 9 (2004) 833-838.

Nernst, W., U¨ ber die elektrolytische Leitung fester Ko¨rper bei sehr hohen Temperaturen. Z. Elektrochem., 6 (1899) 41.

Nishiwaki, F., Inagaki, T., Kano, J., Akikusa, J., Murakami, N., Hosoi, K., Development of disc-type intermediate-temperature solid oxide fuel cell, J. Power Sources, 157 (2006) 809-815.

Pajaczkowska, A and Gloubokov, A., Synthesis, growth and characterization of tetragonal ABCO4 crystals, Prog. Cryst. Growth Charact. Mater., 36 (1998) 123-162.

Polini, R., Pamio, A. & Traversa, E., Effect of synthetic route on sintering behavior, phase purity and conductivity of Sr- and Mg-doped $LaGaO_3$ perovskites, J. Eur. Ceram. Soc., 24 (2004) 1365-1370.

Popa, M., Kakihana, M., Synthesis of lanthanum cobaltite ($LaCoO_3$) by the polymerizable complex route, Solid State Ionics, 151 (2002) 251-257.

Prokudina, S.A.,. Rubinchik, Ya.S ,and. Parlyuchenko, M.M, Inorg. Mater., 10 (1974) 416.

Ramanathan, S., Kakade, M.B., Roy, S.K and Kutty, K.K., Processing and characterization of combustion synthesized YAG powders, Ceram. Intl., 29 (2003), 477-484.

Romanowski, W.R., Golab, S., Pisarski, W.A., Dominiak-Dzik, G., Berkowski, M.and Pajaczkowska, A., Investigation of Eu3+ sites in $SrLaGa_3O_7$, $SrLaGaO_4$ and $SrLaAlO_4$ crystals, J. Phys.Chem. Solids, 58 (1997) 639-645.

Rossignol, C., Ralph, J.M., Bae, J.-M., Vaughey, J.T., $Ln_{1-x}Sr_xCoO_3$ (Ln=Gd, Pr) as a cathode for intermediate-temperature solid oxide fuel cells, Solid State Ionics, 175 (2004) 59-61.

Routbort, J.L., Gorett, K.C., Cook, R.E., Wolfenstine, J., Deformation of perovskite electronic ceramics — a review, Solid State Ionics, 129 (2000) 53–62.

Rozumek, M., Majewski, P., Sauter, L. & Aldinger, F., Homogeneity region of strontium-and magnesium-containing LaGaO3 at temperatures between 1100 and 1773 K in air, J. Am. Ceram. Soc., 86 (2003) 1940-46.

Sahibzada, M., Steele, B.C.H., Zheng, K., Rudkin, R.A., Metcalfe, I.S., Development of solid oxide fuel cells based on a $Ce(Gd)O_{2-x}$ electrolyte film for intermediate temperature operation, Catal. Today, 38 (1997) 459-466.

Sahibzada, M., Benson, S.J., Rudkin, R.A., Kilner, J.A., Pd-promoted $La_{0.6}Sr_{0.4}Co_{0.2}Fe_{0.8}O_3$ cathodes, Solid State Ionics, 113-115 (1998) 285-290.

Sahibzada, M.., Steele, B.C.H., Barth, D., Rudkin, R.A., Metcalfe, I.S., operation of solid oxide fuel cells at reduced temperatures, Fuel, 78 (1999) 639-643.

Sahibzada, M., Steele, B.C.H., Hellgardt, K., Barth, D., Effendi, A., Mantzavinos, D., Metcalfe, I. S., Intermediate temperature solid oxide fuel cells operated with methanol fuels, Chem. Eng. Sci., 55 (2000) 3077-3083.

Sammes, N.M., Tompsett, G.A., Phillips, R.J. & Cartner, A.M., Characterization of doped-lanthanum gallates by X-ray diffraction and Raman spectroscopy, Solid State Ionics, 111 (1998) 1-7.

Sauvet, A.L., Fouletier, J., Electrochemical properties of a new type anode material $La_{1-x}Sr_xCr_{1-y}Ru_yO_{3-\delta}$ for SOFC under hydrogen and methane at intermediate temperatures, Electrochim. Acta., 47 (2001) 987-995.

Sauvet, A.L., Fouletier, J., Gaillard, F., Primet, M., Doped lanthanum chromites as SOFC anode materials, J. Catal., 209 (2002) 25-34.

Schmalzried, H., Röntgenographische Untersuchung der Kationenverteilung in Spinellphasen, Z. Phys. Chem., N.F. 28 (3/4) (1961) 203-219.

Schottky, W., U¨ ber stromlieferende Prozess im Konzentrationsgefa¨lle fester Elektrolyte.Wiss. Ver¨ooff. Siemens Werken, 14 (1935) 1-19.

Setoguchi, T., Inoue, T., Takebe, H., Eguchi, K., Morinaga, K., Arai, H., Fabrication and evaluation of flat thick film type solid oxide fuel cell, Solid State Ionics, 37 (1990) 217-221.

Shi, M., Liu, N., Xu, Y., Yuan, Y., Majewski, P. & F. Aldinger, Synthesis and characterization of Sr- and Mg-doped $LaGaO_3$ by using glycine–nitrate combustion method, J. Alloys Compds., 425 (2006) 348-352.

Shizhong Wang, Yi Jiang, Yahong Zhang, Wenzhao Li, Jingwang Yan, Zigui Lu, Electrochemical performance of mixed ionic-electronic conducting oxides as anodes for solid oxide fuel cell, Solid State Ionics, 120 (1999) 75-84.

Shukla, A.K., Gopalakrishnan, J., Bull. Mater. Sci., 11 (1995) 109.

Simner, S.P. , Bonnett, J.F., Canfield, N.L., Meinhardt, K.D., Shelton, J.P., Sprenkle, V.L., Stevenson, J.W., Development of lanthanum ferrite SOFC cathodes, J. Power Sources, 113 (2003) 1–10.

Sing, K.S.W., Everett, D.H., Haul, R.A.W., Moscou, L., Pierotti, R.A., Rouquerol, J., Siemieniewska, T., Reporting physisorption data for gas/solid systems with special reference to the determination of surface area and porosity, Pure Appl. Chem. 57 (1985) 603-619.

Sinquin, G., Petit, C., Hindermann, J.P., and Kiennemann, A., Study of the formation of LaMO3 (M = Co, Mn) perovskites by propionates precursors: Application to the catalytic destruction of chlorinated VOCs, Catal. Today, 70 (2001) 183-196.

Skinner, S. J., Recent advances in Perovskite-type materials for solid oxide fuel cell cathodes, Intl. J. Inorg. Mater., 3 (2001) 113-121.

Skinner, S. J and Kilner, J.A., Oxygen ion conductors, Mater. Today, (2003) 30-37.

Spinicci, R., Tofanari, A., Faticanti, M., Pettiti, I., Porta, P., Hexane total oxidation on LaMO3 (M = Mn, Co, Fe) perovskite-type oxides, J. Mol. Catal. A: Chem., 176 (2001) 247-252.

Steele, B.C.H., Development and Applications of Ceramic Electrochemical Reactors.In Adam Hilger, editor, Ceramics in energy applications: new opportunities.

Proceedings of the Institute of Energy conference held in Sheffield (UK), 9-11 April 1990., pp 173–182. Institute of Energy, London (UK), 1990.

Steele, B.C.H., Materials for IT-SOFC stacks 35 years R&D: the inevitability of gradualness?, Solid State Ionics, 134 (2000) 3-20.

Stevenson, J.W., Armstrong, T.R., McCreedy, D.E., Pederson, L.R. & Weber, W., Processing and electrical properties of alkaline earth-doped lanthanum gallate, J. Electrochem.Soc., 144 (1997) 3613-3620.

Stolen, S., Gronvold, F., Brinks, H., Atake, T and Mori, H., Heat capacity and thermodynamic properties of LaFeO3 and LaCoO3 from T = 13 K to T = 1000 K, J. Chem. Thermodyn., 30 (1998) 365-377.

Tadokoro, S. K., Porfirio, T.C., Muccillo, R. and Muccillo, E.N.S., Synthesis, sintering and impedance spectroscopy of 8 mol% yttria-doped ceria solid electrolyte, J. Power Sources, 130 (2004) 15-21.

Tas, A.C., Majewski, P. & Aldinger, F., Chemical preparation of pure and Strontium- and /or magnesium-doped lanthanum gallate powders, J. Am. Ceram. Soc., 83 (2000) 2954-60.

Tas, A.C., Schluckwerder, H., Majewski, P.J., and Aldinger, F., Materials Research Society proceedings, vol.606, pp. 237-243 (Eds.) Jones, A.C., Veteran, J., Mullin, D., Cooper, R and Kaushal, S., 2000, USA.

Tietz, F., Buchkremer, H.-P., Stöver, D., Components manufacturing for solid oxide fuel cells, Solid State Ionics, 152-153 (2002) 373-381.

Tikhonovich, V.N., Naumovich, E.N., Logvinovich, D.I., Kharton V.V., and Vecher, A.A., Oxygen deficiency and phase transitions in $SrCo_{1-x-y}Fe_xCr_yO_{3-\delta}$ (x = 0.10-0.40, y = 0-0.05), J. Solid State Electrochem., 7 (2003) 77-82.

Tsai, T., Barnett, S. A., Increased solid-oxide fuel cell power density using interfacial ceria layers, Solid State Ionics, 98 (1997) 191-196.

Tu, H.Y., Takeda, Y., Imanishi, N and Yamamoto, O., $Ln_{0.4}Sr_{0.6}Co_{0.8}Fe_{0.2}O_{3-\delta}$ (Ln=La, Pr, Nd, Sm, Gd) for the electrode in solid oxide fuel cells, Solid State Ionics, 117 (1999) 277-281.

Uchida, H., Arisaka, S., Watanabe, M., High performance electrodes for medium-temperature solid oxide fuel cells: Activation of $La(Sr)CoO_3$ cathode with highly dispersed Pt metal electrocatalysts, Solid State Ionics, 135 (2000) 347-351.

Ullmann, H., Trofimenko, N., Tietz, F., Stöver, D., Khanlou, A. A., Correlation between thermal expansion and oxide ion transport in mixed conducting perovskite-type oxides for SOFC cathodes, Solid State Ionics, 138 (2000) 79-90.

Van Dijk, M.P., de Vries, K.J., Burggaaf, A.J., Oxygen ion and mixed conductivity in compounds with the fluorite and pyrochlore structure, Solid State Ionics, 9 (1983) 913-919.

Van Dijk, M.P., Burggraaf, A.J., Cormack, A.N., Catlow, C.R.A., Defect structures and migration mechanisms in oxide pyrochlores, Solid State Ionics, 17 (1985) 159-167.

Van Herle , J., Ihringer, R., Vasquez Cavieres, R., Constantin, L., Bucheli, O., Anode supported solid oxide fuel cells with screen-printed cathodes, J. Euro. Ceram. Soc., 21 (2001) 1855–1859.

Vasylechko, L., Vashook, V., Savytskii, D., Senyshyn, A., Niewa, R., Knapp, M., Ullmann, H., Berkowski, M., Matkovskii, A. & Bismayer, U., Crystal structure, thermal expansion and conductivity of anisotropic $La_{1-x}Sr_xGa_{1-2x}Mg_{2x}O_{3-y}$ (x=0.05, 0.1) single crystals, J. Solid State Chem., 172 (2003) 396-411.

Vayenas, C.G., Bebelis, S. I., and Kyriazis, C.C., Cogeneration: electricity + chemicals, Chem. Tech, 21 (1991) 422-428.

Vielstich, W., Lamm, A., Gasteiger, H.A., Handbook of Fuel Cells: Fundamentals, Technology, Applications, 4-Volume Set, John Wiley and Sons Inc. May, 2003.

Wagner, C., U¨ ber den Mechanismus der elektrischen Stromleitung im Nernststift.Naturwissenschaften, 31 (1943) 265-268.

Wang, L.S., Barnett, S.A., Deposition, Structure and Properties of Cermet Thin Films Comprised of Ag & Y-stbilized Zirconia, J. Electrochem. Soc., 139 (1992) 1134-1140.

Wang, L.S., Barnett, S.A., Ag-perovskite cermets for thin film solid oxide fuel cell air-electrode applications, Solid State Ionics, 76 (1995) 103-113.

Westphal, D., Mather, G.C., Marques, F.M.B., Jakobs, S and Guth, U., Ionic and electronic conduction in stoichiometric and sub-stoichiometric perovskites, Solid State Ionics, 136-137 (2000) 19-24.

Williamson, G.K., Hall, W.H., X-ray line broadening from filed aluminum and wolfram. Acta Metall., 1 (1953) 22-31.

Yamaji, K., Horita, T., Ishikawa, M., Sakai, N. & Yokogawa, H., Chemical stability of the $La_{0.9}Sr_{0.1}Ga_{0.8}Mg_{0.2}O_{2.85}$ electrolyte in a reducing atmosphere, Solid State Ionics, 121 (1999) 217-224.

Yamaji, K., Negishi, H., Horita, T., Sakai, N. & Yokokawa, H., Vaporization process of Ga from doped $LaGaO_3$ electrolytes in reducing atmospheres, Solid State Ionics, 135 (2000) 389-396.

Yamaji, K., Horita, T., Sakai, N., & Yokokawa, H., Comparison between $La_{0.9}Ba_{0.1}Ga_{0.8}Mg_{0.2}O_{2.85}$ and $La_{0.9}Sr_{0.1}Ga_{0.8}Mg_{0.2}O_{2.85}$ as SOFCs electrolytes, Solid State Ionics, 152-153 (2002) 517-523.

Yamashita, K., Nagai, M., Umegaki, T., Fabrication of green films of single- and multi- component ceramic composites by electrophoretic deposition technique, J. Mat., Sci., 32 (1997) 6661-6664.

Yi, J.Y. & Choi, G.M., The effect of reduction atmosphere on the $LaGaO_3$-based solid oxide fuel cell, J. Eur. Ceram. Soc., 25 (2005) 2655-2659.

Yoon, H.S., Choi, S.W., Lee, D., Kim, B. H., Synthesis and characterization of $Gd_{1x}Sr_xMnO_3$ cathode for solid oxide fuel cells, Journal of Power Sources, 93 (2001) 1-7.

Zha, S., Xia, C., Fang, X., Wang, H., Peng D. and Meng, G., Processing and electrical properties of doped-$LaGaO_3$ by gelcasting, Ceram. Intl., 27 (2001) 649-654.

Zhang, T.S., Ma, J., Kong, L.B., Hing, P., Leng, Y., Chan, S.C and Kilner, J.A., Sinterability and ionic conductivity of coprecipitated $Ce_{0.8}Gd_{0.2}O_{2-\delta}$ powders treated via a high-energy ball-milling process, J. Power Sources, 124 (2003) 26-33.

Zhao, F., Virkar, A.V., Dependence of polarization in anode-supported solid oxide fuel cells on various cell parameters, J. Power Sources, 141 (2005) 79-95.

Zhe Lü, Li Pei, Tian-min He, Xi-qiang Huang, Zhi-guo Liu, Yuan Ji, Xing-hai Zhao, Wen-hui Su, Study on new copper-containing SOFC anode materials, J. Alloy Compds. 334 (2002) 299-303.

Zheng, F and Pederson, L.R., Phase behavior of lanthanum strontium manganites, J. Electrochem. Soc., 146 (1999) 2810-2816.

Zheng, F and Pederson, L.R., Thermodynamic properties of Sr-doped LaMnO3 perovskite in the La-Sr-Mn-O system, J. Electrochem. Soc., 146 (1999) 2817-2820.

Zheng, F., Bordia, R.K., Pederson, L.R., Phase constitution in Sr and Mg doped $LaGaO_3$ system, Mater. Res. Bull., 39 (2004) 141-145.

Zheng, F and Chen, Y., High temperature electrode reactions of Sr and Mg doped $LaGaO_3$ perovskite, J. Mater. Sci. 43, (2008) 2058-2065.

Zhitomirsky, I., Petric, A., Electrophoretic deposition of electrolyte materials for solid oxide fuel cells, J. Mat. Sci., 39 (2004) 825-831.

Zhu, G., Fang, X., Xia, C and Liu, X., Preparation and electrical properties of $La_{0.4}Sr_{0.6}Ni_{0.2}Fe_{0.8}O_3$ using a glycine nitrate process, Ceram. Intl., 31 (2005) 115-119.

Zinkevich, M., Geupei, S., Nitsche, H., Ahrens, M., Aldinger, F., A study of the La2O3–Ga2O3 system by experiment and thermodynamic calculations, J. Phase Equilb. Diff., 25 (2004) 437-447.

Zinkevich, M., Geupel, S., Aldinger, F., Durygin, A., Saxena, S.K., Mei Yang and Zi-Kui Liu, Phase diagram and thermodynamics of the La_2O_3–Ga_2O_3 system revisited, J. Phys. Chem. Solids, 67 (2006) 1901-1907.

ABBREVIATIONS AND SYMBOLS

AC method	Alternating Current Method
AFC	Alkaline Fuel Cell
ASR	Area Specific Resistance
BSCF	Barium Strontium Cobalt Ferrite
BSE	Back-Scattered Electron
CP	Co-precipitation Method
D	Crystallite Size
DC method	Direct Current method
DSC	Differential Scanning Colorimetry
DTA	Differential Thermal Analysis
Ea	Energy of Activation
E_c	Cell Voltage
EDAX or EDS	Energy Dispersive X-Ray Spectroscopy
EIS	Electrochemical Impedance Spectroscopy
E_{meas}	OCP measured
EMF	Electromotive Force
$E_{Nernstian}$	Thermodynamic Nernstian Potential
EPD	Electrophoretic Deposition
E_r	Reversible Cell Voltage
FRA	Frequency Response Analyser
FTIR	Fourier Transform Infrared Spectroscopy
FWHM	Full Width at Half Maximum
GDC or CGO	Gadolinium Doped Ceria
GN	Glycine Nitrate Combustion Method
HIP	Hot Isostatic Pressing
I-P	Current Density – Power Density
ITSOFC	Intermediate Temperature Solid Oxide Fuel Cell
I-V	Current Density-Voltage plot
JCPDS	Joint Committee Powder Diffraction Society
LALLS	Low Angle Laser Light Scattering

LCO	Lanthanum Cobaltite
LDC	Lanthanum Doped Ceria
LFO	Lanthanum Ferrite
LGO	Lanthanum Gallate
LSC	Lanthanum Strontium Cobaltite
LSCF	Lanthanum Strontium Cobalt Ferrite
LSF	Lanthanum Strontium Ferrite
LSGM	Lanthanum Strontium Gallium Magnesium Oxide ($La_{1-x}Sr_xGa_{1-y}Mg_yO_{3-\delta}$)
LSM	Lanthanum Strontium Manganite
MCFC	Molten Carbonate Fuel cell
Ni+CSO or SDC	Nickel and Samarium Doped Ceria cermet
Ni+GDC	Nickel and Gadolinium Doped Ceria cermet
Ni+LSGM	Nickel and Lanthanum Strontium Gallium Magnesium Oxide Cermet
OCP or OCV	Open Circuit Potential or Open Circuit Voltage
P	Pechini method
PAFC	Phosphoric Acid Fuel Cell
PEFC	Polymer Electrolyte Fuel Cell
S_A	BET Surface Area
ScSZ	Scandia Stabilized Zirconia
SE	Secondary Electron
SEM	Scanning Electron Microscopy
SOFC	Solid Oxide Fuel Cell
TEM	Transmission Electron Microscopy
TGA	Thermogravimetric Analysis
t_{ion}	Ionic Transference Number
TPB	Triple Phase Boundary
TSOFC	Tubular Solid Oxide Fuel Cell
XRD	X-Ray Diffraction
YSZ	Yttria Stabilized Zirconia

δ	Oxygen content
ε	Lattice strain
ρ	X-ray density
σ_{bulk}	Bulk Conductivity

LIST OF FIGURES

LIST OF TABLES